



PhD Thesis

# **Synthesis, characterization and functionalization of metal and metal oxide nanoparticles. TEM Microscopy Study**

Author: Leonardo Pérez Mirabet

---

Supervised by:

Prof. Josep Ros Badosa

Prof. Ramón Yáñez López

PhD Program in Chemistry

Chemistry department – Science faculty



2013







PhD Thesis

# **Synthesis, characterization and functionalization of metal and metal oxide nanoparticles. TEM Microscopy Study**

Author: Leonardo Pérez Mirabet

---

Supervised by:

Prof. Josep Ros Badosa

Prof. Ramón Yáñez López

PhD Program in Chemistry

Chemistry department – Science faculty



2013





*Report submitted to aspire to the Doctor degree by:*

Leonardo Pérez Mirabet

*Checked and accepted:*

Prof. Josep Ros Badosa



Prof. Ramón Yáñez López



Bellaterra. Monday, September 16, 2013



Esta tesis está dedicada a mis padres y a mis abuelos, con todo el cariño y la gratitud del mundo.

Es gracias a vosotros que he llegado tan lejos,  
ahora y siempre...

**¡MUCHÍSIMAS GRACIAS!**





*“There's nothing in this universe that can't be explained. Eventually”.*

(Gregory House, M.D.)



# Acknowledgements

Bien, tras leer los agradecimientos de varios de mis compañeros en un vano intento de inspirarme, he decidido que los míos voy a escribirlos a mi manera, para variar...

Lo primero que debo decir es que para mí éstos han sido, sin lugar a dudas, los cinco años más intensos y de mayor cambio de mi vida. Si bien es cierto gran parte de todo lo que he hecho o experimentado en este tiempo ha tenido lugar fuera del ámbito donde he realizado mi tesis doctoral, sí que podríamos decir que la propia tesis ha obrado como telón de fondo del escenario en el cual se ha desarrollado toda la trama. No voy a entrar en detalles, puesto que esta sección lleva por título “acknowledgements” (agradecimientos en inglés) y no “biography” (biografía), pero aquellos que me han conocido durante este período, y sobre todo aquellos que me conocían de antes, sabrán a qué me refiero cuando lean estas líneas.

Así pues, este apartado está dedicado precisamente a todos los que me habéis acompañado no sólo durante estos cinco últimos años, sino también a los que habéis estado conmigo desde siempre. Vamos allá, ¡espero no dejarme a nadie!

En primer lugar quiero agradecer al Dr. **Josep Ros Badosa** y al Dr. **Ramón Yáñez López**, mis directores de tesis, por aceptarme en su grupo de investigación y darme la oportunidad de aprender y formarme como doctor. No sólo me han ayudado en el terreno científico, sino también en el personal, y eso es algo que se puede decir de muy pocos jefes.

Quisiera dar las gracias también a la Dra. **Susagna Ricart**, al Dr. **Joan Suades** y a la Dra. **Josefina Pons** por las charlas y consejos que me han dedicado durante todos estos años, así como al Dr. **Joan Sola**, quien siempre estaba dispuesto a atender y echar una mano a cualquiera que tuviera la suerte de conocerle.

Por supuesto, muchas gracias también al resto de profesores de dentro y fuera de la unidad de Química Inorgánica, especialmente a los doctores **Óscar Palacios** y **Gonzalo Guirado**, con quienes he compartido muchas charlas y sesiones de sushi en Cerdanyola, y al Dr. **Roger Bofill**, a quien tuve el placer de ayudar en mis primeras prácticas de laboratorio como docente.

Incontables gracias también a toda aquella gente de la U.A.B. que me ha ayudado en varios aspectos de mi tesis, como por supuesto al personal del “Servei de Microscopía de la UAB” **Emma Rossinyol**, **Pablo Castro** y **Onofre Castells**, por sus miles de horas ayudándome en mis épicas batallas contra el TEM de máxima resolución, así como a los tres excelentes técnicos de la sala blanca del ICMA B, **Neus Romà**, **Edgar León** y **Enrique Irisarri**, por enseñarme a lidiar con el microondas y la caja de guantes sin morir en el intento. Muchísimas gracias también a **Jordi Arbiol** y a

**Judit Oró**, también especialistas en microscopía electrónica, por ayudarme durante la tesis y mi posterior trabajo de técnico en la UAB. La ayuda de todos ellos ha sido inestimable e indispensable no sólo para hacer bien mi trabajo estos años, sino también para disfrutar con ello.

Especial agradecimiento también al Dr. **Rafal Dunin-Borkowski**, quien me aceptó en el “Center for Electron Nanoscopy” (CEN) para hacer mi estancia doctoral en Dinamarca, y al Dr. **Takeshi Kasama**, quien dirigió mi trabajo durante los meses que estuve allí y me enseñó gran parte de lo que he aprendido sobre microscopía electrónica de transmisión.

Obviamente, quiero dar las gracias a aquellos que han sido mis compañeros de laboratorio durante todos estos años, en especial a quienes más que compañeros ya tengo la suerte de poder llamar amigos:

- Ante todo muchas gracias a **Fran**, así como a **Sergio**, **Bet** y **Toni**, mis veteranos de laboratorio, por ser mis amigos dentro y fuera de la universidad, en especial en mis primeros años de doctorado, en los que necesité un fuerte apoyo personal. En este grupo también incluyo a **María Guix** y a **Fernando Martínez**, quienes pese a no estar en mi laboratorio también me han tendido su amistad sin esperar nada a cambio.
- Muchas gracias también a **Edu** y a **Bohores**, quienes llegaron más tarde pero no por esto han sido menos importantes. Ha sido un placer tenerlos de compañeros y espero nos sigamos viendo como amigos fuera de las fronteras de la UAB.
- Y, por supuesto, muchísimas gracias a un par de personas muy especial e importante para mí: **Marta Sangüesa** y **Josep Recasens**, a quienes conocí en mi último año de carrera y con quienes he pasado algunos de los mejores momentos de los últimos años. Espero, sinceramente, tenerlos a mi lado toda mi vida.

Quisiera mencionar también a otras personas a quienes he conocido en la UAB y que han contribuido a hacer de estos años un período a recordar con cariño:

Muchas gracias a mis amigos de la carrera **Vane** y **Fran** (a quien vuelvo a nombrar aquí) por hacerme reír y pasármelo bien durante incontables días de estudio, a mi amiga **Consu** de inglés, con quien he pasado muchos ratos geniales, y a mis profesores del “Servei de Llengües de la UAB” **Rosemary Twaite**, **Silvia Solà** y **José Ygoa**, quienes aparte de conseguir que me guste el inglés se han portado siempre excelentemente conmigo. Por supuesto también acordarme de mis compañeros de estancia en Dinamarca: **Miriam Varón**, **Giovanni Paladinni** (alias “capichi”), **Christian Chipont** y **Andrea**, con quienes pasé grandes momentos.

Aparte de mi círculo de la UAB, hay todo un conjunto de personas de mi ámbito familiar, así como amigos y antiguos profesores míos:

En primer lugar y ante todo, eternas e incontables gracias a mis padres, **Leonardo** y **Clara**, quienes me han criado con todo el cariño del mundo y me han educado para ser la persona que ahora soy. Sin vuestro apoyo y vuestros consejos éste trabajo, el cual os he dedicado, no habría sido posible.

Gracias también a mis abuelos (a la que aún sigue conmigo y a los que desgraciadamente ya no están) por las mismas razones por las que les he expresado a mis padres, así como al resto de mi familia, en especial a mis tíos **Manolo** y **Rosa**, por estar siempre a mi lado.

A parte de mi familia, quisiera dar las gracias a otra gente que ha contribuido a mi educación y/o formación y sin la cual no me hubiera sido posible llegar tan arriba: mis sinceros agradecimientos a mis profesores de las “**Salesianas de San Andreu**”, en especial a **Charo**, **Paco** y **Monste**, a mis profesores del “**Col·legi Sagrada Família de Sant Andreu**”, especialmente a **Inma Hernández**, **Miquel Guinart** y **Consell**, y cómo no, muchas gracias también a mis profesores de “**Stucom Centre d’ Estudis**”, en especial a **Toni Gregori**, **Rafa Ruiz**, **Jerónimo Sánchez**, **Joan Estany**, **Jordi Pérez** y **Pepa Maymó**. El mérito de todos vosotros es igual de grande que el de los profesores que me han instruido durante mi etapa universitaria.

Muchas gracias también a **Carmen Alda Elorza**, de “**psicolaf**”, por ayudarme con mis quebraderos mentales estos últimos años.

Y por supuesto, darles las gracias a mis amigos de fuera de la UAB, muchos de los cuales han estado conmigo desde mi infancia, por estar siempre a mi lado y darle significado a la palabra “**amistad**”. En especial gracias a:

- Mis amigos de toda la vida, los “**Salaos S.A.**” por mil y una razones para las cuales necesitaría otra tesis de 200 páginas entera para poder explicar. Gracias a **Agus**, **Dani Martín**, **Jordi**, “**Krikri**”, **Jacob**, **Cristian**, **Mario**, **Ferrán**, **Kodi**, **Cris Pla**, “**Kiny**”, **Pepe**, y sobre todo a **Dani Gómez**, con quien comparto muchas aficiones como el cómic y la música, así como a **Carlos** y **Javi**, a quienes conozco desde siempre y considero como mis hermanos.
- Mis amigos de fuera del barrio, **Patri** y **Omar**, por tantos momentos frikis que hemos compartido aquí y en Japón, así como a **Víctor**, por tomarse la molestia de reescribir “**El Hobbit**” de su puño y letra, y cómo no, a una pareja que ha estado conmigo en los buenos momentos y en los malos y por quienes siento un gran aprecio: **Erik** y **Yolanda**.
- Y por último, pero no en último lugar, a un grupito de amigos con quienes he empezado a ir este último año pero que me han demostrado que son unas personas excelentes: **Lourdes** y su hermana **Meri**, **Nika**, **Mireia**, **Óscar**, **Sergio**, **Gemma** y **David**.

A todos vosotros, ¡¡MUCHÍSIMAS GRACIAS POR TODO!!



# Contents

<b>I. Abbreviations</b> .....	23
<b>II. Motivation and Overview</b> .....	25

## **Part I: Introduction and characterization techniques** **27**

### **1. General introduction**

---

1.1 Thesis overview.....	31
1.2 Gold and silver nanoparticles stabilization with thiols and functionalization with Rhenium carbonyls.....	35
1.2.1 Gold and silver nanoparticles. General background.....	35
1.2.2 Synthetic routes.....	36
1.2.3 Transition-metal nanoclusters. Size and shape.....	37
1.2.4 Stabilization against aggregations.....	38
1.2.5 Stabilization with thiols.....	39
1.2.6 Functionalized thiol-stabilized nanoparticles.....	40
1.2.7 Gold and silver nanoparticles capped with rhenium carbonyl species. Future possible radiopharmaceutical applications.....	42
1.3 Iron oxide nanoparticles.....	44
1.3.1 Magnetism. Definition and general background.....	44
1.3.2 Iron oxide materials. Properties and applications.....	48
1.3.3 Iron oxide nanoparticles. Properties, applications and general synthetic routes.....	51
1.3.4 Iron oxide nanoparticles stabilization and functionalization. Surrounding species.....	53
1.4 Related Literature.....	56

## **2. Nanoparticle characterization techniques**

---

2.1 General background and classification.....	67
2.2 No microscopic techniques.....	68
2.2.1 UV- Visible spectroscopy.....	68
2.2.2 Infrared vibrational spectroscopy.....	68
2.2.3 X-ray Photoelectron Spectroscopy (XPS).....	69
2.2.4 Mössbauer spectroscopy.....	72
2.2.5 Magnetic behaviour studies: SQUID and FC-ZFC.....	74
2.2.6 X-Ray diffraction.....	76
2.2.7 Thermogravimetric Analysis (TGA).....	78
2.3 Microscopic techniques.....	80
2.3.1 Electron microscopy.....	80
2.3.2 Bright field TEM (BF TEM).....	90
2.3.3 Electron diffraction.....	91
2.3.4 Z-contrast (or HAADF).....	93
2.3.5 Energy-dispersive X-Ray Spectroscopy (EDX or XEDS).....	94
2.3.6 Energy Electron Loss Spectroscopy (EELS).....	94
2.3.7 Energy-filtered TEM (EFTEM).....	96
2.3.8 Electron holography.....	97
2.4 Related Literature.....	99

## **Part II: Thesis objectives**

**101**

### **3. Thesis objectives**

---

3.1 General description and objectives of the thesis.....	103
---	-----



## Part III: Experimental work, discussion and conclusions 107

### 4. Gold and silver nanoparticles functionalized with sodium 3-mercaptopropoate. Coordination with rhenium carbonyl complexes

---

4.1 General description of the carried out work.....	111
4.2 Experimental procedure.....	112
4.2.1 Materials and reactants.....	112
4.2.2 Synthesis of sodium mercaptopropoate (NaMP)-Capped Au nanoparticles.....	112
4.2.3 Synthesis of sodium mercaptopropoate (NaMP)-Capped Ag nanoparticles.....	113
4.2.4 Synthesis of Rhenium carbonyl initial complex [ <i>fac</i> -Re(H <sub>2</sub> O) <sub>3</sub> (CO) <sub>3</sub> ](CF <sub>3</sub> SO <sub>3</sub> ) for further coordination on nanoparticles' surface.....	113
4.2.5 Reaction of Sodium Mercaptopropoate (NaMP)-Capped Au Nanoparticles with [ <i>fac</i> -Re(H <sub>2</sub> O) <sub>3</sub> (CO) <sub>3</sub> ](CF <sub>3</sub> SO <sub>3</sub> ).....	113
4.2.6 Reaction of Sodium Mercaptopropoate (NaMP)-Capped Au Nanoparticles with [ <i>fac</i> -Re(H <sub>2</sub> O) <sub>3</sub> (CO) <sub>3</sub> ](CF <sub>3</sub> SO <sub>3</sub> ).....	113
4.3 Characterization and result discussion.....	114
4.3.1 TEM Bright Field microphotographs.....	114
4.3.2 X-ray powder diffraction.....	114
4.3.3 Visible-UV spectroscopy.....	114
4.3.4 XPS Analyses.....	118
4.3.4.1 General information obtained from the synthesized nanoparticles.....	118
4.3.4.2 Re (4f) analysis.....	122
4.3.4.3 O (1s) analysis.....	122
4.3.4.4 S (2p) analysis.....	124
4.3.4.5 C (1s) analysis.....	125
4.3.5 TGA Analyses.....	126
4.3.7 Vibrational studies.....	128

4.4 Summary.....	132
4.5 Related literature.....	133

## **5. One-pot synthesis of stable colloidal solutions of $MFe_2O_4$ nanoparticles using oleylamine as both solvent and stabilizer**

---

5.1 General description of the carried out work.....	137
5.2 Experimental procedure.....	139
5.2.1 Materials and reactants.....	139
5.2.2 Solvothermal synthesis of hexane colloidal dispersion of $Fe_3O_4$ magnetite nanoparticles.....	139
5.2.3 Solvothermal synthesis of hexane colloidal dispersion of $MFe_2O_4$ (M= Co, Mn, Cu, Zn) ferrite nanoparticles.....	139
5.2.4 Microwave-assisted synthesis of hexane colloidal dispersion of $Fe_3O_4$ magnetite nanoparticles.....	140
5.2.5 Microwave-assisted synthesis of hexane colloidal dispersion of $MFe_2O_4$ (M= Co, Mn, Cu, Zn) ferrite nanoparticles.....	140
5.3 Characterization and result discussion.....	141
5.3.1 TEM Bright Field microphotographs.....	141
5.3.2 Electron and X-ray diffraction.....	147
5.3.3 Electron-dispersive X-Ray Spectroscopy (EDX).....	149
5.3.4 Thermogravimetric analysis (TGA) and differential scanning calorimetry (DSC).....	154
5.3.5 Infrared (IR) measurements.....	155
5.3.6 Magnetic measurements.....	156
5.4 Summary.....	158
5.5 Related literature.....	161

## **6. Synthesis and characterization of Goethite nanorods. TEM ‘In-situ’ study of the phase change from Goethite to Hematite**

---

6.1 General description of the carried out work.....	165
6.2 Experimental procedure.....	167
6.2.1 Materials and reactants.....	167
6.2.2 Synthesis of Hexa- $\mu_2$ -acetato-triaqua- $\mu_3$ -oxo-triiron(III) nitrate acetic acid solvate, $[\text{Fe}_3\text{O}(\text{OCOCH}_3)_6(\text{H}_2\text{O})_3]\cdot\text{NO}_3$ .....	167
6.2.3 Hydrothermal synthesis of goethite nanorods.....	167
6.2.4 Modified hydrothermal synthesis of goethite nanorods.....	168
6.3 Basic information of all the different iron oxide species found (and formed) during the sample analyses.....	169
6.4 Characterization and results discussion.....	171
6.4.1 TEM Bright Field microphotographs.....	171
6.4.2 Electron and X-ray diffraction.....	178
6.4.3 Mössbauer spectroscopy.....	180
6.4.4 Magnetic measurements (SQUID, FC-ZFC and Electron holography).....	181
6.4.5 Energy-dispersive X-ray spectroscopy (EDX).....	184
6.4.6 Energy Filtered Transmission Electron Microscopy (EFTEM).....	186
6.4.7 Nanorods synthetic procedure carried out using $[\text{Fe}_3\text{O}(\text{OCOCH}_3)_6(\text{H}_2\text{O})_3]\cdot\text{NO}_3$ as a source of iron (III) and without adding any source of iron (II).....	187
6.5 Summary.....	189
6.6 Related literature.....	190

## **7. Synthesis and characterization of $\text{Fe}_3\text{O}_4@Au$ Core-Shell structures**

---

7.1 General description of the carried out work.....	193
7.1.1 Water-dispersible $\text{Fe}_3\text{O}_4@Au$ Core-Shell structures.....	193
7.1.2 Organic media-dispersible $\text{Fe}_3\text{O}_4@Au$ Core-Shell structures.....	194

7.2 Basic information about the most relevant works related to Fe <sub>3</sub> O <sub>4</sub> @Au described in literature.....	195
7.3 Experimental procedure.....	199
7.3.1 Materials and reactants.....	199
7.3.2 Water-dispersible core-shell structures.....	199
7.3.2.1 Synthesis of Tetramethylammonium hydroxide (TMAOH)-capped Fe <sub>3</sub> O <sub>4</sub> nanoparticles.....	199
7.3.2.2 Synthesis of Hexa- $\mu_2$ -acetato-triaqua- $\mu_3$ -oxo-triiron (III) nitrate acetic acid solvate, [Fe <sub>3</sub> O(OCOCH <sub>3</sub> ) <sub>6</sub> (H <sub>2</sub> O) <sub>3</sub> ] $\cdot$ NO <sub>3</sub> .....	199
7.3.2.3 Hydrothermal synthesis of hydrazine (NH <sub>2</sub> NH <sub>2</sub> )- capped Fe <sub>3</sub> O <sub>4</sub> nanoparticles.....	200
7.3.2.4 Synthesis of 1,6-hexanediamine (H <sub>2</sub> N(CH <sub>2</sub> ) <sub>6</sub> NH <sub>2</sub> )- capped Fe <sub>3</sub> O <sub>4</sub> nanoparticles using FeSO <sub>4</sub> as an iron source.....	200
7.3.2.5 Synthesis of 1,6-hexanediamine (H <sub>2</sub> N(CH <sub>2</sub> ) <sub>6</sub> NH <sub>2</sub> )- capped Fe <sub>3</sub> O <sub>4</sub> nanoparticles using FeCl <sub>2</sub> as an iron source.....	200
7.3.2.6 Formation of the gold shell around the previously synthesized magnetite cores.....	201
7.3.2.7 Gold nanoparticles formation with HAuCl <sub>4</sub> and NH <sub>2</sub> OH $\cdot$ HCl.....	201
7.3.3 Organic media-dispersible core-shell structures.....	201
7.3.3.1 Solvothermal synthesis of toluene colloidal dispersion of Fe <sub>3</sub> O <sub>4</sub> magnetite nanoparticles.....	201
7.3.3.2 Formation of the gold shell around the previously synthesized Fe <sub>3</sub> O <sub>4</sub> @Oleylamine cores in toluene medium.....	202
7.3.3.3 Formation of the gold shell around the previously synthesized Fe <sub>3</sub> O <sub>4</sub> @Oleylamine cores in oleylamine medium.....	202
7.3.3.4 Synthesis of oleylamine capped- gold nanoparticles.....	202
7.4 Characterization and results discussion.....	203
7.4.1 Organic media-dispersible Fe <sub>3</sub> O <sub>4</sub> @Au using Fe <sub>3</sub> O <sub>4</sub> @Oleylamine as a core.....	203
7.4.2 Water-dispersible Fe <sub>3</sub> O <sub>4</sub> @Au using Fe <sub>3</sub> O <sub>4</sub> @TMAOH as a core.....	206

7.5 Summary.....	213
7.6 Related literature.....	214



# Abbreviations

acac	Acetylacetonate
A TEM	Analytical Transmission Electron Microscope
BF TEM	Bright Field Transmission Electron Microscopy
CCD	Charge-Coupled Device
CPS	Counts per second
CS	Chemical Shift
DF TEM	Dark Field Transmission Electron Microscopy
DNA	Deoxyribonucleic acid
DP	Diffraction pattern
DSC	Differential Scanning Colorimetry
EDX	Energy-dispersive X-Ray Spectroscopy
EELS	Electron Energy-Loss Spectroscopy
EF TEM	Energy-Filtered TEM
EG	Ethylene glycol
ESCA	Electron Spectroscopy for Chemical Analysis
FC-ZFC	Field Cooling – Zero Field Cooling
FEG	Field Emission Gun
FFT	Fourier Fast Transformation
FT	Fourier Transformation
FWHM	Full Width at Half Maximum
HAADF	High-Angle Annular Dark-Field
HV TEM	High Vacuum TEM
IR	Infrared

MPA	Mercaptopropionic acid
MSA	Mercaptosuccinic acid
MW	Microwave
NaMP	Sodium 3-mercaptopropanoate
PEI	Polyethyleneimine
p-MBA	Mercaptobenzoic acid
QS	Quadruple Splitting
SAM	Self-assembled Monolayer
SE	Secondary electrons
SEM	Scattering Electron Microscope
SPR	Surface Plasmon Resonance
SQUID	Superconducting Quantum Interference Device
STEM	Scanning Transmission Microscope
TEM	Transmission Electron Microscope
TGA	Thermogravimetric Analysis
TMAOH	Tetramethylammonium hydroxide
TOAB	Tetraoctylammonium bromide
TREG	Triethylene glycol
UV	Ultraviolet
VLM	Visible Light Microscope
XPS	X-Ray Photoelectron Spectroscopy
XRD	X-Ray Diffraction



# Motivation and Overview

Nowadays, it is getting more and more common to hear the words “nanoparticles”, “nanoscience” and “nanotechnology” not only in academic environments, but also in our day-to-day. In fact, the number of commercial products synthesized with nanoparticles, or at least those that are formed by different kinds of nanomaterials, increases at a vertiginous rate.

However, it is not easy to understand how nanoparticles work and how their special properties make them worthy of being used in those new developed materials. It is for this reason that I decided to study the very basics of this entire topic: the synthesis and characterization of different kinds of nanostructures.

Therefore, developing new synthetic routes, as well as functionalizing the synthesized nanocrystals so as to make them suitable for different applications, has been the cornerstone of this thesis. Specifically, this research work is focused on synthesizing metallic (gold and silver) and metal oxide (magnetite and mixed ferrite) nanoparticles, as well as  $\text{Fe}_3\text{O}_4@Au$  core-shell nanostructures.

Apart from the synthetic process, their characterization, mainly using TEM-analysis techniques, has been another important part of the carried out work, as it will be explained in depth in this work.



# **Part I**

## **Introduction and characterization techniques**



# Chapter 1

## General Introduction

### Contents

---

1.1 Thesis overview.....	31
1.2 Gold and silver nanoparticles stabilization with thiols and functionalization with Rhenium carbonyls.....	35
1.2.1 Gold and silver nanoparticles. General background.....	35
1.2.2 Synthetic routes.....	36
1.2.3 Transition-metal nanoclusters. Size and shape.....	37
1.2.4 Stabilization against aggregations.....	38
1.2.5 Stabilization with thiols.....	39
1.2.6 Functionalized thiol-stabilized nanoparticles.....	40
1.2.7 Gold and silver nanoparticles capped with rhenium carbonyl species. Future possible radiopharmaceutical applications.....	42
1.3 Iron oxide nanoparticles.....	44
1.3.1 Magnetism. Definition and general background.....	44
1.3.2 Iron oxide materials. Properties and applications.....	48
1.3.3 Iron oxide nanoparticles. Properties, applications and general synthetic routes.....	51
1.3.4 Iron oxide nanoparticles stabilization and functionalization. Surrounding species.....	53
1.4 Related Literature.....	56

## 1. General Introduction

## 1.1 Thesis overview

According to physics, a particle is a small localized object which can be described by their physical properties, such as volume or mass<sup>1</sup>. This concept is a rather general description and it may be redefined as needed by various scientific fields.

Although there is no a specific rule to classify particles, they are usually classified according to their size<sup>2</sup>. In terms of particle diameter,  $\varnothing_{\text{part}}$ , they can be classified as shown in the **Table 1.1.1**

Terminology for particle sizes	
Description	Particle size
Supercoarse	$\varnothing_{\text{part}} > 10 \mu\text{m}$
Coarse	$2.5 \mu\text{m} \leq \varnothing_{\text{part}} \leq 10 \mu\text{m}$
Fine	$0.1 \mu\text{m} \leq \varnothing_{\text{part}} \leq 2.5 \mu\text{m}$
Ultrafine	$\varnothing_{\text{part}} \leq 0.1 \mu\text{m}$

**Table 1.1.1.:** General terminology for particle sizes.

**Figure 1.1.1** provides a visual comparison of the size of a fine particle (1.0  $\mu\text{m}$ ), coarse particle (10  $\mu\text{m}$ ), and a supercoarse particle (100  $\mu\text{m}$ ). There is an equivalent difference in size between Fine and Ultrafine particles size:

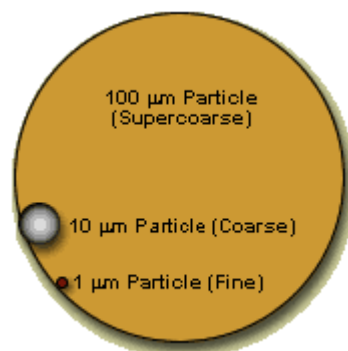


**Figure 1.1.1.:** Visual comparison of different particle sizes.

(from: <http://www.epa.gov/apti/bces/module3/category/category.htm>)

Given this classification, it is correct to talk about nanoparticles (or ultrafine particles) when they have, at least, one dimension lower than 100 nm.

Nanoparticles and nanoparticulate materials exist from ancient times. Although some of these nanoparticles have been synthesized deliberately (or not) by humans, it is also likely to find some natural-synthesized nanoparticles. For instance, mineral

## 1. General Introduction

nanoparticulates such as silica ( $\text{SiO}_2$ ) and the various forms of asbestos as well as black carbon are among the oldest natural nanoparticulate structures<sup>3</sup>. In addition, other mineral oxide nanoparticles such as hematite ( $\text{Fe}_2\text{O}_3$ ) were naturally formed in the ancient times and have persisted so far<sup>3</sup>. What is more, we can also find  $\text{Fe}_3\text{O}_4$  nanoparticle chains inside the ancient bacterium called *Magnetobacter*, which allows it to orientate itself by using natural magnetic fields<sup>4</sup>.

On the other hand, humans have also synthesized nanoparticles for a long time. Actually, it is possible to find some different nanostructures in old glasses, statues or pottery pieces<sup>5</sup>. However, the first mention to nanoparticles may be awarded to Michael Faraday, who was probably the first person who synthesized deliberately gold nanoparticles by reducing  $\text{Na}[\text{AuCl}_4]$  with an aqueous solution of  $\text{Na}[\text{AuCl}_4]$  with phosphorous in carbon disulfide. (**Figure 1.1.2.**) On February 5, 1857, Faraday delivered a Lecture of the Royal Society entitled “*Experimental Relations of Gold (and other Metals) to Light*” in which he exposed his conclusions about extremely finely divided metal particles in suspension<sup>6</sup>.



**Figure 1.1.2:** Faraday's gold nanoparticle dispersion (left), TEM image from this nanoparticles (middle) and Faraday's portrait (right)

(modified from: Edwards P. P.; Thomas J. M., *Angew. Chem. Int. Ed.* **2007**, 46, 5480-5486.)

Several years later, on 1959, Richard Feynman, an American physicist from the Technological Institute of California (Caltech), delivered a conference to the American Physical Society entitled “*There's Plenty of Room at the Bottom*”, in which he pointed the possibility of manipulating the atoms directly one by one, with a nanometric precision. Subsequently, Feynman received the Physics Nobel Award in 1965<sup>7</sup>.

Both the scientific and technological worlds have become very interested in nanoparticles and other kind of nanostructures. Nowadays, some governments spend huge amounts of money in the study of the “Nanoworld”. For instance, the EEUU budget during the 2005-2010 period was about 2.500 million euros, and the current UE budgeted since 2007 has reached 3.300 million euros<sup>8</sup>.



## 1. General Introduction

Nowadays, nanoparticles are of a great scientific interest as they are a kind of bridge between bulk materials and atomic or molecular structures. The bigger difference between these two kinds of materials lies in the fact that bulk materials have constant physical properties regardless of its size, while nanostructures present size-dependent physical properties<sup>9,10</sup>. Thus, the properties of nanoparticles change as their size decreases and as the percentage of atoms at the surface of a material increases and becomes significant in relation to those which are in the interior of the particle<sup>10</sup>.

Thus, the resulting nanoparticle properties are sometimes mostly due to the large material surface area, which overcomes the small bulk material contributions. For instance, nanoparticle suspensions are possible because of the particle surface interaction with the solvent, which is strong enough to exceed density differences, which otherwise could result in a material either floating or forming precipitates inside the medium.

Other size-dependent changes include different optical properties (i.e. gold nanoparticles are red and turn to dark purple when aggregate)<sup>11</sup>, or superparamagnetic behaviour at room temperature in magnetic materials<sup>12</sup>, among others.

As well as size, shape is also a crucial parameter which becomes necessary to control when studying nanoparticle properties. Sometimes, one compound may have different properties when changing its nanoparticle shape<sup>13</sup>.

As a result of all these particular properties, a lot of usefulness can be found in diverse branches of science such as catalysis<sup>14,15,16</sup>, nanosensors<sup>17,18</sup>, biology<sup>19</sup>, medicine<sup>20,21,22</sup>, or opto-electronics<sup>23,24</sup>, as well as unique technological applications<sup>25,26,27</sup>. These potential applications have resulted in a fast expansion of research in these kinds of structures. Nowadays, there is a huge interest in the development of synthetic protocols in order to control size, shape, morphology and crystallinity of metal nanoparticles.

Basically, we can differentiate two main branches of knowledge involving all the different studies and applications of nanostructures:

**-Nanoscience:** It is the study of all kind of nanostructures, involving their properties and the processes that happen at this scale.

**-Nanotechnology:** It is the search of the different applications of the studied nanostructures, by trying to control and manipulate them.

So far, some different kind of nanostructures have been developed and studied in depth. From simple metallic<sup>28,29,30,31</sup> or ceramic<sup>32,33,34</sup> materials until more complex structures, as for example core-shells<sup>35,36,37,38</sup>, all kind of new nanostructures are being not only developed also applied in the mentioned areas.

Obviously, conventional techniques used to analyze bulk materials should be merged with those specially designed to study the material structures at nanoscale, such

## 1. General Introduction

as scattering and transmission electron microscopy, **SEM** and **TEM** respectively. Thus, a large number of recently research works include studies of nanoparticle properties using both classical (for instance, Infra Red,**IR**, or Raman vibrational spectroscopy or classical magnetic behaviour tests) and electron microscopy techniques, among others<sup>39,40,41</sup>.

However, and in spite of the enormous number of scientific works published in the last years, there are still several problems when trying to obtain doable and reproducible synthetic methods. Most of the times the described methods found in literature are so difficult to repeat, and sometimes the stability and properties of the synthesized nanoparticles change so quickly, making them useless for certain kind of future applications. For this reason, several works focused on solving these problems are appearing lately<sup>42</sup>.

Basically, all the different methods to synthesize any kind of nanoparticles can be classified in two general groups:

**-Top-down:** This kind of synthetic procedures involve the breaking down of large material pieces in order to generate the desired smaller resultant nanoparticles from them.

**-Bottom-up:** Implies assembling single atoms and/or molecules so as to build larger nanostructures from them.

This thesis is mainly focused on the synthesis, via bottom-up methods, and characterization of different kind of nanostructures, involving iron oxides and metallic nanoparticles. According to the problems described before, we have focused our efforts in trying to develop or improve different synthetic procedures, as well as studying their properties.

### 1.2 Gold and silver nanoparticles stabilization with thiols and functionalization with Rhenium carbonyls

#### 1.2.1 Gold and silver nanoparticles. General background

Both gold and silver have played an important role in human history. In the case of gold, has been used around the world as a vehicle for monetary exchange, either in the form of gold coins or other bare metal quantities. The first references we can find about gold extraction date from Varna (Bulgaria) about the 5<sup>th</sup> millennium B.C.<sup>43</sup> In the case of silver, some slag heaps found in Asia indicate silver was being separated from lead as early as the 4<sup>th</sup> millennium B.C. using surface mining<sup>44</sup>. In both cases, they have been considered two of the most valuable metals.

As in ancient times materials were used for both esthetical and curative purposes, colloidal gold was used to make ruby glass and for coloured ceramics. An example of this fact is the Lycurgus Cup (**Figure 1.2.1.1**), which was created in the 5<sup>th</sup> to the 4<sup>th</sup> century B.C. Given the presence of gold colloids, it is ruby red in transmitted light and green in reflected light. On the other hand, silver nanocrystals have also been found in pottery of XVI century<sup>45,46</sup>.



**Figure 1.2.1.1:** Lycurgus' Cup, saw in reflected light (left) and in transmitted light (right).

Since then so far, gold and silver colloids have become an interesting research topic for many scientists around the world. Over the 20<sup>th</sup> century, several methods for the preparation of gold and silver colloids have been reported and reviewed<sup>47,48,49</sup>. In the last ten years, both gold and silver nanoparticles have been the subject of an increasing number of studies<sup>50,51,52,53</sup>.

In order to understand the general properties of this kind of particles, it is necessary to study the general background of the transition-metal nanoclusters, in which gold and silver nanoparticles are included.

### 1.2.2 Synthetic routes

Nanoclusters, as aforementioned, have generated intense interest over the last two decades due to their unique properties which lie between those of bulk and single-particle species<sup>54</sup>. Transition-metal nanoclusters, in particular, have many potential uses, including quantum computers<sup>55</sup> or quantum dots<sup>56,57</sup> chemical sensors<sup>58,59,60</sup>, or catalysis<sup>61,62</sup> among others.

So far, several types of transition-metal -nanoclusters, not only formed of gold or silver, but also of palladium<sup>63</sup>, platinum<sup>64</sup>, ruthenium<sup>65</sup> and others, have been synthesized and described in the literature.

General studies about transition-metal nanoclusters have been done in the last years, both studying several synthetic routes and their common physical properties. In 1994, Professor John Bradley classified the synthetic methods in four general groups, which are based on bottom-up synthetic procedures<sup>66</sup>:

- I. Transition metal salt reduction.
- II. Thermal decomposition and photochemical methods.
- III. Ligand reduction and displacement from organometallics.
- IV. Metal vapor synthesys.

Afterwards, in 1995, Professor Manfred Reetz added a fifth method<sup>67</sup>:

- V. Electrochemical synthesis.

In all cases, the processes are based on the ‘facile deposition of metallic precipitates’, which means to start working with a transition-metal initial compound (a metal salt or metal complex) and to reduce and precipitate it in a controlled way via one of the mentioned methods.

A part from synthesizing, it is also of a great importance to develop reproducible syntheses of a predetermined size, structure, shape and composition. As mentioned before, nanoparticle properties depend on these parameters, and transition-metal nanoparticles are not an exception.






### 1.2.3 Transition-metal nanoclusters. Size and shape

A great variety of nanoclusters with different shapes can be obtained via some different synthetic procedures. As gold nanoparticles are relatively easy to synthesize in some different sizes and shapes, several studies, both theoretical and experimental, have been carried out in order to study the atom distribution in the gold formed nanoparticles<sup>68,69</sup>.

Despite the fact that it is almost unlikely to study the exact structure of big nanoparticles, it is likely to describe how atoms organize themselves when forming small clusters. We can talk about “full-shell” or “magic number” clusters for those which have a complete and regular outer geometry. These full-shell clusters are formed by successive metal atom shells around a single metal atom. According to this rule, it is possible to form the following equation<sup>70</sup>:

where, in this equation:

Thus, full-shell metal nanoparticles, for instance gold and silver ones, usually follow the pattern shown in **Figure 1.2.3.1** of structure and number of atoms per particle:

Full-Shell "Magic Number" Clusters					
Number of shells	1	2	3	4	5
Number of atoms in cluster	M <sub>13</sub>	M <sub>55</sub>	M <sub>147</sub>	M <sub>309</sub>	M <sub>561</sub>
Percentage surface atoms	92%	76%	63%	52%	45%

**Figure 1.2.3.1:** Evolution of metal nanoclusters according to “full-shell”.

(from: Aiken II J.D.; Finke R.G., *J. Mol. Catal. A: Chem.*, **1999**, 145, 1-44.)

However, for bigger or different shape nanoparticles, it is very difficult to determine exactly the nanoparticle structure. Moreover, those atoms which are in the outset shell will always be affected for all the interface phenomena, and they will also play a key role in the stability of the formed nanoparticle.

### 1.2.4 Stabilization against aggregations

As described before, nanoparticle surface atoms are very important when studying the stability and reactivity of nanoparticles. In fact, when the percentage of atoms on the surface of the nanoparticle increases, they become more reactive yet less stable. Nanoclusters are only kinetically stable, which means they must be stabilized against aggregation; otherwise, they will aggregate into large particles and, eventually, they will become bulk material so as to reach their thermodynamic point of minimal energy<sup>71</sup>.

In order to avoid the aggregation process, stabilization must be achieved. This can be done in two different ways:

- **Electrostatic stabilization:** It occurs by the adsorption of ions on the nanoparticle surface. This adsorption generates an electrical double layer<sup>72</sup> resulting in a Coulombic repulsion force between individual particles.
- **Steric stabilization:** It occurs when nanoparticle surfaces are surrounded by layers of sterically bulky materials<sup>73</sup>, which form a steric barrier and prevent close contact between individual particles.

Those two processes, which are shown in **Figure 1.2.4.1**, are not only necessary when working with metal nanoparticles but also when synthesizing almost any kind of nanoparticles in solution.

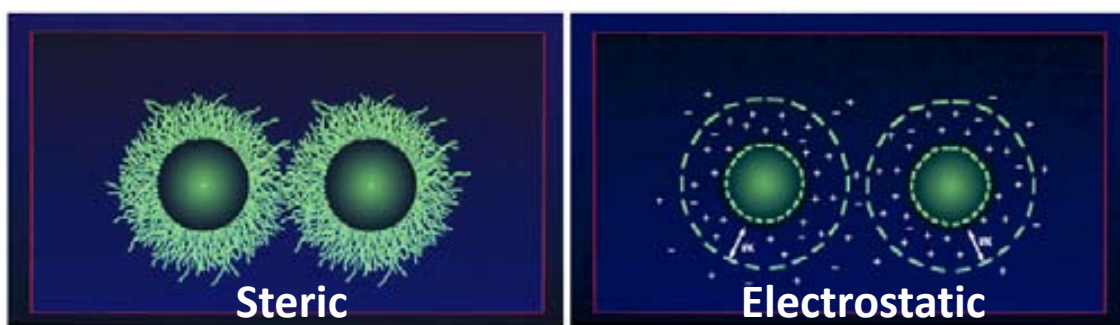


**Figure 1.2.4.1:** Graphic examples of Steric stabilization (left) and Electrostatic Stabilization (right).

(modified from: <http://www.pall.com/main/Fuels-and-Chemicals/Literature-Library-Details.page?id=5207>)

There are lots of examples of both gold and silver nanoparticles synthesized in some different media and stabilized via one of the two mentioned methods. When trying to achieve electrostatic stabilization, it is common to use a kind of reductant salt, such as sodium citrate  $\text{NaC}_6\text{H}_7\text{O}_7$ <sup>74</sup>, whose ions surround the formed nanoparticles and form the double layer.

On the other hand, when stabilizing nanoparticles via sterically bulky materials, some kind of surfactants can be used. Depending on the potential use of the resulting

nanoparticles, they can be surrounded by dendrimers<sup>75</sup>, polymers<sup>76</sup>, biomolecules such as DNA<sup>77</sup> or proteins<sup>78</sup> or organic ligands<sup>79</sup>.

### 1.2.5 Stabilization with thiols

To stabilize gold or silver nanoparticles, sulfur-containing species are among the most commonly used kind of ligands. Although different species with sulfur, such as xanthates<sup>80</sup> or disulfides<sup>81</sup> are sometimes used for this purpose, thiols have been the most extensively studied ones. This happens because of their affinity to metals like gold and silver. In fact, alkane thiols and other thiol-derived ligands are able to chemisorb on the metal surface by forming ‘metal-S’ bonds and leaving their hydrocarbon chains pointing outwards (**Figure 1.2.5.1**) which is called a self-assembled monolayer (**SAM**). In this way, they protect nanoparticles from agglomeration and reduce their surface activity.

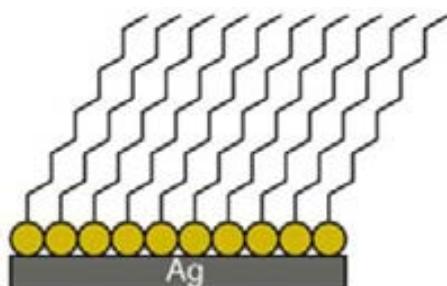


**Figure 1.2.5.1:** Illustration of the typical self-assembled monolayer (SAM) on silver surface. (from: <http://mrsec.wisc.edu/Edetc/nanolab/Agthiol/>)

Some works about thiol-metal SAMs have been reported, most of them using gold substrates, studying some parameters and properties (for instance their structure, defects and dynamics) of these kinds of supramolecular structures. These studies have been carried out both for SAMs formed on solid substrates<sup>82</sup> and on nanoparticle surfaces<sup>83,84</sup>.

It deserves special attention the work reported by P.D. Jadzinsky, et al<sup>85</sup>. In this work homogeneous gold nanoparticles capped with *p*-mercaptobenzoic acid (**p-MBA**) were synthesized and crystallized, allowing the study of their exact structure via X-ray analysis (**Figure 1.2.5.2**). It is shown here that the attached thiols are organized around the particle in a characteristic way which minimizes the surface energy. In order to achieve this low-energy state, interactions between two or more thiols take place. This work also explains that gold-sulfur interactions depend on the position of the gold atom in the nanoparticle surface.

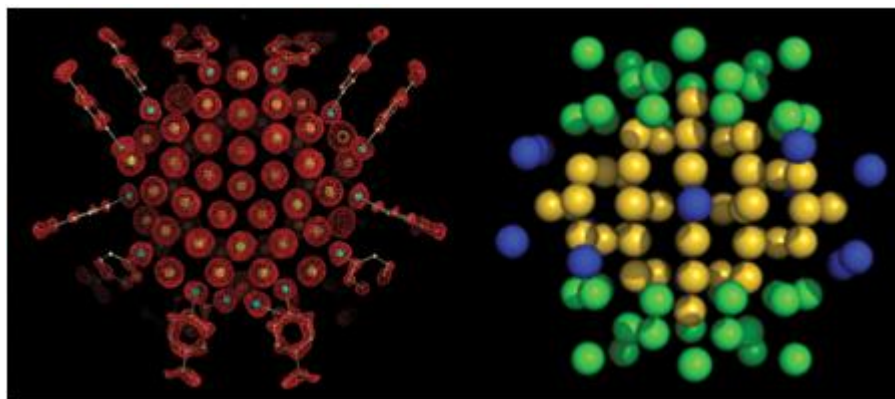


**Figure 1.2.5.2:** X-ray crystal structure determination of the gold nanoparticles capped with *p*-mercaptopbenzoic acid. (Modified from: P.D. Jadzinsky, et al. *Science* 318, 430, 2007, 430-

Despite the differences between these particles shown and any other thiol-capped gold nanoparticles, this work contributes enormously to the understanding of thiol-metal SAMs. In fact, F. Gygi, et al.<sup>86</sup> reported a theoretical study concerned in this structure, studying its electronic properties.

It is generally very difficult to study the structure of nanoparticles and their surfaces with this grade of detail, mostly due to the difficulty of crystallize them. For this reason, so far, this mentioned work is a remarkable exception among all the other studies reported in this field.

Apart from this example, a large number of works related to the synthesis and characterization of gold and silver nanoparticles using alkane thiols and thiol-derived surfactants have been reported. For example: mercaptosuccinic acid (MSA)<sup>87</sup>, 3-mercaptopropanoic acid (MPA)<sup>88</sup>, *p*-mercaptophenol<sup>89</sup>,  $\omega$ -bromoalkanethiols<sup>90</sup>,  $\omega$ -carboxylic acid-alkanethiols<sup>91</sup>,  $\omega$ -hydroxyl-alkanethiols<sup>92</sup>, oligo(ethyleneglycol)thiols<sup>93</sup>, thiol gelators<sup>94</sup>, amphiphilic thiols<sup>95</sup>, dihydrolipoic-derived acids<sup>96</sup>, phosphonic thiols<sup>97</sup>, sulfonic thiols<sup>98</sup>, thiol surfactants<sup>99</sup>, thiol-ammonium ligands<sup>100</sup>, chiral thiols<sup>101</sup>, and other functionalized thiols<sup>102</sup> have also been reported.

### 1.2.6 Functionalized thiol-stabilized nanoparticles

Thiol-derived species with another functional group, such as a carboxylic acid, can both stabilize nanoparticles and act as a coordinating ligand at the same time. The structure of that kind of thiols consists of three main parts (**Figure 1.2.6.1**):

1. A ‘Terminal Sulfur Group’, which binds the molecule to the nanoparticle surface through the ‘S’ atom.
2. An alkyl or aryl hydrocarbon chain, also called ‘Spacer Group’, which separates both sulfur and ‘Head’ groups. By varying the length as well as the structure



## 1. General Introduction

(alkyl or aryl) nature of this part, it is possible to change some properties of the resulting stabilized nanoparticles, as well as their stability inside the medium.

3. A 'Head Group' at the other end of the molecule, which is pointing outwards. This group plays a key role both in the stabilization and reactivity of the stabilized nanoparticles. For instance, it can act coordinating metallic ions.

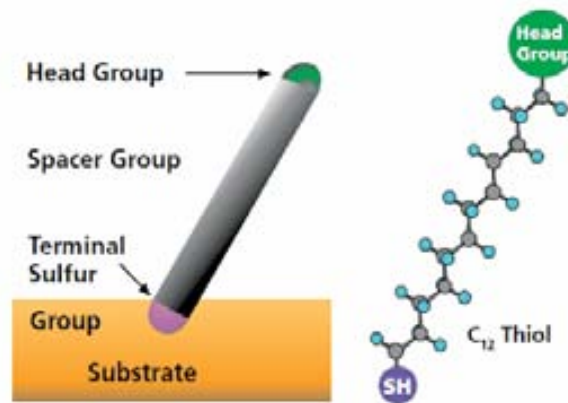


**Figure 1.2.6.1:** General structure of thiol-derived specie with a non-defined 'Head Group'. (from: <http://www.sigmaaldrich.com/technical-documents/articles/material-matters/self-assembled-monolayers.html>)

When combining the stability of gold or silver nanoparticles capped with thiols with the reactivity of transition metals, a new range of possible applications appears, for example, in catalysis<sup>103</sup>, sensors<sup>104</sup> or biomolecular<sup>105</sup> processes. So far, some different ligands have been reported in literature. Even though the most common ones are those which act as an N-, O- or P- donors, resulting organometallic complexes have also been used<sup>106</sup>.

A large number of different functionalized ligands attached to metal nanoparticles and their applications after coordinating transition metals were described in a Wilton-Ely's review<sup>107</sup>. Of a particular interest for this thesis is the work reported by S. Wang, et al.<sup>108</sup> in which gold nanoparticles stabilized with 3-mercaptopropionic acid (MPA) functionalized with ruthenium carbonyls were synthesized for catalysis applications. To obtain the resulting nanoparticles, sodium mercaptopropionate-capped gold nanoparticles were mixed with triruthenium dodecacarbonyl (**Figure 1.2.6.2**).

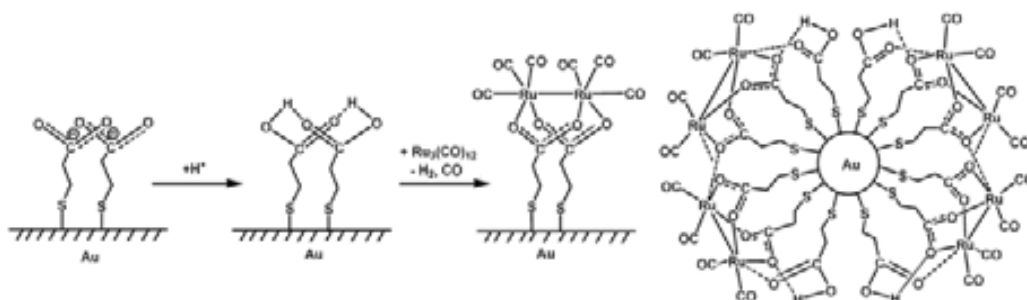


**Figure 1.2.6.2:** Process carried out for the synthesis reported by S. Wang, et al. (modified from: S. Wang; W-S Sim, Langmuir, 22 2006, 7861-7866)

### 1.2.7 Gold and silver nanoparticles capped with rhenium carbonyl species. Future possible radiopharmaceutical applications

One of the goals of the present thesis is to prepare gold and silver nanoparticles capped with MPA and functionalized with rhenium carbonyl species for future radiopharmaceutical applications.

One typical objective of radiopharmacy is the use of radiolabeled compounds for diagnostic and therapeutic purposes. In fact, it is very common to use rhenium and technetium carbonyls in this field due to their properties. In particular technetium-99m is a widely known  $\gamma$ -emitter employed for diagnosis in nuclear medicine and rhenium-188 is a  $\gamma$ - and  $\beta$ -emitter, which makes it a good candidate for therapeutic purposes<sup>109,110,111</sup> (Figure 1.2.7.1).

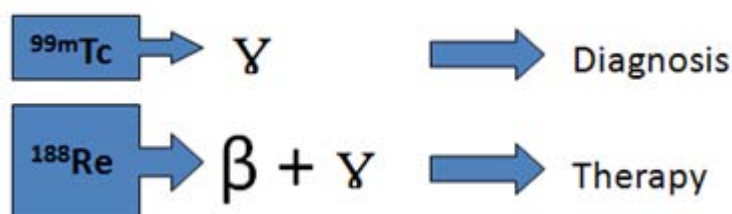


**Figure 1.2.7.1:** General scheme about the uses and kind of radiation emitted by  $^{99m}\text{Tc}$  and  $^{188}\text{Re}$ .

Although the use of both rhenium and technetium carbonyls have been delayed during a long time because of the absence of a good synthetic route, this fact changed due to the reports of simple methods to prepare  $[\text{M}(\text{H}_2\text{O})_3(\text{CO})_3]^+$  ( $\text{M} = ^{99m}\text{Tc}, ^{188}\text{Re}$ )<sup>112, 113, 114</sup>. Currently, a wide range of complexes are being prepared by simple substitution of the water molecules present in the mentioned complexes by appropriate ligands<sup>115,116,117,118,119,120</sup>. In addition, nanoparticles play a relevant role in radiopharmacy<sup>121</sup>, being used in lymphoscintigraphy for the detection of sentinel lymph nodes<sup>122</sup>. What is more,  $^{188}\text{Re}$  nanoparticles present promising applications for malignant tumour therapy<sup>123</sup>. Thus, by coating gold or silver nanoparticles with rhenium carbonyl, via convenient reaction with  $[\text{M}(\text{H}_2\text{O})_3(\text{CO})_3]^+$ , a new approach could be employed so as to synthesize new  $^{99m}\text{Tc}$  and  $^{188}\text{Re}$  radiopharmaceutical colloids.

It is mandatory to point out that both gold and silver nanoparticles, apart from being relatively easy to synthesize in aqueous medium, are human biocompatible species which should not present any kind of danger after being introduced into human body<sup>124,125,126</sup>. In the case of silver nanoparticles, they present a powerful antibacterial activity<sup>127,128</sup>, so in their case the resulting functionalized nanoparticles could combine both the antibacterial character of silver with the diagnostic properties of  $^{99m}\text{Tc}$  or the therapeutic possibilities of  $^{188}\text{Re}$ .

## 1. General Introduction

Specifically, the work related in chapter X relates the characterization of synthesized metal (gold or silver) nanoparticles stabilized with **MPA** and complexed with *fac*-[M(H<sub>2</sub>O)<sub>3</sub>(CO)<sub>3</sub>]<sup>+</sup>, using [Re(H<sub>2</sub>O)<sub>3</sub>(CO)<sub>3</sub>](CF<sub>3</sub>SO<sub>3</sub>) as a precursor. The experimental work was carried out with a mixture of Re-185 (37.4%) and Re-187 (62.6%), which are no radioactive rhenium isotopes. (**Figure 1.2.7.2**)

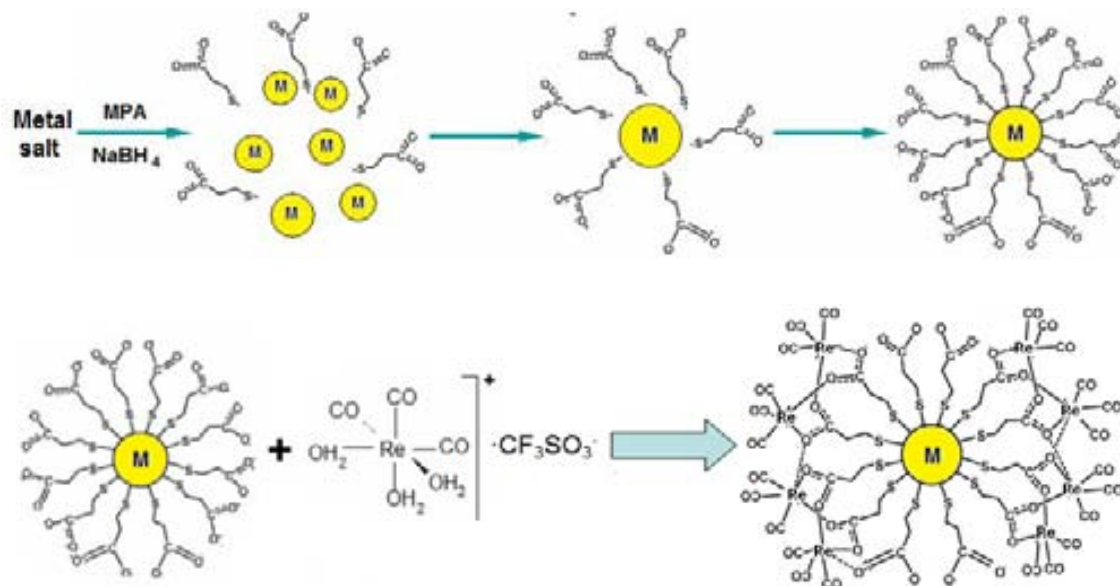


**Figure 1.2.7.2:** General scheme about the gold nanoparticles formation as well as their fictionalization process with rhenium carbonyl species.

## 1.3 Iron oxide nanoparticles

### 1.3.1 Magnetism. Definition and general background

Magnetism is a physical phenomenon through which certain materials exert attraction or repulsion forces over others. Certain well-known materials, such as nickel, iron or cobalt and their alloys, also called ‘magnets’ show easily detectable magnetic properties<sup>129</sup>. However, all materials can be influenced by a magnetic field<sup>130</sup>.

The magnetic behaviour of any material depends mainly on its own structure and, particularly, on its electronic configuration<sup>133</sup>. Given the fact that electrons are small magnets, the number and distribution of electrons inside a material will determine its final magnetic properties.

Basically, there are two different magnetic fields associated to electrons. The first one is an intrinsic magnetic field, characteristic of the electron itself<sup>131</sup>, and the second one is a field generated by the orbital movement of the electron around the atomic nucleus<sup>132</sup>. Generally, all the resulting electron magnetic fields are randomly oriented in some different directions. However, under certain conditions they can be aligned, producing a measurable total magnetic field<sup>133</sup>.

Both kinds of magnetic fields generate magnetic dipoles, which have two opposite parts, a “North Pole” and a “South Pole” (Figure 1.3.1.1). As magnetic fields have both energy and physical systems which are stabilized with low-energy configurations, when a magnetic dipole is under the effect of a magnetic field, it tends to be oriented only with one pole different to the field, by cancelling it as much as possible and decreasing the energy levels of the magnetic field – magnetic dipole system<sup>136</sup>.

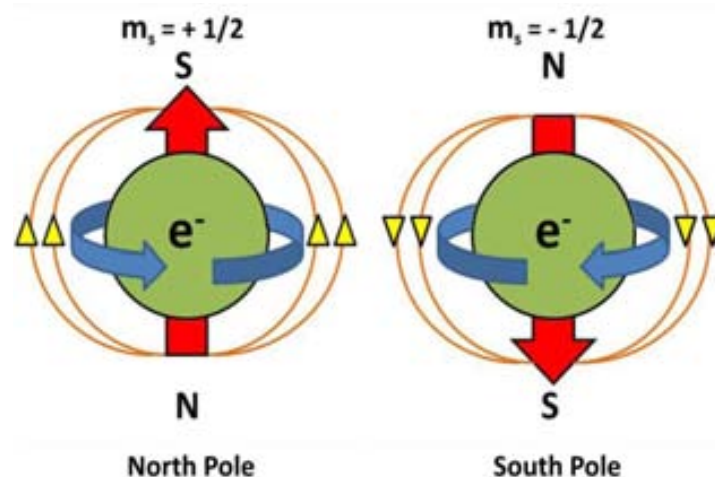


**Figure 1.3.1.1:** Illustration of the intrinsic magnetic field of the electron, which generates a magnetic dipole. Its orientation depends on the electron quantum spin,  $m_s$ .

## 1. General Introduction

The total atomic magnetic moment is the sum of the entire magnetic moments of the individual electrons<sup>134</sup>. Normally, this magnetic moment is reduced by the resulting magnetic dipoles, which are prone to being opposed to others. Thus, when an atom has all its electronic orbitals full of paired electrons, the resulting atomic magnetic moment is normally cancelled. On the other hand, atoms with unpaired electrons or half full orbitals have a magnetic moment different from zero, which strength depends on the number of unpaired electrons.

Since the difference in the electronic configuration of different elements determines the nature and magnitude of the magnetic atomic moments, it is possible to find materials with different magnetic properties. According to their magnetic behaviour, it is possible to sort the different materials in the following groups<sup>135</sup>:

**No magnetic materials:** There is no magnetic reaction to an applied magnetic field.

**Example:** Vacuum.

**Diamagnetic materials:** Weakly magnetic materials, which tend to oppose themselves to an applied magnetic field, and therefore, to be repelled by a magnetic field. They have all their electronic orbitals full of paired electrons.

**Examples:** Bismuth (Bi), silver (Ag), lead (Pb), water.

**Paramagnetic materials:** Magnetic materials only attracted when in presence of an externally applied magnetic field. They have unpaired electrons.

**Examples:** Air, aluminum (Al), palladium (Pd).

**Ferromagnetic materials:** Magnetic materials that retain their magnetization in the absence of an external field, so that they can generate a magnetic field themselves. There is a tendency for the intrinsic magnetic moments of neighboring electrons to point all of them in the same direction. Therefore, those magnetic moments of atoms in a ferromagnetic material make them behave like tiny permanent magnets. When the external field is removed, their electrons remain together and align themselves into small regions with a certain degree of uniform alignment called magnetic domains.

**Examples:** Iron (Fe), cobalt (Co), nickel (Ni) or ferrites.

**Antiferromagnetic materials:** Materials with a zero net magnetic moment. So, they cannot generate a magnetic field. Unlike ferromagnetic materials, there is a tendency for the intrinsic magnetic moments of neighboring electrons to point in

opposite directions. All of them have a characteristic ‘Neel Temperature’, above which every antiferromagnetic material becomes paramagnetic.

**Example:** Manganese oxide (MnO).

**Ferrimagnetic materials:** Materials that, like ferromagnetic ones, retain their magnetization in the absence of an external field. However, like antiferromagnetic materials, neighbouring pairs of electron spins point towards opposite directions. Despite this fact, there is more magnetic moment from one kind of electrons that point in one direction, than from the others, which result in a net magnetic moment different from zero.

**Example:** Magnetite (Fe<sub>3</sub>O<sub>4</sub>).

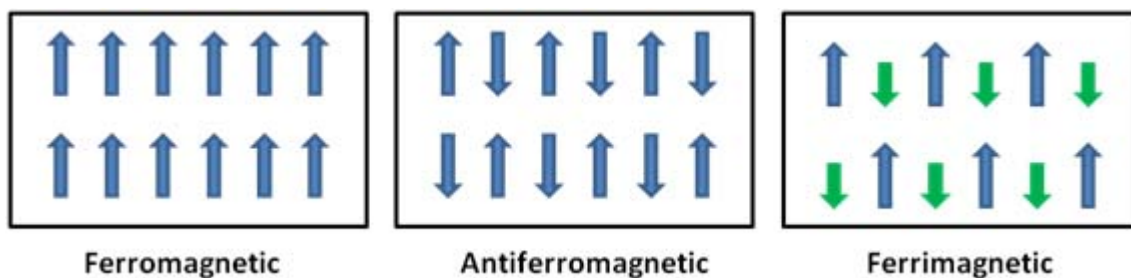


**Figure 1.3.1.2:** Illustration of the magnetic moment orientations in ferromagnetic, antiferromagnetic and ferrimagnetic materials.

Apart from all the described materials, there is another ‘special’ kind which just ‘shows up’ when working with tiny nanometric materials, for they behave differently after reaching a certain size:

**Superparamagnetic materials:** They are ferromagnetic or ferrimagnetic materials small enough to act as a single magnetic domain or electronic spin. They are so small that are affected by the thermal energy, which changes their magnetic moments. As a result, above a certain temperature, their response to a magnetic field is qualitatively similar to the expected for paramagnetic materials, but much larger.

**Example:** Magnetite or ferrite nanoparticles of a certain size.

The magnetic strength of a material is called **magnetization**, **M**. For bulk ferromagnetic materials, **M** is the vector sum of all the magnetic moments of the atoms per volume unit of the material<sup>136</sup>. Since bulk materials consist on magnetic domains, each one with its own magnetization vector, **M** decreases when the magnetization vectors are not aligned. So, for smaller materials, the number of domain decreases as well. When the length scale of material becomes smaller than a critical size, **dc**, there is just a single domain which magnetization vector coincides with **M**<sup>136</sup>, as is shown in **Figure 1.3.1.3**. In that case, for certain kinds of materials, they can behave as superparamagnets.

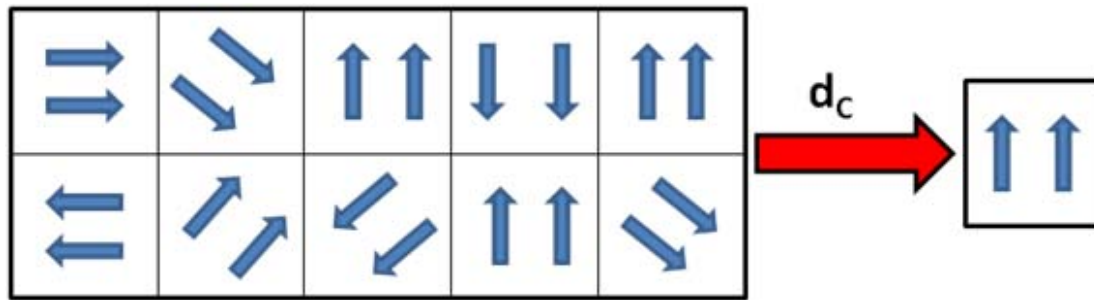


**Figure 1.3.1.3:** Illustration of a bulk material with multiple domains (right) and a small material with only one single domain. For the bulk material,  $\mathbf{M}$ , results from the vectorial sum of all the magnetization vectors. For the small material, it coincides with the magnetization vector of the single domain.

Thus, when a ferromagnet with a certain  $\mathbf{M}$  is subjected to a magnetic field with a strength  $\mathbf{H}$ , the resulting magnetization curve (**Fig 1.3.4**) shows that  $\mathbf{M}$  increases with  $\mathbf{H}$  until reaching a saturation value,  $\mathbf{M}_s$ . Since not all domains return to their original orientations when  $\mathbf{H}$  is decreased after reaching the magnetic saturation point, the magnetization curve displays a hysteresis loop. Thus, when the magnetic field is removed, a remnant magnetization can be observed,  $\mathbf{M}_R$ . In order to remove it, a coercive field,  $\mathbf{H}_C$ , must be applied in the opposite direction to the initially applied field<sup>133</sup>.

On the other hand, single domain magnetic materials (**Fig 1.3.4**), for instance iron oxide nanoparticles smaller than about 20 nm, have no hysteresis loop. This kind of behaviour is called superparamagnetic<sup>133</sup>.

This kind of experiment, usually ruled by using a **SQUID (superconducting quantum interference device)**, which is a very sensitive magnetometer used to measure extremely subtle magnetic fields, is very useful when trying to determine the magnetic behaviour of a material<sup>136</sup>. This technique will be subsequently explained, as well as others, in the corresponding section of this work.



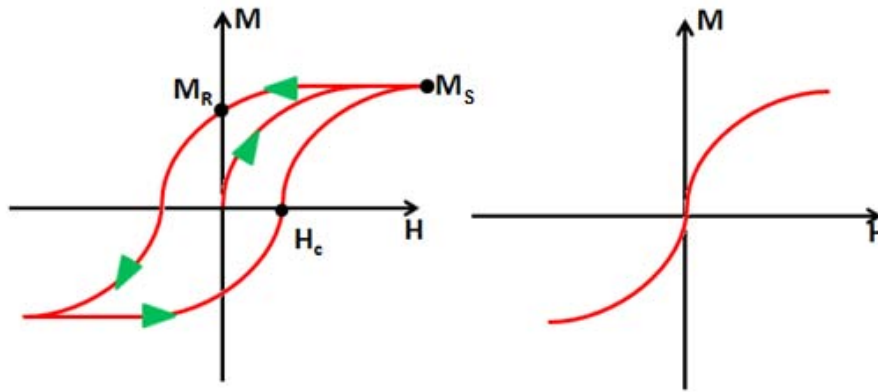


**Figure 1.3.1.4:** Illustration of a typical hysteresis loop produced when applying a magnetic field on a ferromagnet (left) and the resulting data obtained when ruling the same experiment on a superparamagnetic material (right).

One of the most studied groups of materials, since some of them are well-known magnetic materials very widespread in nature, is the family of iron oxides.

### 1.3.2 Iron oxide materials. Properties and applications

Iron oxides have been studied in depth since some of them are materials with a measurable magnetic behaviour, and they are also especially easy to find or produce, and stable enough to work with<sup>137</sup>. Their magnetic properties are given to the iron atom, which has a strong magnetic moment due to its four unpaired electrons in the  $3d$  orbitals. Thus, when crystals have iron atoms (with any of its typical oxidation state) inside its structure, different magnetic states can arise.

Generally, the crystal structure of any kind of iron oxide can be considered as close-packed planes of oxygen anions with iron cations taking up some of the resulting octahedral or tetrahedral interstitial sites, as shown in **Figure 1.3.2.1**:

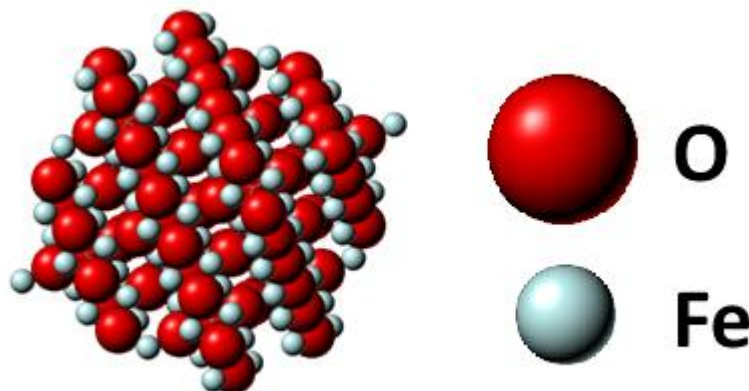


**Figure 1.3.2.1:** Oxygen packaging for a magnetite crystal, with oxygen atoms (in red) forming close-packed planes and the smaller iron cations (in black) occupying some interstitial sites.



## 1. General Introduction

There are some different kinds of iron oxides in nature, but the three most common are **magnetite** ( $\text{Fe}_3\text{O}_4$ ), **maghemite** ( $\gamma\text{-Fe}_2\text{O}_3$ ) and **hematite** ( $\alpha\text{-Fe}_2\text{O}_3$ ). Since those three different forms are, besides, very important technologically, they have been the object of many different studies so far<sup>138,139,140,141,142,143</sup>. Some of their physical and magnetic properties are summarized in **Table 1.3.2.1**<sup>141</sup>:

Property	Iron Oxide		
	Magnetite	Maghemite	Hematite
Molecular formula	$\text{Fe}_3\text{O}_4$	$\gamma\text{-Fe}_2\text{O}_3$	$\alpha\text{-Fe}_2\text{O}_3$
Density ( $\text{g/cm}^3$ )	5.18	4.87	5.26
Melting point ( $^\circ\text{C}$ )	1583-1597	-----	1350
Type of magnetism	Ferrimagnetic	Ferrimagnetic	Weakly ferromagnetic (or ferromagnetic)
Curie temperature ( $^\circ\text{K}$ )	850	820-986	956
Free energy formation $\Delta G_f^\circ$ (KJ/mol)	-711.1	-1012.6	-742.7
Crystallographic system	Cubic	Cubic with a tetragonal supercell	Rhombohedral or hexagonal
Structural type	Inverse spinel	Defect spinel	Corundum
Lattice parameter (nm)	$a=0,83$	$a=0,83$ (cubic) $a=0,83$ ; $c=2,5$ (tetragonal)	$a=0,50$ ; $c=1,38$ (hexagonal) $a_{\text{Rh}}=0,54$ , $\alpha=55,3^\circ$ (rhombohedral)

**Table 1.3.2.1:** Physical and magnetic properties of Magnetite, Maghemite and Hematite.

Their different elementary cells are shown in **Figure 1.3.7**. In the case of magnetite and maghemite, both derive from a spinel ( $\text{MgAl}_2\text{O}_4$ ) structure. Spinel is a kind of mineral with a general formula  $\text{A}^{2+}\text{B}_2^{3+}\text{O}_4^{2-}$ , which form a cubic crystal system. As aforementioned, oxide anions are arranged in a cubic close-packed lattice, with the cations **A** and **B** occupying some or all the octahedral and tetrahedral sites in the lattice. In the case of magnetite,  $\text{A}^{2+} = \text{Fe}^{2+}$  and  $\text{A}^{3+} = \text{Fe}^{3+}$ . In the case of maghemite, however, there are only  $\text{Fe}^{3+}$  cations inside the oxide anions lattice. On the other hand, hematite has a “corundum-like” ( $\text{Al}_2\text{O}_3$ ) structure, with a rhombohedral or hexagonal crystal system. In that case, iron cations are taking up tetrahedral sites in the oxygen close-packed lattice<sup>141</sup>.

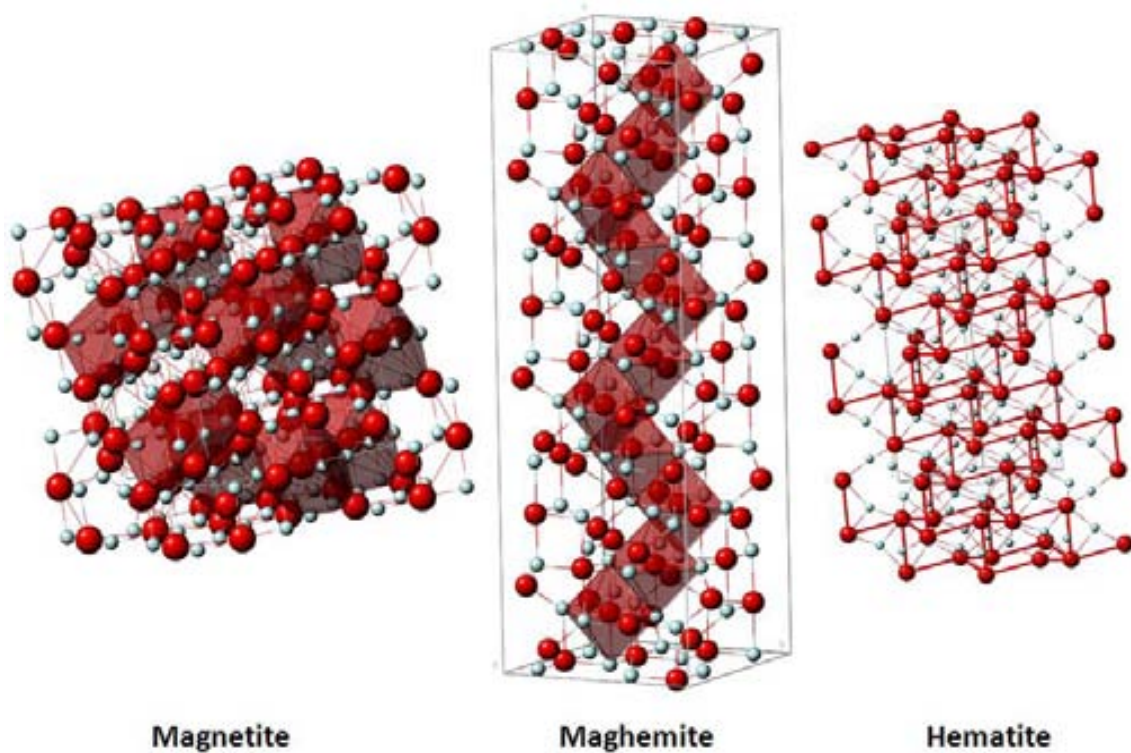


**Figure 1.3.7:** Illustration of the elementary cells of Magnetite (cubic), Maghemite (cubic with a tetragonal supercell) and Hematite (Rhombohedral or hexagonal)

Since each iron oxide structure is quite different from others, their possible applications are obviously different too. For instance, magnetite and maghemite are commonly used in magnetic recording tapes<sup>144,145</sup>, as a sorbents<sup>146</sup>, or even as a pigments<sup>147</sup>.

Apart from the mentioned uses, the magnetic properties of iron oxides have been also widely used in a broad range of applications, as magnetic seals<sup>148,149</sup>, ferrofluids<sup>150,151</sup>, catalysis<sup>152,153</sup> or even medical applications<sup>154,155</sup>. It is mandatory to point out, however, that synthesizing iron oxide nanoparticles with specific sizes, shapes, and surfaces is becoming very important in order to spread the range of applications of those kinds of materials.

### 1.3.3 Iron oxide nanoparticles. Properties, applications and general synthetic routes

As aforementioned, nanoparticles have special properties owing to their size. This way, by combining the inherent magnetic properties of iron oxides with the special ones that they can achieve when their size is reduced to a nanometric scale, some new interesting properties and applications can be obtained.

In this vein, many different synthetic procedures, mainly focused on synthesizing magnetite and maghemite nanoparticles, have been developed so far. The five most important, all based in bottom-up synthetic procedure, (**Figure 1.3.8**) are described as follows:

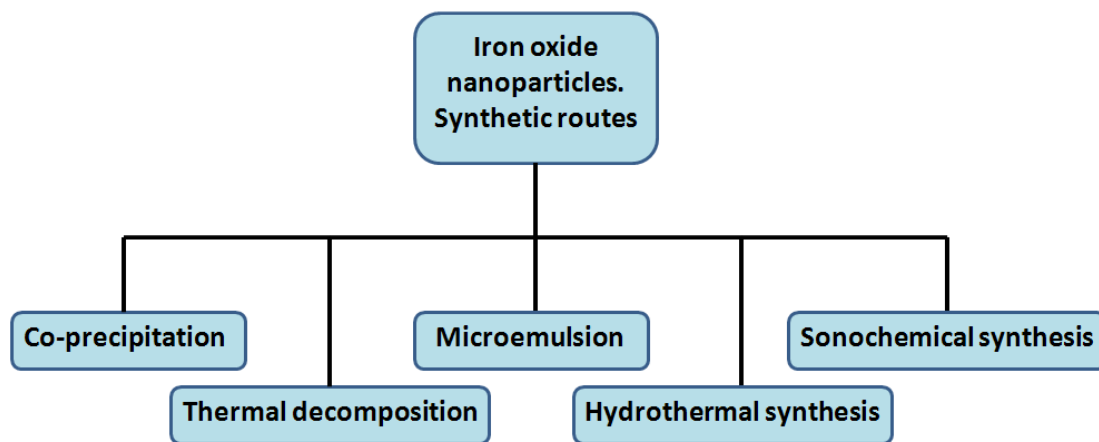


**Figure 1.3.3.1:** Diagram of the five main different iron oxide nanoparticles synthetic routes.

**Co-precipitation:** This is the most conventional method for obtaining  $\text{Fe}_3\text{O}_4$  or  $\gamma\text{-Fe}_2\text{O}_3$  nanoparticles. It is based on mixing ferric and ferrous ions (1:2 molar ratios) generally in highly basic solutions, although they may also be synthesized in acidic media<sup>156</sup>. The reaction can be heated or carried out at room temperature, and the atmosphere may be also controlled so as to avoid unexpected oxidation processes. The resulting nanoparticle properties will be determined by the initial reaction parameters, such as the reaction temperature, pH value, or the ionic strength of the media, among others.

Even though this is an easy method to obtain stable nanoparticles in an aqueous media, sometimes it is necessary to add a surfactant to the medium in order to narrow the range of obtained nanoparticles<sup>157,158</sup>.

**Thermal decomposition:** This method is based on decomposing and oxidizing iron precursors, such as  $\text{Fe}_3(\text{CO})_{12}$ <sup>159</sup>, or  $\text{Fe}(\text{acac})_3$ <sup>160</sup> (acac = acetylacetonate) in an organic medium by using high temperatures.

## 1. General Introduction

This method has many advantages, because it produces highly monodispersed nanoparticles with a narrow size distribution. However, its disadvantage is that the resulting nanoparticles can generally be only dissolved in nonpolar solvents<sup>161</sup>.

**Microemulsion:** This method is based on producing a thermodynamically stable and homogeneous dispersion of two immiscible phases (generally water and oil) by using a surfactant, which molecules may form a monolayer at the resulting interface. By doing so, inverse micelles are formed, which internal spaces act as ‘nanoreactors’, by controlling the size and form of the resulting nanoparticles<sup>162,163</sup>, as shown in **Figure 1.3.3.1**.

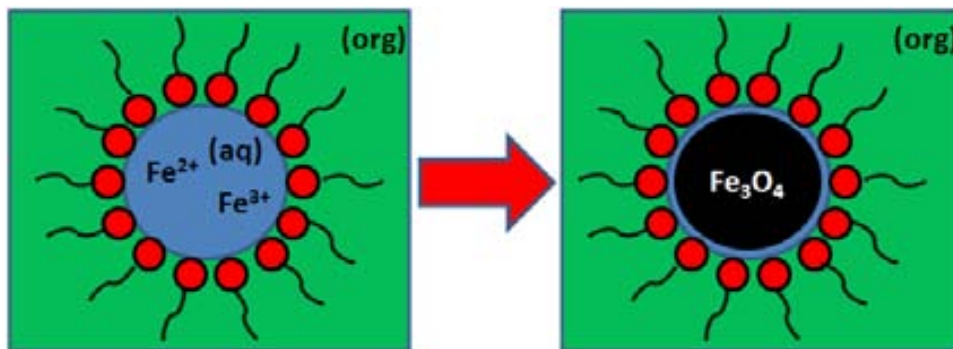


**Figure 1.3.3.1:** Illustration of a magnetite nanoparticle formation inside an inverse micelle

**Hydrothermal synthesis:** This method includes many chemical technologies used to form nanoparticles in a sealed reactor by applying high temperatures and high vapour pressure to an aqueous solution<sup>164,165</sup>. The grains formed this way have generally a good crystallinity, better than those formed via other methods. As a consequence, this synthetic method is useful when preparing iron oxide or other kinds of nanostructures with unusual shapes<sup>166,167</sup>.

**Sonochemical synthesis:** This method is based on the chemical effects produced by the ultrasounds arising from acoustic cavitation, which are the formation, growth and implosive collapse of bubbles in liquid. During the cavitation process, the bubble implosions generate localized hotspots in which nanoparticles can be formed<sup>168</sup>. Sometimes, those particular conditions allow the nanoparticle synthesis under unusual conditions, in which it would be impossible to synthesize them<sup>169</sup>. In addition, the nanoparticles formed by this method may present improved properties in comparison with those synthesized via other methods<sup>170,171</sup>.

### 1.3.4 Iron oxide nanoparticles stabilization and functionalization. Surrounding species

In some cases, and depending on their final purpose, the synthesized nanoparticles must be surrounded and protected with a proper surface coater, which not only stabilize the resulting nanoparticles in front of aggregation, but also functionalize them so that they can be applied in many different fields. So far, W. Wu, et al.<sup>172</sup> has reported the most accurate classification of all the different species which can be applied to protect and functionalize iron oxide nanoparticles. (**Figure 1.3.4.1**)

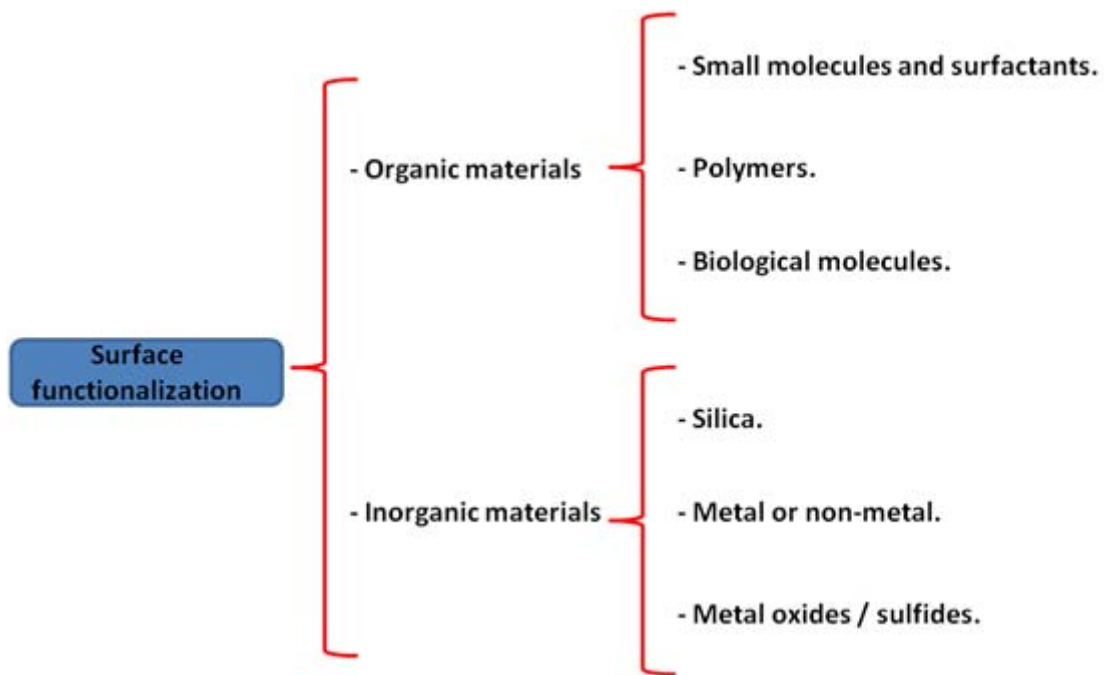


**Figure 1.3.4.1:** W. Wu, et al. Classification of different kinds of surfactants for iron oxide nanoparticles. (Source: Wu W.; Jiang C., *Nanoscale Res. Lett.*, **2008**, 3, 397-415)

Basically, Wu divided all the possible surfactants in two main groups, organic and inorganic materials:

**Organic materials:** Organic materials or compounds are overall used to stabilize the iron oxide nanoparticle surface so as to avoid agglomeration and also to functionalize them, increasing their range of applications. In the case of polymers, which have unique physical and chemical properties, some works using natural (Dextran<sup>173,174</sup> or Gelatin<sup>175,176</sup>) and synthetic polymers, such as Poly(ethyleneglycol)<sup>177</sup> or Poly(vinylpyrrolidone)<sup>178</sup> have been reported so far. When working with biological molecules, some works using proteins<sup>179,180</sup>, antibodies<sup>181</sup> or DNA<sup>182</sup> have been published, showing that those species greatly improve the particles biocompatibility.

## 1. General Introduction

In the case of small molecules or surfactants, they can be also divided in three different kinds: oil-soluble, water-soluble and amphiphilic ligands. Among the most used oil soluble ligands, in which is based the work explained in the chapter 5 of this thesis, some works using oleic acid<sup>183,184</sup> ( $\text{CH}_3(\text{CH}_2)_7\text{CH}=\text{CH}(\text{CH}_2)_7\text{CO}_2\text{H}$ ) and/or oleylamine<sup>185</sup>, ( $\text{CH}_3(\text{CH}_2)_7\text{CH}=\text{CH}(\text{CH}_2)_7\text{NH}_2$ ) have been reported so far, as well as procedures to turn oil-soluble nanoparticles into water-soluble type, via ligand exchange procedures<sup>186</sup>.

**Inorganic materials:** Inorganic materials or compounds can be used as an alternative when trying to functionalize and stabilize iron oxide nanoparticles and control some of their properties, such as their shape, surface composition and magnetic properties.

Basically, when functionalizing iron oxide nanoparticles with inorganic compounds, it is possible to protect them from oxidation properties and to scope their applications as well<sup>187</sup>.

Both silica and metal oxides-sulphides functionalizations can supply tons of possible advantages and applications to the formed iron oxide nanoparticles. For instance, silica is a biocompatible and hydrophilic material that is able not only to bind various biological or synthetic ligands to its surfaces but also to allow the formation of more complex nanostructures by adding other kinds of particles inside the resulting silica coating shell<sup>188,189</sup>. On the other hand, metal oxides/sulphides can show optical and electrical properties ( $\text{TiO}_2$ , CdSe, etc.)<sup>190,191</sup> or magnetic properties ( $\text{CoO}$ ,  $\text{MFe}_2\text{O}_4$  ( $\text{M}=\text{Co}$ ,  $\text{Cu}$ ,  $\text{Mn}\dots$ ))<sup>192,193</sup> that, combined with the initial iron oxide nanoparticles, can generate some new nanostructured compounds with special properties and applications.

In the case of metal iron nanoparticle functionalization, gold coating is something worthy of being empathized. Despite the fact that gold (and also silver) single-metal functionalization conduces to a descending of the  $M_s$  value of the iron oxide, this kind of coating not only stabilizes the nanoparticles in solution, but also makes the resulting “core-shell” structure capable of binding ‘-SH’ terminated molecules, such as the aforementioned thiols, on its resulting surface. One of the main methods to recover iron oxide nanoparticles with gold is based on producing a gold salt reduction on the iron oxide nanoparticle surfaces<sup>194</sup>, as shown in **Figure 1.3.4.2**.

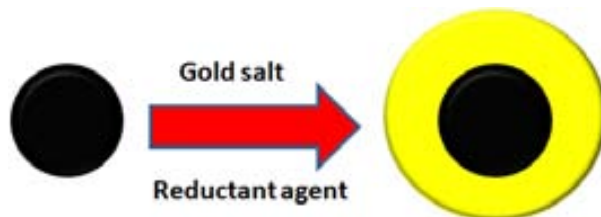


**Figure 1.3.4.2:** Illustration of a common procedure carried out so as to obtain  $\text{Fe}_3\text{O}_4@\text{Au}$  Core-Shell nanostructures.

With this purpose, some research works, trying to recover magnetite or maghemite nanoparticles with a gold shell have been reported so far<sup>195,196,197</sup>. However, and despite the fact that all authors claim to have achieved a perfect Fe<sub>3</sub>O<sub>4</sub>@Au (or Fe<sub>2</sub>O<sub>3</sub>@Au) Core-Shell structure, so far there are no enough TEM micrograph evidences supporting that fact.

For those reasons, the chapter 7 of this thesis is based on studying a Fe<sub>3</sub>O<sub>4</sub>@Au core-shell structure formation, via direct reduction of tetrachloroauric acid, HAuCl<sub>4</sub>, on the Fe<sub>3</sub>O<sub>4</sub> nanoparticle surface.

### 1.3.5 Iron oxide nanoparticles with different sizes, shapes and properties:

Apart from size and composition, special nanoparticles' properties depend also on their shape (**Figure 1.3.5.1**). In fact, for 'special-shape' nanoparticles, those properties are different from those observed in their spherical counterparts. Thus, the synthesis of uniform nanoparticles is of great importance when trying to control their electrical, optical and magnetic properties<sup>198, 199</sup>.

For this reason, some progresses have been made recently in the study of how nanoparticles' shape and size changes when modifying experimental conditions; not only when changing pressure, temperature or time reaction<sup>200</sup>, but also when adding certain reactants or surfactants to the reaction medium<sup>201</sup>.

A remarkable work reported by H. Yang, et al. explains how to obtain monodisperse magnetite nanocubes that by adding benzyl ether to a mixture of oleylamine and oleic acid<sup>202</sup>. Another important work, reported by C-J. Jia, et al. is based on obtaining iron oxide magnetic nanorings by modifying de pH media and the initial 'iron/sulphate/phosphate'<sup>203</sup>.

The chapter 6 of this thesis is based on the synthesis and study of iron oxide nanoparticles with cylindrical shape, also called nanorods.



**Figure 1.3.5.1:** Illustration of three different forms that can be taken by iron oxide nanoparticles, depending on the synthetic method.



---

### 1.4 Related Literature:

- <sup>1</sup> Website: <http://perc.ufl.edu/particle.asp>
- <sup>2</sup> Website: <http://www.epa.gov/apti/bces/module3/category/category.htm>
- <sup>3</sup> Murr L. E., *Mater Charact.* **2009**, 60, 261-270.
- <sup>4</sup> Pan Y.; Petersen N.; Winklhafer M.; Davila A.F.; Liu Q.; Frederichs T.; Hanzlik M.; Zhu R., *Earth Planet. Sci. Lett.* **2005**, 311-325.
- <sup>5</sup> Padovani S.; Sada C.; Mazzoldi B.; Brunetti B.; Borgia I., *J. Appl. Phys.* **2003**, 93 (12), 10057-10063.
- <sup>6</sup> Edwards P. P.; Thomas J. M., *Angew. Chem. Int. Ed.* **2007**, 46, 5480-5486.
- <sup>7</sup> Societal Implications of Nanoscience and nanotechnology. NSET Workshop Report. Edited by M.C. Rocco and William Sims Bainbridge, National Science Foundation (USA). March **2001**. Arlington, Virginia.
- <sup>8</sup> Vallés J.L. Nanoscience and Nanotechnology Research in the Framework Programme of the European Community. China-EU Forum on nanosized Technology. Beijing, P.R. of China. December, **2002**.
- <sup>9</sup> Hsieh C-w.; Hsieh S., *J. Mater. Chem.*, **2011**, 21, 16900-16904.
- <sup>10</sup> Grassian V.H. *J. Phys. Chem. C.*, **2008**, 112, 18303–18313.
- <sup>11</sup> Ghosh S.K.; Pal T., *Chem. Rev.*, **2007**, 107, 4797-4862.
- <sup>12</sup> Hao R.; Xing R.; Xu Z.; Hou Y.; Gao S.; Sun S. *Adv. Mater.*, **2010**, 22, 2729-2742.
- <sup>13</sup> Lee K-S.; El-Sayed M. A., *J. Phys. Chem. . B.*, **2006**, 110, 19220-19225.
- <sup>14</sup> Astruc, D.; Lu, F.; Aranzaes, J. R. *Angew. Chem. Int. Edit.*, **2005**, 44 (48), 7852-7872; 1.
- <sup>15</sup> Chauan B. P. S.; Sarkar A.; Chauan M.; Roka A., *Appl. Organometal. Chem.* **2009** , 23, 385–390.
- <sup>16</sup> Komanoya T.; Kobayashi H.; Hara K.; Chun W-J.; Fukuoka A, *Applied Catalysis A: General.* **2011**, 407, 188– 194.
- <sup>17</sup> Ewald J.C.; Reich S.; Baumann S.; Frommer W.B.; Zamboni N., *PLoS One*, **2011**, 6 (12), 1-7.
- <sup>18</sup> Hoa N. D.; El-Safty S.A., *Appl. Organometal. Chem.*, **2009** , 23, 385–390.
- <sup>19</sup> De M.; Ghosh P. S.; Rotello V. M., *Adv. Mater.* **2008**, 20, 4225–4241.
- <sup>20</sup> Yildiz I.; Shukla S.; Steinmetz N. F., *Curr. Opin. Biotechnol.*, **2011**, 22. 901–908.
- <sup>21</sup> Bhattacharyya S.; Kudgus R. A.; Bhattacharya R.; Mukherjee P., *Pharm Res*, **2011**, 28, 237–259.
- <sup>22</sup> Medina C.; Santos-Martinez M. J.; Radomski A.; Corrigan O. I.; Radomski M. W., *Br. J. Pharmacol.*, **2007**, 150, 552–558.
- <sup>23</sup> Godlewski M.; Wolska E.; Yatsunencko S.; Opaliska A.; Fidelus J., *Low Temp. Phys*, **2009**, 35 (1) , 48-52.



- <sup>24</sup> Warren S. C.; Thimsen E., *Energy Environ. Sci.*, **2012**, 5, 5133–5146.
- <sup>25</sup> Moura M. R.; Mattoso L. H. C.; Zucolotto V., *J. Food Eng.*, **2012**, 109, 520-524.
- <sup>26</sup> Yang B. M.; Huang C. J.; Lai W. L.; Chang C. C.; Kao C. M., *Desalination*, **2012**, 284, 182-190.
- <sup>27</sup> Talom R. M.; Fuks G.; Kaps L.; Oberdisse J.; Cerclier C.; Gaillard C.; Mingotaud C.; Gauffre F., *Chem. Eur. J.* **2011**, 17, 13495 – 13501.
- <sup>28</sup> Canitez F. K.; Yavuz M. S.; Ozturk R., *J Nanopart Res*, **2011**, 13, 7219–7228.
- <sup>29</sup> Anandhakumar S.; Vijayalakshmi S. P.; Jagadeesh G.; Raichur A. M., *ACS Appl. Mater. Interfaces* **2011**, 3, 3419–3424.
- <sup>30</sup> Chen W.; Davies J. R.; Ghosh D.; Tong M. C.; Konopelski J. P.; Chen S., *Chem. Mater.* **2006**, 18, 5253-5259.
- <sup>31</sup> Kim J. W.; Lim B.; Jang H-S.; Hwang S. J.; Yoo S. J.; Ha J. S.; Cho E. A.; Lim T-H.; Nam S. W.; Kim S-K., *Int. J. Hydrogen Energy*, **2011**, 36, 706-712.
- <sup>32</sup> Vollath D.; Szabó D. V.; Haubelt J., *J. Eur. Ceram. Soc.*, **1997**, 17, 13 17-1324.
- <sup>33</sup> Manivasakan P.; Rajendran V., *J. Am. Ceram. Soc.*, **2011**, 94 (5), 1410–1420.
- <sup>34</sup> Oshitani J.; Kataoka N.; Yoshida M.; Gotoh K.; Imamura, K.; Tanaka H., *Chem. Lett.*, **2011**, 40, 400-401.
- <sup>35</sup> You B.; Zhou D.; Yang F.; Ren X., *Colloids Surf. A*, **2011**, 392, 365– 370.
- <sup>36</sup> Trotochaud L.; Boettcher S. W., *Chem. Mater.*, **2011**, 23, 4920–4930.
- <sup>37</sup> Zhou W.; Hu X.; Bai X.; Zhou S.; Sun C.; Yan J.; Chen P., *Appl. Mater. Interfaces*, **2011**, 3, 3839–3845.
- <sup>38</sup> György E.; Pino A. P.; Roqueta J.; Ballesteros B.; Miguel A. S.; Maycock C. D.; Oliva A. G., *J. Phys. Chem. C*, **2011**, 115, 15210–15216.
- <sup>39</sup> Tantra R.; Jing S.; Pichaimuthu S. K.; Walker N.; Noble J.; Hackley V. A., *J Nanopart Res*, **2011**, 13, 3765–3780.
- <sup>40</sup> Poda A. R.; Bednar A. J.; Kennedy A. J.; Harmon A.; Hull M.; Mitrano D. M.; Ranville J. F.; Steevens J., *J. Chromatogr. A.*, **2011**, 1218, 4219– 4225.
- <sup>41</sup> Malloy A., *Mater. Today*, **2011**, 14 (4), 170-173.
- <sup>42</sup> Liu S.; Tao D.; Zhang L., *Powder Technol.*, **2012**, 217, 502-509.
- <sup>43</sup> Daniel M-C.; Astruc D., *Chem. Rev.*, **2004**, 104, 293-346.
- <sup>44</sup> Hammond C. R., *The Elements, in Handbook of Chemistry and Physics 81st edition*. CRC press. **2000**.
- <sup>45</sup> Freestone I.; Meeks N.; Sax M.; Higgitt., *Gold Bulletin*, **2007**, 40, 270-275.
- <sup>46</sup> Borgia I.; Brunetti B.; Mariani I.; Sgamellotti A.; Cariati F.; Fermo P.; Mellini M.; viti C.; Padeletti G., *Appl. Surf. Sci.*, **2002**, 185, 206-216.
- <sup>47</sup> Seol S. K.; Kim D.; Jung S.; Hwu Y., *Mater. Chem. Phys.*, **2011**, 131, 331-335.

- <sup>48</sup> Li Y.; Zaluzhna O.; Zangmeister C.D.; Allison T.C.; Tong Y.Y., *J. Am. Chem. Soc.*, **2012**, 134, 1990-1992.
- <sup>49</sup> Zhang Q.; Xie J.; Yu Y.; Lee J.Y., *Nanoscale.*, **2010**, 2, 1962-1975.
- <sup>50</sup> Fan C.; Poumellec B.; Zeng H.; Desmarchelier R.; Bourguignon B.; Chen G.; Lancry M., *J. Phys. Chem.*, **2012**, 116, 2647-2655.
- <sup>51</sup> Gold Nanoparticles: Properties, Characterization and Fabrication. Nova Science Pub. Inc. Edited by P.E. Chow. April, **2010**.
- <sup>52</sup> Kiss F.D.; Miotto R.; Ferraz A.C., *Nanotechnology*, **2011**, 22, 275708-27571.
- <sup>53</sup> Kholoud M.M.; El-Nour A.; Eftaiha A.; Al-Warthan A.; Ammar R.A.A., *Arabian J. Chem.*, **2010**, 3, 135-140.
- <sup>54</sup> Pool R., *Science*, **1990**, 248, 1186-1188.
- <sup>55</sup> Glanz J., *Science*, **1995**, 269, 1363-1364.
- <sup>56</sup> Lin S-Y.; Chen N-T.; Sun S-P.; Chang J.C.; Wang Y-C.; Yang C-S.; Lo L-W., *J. Am. Chem. Soc.*, **2010**, 132, 8309-8315.
- <sup>57</sup> Jiang L.; Wang W.; Wu D.; Zhan J.; Wang Q.; Wu Z.; Jin R., *Mater. Chem. Phys.*, **2007**, 104, 230-234.
- <sup>58</sup> Haes A.J.; Stuart D.A.; Nie S.; Van Duyne R.P., *J. Fluorescence*, **2004**, 14, 355-367.
- <sup>59</sup> Liu C.; Hayashi K.; Toko K., *Sens. Actuators, B*, **2012**, 161, 504-509.
- <sup>60</sup> Yuan Y.; Zhang J.; Zhang H.; Yang X., *Analyst*, **2012**, 137, 496-501.
- <sup>61</sup> Feng L.; Gao G.; Huang P.; Wang K.; Wang X.; Luo T.; Zhang C., *Nano Biomed. Eng.*, **2010**, 2, 258-267.
- <sup>62</sup> Lu Y.; Chen W., *J. Power Sources*, **2012**, 197, 107-110.
- <sup>63</sup> Ganesan M.; Freemantle R.G.; Obare S.O., *Chem. Mater.*, **2007**, 19, 3465-3471.
- <sup>64</sup> Zhang J.; Li Q.; Pan C.; Bjerrum N.; Ulstrup J., *Chem. Phys. Chem.*, **2010**, 11, 2844-2853.
- <sup>65</sup> González-Gálvez D.; Nolis P.; Philippot K.; Chaudret B.; Leeuwen P.W.N.M., *ACS Catal.*, **2012**, 2, 317-321.
- <sup>66</sup> Schmid G. (Ed.), *Clusters and Colloids: From Theory to Applications*, Chap. 6, VCH Publishers, New York, **1994**.
- <sup>67</sup> Reetz M.T.; Helbig W.; Quaiser S.A., *Chem. Mater.*, **1995**, 7, 2227-2228.
- <sup>68</sup> Ascencio J. A.; Gutierrez-Wing C.; Espinosa M. E.; Marin M.; Tehuacanero S.; Zorrilla C.; Yacaman M. J. M., et al., *Surf. Sci.*, **1998**, 396, 349-368.
- <sup>69</sup> Yacaman M. J.; Ascencio J. A.; Liu H.B.; Gardea-Torresdey J., *J. Vac. Sci. Technol. B.*, **2001**, 19, 1091-1103.
- <sup>70</sup> Schmid G., *Endeavour*. **1990**, 14, 172-178.
- <sup>71</sup> Aiken II J.D.; Finke R.G., *J. Mol. Catal. A: Chem.*, **1999**, 145, 1-44.

- <sup>72</sup> Bard A.J.; Faulkner L.R., *Electrochemical Methods*. Wiley, New York, **1980**.
- <sup>73</sup> Hunter R.J.; *Foundations of Colloid Science*, Vol. 1, Oxford Univ. Press, New York, **1987**.
- <sup>74</sup> McFarland A.D.; Haynes C.L.; Mirkin C.A.; Van Duyne R.P.; Godwin H.A., *J. Chem. Educ.*, **2004**, 81, 544A-544B.
- <sup>75</sup> Lang H.; Maldonado S.; Stevenson K.J.; Chandler B.D., *J. Am. Chem. Soc.*, **2004**, 126, 12949-12956.
- <sup>76</sup> Lee W.L.; Choi S.H.; Jeong H.M.; Rhyu S-H.; Chi K-W.; Yoon K.S., *J. Appl. Polym. Sci.*, **2011**, 122, 2497–2502.
- <sup>77</sup> Alexander C.M.; Maye M.M.; Dabrowiak J.C., *Chem. Commun.*, **2011**, 47, 3418–3420.
- <sup>78</sup> Porta F.; Speranza G.; Krpetic Z.; Dal Santo V.; Francescato P.; Scari G., *Mater. Sci. Eng. B.*, **2007**, 140(3), 187-194.
- <sup>79</sup> Toshima N., *Macromol. Symp.* **2003**, 204, 219-226.
- <sup>80</sup> Efrima S.; Pradhan N., *C.R. Chimie*, **2003**, 6, 1035-1045.
- <sup>81</sup> Martínez A.; Iglesias I.; Lozano R.; Teijon J.M.; Blanco M.D., *Carbohydr. Polym.*, **2011**, 83, 1311-1321.
- <sup>82</sup> Vericat C.; Vela M.E.; Salvarezza R.C., *Phys. Chem. Chem. Phys.*, **2005**, 7, 3258-3268.
- <sup>83</sup> Badia A.; Cuccia L.; Demers L.; Morin F.; Lennox R.B., *J. Am. Chem. Soc.*, **1997**, 119, 2682-2692.
- <sup>84</sup> Badia A.; Demers L.; Dickinson L.; Morin F.G.; Lennox R.B.; Reven L., *J. Am., Chem. Soc.*, **1997**, 119, 11104-11105.
- <sup>85</sup> Jadzinsky P.D.; Calero G.; Ackerson C.J.; Bushnell D.A.; Kornberg R.D., *Science*, **2007**, 318, 430-433.
- <sup>86</sup> Li Y.; Galli G.; Gygi F., *Science*, **2008**, 2, 1896-1902.
- <sup>87</sup> Annamalai, L.; Rao B.; Udaya T.; Thalappil P., *Int. J. Nanosci.*, **2011**, 10, 839-843.
- <sup>88</sup> Shiraishi Y., Arakawa D., Toshima N., *Eur. Phys. J.*, **2002**, 8, 377-383.
- <sup>89</sup> Chow E.; Gengenbach T.R.; Wiecek L.; Raguse B., *Sens. Actuators, B*, **2010**, 704-711.
- <sup>90</sup> Templeton A.C., Hostetler M.J., Kraft C.T., Murray R.W., *J. Am. Chem. Soc.*, **1998**, 120, 1906-1911.
- <sup>91</sup> Paulini R., Frankamp B.L., Rotello V.M., *Langmuir*, **2002**, 18, 2368-2373.
- <sup>92</sup> Templeton A.C.; Hostetler M.J.; Warmoth E.K.; Chen S.; Hartshorn C.M.; Krishnamurthy V.M.; Forbes M.D.E.; Murray R.W., *J. Am. Chem. Soc.*, **1998**, 120, 4845-4849.
- <sup>93</sup> Zhang F.; Skoda M.W.A.; Jacobs R.M.J.; Zorn S.; Martin R.A.; Martin C.M.; Clark G.F.; Goerigk G.; Schreiber F., *J. Phys. Chem. A.*, **2007**, 111, 12229-12237.
- <sup>94</sup> Kimura M.; Kobayashi S.; Kuroda T.; Hanabusa K.; Shirai H., *Adv. Mat.*, **2004**, 16, 335-338.
- <sup>95</sup> Gentilini C.; Evangelista F.; Rudolf P.; Franchi P.; Lucarini M.; Pasquato L., *J. Am. Chem. Soc.*, **2008**, 130, 15678–15682.

- 
- <sup>96</sup> Roux S.; Garcia B.; Bridot J-L.; Salome M.; Marquette C.; Lemelle L.; Gillet P.; Blum L.; Perriat P.; Tillement O., *Langmuir*, **2005**, 21, 2526–2536.
- <sup>97</sup> Fiurasek P., Reven L., *Langmuir*, **2007**, 23, 2857-2866.
- <sup>98</sup> Yoonessi M., Seykel E., Pender M.J., *Langmuir*, **2009**, 25, 3369-3373.
- <sup>99</sup> Zhou X., El Khoury J.M., Qu L., Dai L., Li Q., *J. Colloid. Interf. Sci.*, **2007**, 308, 381- 384.
- <sup>100</sup> Warren S.C., *J. Am. Chem. Soc.*, **2006**, 128, 12074- 12075.
- <sup>101</sup> Gautier C., Bürgi T., *J. Am. Chem. Soc.*, **2008**, 130, 7077-7084.
- <sup>102</sup> Wu Z., Suhan J., Jin R.C., *J. Mater. Chem.*, **2009**, 19, 622-626.
- <sup>103</sup> Ghosh A.; Basak S.; Wunsch B.H.; Kumar R.; Stellacci F., *Angew. Chem. Int. Ed.*, **2011**, 50, 7900 –7905.
- <sup>104</sup> Haes A.J.; Chang L.; Klein W.L.; Duyne R.P.V., *J. Am. Chem. Soc.*, **2005**, 127, 2264-2271.
- <sup>105</sup> Abad J.M.; Mertens S.F.L.; Pita M.; Fernandez V.M.; Schiffrin D.J., *J. Am. Chem. Soc.*, **2005**, 127, 5689-5694.
- <sup>106</sup> Fratoddi I.; Venditti I.; Battocchio C.; Polzonetti G.; Bondino F.; Malvestuto M.; Piscopiello E.; Tapfer L.; Russo M.V., *J. Phys. Chem. C.*, **2011**, 115, 15198–15204.
- <sup>107</sup> Wilton-Ely J.D.E.T., *Dalton Trans.*, **2008**, 25-29.
- <sup>108</sup> Wang S.; Sim W.S., *Langmuir*, **2006**, 22, 7861–7866.
- <sup>109</sup> Steigman J., Eckelman W.C., *The chemistry of Technetium in Medicine*, Nuclear Science Series National Academic Press: Washington D.C., **1992**.
- <sup>110</sup> Dilworth J.R., Parrott S.J., *Chem. Soc. Rev.*, **1998**, 27, 43- 55.
- <sup>111</sup> Schwochau K., *Technetium, Chemistry and Radiopharmaceutical Application* Wiley-VCH: Weinheim, **2000**.
- <sup>112</sup> Alberto R, Schibli R., Egli A., Schubiger P.A., *J. Am. Chem. Soc.*, **1998**, 120, 7987- 7988.
- <sup>113</sup> Alberto R., Ortner K., Wheatley N., Schibli R., Schubiger A.P., *J. Am. Chem. Soc.*, **2001**, 123, 3135 - 3135.
- <sup>114</sup> Schibli R.; Schwarzbach R.; Alberto R.; Ortner K.; Schmalte H.; Dumas C.; Egli A.; Schubiger P.A., *Bioconjugate Chem.*, **2002**, 13, 750- 756.
- <sup>115</sup> Alberto R., Schibli R., Waibel R., Abram U., Schubiger A.P., *Coord. Chem. Rev.*, **1999**, 190, 901 – 919.
- <sup>116</sup> Metzler-Nolte N., *Angew. Chem. Int. Ed.*, **2001**, 40, 1040 – 1043.
- <sup>117</sup> Schibli R., Schubiger P.A., *Eur. J. Nucl. Med. Mol.*, **2002**, 29, 1529 – 1542.
- <sup>118</sup> Alberto R., *Top. Curr. Chem.*, **2005**, 252, 1–44.
- <sup>119</sup> Alberto R., *J. Organomet. Chem.*, **2007**, 692, 1179–1186.
- <sup>120</sup> Alberto R., *Eur. J. Inorg. Chem.*, **2009**, 21–31.

- <sup>121</sup> Huang W.-Y.; Davis J.J., *Dalton Trans.*, **2011**, 40, 6087–6103.
- <sup>122</sup> Wilhelm A.J.; Mijnhout G.S.; Franssen E.J.F., *Eur. J. Nucl. Med.*, **1999**, 26, S36–S42.
- <sup>123</sup> Tu W.; Denizot B.J., *J. Colloid. Interface. Sci.*, **2007**, 310, 167-170.
- <sup>124</sup> Dhar S.; Mali V.; Bodhankar S.; Shiras A.; Prasad B.L.V.; Polkharkar V., *J. Appl. Toxicol.*, **2011**, 31, 411–420.
- <sup>125</sup> Ghodake G.; Eom C.-Y.; Kim S.W.; Jin E.S., *Bull. Korean Chem. Soc.* **2010**, 31, 2771-2775.
- <sup>126</sup> Yanyan Z.; Xuemei W., *Nano Biomed. Eng.*, **2010**, 2, 208-213.
- <sup>127</sup> Xu H.; Qu F.; Xu H., Lai W.; Wang Y.A.; Aguilar Z.P.; Wei H., *Biometals*, **2012**, 25, 45–53.
- <sup>128</sup> Pinto R.J.B.; Fernandes S.C.M.; Freire C.S.R.; Sadocco P.; Causio J.; Pascoal Neto C.; Trindade T., *Carbohydr. Res.*, **2012**, 348, 77-83.
- <sup>129</sup> Wantenaar G.H.J.; Campbell S.J.; Chaplin D.H.; Wilson G.V.H., *J. Magn. Magn. Mater.*, **1987**, 65, 71-75.
- <sup>130</sup> *International Geophysics*, **2003**, 86, 7-30.
- <sup>131</sup> Bransden B.H.; Joachain C.J.J., *Physics of Atoms and Molecules*, Longman, **1983**.
- <sup>132</sup> Williams D.; Mandal N.G.; Sharma A., *Anaesthesia & Intensive Care Medicine*, **2009**, 10, 62-64.
- <sup>133</sup> Teja A.S.; Koh P.-Y., *Prog. Cryst. Growth Charact. Mater.*, **2009**, 55, 22-45.
- <sup>134</sup> Oudet X.; Lochak G., *J. Magn. Magn. Mater.*, **1987**, 65, 99-122.
- <sup>135</sup> Meyers H.P., *Introductory solid state physics*, CRC Press., **1997**.
- <sup>136</sup> Koch H., *Physica C.*, **2008**, 468, 1112-1114.
- <sup>137</sup> Cornell R.M.; Schwertmann, U., *The iron oxides: structure, properties, reactions, occurrences and uses*, Wiley VCH, **2003**.
- <sup>138</sup> Kostrov A., *Earth Planet. Sci. Lett.*, **2001**, 186, 245-253.
- <sup>139</sup> Komarneni S.; Hu W.; Noh Y.D.; Van Orden A.; Feng S.; Wei C.; Pang H.; Gao F.; Lu Q.; Katsuki H., *Ceram. Int.*, **2012**, 38, 2563–2568.
- <sup>140</sup> Kasama T.; Church N.S.; Feinberg J.M.; Dunin-Borkowski R.E.; Harrison R.J., *Earth Planet. Sci. Lett.*, **2010**, 297, 10-17.
- <sup>141</sup> Spiers K.M., Cashion J.D., *J. Magn. Magn. Mater.*, **2012**, 324, 862-868.
- <sup>142</sup> Mumm A.S., Dart R.C., Say P., *J. Geochem. Explor.*, **2012**.
- <sup>143</sup> Madden A.S.; Madden M.E.E.; Larson P.R.; Miller M.A., *Earth Planet. Sci. Lett.*, **2010**, 298, 377-384.
- <sup>144</sup> Mizoh Y., *Wear*, **1996**, 252-264.
- <sup>145</sup> Osaki H., *Wear*, **1996**, 244-251.

- 
- <sup>146</sup> Yang X. ; Roonasi P. ; Jolstera R. ; Holmgren A., *Colloids Surf., A*, **2009**, 343, 24-29.
- <sup>147</sup> Legodi M.A., Waal D., *Dyes Pigm.*, **2007**, 74, 161-168.
- <sup>148</sup> Abramchuk S.; Kramarenko E.; Stepanov G.; Nikitin L.V.; Filipcsei G.; Khokhlov A.R.; Zrinyi M., *Polym. Adv. Technol.*, **2007**, 18, 883-890.
- <sup>149</sup> Abramchuk S.; Kramarenko E.; Grishin D.; Stepanov G.; Nikitin L.V.; Filipcsei G.; Khokhlov A.R.; Rinyi M., *Polym. Adv. Technol.*, **2007**, 18, 513-518.
- <sup>150</sup> Behdadfar B.; Kermanpur A.; Sadeghi-Aliabadi, H.; Morales M.P.; Mozaffari M., *J. Solid State Chem.*, **2012**, 187, 20-26.
- <sup>151</sup> Brullot, W.; Reddy N.K.; Wouters J.; Valev V.K.; Goderis B.; Vermant J.; Verbiest T., *J. Magn. Magn. Mater.*, **2012**, 324, 1919-1925.
- <sup>152</sup> Miser D.E.; Shin E-J.; Hajaligol M.R.; Rasouli F., *Appl. Catal., A*, **2004**, 258, 7-16.
- <sup>153</sup> Huang C-P.; Chen C-R.; Huang Y-F.; Lu Y-W.; Huang Y-H., *J. Mol. Catal. A: Chem.*, **2009**, 304, 121-127.
- <sup>154</sup> Dias A.M.G.C. ; Jussain A. ; Marcos A.S.; Roque A.C.A., *Biotechnol. Adv.*, **2011**, 29, 142-155.
- <sup>155</sup> Corot C.; Robert P.; Idee J-M.; Port M., *Adv. Drug Delivery Rev.*, **2006**, 58, 1471-1504.
- <sup>156</sup> Massart R., *IEEE Trans. Magn.*, **1981**, 17, 1247-1248.
- <sup>157</sup> Nyrió-Kósa I., *Eur. J. Mineral*, **2009**, 21, 293-302.
- <sup>158</sup> Lida H., *J. Colloid Interface Sci.*, **2007**, 314, 274-280.
- <sup>159</sup> Amara D.; Felner I.; Nowik I.; Margel S., *Colloids Surf., A*, **2009**, 339, 106-110.
- <sup>160</sup> Maity D.; Kale S.N.; Kaul-Ghanekar R. ; Xue J-M.; Ding J., *J. Magn. Magn. Mater.*, **2009**, 321, 3093-3098.
- <sup>161</sup> Park J.; An K.; Hwang Y.; Park J-G.; Noh H-J.; Kim J-Y.; Park J-H.; Hwang N-M.; Hyeon T., *Nat. Mater.*, **2004**, 3, 891-895.
- <sup>162</sup> Vidal-Vidal J., *Colloids Surf., A*, **2006**, 288, 44-51.
- <sup>163</sup> Chin A.B.; Yaacob I.I., *J. Mater. Process. Technol.*, **2007**, 191, 235-237.
- <sup>164</sup> Dong Q.; Kumada N.; Yonesaki Y.; Takei T.; Kinomura N., *J. Ceram. Soc. Jpn.*, **2009**, 117, 881-886.
- <sup>165</sup> Han C.; Zhao D.; Deng C.; Hu K., *Mater. Lett.*, **2012**, 70, 70-72.
- <sup>166</sup> Jing Z.; Han D.; Wu S., *Mater. Lett.*, **2005**, 59, 804-807.
- <sup>167</sup> Wang H.; Ma Y.; Yi G.; Chen D., *Mater. Chem. Phys.*, **2003**, 82, 414-418.
- <sup>168</sup> Suslick K.S., *Science*, **1990**, 1439-1445.
- <sup>169</sup> Dang F., Kamada K.; Enomoto N.; Hojo J.; Enpuku K., *J. Ceram. Soc. Jpn.*, **2007**, 867-872.
- <sup>170</sup> Dang F.; Enomoto N.; Hojo J.; Enpuku K., *Chem. Lett.*, **2008**, 37, 530-531.

- 
- <sup>171</sup> Dang F.; Enomoto N.; Hojo J.; Enpuku K., *Ultrason. Sonochem.*, **2009**, 16, 649-654.
- <sup>172</sup> Wu W.; He Q.; Jiang C., *Nanoscale Res. Lett.*, **2008**, 3, 397-415.
- <sup>173</sup> Hradil J., *China Particulology*, **2007**, 5, 162-168.
- <sup>174</sup> Bautista M.C.; Vomati-Miguel O.; Morales M.P.; Serna C.J.; Veintemillas-Verdaguer S., *J. Magn. Magn. Mater.*, **2005**, 293, 20-27.
- <sup>175</sup> Gaihre B.; Khil M.S.; Myung S.; See D.R.; Kim H.Y., *Int. J. Pharm.*, **2009**, 365, 180-189.
- <sup>176</sup> Gaihre B.; Aryal S.; Barakat N.A.M.; Kim H.Y., *Mater. Sci. Eng. C.*, **2008**, 28, 1297-1303.
- <sup>177</sup> Paul K.G.; Frigo T.B.; Groman J.Y.; Groman E.V., *Bioconjug. Chem.*, **2004**, 15, 394-401.
- <sup>178</sup> Liu H-L., *J. Mag. Mag. Mat.*, **2007**, 310, e815-e817.
- <sup>179</sup> Jansch M.; Stumpf P.; Graf C.; Ruehl E.; Mueller R.H., *Int. J. Pharm.*, **2012**, 428, 125-133.
- <sup>180</sup> Andersson B.V.; Skoglund C.; Uvdal K.; Solin N., *Biochem. Biophys. Res. Commun.*, **2012**, 419, 682-686.
- <sup>181</sup> Xu H.; Aguilar Z.P.; Yang L.; Kuang M.; Duan H.; Xiong Y.; Wei H.; Wang A., *Biomater.*, **2011**, 32, 9758-9765.
- <sup>182</sup> Mornet S.; Vekris A.; Bonnet J.; Duguet E.; Grasset F.; Choy J-H.; Portier J., *Mat. Lett.*, **2000**, 42, 183-188.
- <sup>183</sup> Zhang L.; He R.; Gu H-C., *Appl. Surf. Sci.*, **2006**, 253, 2611-2617.
- <sup>184</sup> Wang C.Y., *Chin. Chem. Lett.*, **2010**, 21, 170-182.
- <sup>185</sup> Klokkenburg, M., et al., *Vib. Spectrosc.*, **2007**, 43, 243-248.
- <sup>186</sup> Vo, D.Q.; Kim, E.-J.; Kim, S., *J. Colloid Interface Sci.*, **2009**, 337, 75-80.
- <sup>187</sup> Amin F.; Yushchenko, D.A.; Montenegro J.M.; Parak W.J., *ChemPhysChem*, **2012**, 13, 1030-1035.
- <sup>188</sup> Yu S., *J. Exp. Med.*, **2012**, 228, 317-323.
- <sup>189</sup> Tomohiko N., *Biomed. Eng.*, **2012**, 5-6, 625-632.
- <sup>190</sup> Zhu H.; Zhang, W.; Yu S.f., *Nanonscale*, **2013**, 5, 1797-1802.
- <sup>191</sup> Mirzaei J.; Urbanski M.; Yu K.; Kitzerow H-S.; Hegmann T., *J. Mater. Chem.*, **2011**, 21, 12710-12716.
- <sup>192</sup> Yang Z.; Lisiecki I.; Walls M., *ACS Nano*, **2013**, 7, 1342-1350.
- <sup>193</sup> Banerjee A.; Bid S.; Dutta H.; Chaudhuri S.; Das D.; Pradhan K., *Mater. Res.*, **2012**, 15, 1022-1028.
- <sup>194</sup> Xu X.; Hou Y.; Sun S., *J. Am. Chem. Soc.*, **2007**, 129, 8698-8699.
- <sup>195</sup> Wheeler D. A.; Adams S.A.; Lopez-Luke T.; Torres-Castro A.; Ahang J.Z., *Ann. Phys.*, **2012**, 11, 670-679.
- <sup>196</sup> Kalska-Szostko B.; Rogowska M.; Dubis A.; Szymanski K., *Appl. Surf. Sci.*, **2012**, 258, 2783-2787.
- <sup>197</sup> Lou L., *App. Surf. Sci.*, **2012**, 258, 8521-8526.

- <sup>198</sup> Song Q.; Zhang Z. J., *J. Am. Chem. Soc.*, **2004**, 126, 6164-6168.
- <sup>199</sup> Sun S.; Zeng H., *J. Am. Chem. Soc.*, **2002**, 124, 8204-8205.
- <sup>200</sup> Dong Q., Kumada N.; Yonesaki Y.; Takei T.; Kinomura N., *J. Ceram. Soc. Jpn.*, **2009**, 117, 881-886.
- <sup>201</sup> Kim D.; Lee N.; Park M.; Kim B.H.; An K.; Hyeon T., *J. Am. Chem. Soc.*, **2009**, 131, 454-455.
- <sup>202</sup> Yang H., *J. Appl. Phys.*, **2008**, 103, 07D526.
- <sup>203</sup> Jia C-J, Sun L-D.; Luo F.; Han X.-D. Heyderman L.J.; Yan Z.-G.; Yan C.-H.; heng K.; Zhang Z.; Takano M., *J. Am. Chem. Soc.*, **2008**, 130, 16968-16977.



## Chapter 2

# Nanoparticle characterization techniques

### Contents

---

2.1 General background and classification.....	67
2.2 No microscopic techniques.....	68
2.2.1 UV- Visible spectroscopy.....	68
2.2.2 Infrared vibrational spectroscopy.....	68
2.2.3 X-ray Photoelectron Spectroscopy (XPS).....	69
2.2.4 Mössbauer spectroscopy.....	72
2.2.5 Magnetic behaviour studies: SQUID and FC-ZFC.....	74
2.2.6 X-Ray diffraction.....	76
2.2.7 Thermogravimetric Analysis (TGA).....	78
2.3 Microscopic techniques.....	80
2.3.1 Electron microscopy.....	80
2.3.2 Bright field TEM (BF TEM).....	90
2.3.3 Electron diffraction.....	91
2.3.4 Z-contrast (or HAADF).....	93
2.3.5 Energy-dispersive X-Ray Spectroscopy (EDX or XEDS).....	94
2.3.6 Energy Electron Loss Spectroscopy (EELS).....	94
2.3.7 Energy-filtered TEM (EFTEM).....	96
2.3.8 Electron holography.....	97
2.4 Related Literature.....	99

## 2. Nanoparticle characterization techniques

## 2. Nanoparticle characterization techniques

### 2.1 General background and classification

It has been emphasized on several occasions that nanoparticles have special properties which make them useful for some different applications. In order to analyze these different properties, it is always necessary to use different kinds of techniques.

This chapter is concerned in explaining the basics of the main kinds of techniques used in this thesis to characterize the synthesized nanoparticles.

Basically, all the used characterization techniques have been classified in two main groups, as shown in the following diagram (**Figure 2.1.1**):

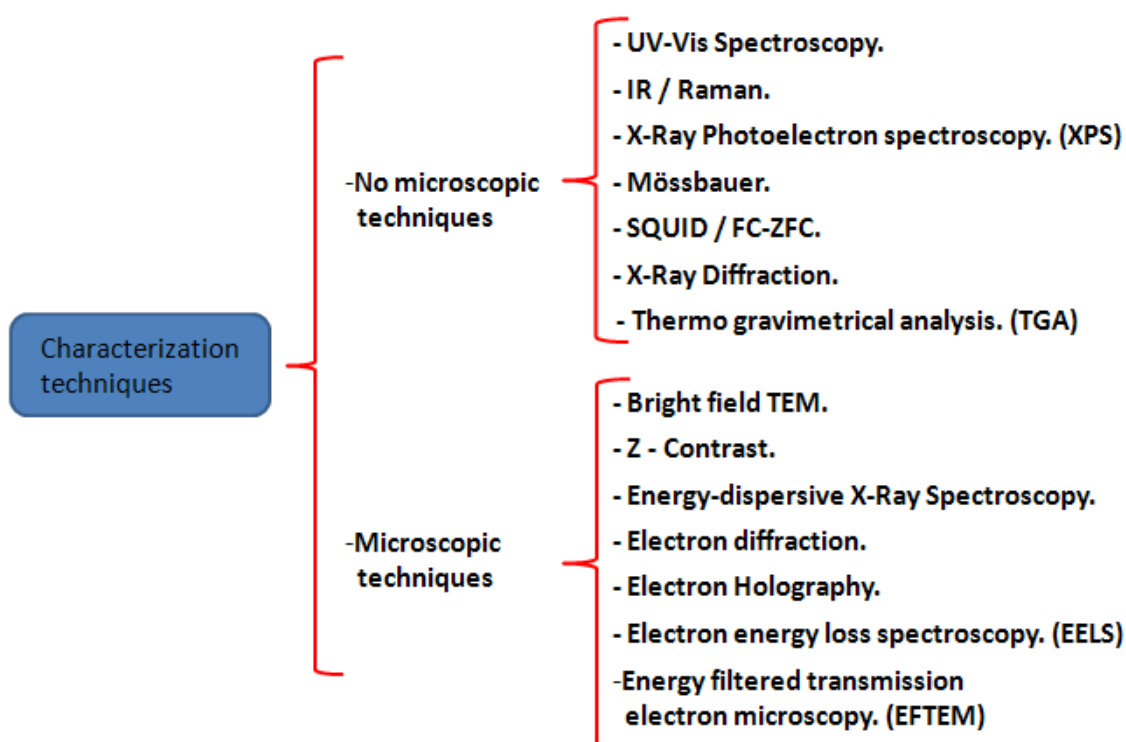


**Figure 2.1.1:** Classification of the characterization techniques used in this thesis.

Since some of the techniques described here have already been used in a great variety of different scientific works, their description in this section is mainly focused on explaining those which are relative unknown or, at least, less frequent in other fields apart from the typical nanoparticle characterization.

## 2. Nanoparticle characterization techniques

### 2.2 Non microscopic techniques

#### 2.2.1 UV- Visible spectroscopy

This technique is based on the light absorption or reflectance spectroscopy in the ultraviolet-visible electromagnetic spectral regions, in which molecules and other chemical compounds undergo electronic transitions.

Metal nanoparticle light absorption is produced by the coherent oscillation of their conduction band electrons, induced by their interaction with the electromagnetic field of the incident light. The resultant oscillation modes are called surface plasmons. Thus, an absorption band results when the frequency of the incident photon resonates with the conduction band electron oscillation, and this is known as a surface plasmon resonance (SPR) (**Figure 2.2.1.1**).

For silver and gold nanoparticles, their plasma frequency lies in the visible part of the electromagnetic spectrum and, as the resonance frequency of this SPR strongly depends on some different properties of nanoparticles such as their size, shape, interparticle interactions, dielectric properties and local environment, some useful information can be obtained when using this technique.

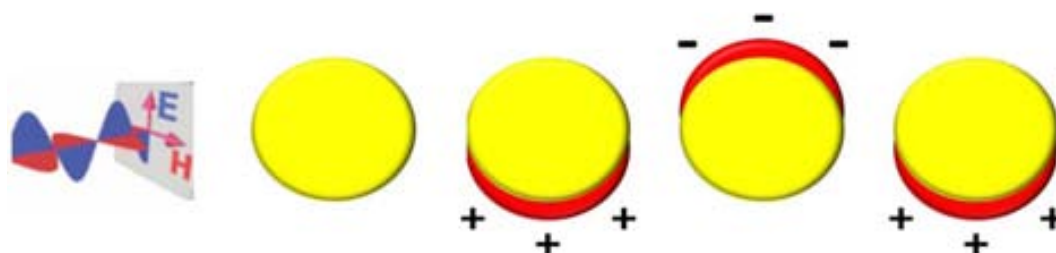


**Figure 2.1.1.1:** Illustration of the surface plasma resonance (SPR)

#### 2.2.2 Infrared vibrational spectroscopy

This technique is based on the light absorption spectroscopy in the infrared region of the electromagnetic spectrum. In this case, the absorption is produced when the wavelength of the incident light matches one of the vibrational modes of bonds or molecular groups. In this vein, it is possible to analyze the chemical composition of the organic compounds surrounding and stabilizing the nanoparticles.

## 2. Nanoparticle characterization techniques

### 2.2.3 X-ray Photoelectron Spectroscopy (XPS)

This technique, also known as ESCA, (Electron Spectroscopy for Chemical Analysis) is a qualitative spectroscopic technique that measures different parameters of solid surface materials, such as their elemental composition, empirical formula, and the chemical and electronic state of the elements present in the analyzed sample. Thus, this technique is very useful to analyze material surfaces because it can supply a lot of information from a great variety of different solid samples.

This technique is based on the photoelectric effect. Thus, when a solid material is subjected to monochromatic R-X photons under high vacuum conditions, this material emits electrons with a certain energy kinetic energy, as shown in **Figure 2.2.3.1**:

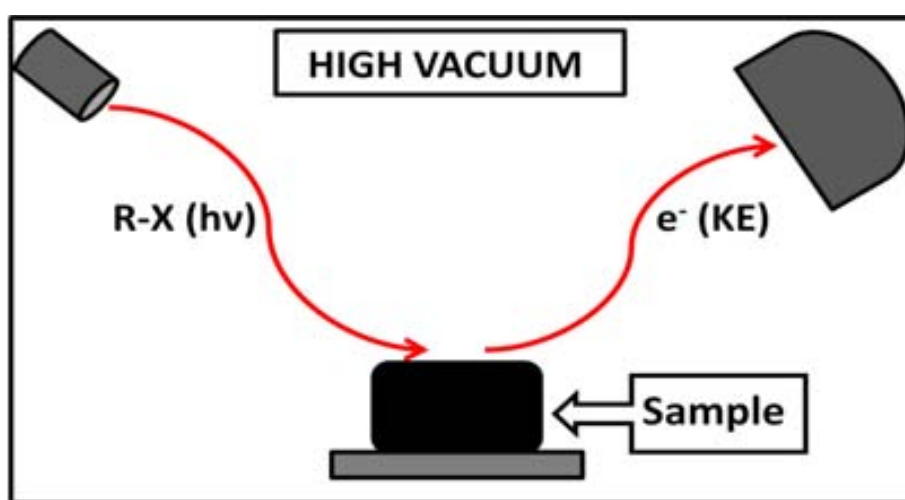


**Figure 2.2.3.1:** Illustration of the typical XPS analysis set up.

In this vein, the resulting emitted electrons have a kinetic energy given by this equation:

**Figure 2.2.3.2:** Kinetic energy of the resulting emitted electrons.

Where **KE** is the kinetic energy of the resulting emitted electrons, **hν** is the energy of the initial photons, **BE** is the binding energy of the atomic orbital in which the emitted electrons were initially, and **ϕ** is a function of the spectrometer work.

Since each element has a unique group of binding energies, this value can be isolated from the equation (**KE** is measured, and **ϕ** and **hν** are fixed in the experiment) in order not only to identify and quantify the different elements present in the sample, but also to know their chemical environment.

## 2. Nanoparticle characterization techniques

The resulting emitted electrons during the analysis are the internal ones. However, apart from the typical **XPS** photoelectric emission, there is also an **AUGER** emission, which is given by an X-Ray fluorescence process, in which an excited electron (L) relaxes itself and occupies a vacancy in a less energetic orbital (K). Thus, the difference of energy is given to another electron in an L orbital, which is finally emitted out of the atom via **KLL** emission. This process happens with  $10^{-15}$  seconds of delay in comparison with the photoelectric emission, as shown in the following image:

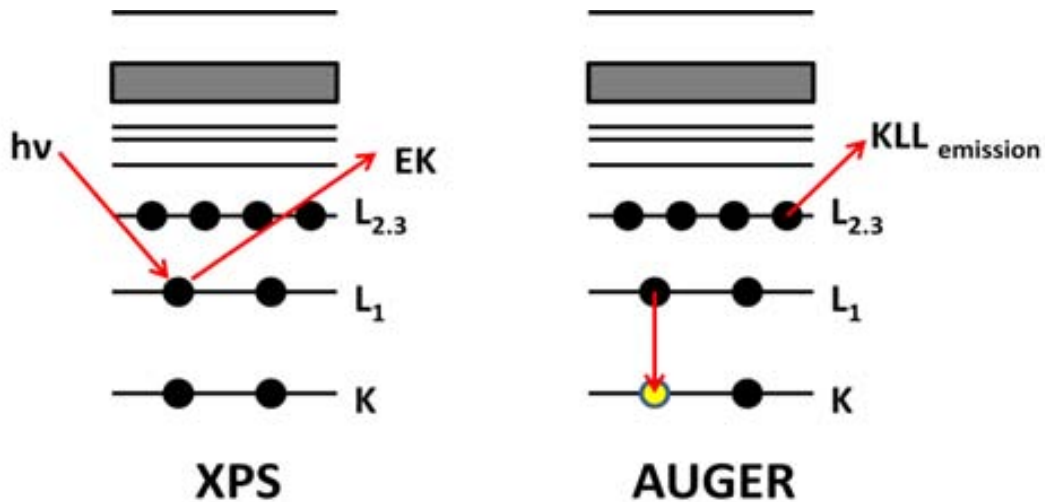


**Figure 2.2.3.2:** Illustration of XPS and AUGER processes.

Despite the fact that both emissions appear in the general spectrum of the sample, it is the **XPS** emission the one useful to obtain information about the sample surface composition. Thus, the resultant **XPS** spectrum is characteristic of the elements present in the sample and it shows the electronic structure of the material. As shown in **Figure 2.2.3.3**, all the obtained spectra show the number of electrons per energy interval (**CPS**) in front of their corresponding binding energy:

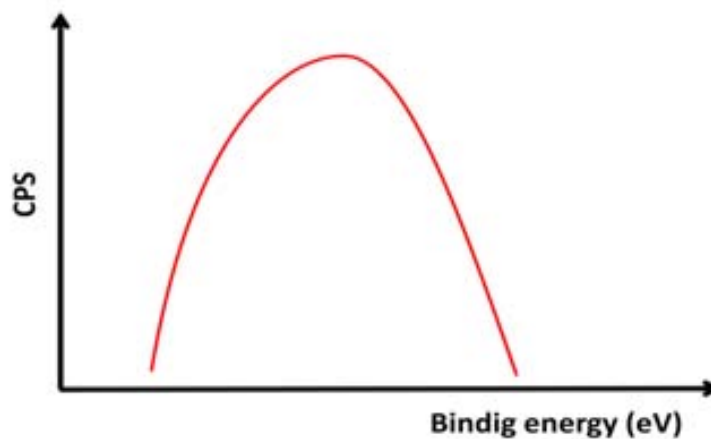


**Figure 2.2.3.3:** Illustration of the typical XPS spectrum focused in one element.

## 2. Nanoparticle characterization techniques

When there are different elements (or different chemical environments for the same element) in a particular zone of the spectrum, the resulting peak signal is the sum of the different element contributions. Thus, by mathematically analyzing the obtained signal, it is possible to identify (and quantify) the different element contributions, as shown in **Figure 2.2.3.4**:

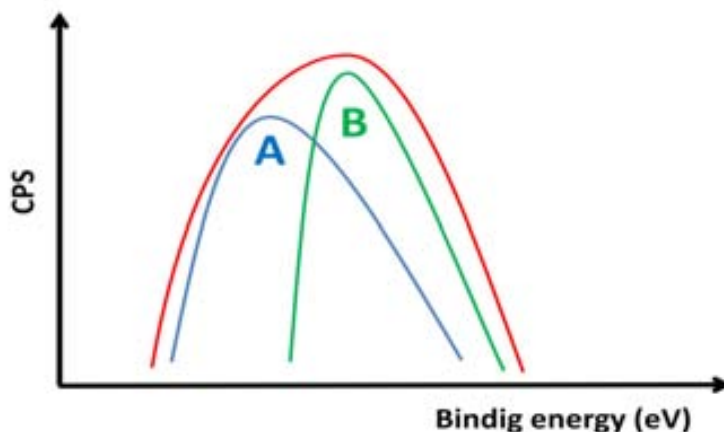


**Figure 2.2.3.4:** Illustration of a typical XPS spectrum mathematically operated to show two different contributions to the original signal.

As a result, by analyzing XPS spectra, it is possible to obtain:

- Quantitative data: By analyzing the peak height and width.
- Chemical state identification: By analyzing the peak positions as well as their space with the neighbor peaks.

Thus, according to the XPS technique properties, it is possible to use it to measure:

- Elemental composition of the surface (top 1-10 nm usually)
- Empirical formula of pure materials (except for H and He, which can't be detected by XPS technique)
- Elements that contaminate a surface.
- Chemical or electronic state of each element in the surface.
- Uniformity of elemental composition across the top surface.

In this thesis, XPS analysis have been carried out to analyze the surface of gold and silver nanoparticles capped with NaMP and functionalized with Re carbonyl species, as it is shown in chapter 4.

## 2. Nanoparticle characterization techniques

### 2.2.4 Mössbauer spectroscopy

This technique is based on the ‘Mössbauer Effect’. It was discovered by Rudolf Mössbauer in 1957, and it is based on the free-coil resonant absorption and emission of gamma rays ( $\gamma$ -Rays) in solids.

Given their own nature,  $\gamma$ -Rays are emitted and absorbed by transitions in the atomic nucleus. Thus, for atoms forming part of a solid, a fraction of the nuclear events can happen without important recoil effects. This fact is known as a resonance (or emission – reception) effect, and the whole process is shown in **Figure 2.2.4.1**:

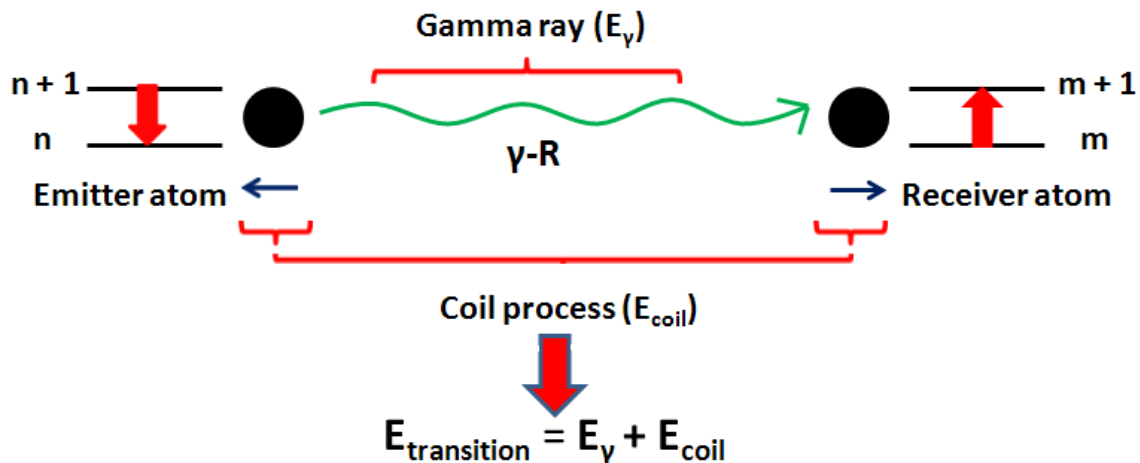


**Figure 2.2.4.1:** Illustration of the resonance, or emission-reception effect.

In this vein, the resonance condition? (**Figure 2.2.4.2**) is necessary for this process to happen.

$$E_{\text{coil}} \leq \frac{E_{\text{transition}}}{2}$$

**Figure 2.2.4.2:** Resonance condition.

Thus, as in liquid and gaseous materials atoms are almost ‘free’ inside the material structure,  $E_{\text{coil}}$  values are higher than those in solid materials, and the Mössbauer effect cannot be studied properly.

The typical methodology to use Mössbauer spectroscopy is based on exposing a solid sample under the effect of a  $\gamma$  radiation, and using a detector to measure the radiation intensity transmitted through the sample, as shown in **Figure 2.2.4.3**. In order to achieve a radiation absorption process by the sample, one condition must be



## 2. Nanoparticle characterization techniques

accomplished: the  $\gamma$ -Ray source and the sample atoms must be done of the same kind of isotopes.

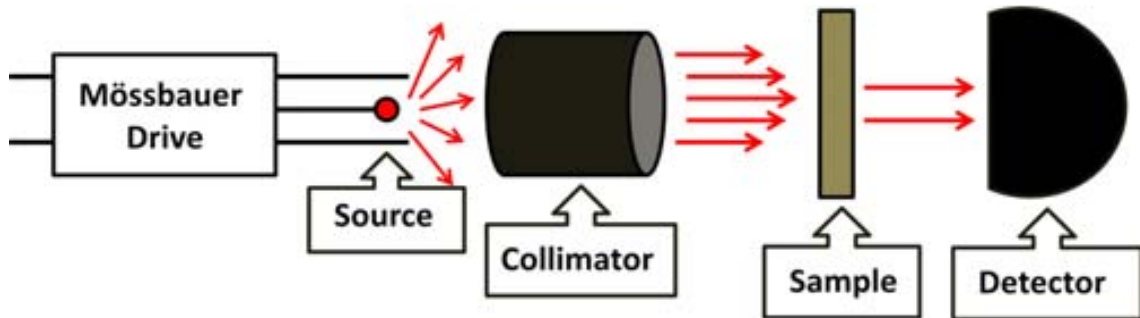


**Figure 2.2.4.3:** Mössbauer experimental methodology.

In this vein, a portion of the emitted gamma rays will have the exact energy necessary to be absorbed by the sample atoms, with a few differences given the chemical environment of the sample isotopes, which is what this technique analyzes.

During the analysis process, the energy of the source gamma rays is varied by Doppler Effect, moving and accelerating the radiation source with a lineal motor. Thus, the resultant spectrum shows information about the percentage of energy transmitted by the sample (% Transmission) in front of the velocity of the radiation source ( $v$ ), as shown in **Figure 2.2.4.4**:

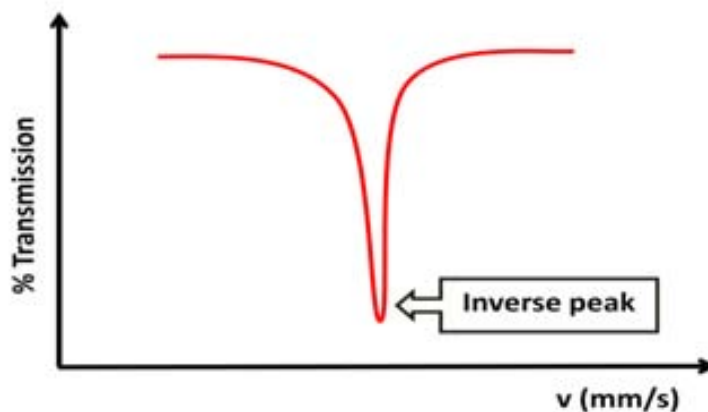


**Figure 2.2.4.4:** Illustration of the typical inverse peak obtained when carrying out Mössbauer spectroscopy. For the velocities that match with the resonant energetic levels of the sample, some of the  $\gamma$ -Rays are absorbed, decreasing the intensity of the sample transmission.

Thus, the useful information about the chemical environment of the sample nucleus is given by the number of the resulting peaks, their positions and their intensities, and these parameters are determined by three different kinds of nuclear interactions.

## 2. Nanoparticle characterization techniques

- **Isometric or chemical shift, CS:** It reflects the atomic chemical bonds. It is related with the electronic density of the nucleus, and it is reflected in the spectrum as a shift on the inversed peaks positions.
- **Quadrupole Splitting, QS:** It reflects the interaction between the nuclear quadrupole and its surrounding electric field. This interaction is reflected in the spectrum by dividing each peak into two peaks.
- **Magnetic or hyperfine splitting, (Zeeman effect):** It reflects the interaction between the nucleus and any surrounding magnetic field. It is a very important effect in compounds with an internal magnetic field.

Consequently, when analyzing, for instance, a ferric compound (such as magnetite,  $\text{Fe}_3\text{O}_4$ ) the resulting spectrum will show six peaks for each kind of iron inside the structure, as shown in **Figure 2.2.4.5**. By the way, the relative positions of the peaks will be also determined by the isometric shift.

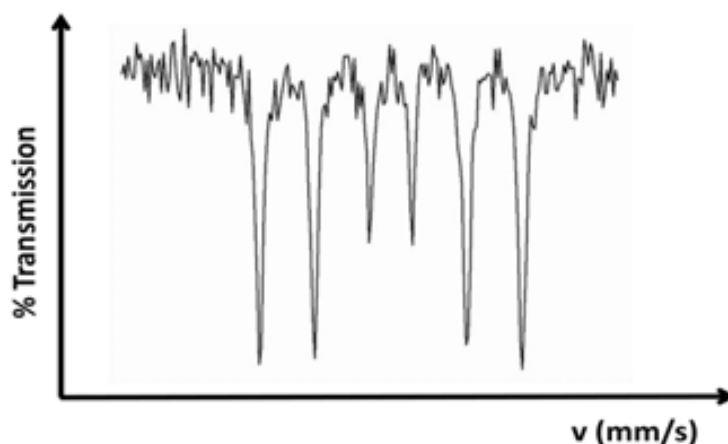


**Figure 2.2.4.5:** Typical Mössbauer spectrum for a ferric specie.

Thus, this technique can be basically applied not only in qualitative and quantitative analysis of materials, but also on the study of the chemical environments of certain elements inside a material.

However, Mössbauer spectroscopy has an important limitation: not all the elements can be analyzed via this technique, it is mandatory to find a convenient source of  $\gamma$ -Rays. For instance, in the case of iron compounds, such as the iron oxide nanoparticles synthesized and analyzed in this thesis, it is necessary to use  $^{57}\text{Co}$ , which turns into  $^{57}\text{Fe}$  by emitting  $\beta$ -radiation. In this vein, the  $^{57}\text{Fe}$  can be used for the iron analysis because it also turns into  $^{57}\text{Fe}$  by emitting  $\gamma$ -rays.

### 2.2.5 Magnetic behaviour studies: SQUID and FC-ZFC

Given the fact that the **SQUID (Superconducting Quantum Interference Device)** magnetic studies have been described in the section 1.3 of this thesis, this section is just focused on explaining the **FC-ZFC (Field Cooling- Zero Field Cooling)** technique.

This technique, which also supplies useful information about the magnetic properties of the materials, is based on measuring the **M** of the sample as a function of **T**. Basically; it consists of two chief steps: the **ZFC** and the **FC** curves formation, which together leads to a graphic similar to the one shown in **figure 2.2.5.1**:

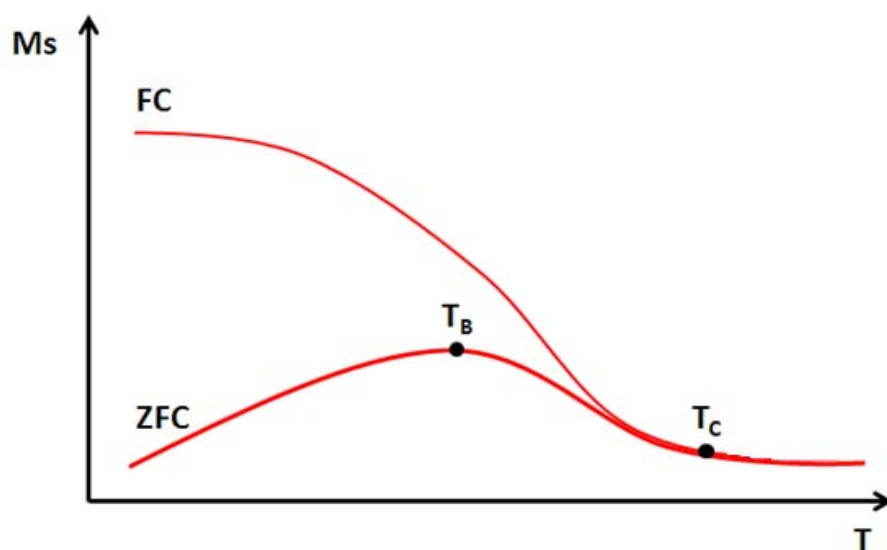


**Figure 2.2.5.1:** Illustration of typical **FC-ZFC** curves produced when applying a magnetic field on a sample and studying how varies the **M<sub>s</sub>**, when changing **T**.

First of all, the **ZFC** curve is formed by cooling the sample without any magnetic field and then applying a magnetic field small enough (about 50 Oe) to leave the inner magnetic moments of the material unaffected and maintaining it during the further heating process, in which **M** increases until reaching a peak that corresponds to the **T<sub>B</sub>** (blocking temperature) of the material. After reaching this point, the **M** decreases as a consequence of a misalignment of the magnetic moments also caused by the increase of the temperature.

Generally, the heating process is kept beyond the material's **T<sub>c</sub>**, and then the **FC** curve is 'drawn' by cooling again the sample at fixed **H**, which leads to higher values of **M**.

Basically, the difference between two points corresponding to the **FC** and **ZFC** curves at the same **T** may be compared with the difference of two points of the already explained **SQUID** hysteresis cycle, corresponding to the initial magnetization curve generated when applying a magnetic field for the first time and the **M** obtained for the same value of applied **H**. This comparison may be clearly observed in **figure 2.2.5.2**:

## 2. Nanoparticle characterization techniques

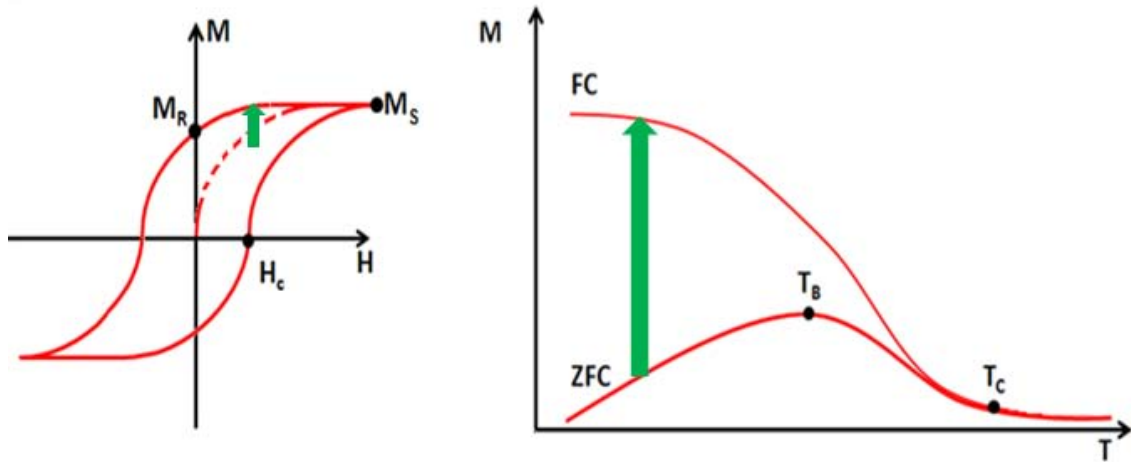


**Figure 2.2.5.2:** Image showing the same  $M_S$  difference taken from both SQUID and FC-ZFC graphics.

Specifically, the **ZFC** curve allows us to measure the material's blocking temperature,  $T_B$ , which supplies information about the nanoparticles' distribution size. When combining both **ZFC/FC** curves, on the other hand, it can be determined the magnetic irreversibility range of the material.

### 2.2.6 X-Ray diffraction

X-Ray diffraction is based on a constructive interference of X-ray waves process that is produced in certain space directions. That means that the waves must be in phase, which happens when their trajectory difference is zero or a whole multiple of wavelengths.

The directions in which this phenomenon takes place when applying an X-ray radiation on a material with a periodic atomic structure (crystal) can be predicted by Bragg's law, which establishes that the interference is constructive when the following condition is accomplished:

$$n\lambda = 2d\sin\theta, \text{ where}$$

- $n$  is a whole number.
- $\lambda$  is the wavelength of the X-Ray radiation.
- $d$  is the distance between planes inside the
- $\theta$  is the angle between the incident and the dispersed rays.

## 2. Nanoparticle characterization techniques

This phenomenon can be visually illustrated in **Figure 2.2.6.1**:

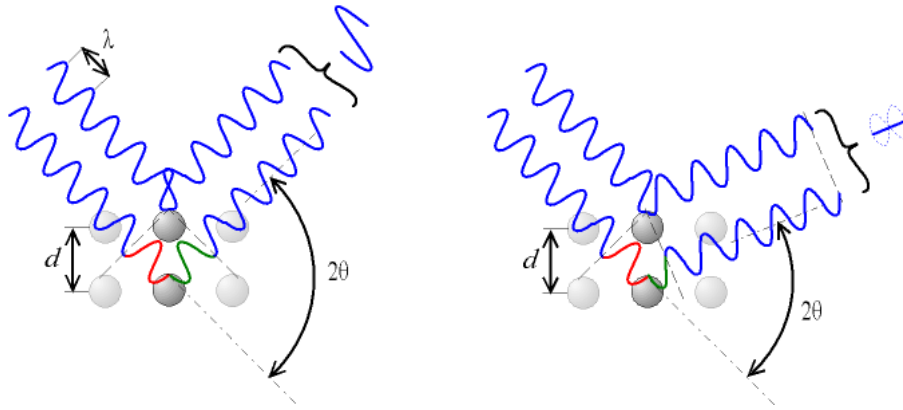


**Figure 2.2.6.1:** Illustration of two X-ray waves in phase forming a constructive interference (**left**) and two X-ray waves in opposite phase forming a destructive interference (**right**)

In this vein, all the constructive interferences can be registered in an X-ray diffractogram (**figure 2.2.6.2**), in which the diffraction intensity is shown as function of the scattering angle. Each diffractogram is taken using a specific wavelength.

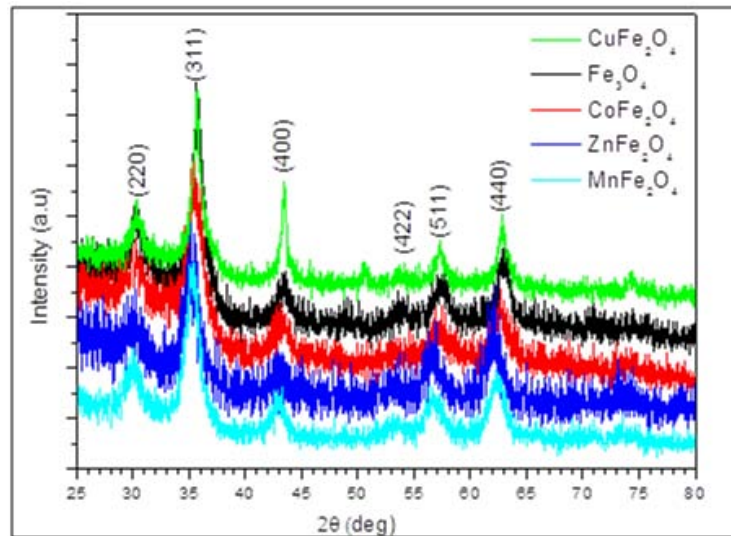


**Figure 2.2.6.2:** Diffractograms corresponding to diverse mixed ferrite nanoparticles synthesized for this thesis.

The positions of the resulting peaks depend on the interplanar spacing distances. So, the bigger is the distance between identical planes, the smaller is the value of  $2\theta$  at which the corresponding peak appears, and vice versa.

## 2. Nanoparticle characterization techniques

Thus, by carrying out X-ray diffractions from solid samples, it is possible to identify whether a material is crystalline or not, and in case it is, it is also possible to know which crystal (or mixture of crystals) we are working with.

In this thesis, X-Ray diffraction has been carried out in order to analyze the crystal structure of all the synthesized nanoparticles.

### 2.2.7 Thermogravimetric Analysis (TGA)

Thermogravimetric analysis is based on heating a mixture to a high enough temperature so that one or some of the components decompose into a gas, via dissociating themselves into the air. During the whole process, the changes in weight in relation to a temperature are measured under controlled atmosphere. The resulting thermogram shows how the sample mass decreases while temperature increases, as shown in **figure 2.2.7.1**:

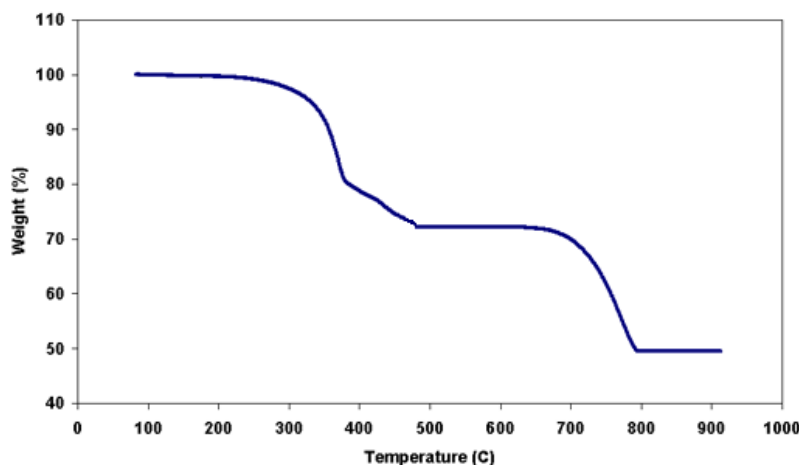


**Figure 2.2.7.1:** Example of thermograph for a hypothetical mixture. Each slope corresponds to a weight loss produced by the evaporation of one or more compounds of the analyzed mixture.

In order to carry out these analyses properly, it is necessary to achieve a high degree of precision in three different measurements: weight, temperature and variation of temperature.

Thermogravimetric analyses are useful to determine the composition and purity of a sample. In this vein, this technique uses heat and stoichiometry ratios to determine the percent by mass of different compounds (with different boiling points) in a mixture.

Another technique usually combined with **TGA** is the **Differential Scanning Calorimetry (DSC)**, which is based on comparing the difference of the amount of heat necessary to increase the temperature of a reference and a sample as function of the

## 2. Nanoparticle characterization techniques

temperature applied to the sample and reference holders. Normally, the temperature of both increases linearly as a function of time throughout the experiment.

Since the amounts of heat needed to flow to the reference and the analyzed sample will be different to maintain both species nearly at the same temperature when heating them, the resulting diagram shows the heat flow differences between the reference and the sample as function of the holders' temperature, as shown in **figure 2.2.7.2**.

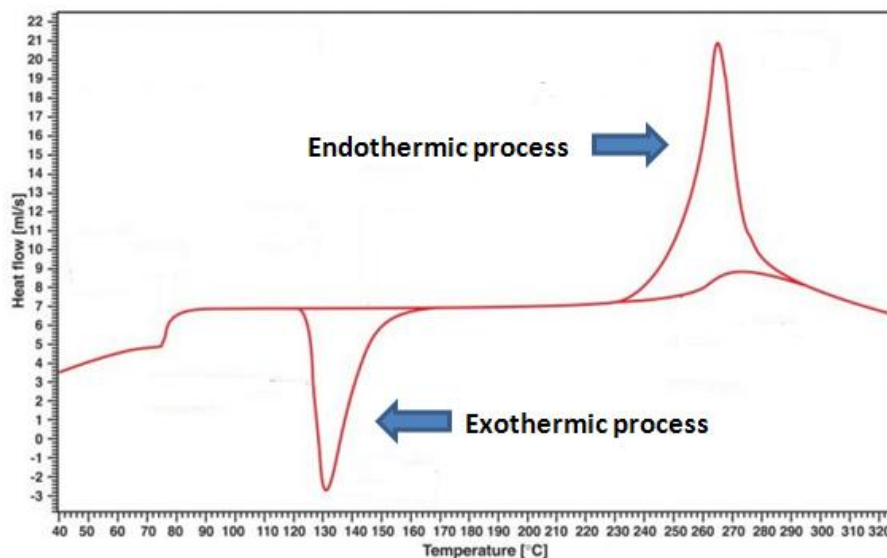


**Figure 2.2.7.2:** Example of a DSC diagram obtained for a hypothetical compound compared with a reference.

Thus, **DSC** can be carried out in order to detect physical transformations such as phase transitions, because

In this thesis, both **TGA** and **DSC** analysis have been carried out in order to analyze the composition of some different synthesized nanoparticles.

### 2.3 Microscopic techniques

#### 2.3.1 Electron microscopy

As mentioned in the last chapter, when studying some properties of nanoparticles such as their size and shape, the use of electron microscopes is a must. So far, some different kinds of microscopes have been designed so as to study multiple parameters of a large number of different samples, since organic tissues until inorganic materials. However, all types of electron microscope use a beam of electrons to illuminate a specimen and produce a magnified image.

Independently of the type of electron microscope, in all cases their resolution power is far greater than light-powered optical microscopes because of electron wavelengths, which are about 100,000 times shorter than photon wavelengths.

Every electron microscope uses electromagnetic and electrostatic “lenses” to control and focus the electron beam, generated by an electron gun, to form an image.

As aforementioned, there are some different kinds of electron microscopes that can be used to different applications. However, the most representatives are **Transmission Electron Microscope (TEM)** and **Scanning Electron Microscope (SEM)**. In both cases, electrons are emitted by an electron gun forming a beam which is accelerated by an anode-cathode device and focused by the mentioned lenses. From that point, the two microscopes work differently.

Thus, in **TEM** the electron beam is transmitted through the specimen, which lets some electrons get through and scatters others out of the beam. After emerging from the specimen, both scattered and non-scattered electrons carry information about the structure of the specimen, which is magnified by the objective lens of the microscope and can be viewed in some different ways, for instance by projecting the magnified image onto a phosphor-coated viewing screen or recording the image in a CCD (charge-coupled device) camera and displaying the image on a computer monitor.

On the other hand, **SEM** microscopes produce images bathing the sample with a focused electron beam which is scanned across an area of the specimen. Once the electrons hit the specimen, some of them lose energy via different mechanisms. This lost energy turns into heat, light or X-ray emission, or other kinds of alternative forms. All the resultant emissions have information about the properties of the sample surface, for instance its composition and form.



## 2. Nanoparticle characterization techniques

The schematic structure of **TEM** and **SEM** microscopes are shown in **Figure 2.3.1.1**:

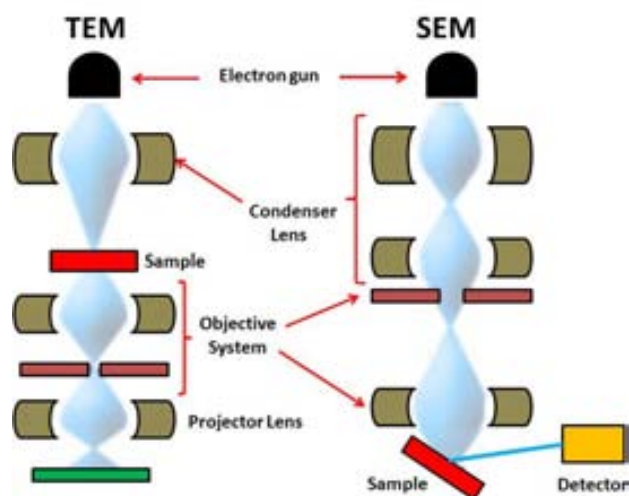


**Figure 2.3.1.1:** Internal structure of **TEM** (left) and **SEM** (right) microscopes.

So as to analyze the nanoparticles synthesized in this thesis, several electron microscopic techniques have been carried out using in almost all cases **TEM** (**Figure 2.3.1.2**), both in the “Servei de Microscopia de la UAB” and in the “Center for Electron Nanoscopy”, during three months of stay in Denmark.

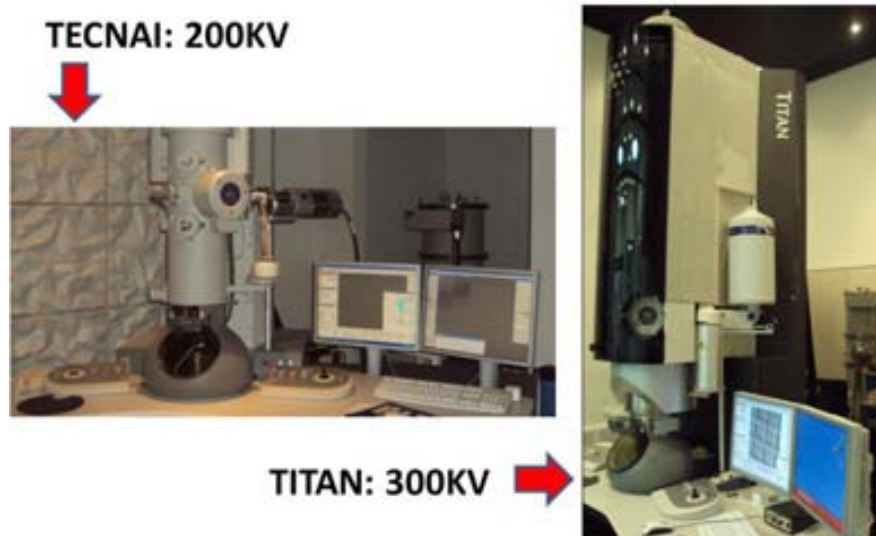


**Figure 2.3.1.2:** Pictures taken from the two different **TEM** microscopes, **Tecnai** and **Titan** used during the three months stay carried out for this thesis. In the first one, electrons are accelerated at 200 KV, meanwhile Titan accelerates them at 300 KV.

## 2. Nanoparticle characterization techniques

There is a variation of **TEM** called Scanning Transmission Microscope (**STEM**) in which the electron beam is focused into a narrow spot which scanned over the specimen in the same way than **SEM** does, but in this case the observed electrons are those that have gone through the specimen, just like in classical **TEM**. In this way, **STEM** is useful (and necessary) when carrying out certain microscopic techniques, such as **Z-Contrast**.

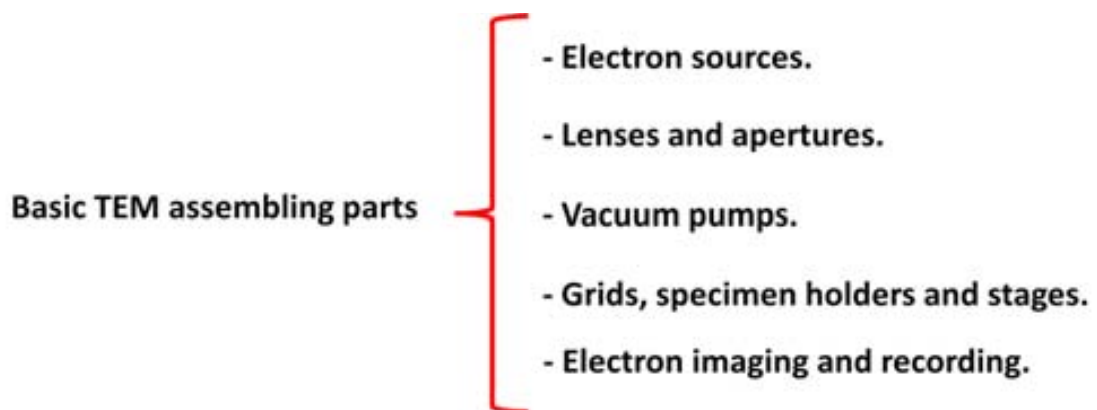
Given the fact that some of the **TEM** techniques used in this thesis require a certain degree of knowledge about the microscope operation, it is mandatory to explain how it works more in depth:

Basically, this explanation can be divided in two parts:

- The microscope assembly.
- The electron scattering process.

### **The microscope assembly**

Despite different kinds of **TEM** can be built depending on the final analytical purposes and the different samples they are supposed to work with, the general transmission electron microscopy assembly consists of:



#### **I) Electron sources:**

In order to ‘illuminate’ the specimen, it is very important to have a reliable source of electrons with enough brightness and electron beam coherency. Right now, there are basically two types of commercial sources: thermionic and field-emission sources. The first ones are tungsten filaments or lanthanum hexaboride ( $\text{LaB}_6$ ) crystals, which free electrons when heated, and the second ones (also called ‘guns’) consist of fine tungsten needles, and produce electrons when a large electric potential is applied between them and an anode.

## 2. Nanoparticle characterization techniques

Apart from the different working systems, there are other important differences between the two kinds of sources. For instance, tungsten and  $\text{LaB}_6$  thermionic sources are far cheaper than field-emission sources. On the other hand, field-emission sources give more monochromatic electrons and produce brighter and more coherent electron beams. In any case, both kinds of electron sources are always situated on the top of the microscope column.

**Figure 2.3.1.3** shows schematic diagrams of a thermionic and a field-emission source.

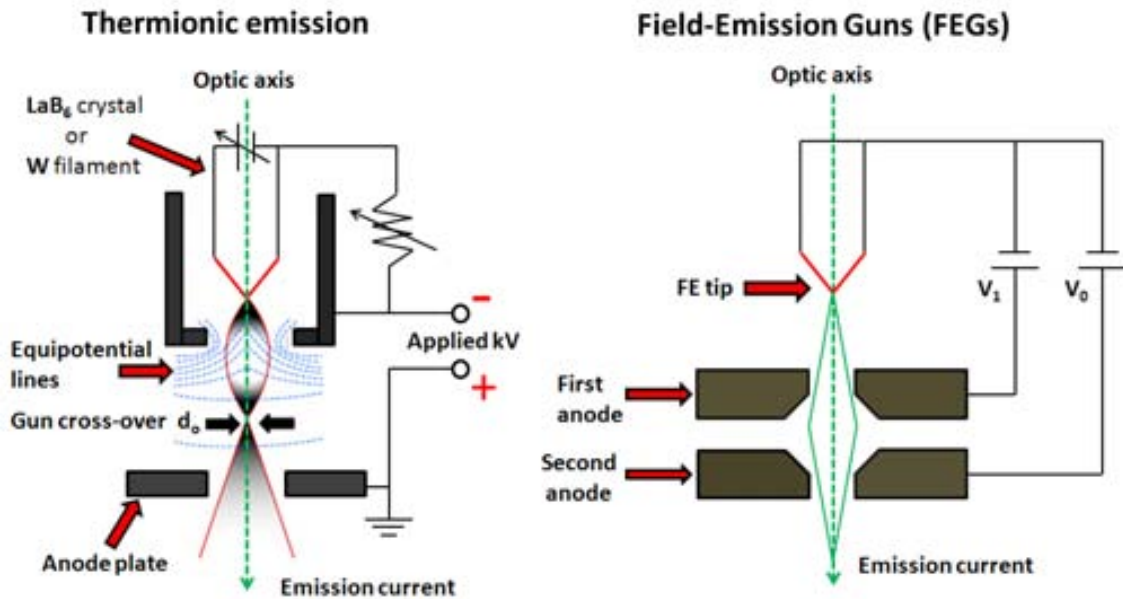


**Figure 2.3.1.3:** Schematic diagram of a thermionic electron gun (left) and a Field-Emission gun (right)

In the thermionic sources a high voltage is placed between the cathode and the anode (the  $\text{LaB}_6$  or  $\text{W}$  piece works as a cathode). The resultant electric field focuses the electrons into a crossover  $d_0$  which is the actual source for the lenses in the **TEM** illumination system.

In the case of the field-emission guns, the **FE** works as a cathode respect to two anodes. The first one provides the extraction voltage to pull electrons out of the tip, while the second one works like an electrostatic lens to produce a crossover.

## 2. Nanoparticle characterization techniques

### II) Lenses and apertures:

So as to keep the electron beam focused as it travels through the microscope column, both before and after hitting the specimen, it is necessary to use electromagnetic lenses, which are the **TEM**'s equivalent of the glass lenses in a visible light microscope (**VLM**). However, and despite this resemblance, both kinds of lenses show very important differences.

In **VLMs**, it is necessary to move the glass lenses in the focused light axis in order to control the illumination intensity and to focus the image. Besides, as the focal length of a glass lens is fixed, it is necessary to change lenses to change de magnification. By contrast, the **TEM**'s lenses positions are fixed but it is possible to change all the parameters (illumination intensity, focus and magnification) by changing the strength of the lenses. Since in most cases the **TEM**'s lenses are electromagnetic, that means changing the electric current inside the lens.

As shown in **Figure 2.3.1.4**, an electromagnetic lens is formed mainly by two parts. The first one is a cylindrically core of soft magnetic material, such as iron, with a hole in the middle. This structure is called polepiece. There are two polepieces in most lenses, and the distance between them is called gap, which magnitude is important when focusing the electron beam. The second one consists of a coil of copper wire which surrounds each polepiece. When a current passes through the coil, a magnetic field is created inside the lens, controlling and focusing the electron beam.

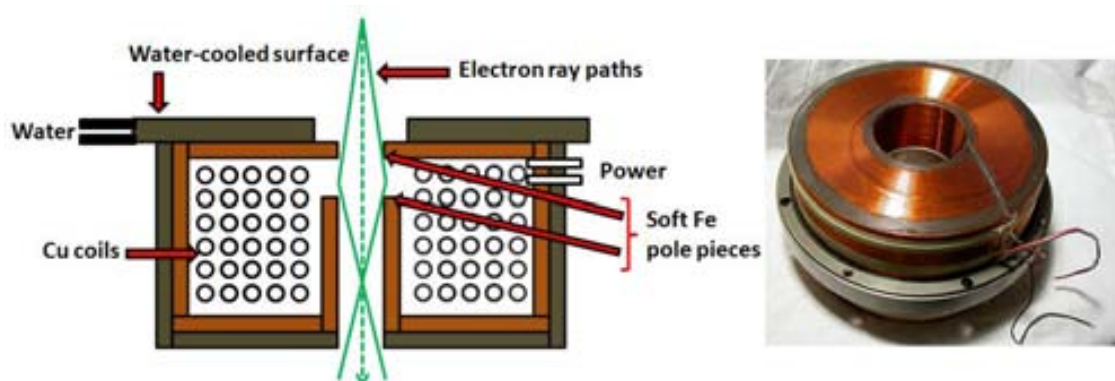


**Figure 2.3.1.4:** Schematic diagram of an electromagnetic lens (left) and picture taken from a real electromagnetic lens (right)

Since electromagnetic lenses are not perfect, they suffer from spherical and chromatic aberrations which limit their capability to collect and control all the electrons from the beam and their wavelength as well. Therefore, it is necessary to control these aberrations by inserting limiting apertures that select electrons closest to the optic axis, because these are least affected by the lens aberrations. Basically, apertures are formed by a single metal diaphragm with “holes”, and work as shown in **figure 2.3.1.5**.

## 2. Nanoparticle characterization techniques

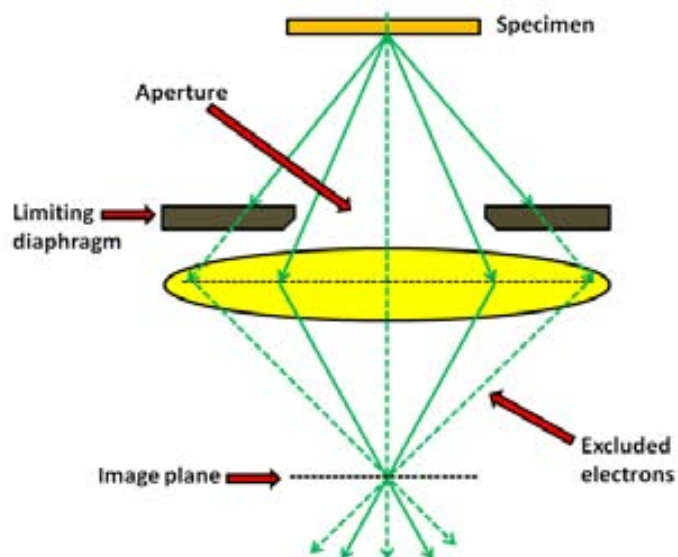


**Figure 2.3.1.5:** Schematic diagram illustrating how a diaphragm let some electrons through the aperture and restricts others, depending on their angular spread.

Having a good vacuum system is very important in order to avoid specimen contamination and also to control electron scattering inside the microscope, which happens also in presence of gases. For these reasons, **TEM**'s vacuum usually reaches a  $10^{-5}$  Pa pressure. Depending on the sample and the experiment requirements, however, it is possible to reach a  $10^{-7}$  Pa pressure in 'High Vacuum **TEMs**' (**HVTEMs**)

In order to create a vacuum inside the microscope, some different kinds of pumps can be used and combined, such as mechanical, diffusion, ion, turbomolecular and cryogenic pumps. Mechanical, diffusion and turbomolecular pumps are based on pulling in air from one end and expelling it from the other. However, ionic and cryogenic pumps work differently. Ionic pumps emit electrons that ionize air molecules and attract them to a cathode, and cryogenic pumps, on the other hand, use cold surface areas to remove air molecules from ambient pressure.

Generally, a **TEM** possesses at least two different pumping systems: the first one creates the vacuum inside the column, and the second one evacuates the camera and the screen chamber. The whole vacuum system is controlled by a computer, and the **TEM** is permanently under vacuum, except when it is being repaired.

## 2. Nanoparticle characterization techniques

### IV) Grids, specimen holders and stages:

The first think that must be taken into consideration when preparing a **TEM** experiment is how to transform the sample to study into an appropriate microscope specimen. Depending on the kind of sample, some different preparatory techniques may be used. The optimal specimen must be thin enough to allow some electrons to get through it. For instance, when working with a bulk material, it has to be reduced to a 3-mm diameter disc (or smaller) with electron-transparent regions. However, all the samples prepared during this thesis are nanoparticles that can be dispersed in aqueous or organic media. Therefore, in all cases, the specimens have been prepared just by placing a nanoparticle dispersion drop on a special **TEM** grid and evaporating all the solvent so as to keep the nanoparticles fixed on the grid surface.

All the used grids are formed by copper and they are recovered by a thin carbon monolayer, on which the nanoparticles are fixed after evaporating all the solvent. Basically, two variations of these grids have been used: the first kind of grid has a continuous carbon monolayer surface, and the second one, called ‘holly carbon’ has some hollows on the carbon monolayer. ‘Holly carbon’ grids are useful to study big particles, because they improve the contrast of the image in the regions (hollows) where there is no carbon. **Figure 2.3.1.6** shows the form of a Cu grid, with a continuous carbon and a ‘holly’ carbon recovering.

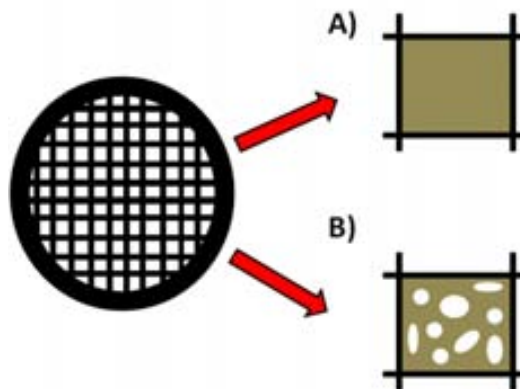


**Figure 2.3.1.6:** Picture illustrating the two different Cu grid supports used in this thesis. The first one “A” has a continuous carbon surface, and the second one, “B” has a carbon with hollows surface.

Once the specimen has been properly prepared, to insert the specimen into its corresponding place inside the **TEM** column, it is necessary to use two special components, the holder and the stage.

Basically, the holder is a rod that keeps the specimen attached and introduces it inside de microscope column. It also allows tilting or rotating the specimen and, depending on the kind of holder, it is also possible to work with the specimen under different conditions, by changing it during the **TEM** analysis. For instance, it is possible



## 2. Nanoparticle characterization techniques

to heat or cool it, or to perform other changes. Independently of the kind of holder, everyone has some common parts that are shown in **figure 2.3.1.7**.

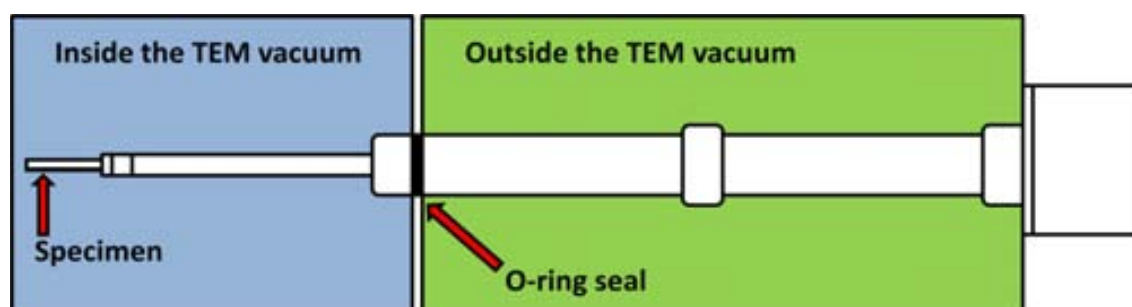


**Figure 2.3.1.7:** Schematic illustration of the main parts of a holder. The specimen is placed at the end of it, supported by a drilled cup and held by a clamping ring or a screw. The 'O-ring' seals the part of the holder that is inside the column vacuum.

It is very important to use a cold trap or cold finger, which keeps the sample holder stage cold and cryo-pumps the region that surrounds the specimen. By doing so, it 'cleans' the sample holder and generates a pre-vacuum just before inserting the specimen inside the microscope column.

The stage is a part of the **TEM** that works as an 'entrance' to the holder. It includes airlocks to allow the insertion of the specimen holder into de vacuum with minimal increase in pressure inside other microscope areas.

Sometimes, after placing the specimen into the holder, it may be useful to introduce it into a plasma cleaner, which is useful both to remove specimen surface hydrocarbon contamination and also to modify the surface itself. Basically, it consists of a mixture of ions and electrons that break the carbon-hydrogen bonds. All the specimens studied during the stay in the Center for Electron Nanoscopy (Denmark) were treated with a plasma cleaner which plasma was formed by a mixture of 25% of oxygen and 75% of argon. **Figure 2.3.1.8** shows a picture of the used plasma cleaner.



**Figure 2.3.1.8:** Picture of the plasma cleaner used to clean the surface of all the specimens analyzed via **TEM**.

## 2. Nanoparticle characterization techniques

### V) Electron imaging and recording:

Since human eyes are not sensitive to electrons, it has been necessary to develop different devices capable of translating the electron-intensity distributions generated by the specimen into visible-light distributions, which can be clearly observed by humans.

Basically, two different kinds of devices are used in a **TEM** so as to treat the electron-intensity signals: viewing screens and electron detectors.

The **TEM** viewing screens are placed nearly at the bottom of the microscope column, below the projector lenses and above the electron detector camera. It can be formed by zinc sulfide, ZnS, or phosphor, P, which emit light with a wavelength inside the optical region of the electromagnetic spectrum when hit by the electron beam.

As it will be explained in the next sections, electrons can be scattered (or not) in different directions, depending on the way in which they interact with the specimen. Thus, electron detectors can be placed in different positions inside the microscope, depending on which kind of electrons are being analyzed. However, the most common electron detector that can be found in a standard **TEM** is the charge-coupled device (**CCD**) detectors, which are becoming the more usual instruments for real-time TV recording of images and diffraction patterns (**DPs**), as well as other techniques, such as 'Electron Energy Loss Spectroscopy' (**EELS**) and 'Energy-Filtered TEM' (**EFTEM**) as it will be explained in the following sections. Basically, **CCDs** are devices that store charge generated by electron beams or lights. The device itself may have millions of pixels, which act as individual capacitors that can accumulate more or less charge proportionally to the intensity of the incident radiation. The stored charge in each pixel is then fed into an amplifier and digitized, creating a digital image of the electron (or light) incident pattern.

As aforementioned, additional microscope assemblies can be added in order to increase the number of techniques that can be carried out with the **TEM**.

### The electron scattering process

It is thanks to the electron scattering process (which takes place when the electron beam hits the specimen) that it is possible to obtain **TEM** images and **DPs**. In fact, non-scattering objects are invisible. Thus, when working with electron microscopy techniques, understanding the basics of the electron scattering processes becomes a must. First of all it is important to understand that electrons can be referred as particles or as waves. Therefore, depending on the situation, it may be easier to think of electrons either as one thing or the other to explain the scattering processes properly.

Scattered electrons can be mainly separated into those that suffer 'elastic' and 'inelastic' scattering. It is called elastic scattering when the electron does not lose



## 2. Nanoparticle characterization techniques

energy after hitting the specimen. On the other hand, inelastic scattering occurs when the electron does lose energy after the hitting process.

According to the wave nature of electrons, they can be scattered ‘coherently’ and ‘incoherently’. In the first case, the scattered electrons remain in phase step, meanwhile in the second case there is no phase relationship between them. Usually, scattered electrons are coherent and inelastic electrons are incoherent.

Finally, the scattering process may end up in different angular distributions. Depending on the angle of scattering with respect to the incident to the beam and the specimen (which is normal to the beam) there may be ‘forward scattering’ when the scattering angle is  $< 90^\circ$  and ‘backward scattering’ when this angle is  $> 90^\circ$ .

Apart from the scattered electrons that belong to the initial electron beam, other electrons can be emitted from the specimen due to excitation processes happened when the incident beam hits it. Those are called ‘Secondary Electrons’ (SEs)

**Figure 2.3.1.9** shows graphically the different kinds of electron scattering that may take place when hitting a thin specimen, like the ones that can be studied in the **TEM**.

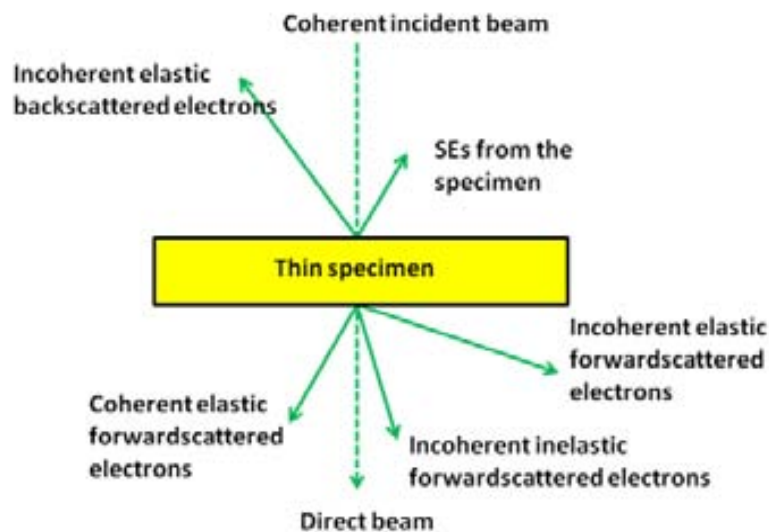


**Figure 2.3.1.9:** Diagram showing the different kinds of electron scattering from a thin specimen.

Elastically scattered electrons are, by far, the major contrast sources in **TEM** images and diffraction patterns. However, inelastically scattered are also equally important. The main point is that each electron that comes from the specimen carries information about it that can be processed in order to study the specimen in depth, as it will be explained as follows.

## 2. Nanoparticle characterization techniques

### 2.3.2 Bright field TEM (BF TEM)

This is the most common technique used when working with **TEM** microscopes. As mentioned before, when the electron beam is transmitted through the specimen, some electrons are scattered and some are not. Those that pass through the sample without being scattered or those that have been forward elastically scattered with a small angle of deviation interact with the phosphorous-coated screen or with the **CCD** camera producing a signal of certain intensity. In this vein, the resulting contrast image is generated by the spatial distribution of the elastically scattered electrons. In other words, thick regions of the specimen, or regions containing atoms with high atomic number will appear dark, while thin regions or regions containing no atoms or atoms with low atomic number will appear bright, forming a two dimensional projection of the sample down the optic axis, as shown in **Figure 2.3.2.1 [Ref]**.

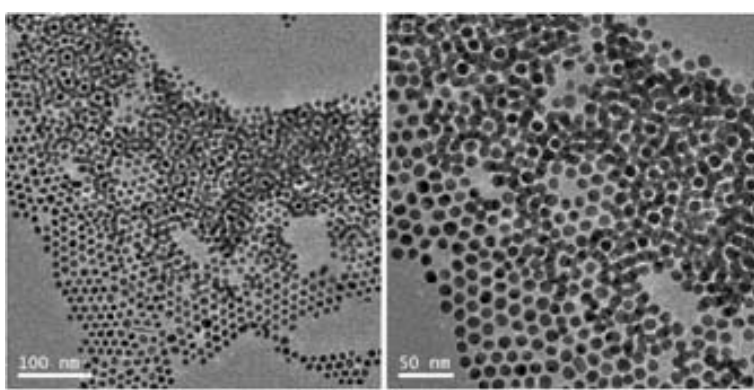


**Figure 2.3.2.1:** BF TEM image taken from gold nanoparticles dispersible in organic medium, supported on a carbon grid.

As shown in this image, gold nanoparticles (with a higher electron density) appear as darker spots, meanwhile the rest of the image, corresponding to the carbon grid used as a surface where to place the nanoparticles appears brighter, because of the lower electron density of the carbon.

The key step is to use the objective aperture so as to select electrons that have suffered more or less than a certain angular deviation. When doing **BF TEM**, this aperture allows electrons with small (or zero) deviation to form the contrast image. However, it is also possible to obtain ‘Dark Field’ (**DF TEM**) images, by only allowing some of the elastically scattered electrons with a bigger angle to form the contrast images. In this case, regions of the specimen with the fewest atoms or electron density will appear darker and vice versa.

In this thesis, Bright field **TEM** images have been taken from all nanoparticles synthesized in this thesis, in order to observe their size and shape distribution.

### 2.3.3 Electron diffraction

Electron diffraction is usually carried out using a **TEM** microscope, and it is used to study matter by firing electrons at the specimen and obtaining an interference pattern. In this case, contrast is formed by the angular distribution of the small angle elastically scattered electrons that hit the viewing screen or the **CCD** camera. In fact, electron diffraction is by far the most important scattering phenomenon that takes place in the **TEM**, and it is of a great utility to study the structure of different crystalline materials since it determines the spacing of planes and gives a great amount of crystallographic information about those materials.

In this vein, electron diffraction can be considered the **TEM** analogous of X-Ray diffraction. Despite the fact that that X-ray photons interact with matter in a different way than electrons, it is possible to explain the electron diffraction process mainly using Bragg's Law for those electrons that have been scattered and deviated from the electron beam in an angle  $< 5^\circ$ . Therefore, in those cases, the electron beam will be diffracted by the crystallographic planes in the way shown in **Figure 2.3.3.1**:

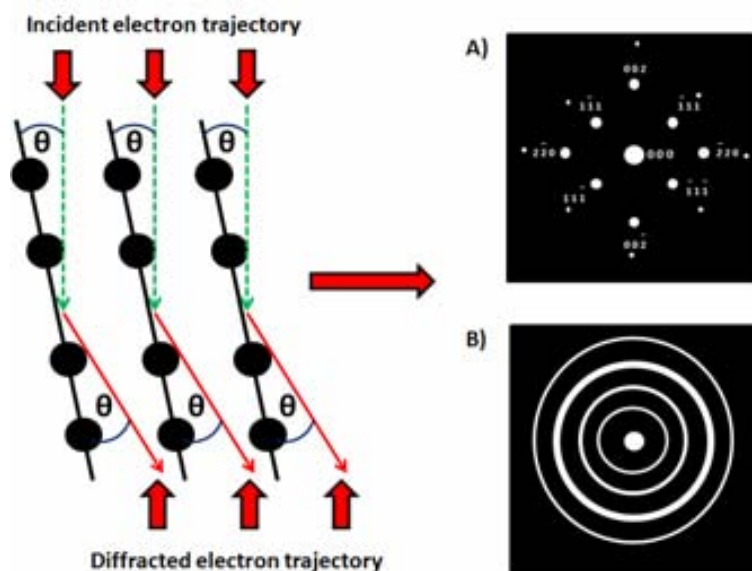


**Figure 2.3.3.2:** Illustration of how incident electrons are diffracted by the crystallographic planes of the specimen and how this process results into diffraction patterns.

Both 'A' and 'B' are typical **DP** images supposedly taken from real specimens. 'A' corresponds to a single crystal **DP** with a specific orientation respect to the electron beam axis. In this case each diffraction plane family appears as a pair of spots around a central spot which is formed by the non-diffracted electrons. The larger is the interplanar spacing, the nearest to the central spot will appear the corresponding plane spot, and vice versa. 'B' corresponds to a **DP** taken from a big group of crystals (i.e. nanoparticles) all with a random orientation respect to the beam axis. In this case, each

## 2. Nanoparticle characterization techniques

different orientation of any crystal gives a couple of spots with a corresponding distance from the central spot but at different orientation in the image. As a result of the sum of all the different pairs of spots, circle-like fringes are formed in the final **DP**, each one corresponding to one plane family.

This technique procedure is carried out in a very similar way than for BF TEM analyses. In the case of electron diffraction, however, the diffraction pattern can be observed onto the screen instead of the image by manipulating the intermediate magnetic lenses of the microscope and therefore changing the distance of the back focal plane in which the diffraction pattern is formed, making this coincide with the projection lens view plane, as shown in **Figure 2.3.3.2**:

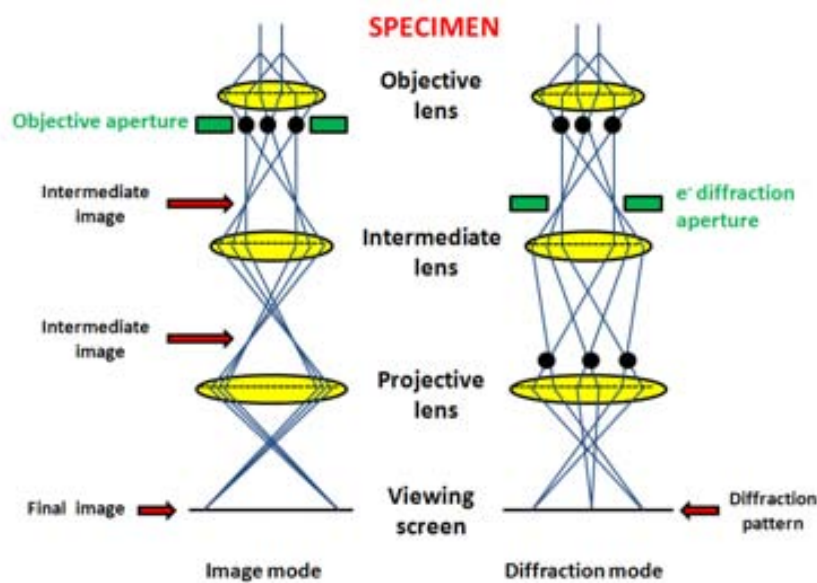


**Figure 2.3.3.2:** Visual diagram showing the differences between “Image” and “Diffraction” working modes of the TEM.

Apart from changing the intensity of the intermediate lens, it is also necessary to remove the objective aperture so as to allow all the scattered electrons to form the corresponding diffraction pattern. However, by doing so, the formed **DP** contains electrons from the whole area of the specimen that is being illuminated by the beam. As a consequence, the obtained pattern becomes useless because the direct (not-scattered) beam is too intense and it saturates the **DP**. In order to solve this problem, an ‘electron diffraction aperture’ is placed in the plane of an imaging lens, creating a virtual aperture at the plane of the specimen.

## 2. Nanoparticle characterization techniques

### 2.3.4 Z-contrast (or HAADF)

As aforementioned, **Z-contrast** can only be applied when working in **STEM** mode. When performing **STEM** it is also possible to obtain 'Bright Field' or 'Dark Field' images, depending on which electrons are being selected to form the image. However, no apertures but detectors are used in this mode to discriminate between electrons in function of their deviation angle. The way in which different electrons are detected is shown in **Figure 2.3.4.1**:

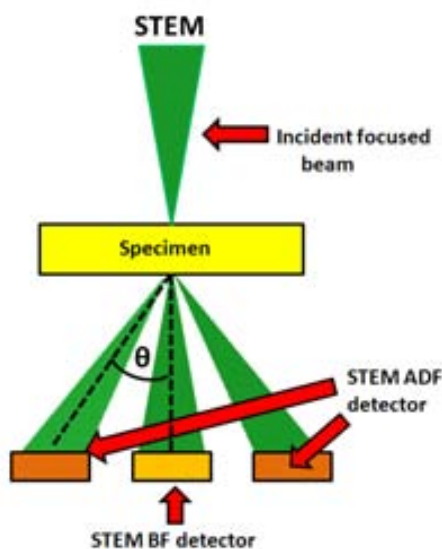


**Figure 2.3.4.1:** Illustration of the on-axis Bright Field 'BF' detector and the off-axis 'Annular Dark Field' (ADF) detector that can be used to create the two different kinds of STEM images.

When images are formed with electrons scattered at small angles ( $< 5^\circ$ ) what generates the contrast is the mass-thickness of the different specimen regions. However, at higher angles ( $> 5^\circ$ ), it is possible to detect scattered beams which (low) intensity depends only on the atomic number (**Z**) of the atoms that conforms the specimen. Those beams carry information useful both to generate detailed images with atomic resolution formed by the '**Z-contrast**' and to obtain elemental information about the specimen. Since the first ADF detectors used to collect both Bragg and non-Bragg scattered electrons, in order to analyze only non-Bragg scattered electrons, an ADF detector with a large central aperture was necessary. The resulting detector is called '**High Angle Annular Dark Field**' (HAADF).

Therefore, **Z-contrast** (or **HAADF**) is a technique capable of obtaining atomic resolution images in which the different regions of the specimen appear darker or brighter depending on the atomic number (**Z**) of the atoms that form it.

## 2. Nanoparticle characterization techniques

### 2.3.5 Energy-dispersive X-Ray Spectroscopy (EDX or XEDS)

Apart from elastic and inelastic scattered electrons, X-ray photons are also generated when the electron beam strikes the specimen. Since each element originates an X-ray with a specific energy, it is possible to analyze the chemical composition of the specimen via using an X-ray energy-dispersive spectrometer (**XEDS** or **EDX**). By adding this assembly to the **TEM** it is converted into an 'Analytical Transmission Electron Microscope' (**ATEM**). The whole process is exemplified in **figure 2.3.5.1**:

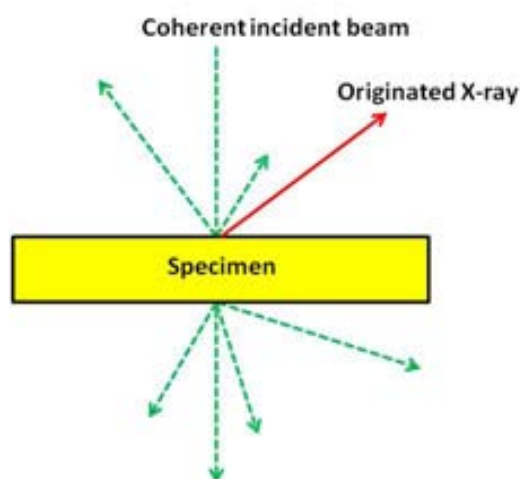


**Figure 2.3.5.1:** Diagram showing the X-ray emission originated when striking the sample with an electron beam. All different kinds of electron scattering from a thin specimen are also shown as broken arrows.

The **XEDS** uses silicon, Si, as a semiconductor so as to transform the energy of X-ray into electric signals. Specifically, when X-rays hit the semiconductor, electrons are transferred from the valence to the conduction band, creating thousands of electron-hole pairs. Since the number of the created electron holes is directly proportional to the energy of the X-ray photon and this energy depends on the element in which the X-ray has been generated, it is possible, as aforementioned, to analyze the chemical composition of the specimen.

All the information received by the spectrometer is processed by a computer and transformed into a spectrum, which shows the number of electric counts as function of a range of energies, measured in KeV.

### 2.3.6 Energy Electron Loss Spectroscopy (EELS)

**EELS** consists of analyzing the energy distribution of electrons that have gone through the specimen, which may have suffered elastic or inelastic scattering.

The analyzed electrons carry an enormous amount of information about the chemical and electronic structure of the specimen atoms. Thanks to them, it is possible

## 2. Nanoparticle characterization techniques

to know not only its atomic composition, but also the valence state and the chemical environment of its different atoms.

So as to collect and analyze those electrons, a special assembly (situated below the microscope column) is required. Firstly, the electrons go through a magnetic prism, which acts both as a spectrometer and as a lens by deflecting them through  $\geq 90^\circ$  according to their energy, in a similar way than glass prisms work with visible white light. In this vein, those that have lost energy are deflected further than those that have not. After going through a projector, a spectrum is formed in the dispersion plane, as shown in **Figure 2.3.6.1**:

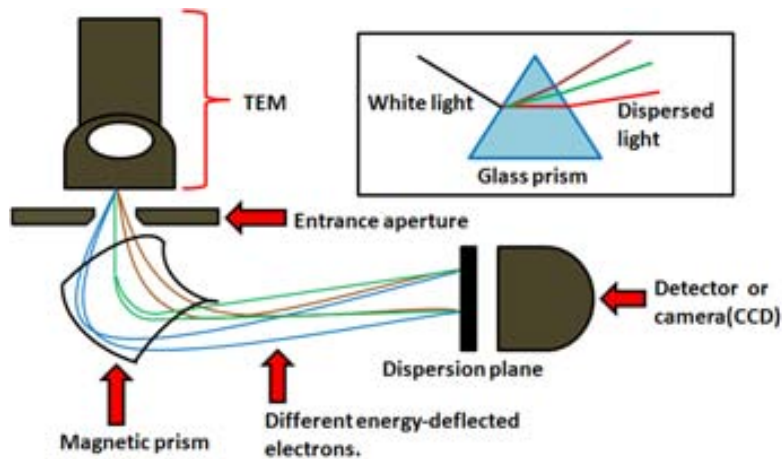


**Figure 2.3.6.1:** Diagram showing how the **EELS** assembling works, and its comparison with a glass prism working.

The resulting **EELS** spectra show the number of electron counts (intensity) as function of the energy loss of the electrons, as shown in **Figure 2.3.6.2**:

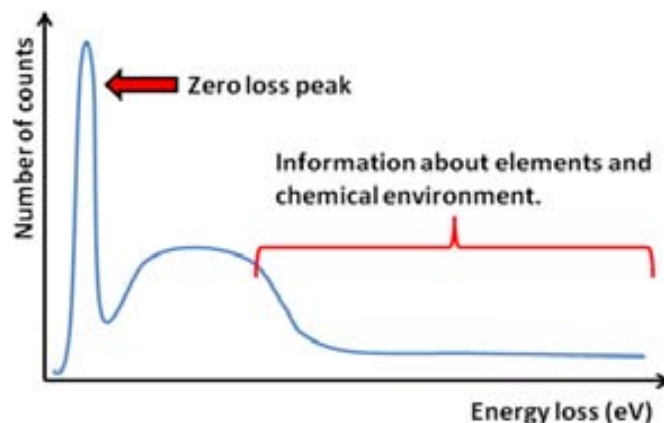


**Figure 2.2.4.5:** Typical **EELS** spectrum.

**EELS** is told to be an **EDX**'s complementary technique, since both supply information about the chemical composition of the specimen. In fact, **EELS** works better with light (with small  $Z$ ) elements meanwhile **EDX** does it with heavier elements,



## 2. Nanoparticle characterization techniques

which makes them complementary. It is worth mentioning, however, that **EELS** is different from **EDX** in some important points, since **EELS** can detect and quantify all the elements in the periodic table, and it also has better spatial resolution and analytical sensitivity. On the other hand, **EELS** is a very demanding experimental technique, because it requires very thin specimens to work as well as deeper physics background than **EDX**.

### 2.3.7 Energy-filtered TEM (EFTEM)

This technique is basically a direct application of **EELS**. It is a powerful **AEM** technique since it creates elemental maps, which are specimen images (or diffraction patterns) that show the spatial layout of a selected element in a specific specimen region.

**EFTEM** is basically carried out by using a slit to select (or to filter out) electrons with a specific energy that come through the spectrometer, and using a **CCD** camera to form the corresponding image or **DP**, as shown in **Figure 2.3.7.1**:

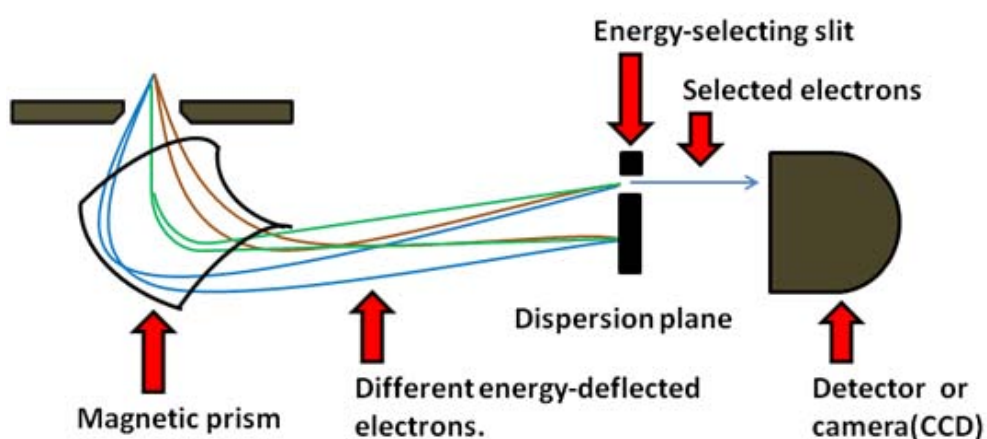


**Figure 2.3.7.1:** Diagram showing how the **EFTEM** technique works, by using an energy-selecting slit.

Despite not being as commonly used as **EFTEM**, **XEDS** can also be used in order to create elemental maps from specific regions of the specimen. However, in this thesis, only **EFTEM** images have been taken from some of the synthesized nanoparticles.



### 2.3.8 Electron holography

Since electrons can be considered not only as particles but also as waves, they have amplitude and phase. After hitting the specimen, the electron wave can change both parameters giving rise to image contrast.

Despite the fact that normally both amplitude and phase contrast contribute to an image, when working in different **TEM** modes, special conditions are selected so that one kind of contrast dominates over the other. In this vein, when working with **BF** and **DF** images, what predominates is the amplitude contrast. However, when doing electron holography, the phase contrast prevails.

Phase contrast is generated when more than one beam contributes to the image. In other words, it arises due to the phase differences between different electron waves scattered through the specimen, forming an interference pattern from which an hologram can be formed. **Figure 2.3.8.1** shows a hologram formed by two light (laser) beams, one of which hits an object:

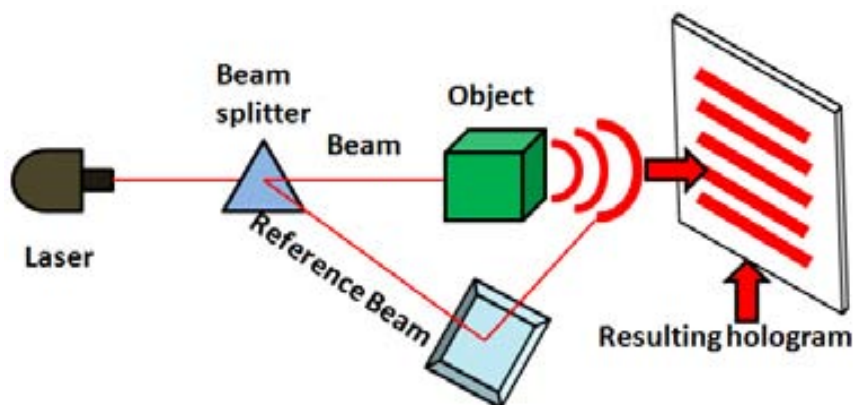


**Figure 2.3.8.1:** Diagram showing how to obtain a hologram by using two different beams, one that hits an object and other that does not.

When working inside **TEM**, however, the necessary assembly is a bit different. In order to do electron holography, a region of the beam must hit the specimen, while the other must not. At some point, inside the column, a wire called ‘Fresnel Biprism’ (which can be made of glass fiber coated with Cr or Au) splits the beam in two parts, generating two ‘pseudo beams’ with a phase difference between the one that has hit the beam and the one that has not. Both resulting ‘pseudo beams’ overlap each other in a specific part of the viewing screen (or digital camera) and form a resulting interference pattern from which a resulting hologram can be obtained.

In order to visualize this procedure better, the whole process is properly shown in Figure 2.3.8.2.

## 2. Nanoparticle characterization techniques

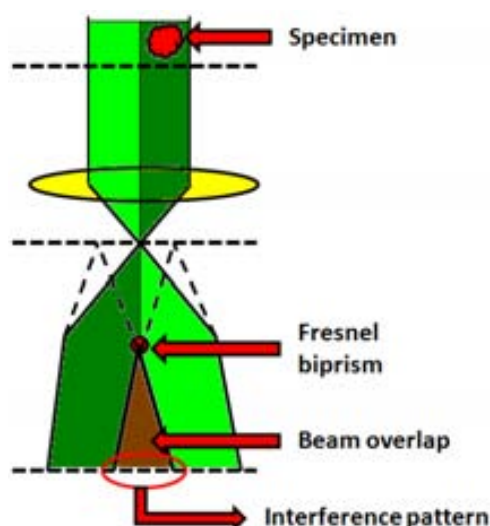


**Figure 2.3.8.1:** Schematic diagram of the setup for electron holography.

Apart from the setup differences, electron holography also differs from classical optical holography in the fact that electrons interact with the specimen atoms in a different way than photons do. One important example of this fact can be observed when carrying out electron holography on magnetic specimens. In that case, it is possible to study the magnetic behaviour of this kind of materials by analyzing how the phase of the electrons changes after hitting the specimen.

In case of magnetic materials, the resulting phase shift is mainly due to two different factors of the specimen: its 'mean inner potential' and its 'magnetic contribution'. The main objective when running this technique consists of decreasing its mean inner potential in order to equal the phase shift to the magnetic contribution, and it can be done by taking two images from the same region of the specimen, before and after turning it over. Since the mean inner potential does not depend on the orientation in which the electron beam hits the specimen and the magnetic contribution does depend on it, after taking both images and resting the differences of phase, the resulting value will be only given to the change in the magnetic contribution.

Obviously, all that treatment has to be done via computer analysis after a **TEM** session. Depending on both the specimen nature and the accuracy of the analysis, it may take days or even weeks to complete the study for a single sample.

In this thesis, electron holography has been carried out on iron oxide nanorods so as to study their magnetic behaviour, as it will be properly explained in the corresponding chapter.

## 2. Nanoparticle characterization techniques

### 2.4 Related Literature:

- <sup>1</sup> Owen T., *Fundamentals of modern UV-visible spectroscopy*, Hewlett-Packard, **1996**.
- <sup>2</sup> Mayergoyz I.D., *Plasmon resonances in Nanoparticles*, World Scientific Pub. Co. Inc., **2013**.
- <sup>3</sup> Stuart B., *Infrared Spectroscopy: Fundamentals and Applications*, Wiley, **2004**.
- <sup>4</sup> Watts J.F.; Wolstenholme J., *An Introduction to Surface Analysis by XPS and AES*, Wiley, **2003**.
- <sup>5</sup> Fadley C.S., *J. Electron. Spectrosc. Relat. Phenom.*, **2010**, 178-179, 2-32.
- <sup>6</sup> Yoshida Y.; Langouche G., *Mössbauer Spectroscopy: Tutorial Book*, Springer, **2012**.
- <sup>7</sup> McElfresh M., *Fundamentals of Magnetism and magnetite Measurements*, Purdue University, **1994**.
- <sup>8</sup> Cullity B. D.; Graham C.D., *Introduction to Magnetic Materials*, Wiley-IEEE Press, 2008.
- <sup>9</sup> Morris A. H., *The Physical Principles of Magnetism*, Wiley-IEEE Press, **2001**.
- <sup>10</sup> Bruce P. G., *Powder Diffraction: Theory and Practice*, Royal Society of Chemistry, **2008**.
- <sup>11</sup> Gabbot P., *Principles and Applications of Thermal Analysis*, Wiley-Blackwell, **2007**.
- <sup>12</sup> Williams D. B.; Carter C. B., *Transmission Electron Microscopy*, Springer, **2009**. (Volumes 1-4)
- <sup>13</sup> Dunin-Borkowski R.E.; Kasama T.; Beleggia M.; Giulio P., *Handb. Nanosc.*, **2012**, 1, 221-251.
- <sup>15</sup> Shindo D.; Murakami Y., *J. Phys. D: Appl. Phys.*, **2008**, 41, 183002/1-183002/21.

## 2. Nanoparticle characterization techniques

# **Part II**

## **Thesis objectives**



# Chapter

## Thesis objectives

### Contents

---

3.1 General description and objectives of the thesis.....	103
---	-----

### 3. Thesis objectives



## 3. Thesis objectives

### 3.1 General description and objectives of the thesis

This doctoral thesis has been done inside the research group “Partícules Inorgàniques amb Lligands Funcionals”. The main field of research is based on developing new synthetic routes to obtain metallic and metal oxide nanoparticles, as well as fully characterizing them via microscopic and non-microscopic analytical techniques.

Specifically, the chief objectives of this Thesis are the following ones:

- Synthesis of metallic (gold or silver) water-dispersible nanoparticles and to functionalize them with rhenium carbonyl species, making them useful for further assays in the field of radio pharmacy.
- Synthesis of magnetite,  $\text{Fe}_3\text{O}_4$ , and mixed ferrites  $\text{MFe}_2\text{O}_4$  ( $\text{M} = \text{Co}, \text{Mn}, \text{Cu}, \text{Zn}$ ) nanoparticles, easy and cheap enough to make them attractive for further analysis and applications in materials' science.
- Formation of magnetite nanostructures with non-spherical shapes, such as nanorods, in order to study how the magnetic (and other) properties are affected by the influence of the shape.
- Development of a reproducible synthetic method to obtain either water or organic-media dispersible  $\text{Fe}_3\text{O}_4@Au$  core-shell nanostructures as well to study and verify the presence of the magnetite cores inside the gold shells.
- Characterization of all the synthesized nanostructures via using the correct microscopic and non-microscopic techniques in order to study their main properties.

### 3. Thesis objectives

# **Part III**

## **Experimental work, discussion and conclusions**



## Chapter 4

# Gold and silver nanoparticles functionalized with sodium 3-mercaptopropanoate. Coordination with rhenium carbonyl complexes

### Contents

---

4.1 General description of the carried out work.....	111
4.2 Experimental procedure.....	112
4.2.1 Materials and reactants.....	112
4.2.2 Synthesis of sodium mercaptopropanoate (NaMP)-Capped Au nanoparticles.....	112
4.2.3 Synthesis of sodium mercaptopropanoate (NaMP)-Capped Ag nanoparticles.....	113
4.2.4 Synthesis of Rhenium carbonyl initial complex [ <i>fac</i> -Re(H <sub>2</sub> O) <sub>3</sub> (CO) <sub>3</sub> ](CF <sub>3</sub> SO <sub>3</sub> ) for further coordination on nanoparticles' surface.....	113
4.2.5 Reaction of Sodium Mercaptopropanoate (NaMP)-Capped Au Nanoparticles with [ <i>fac</i> -Re(H <sub>2</sub> O) <sub>3</sub> (CO) <sub>3</sub> ](CF <sub>3</sub> SO <sub>3</sub> ).....	113
4.2.6 Reaction of Sodium Mercaptopropanoate (NaMP)-Capped Au Nanoparticles with [ <i>fac</i> -Re(H <sub>2</sub> O) <sub>3</sub> (CO) <sub>3</sub> ](CF <sub>3</sub> SO <sub>3</sub> ).....	113
4.3 Characterization and result discussion.....	114
4.3.1 TEM Bright Field microphotographs.....	114
4.3.2 X-ray powder diffraction.....	114
4.3.3 Visible-UV spectroscopy.....	114

## 4. Gold and silver nanoparticles surface functionalized

4.3.4 XPS Analyses.....	118
4.3.4.1 General information obtained from the synthesized nanoparticles.....	118
4.3.4.2 Re (4f) analysis.....	122
4.3.4.3 O (1s) analysis.....	122
4.3.4.4 S (2p) analysis.....	124
4.3.4.5 C (1s) analysis.....	125
4.3.5 TGA Analyses.....	126
4.3.7 Vibrational studies.....	128
4.4 Summary.....	132
4.5 Related literature.....	133

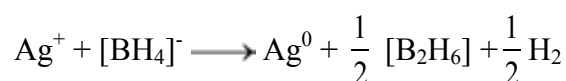
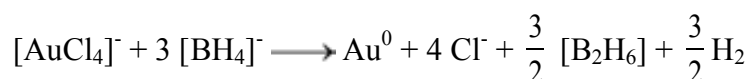
### 4. Gold and silver nanoparticles functionalized with sodium 3-mercaptopropionate. Coordination with rhenium carbonyl complexes

This chapter explains the synthesis, functionalization and characterization of gold (and silver) nanoparticles capped with sodium 3-mercaptopropionate (**NaMP**) and functionalized with rhenium carbonyl complexes. In all cases, the resulting nanoparticles have been completely characterized via different techniques, before and after carrying out the rhenium carbonyl coordination on the surface of the nanoparticles. The rhenium carbonyl complexes used in this work have also been synthesized and characterized, by following a synthetic procedure previously reported in the literature.

The discussion of the results obtained when carrying out the nanoparticles characterization is also explained in detail in this chapter.

#### 4.1 General description of the carried out work

Water dispersible gold and silver nanoparticles coated with sodium 3-mercaptopropionate **NaMP** ligand have been prepared by a modification of a method previously described in the literature, via metal salts reduction by using the sodium borohydride,  $\text{NaBH}_4$ , as a reductor agent:



Consequently, **NaMP**-coated metal nanoparticles have been obtained by the reduction of  $\text{HAuCl}_4$  or  $\text{AgNO}_3$  dissolved in ethanol with freshly dissolved  $\text{NaBH}_4$  in cold water in the presence of an excess of **MPA** (6 eq. **MPA** / 1 eq.  $[\text{AuCl}_4]^-$ ). These reactions have been carried out with an excess of  $\text{NaBH}_4$  (1 eq.  $[\text{AuCl}_4]^-$  / 9 eq.  $\text{NaBH}_4$ ; 1 eq.  $\text{Ag}^+$  / 3 eq.  $\text{NaBH}_4$ ) so as to guarantee an enough basic medium to stabilize the carboxylic group in the anionic form (pH = 6-7 for Au and pH = 7-8 for Ag).

Nanoparticles have been separated from the reaction mixture via centrifugation, dispersed in pure water and purified with dialysis against water. **NaMP**-coated gold and silver nanoparticles have been isolated as black solids, both dispersible in water. In these metal aggregates, the bifunctional ligand 3-mercaptopropionate is bonded to the nanoparticle surface through the S atom whereas the anionic carboxylate group remains uncoordinated and strongly interacts with water making nanoparticles hydrophilic. With the aim of complexing the carboxylate groups to *fac*- $[\text{Re}(\text{CO})_3]^+$  metal fragments, the reaction between **NaMP-Au** and **NaMP-Ag** nanoparticles and  $[\text{Re}(\text{H}_2\text{O})_3(\text{CO})_3]^+$  has

## 4. Gold and silver nanoparticles surface functionalized

been performed in water. Mixtures of **NaMP**-coated metal nanoparticles and the rhenium carbonyl compound have been stirred during 24h at room temperature leading to red or yellow colored solutions containing dispersions of rhenium carbonyl functionalized gold and silver nanoparticles **ReMP-Au** and **ReMP-Ag** respectively. Excess of water-soluble reagents and inorganic salts have been removed from the solution by means of 24 h dialysis in water. Centrifugation, filtration and ethanol and dichloromethane washing led to black solids of **ReMP-Au** and **ReMP-Ag**. These new nanoparticles are very dispersible in water but insoluble in alcohols and hydrocarbons.

### 4.2 Experimental procedure

#### 4.2.1 Materials and reactants

HAuCl<sub>4</sub>·H<sub>2</sub>O (Aldrich, ≥49% Au basis), AgNO<sub>3</sub> (Aldrich, >99%), NaBH<sub>4</sub> (Fluka, >96%), 3-mercaptopropionic acid (**MPA**) (Aldrich, 99+%), Re<sub>2</sub>(CO)<sub>10</sub> (Strem 98%), Br<sub>2</sub> (Fluka ≥ 99.5%), Ag(O<sub>3</sub>SCF<sub>3</sub>) (Strem 99%), All reactions were carried out in either Millipore water, absolute ethanol (AR grade), diethyl ether (AR grade), Hexane (AR grade) or dichloromethane (AR grade).

#### 4.2.2 Synthesis of sodium mercaptopropionate (NaMP)-Capped Au nanoparticles

The synthesis of **NaMP**-capped Au nanoparticles was performed by following a previously reported procedure by Wang *et al.*<sup>1</sup>, with some modifications. To a vigorously stirred solution containing 308 mg (0.89 mmol, 1 equiv.) of HAuCl<sub>4</sub> and 0.5 mL of 3-mercaptopropionic acid (4.44 mmol, 5 equiv.) in 100 mL of absolute ethanol were added, at 0°C under a N<sub>2</sub> atmosphere and vigorous stirring, 5 mL of a water solution containing 306 mg of NaBH<sub>4</sub> (8.1 mmol, 9 equiv.). The resulting pH after addition was 6-7. The black precipitate was collected by centrifugation and washed with absolute ethanol and diethyl ether. Then, it was dispersed in water to form an intense red suspension, and purified by dialysis against pure water for 24h to remove residual inorganic ions. The dialyzed suspension was concentrated and dried at 45 °C under reduced pressure. Finally, about 237 mg **NaMP**-capped Au nanoparticle powder were obtained. The obtained powder is easily dispersible in water to form a stable intense red solution.



## 4. Gold and silver nanoparticles surface functionalized

### 4.2.3 Synthesis of sodium mercaptopropionate (NaMP)-Capped Ag nanoparticles

The synthesis of NaMP-capped Ag nanoparticles was adapted and modified from the procedure mentioned before<sup>1</sup>, replacing H<sub>2</sub>AuCl<sub>4</sub> by 152 mg (0.89 mmol, 1 equiv.) of AgNO<sub>3</sub> and using only 102 mg of NaBH<sub>4</sub> (2.7 mmol, 3 equiv.) obtaining a resulting pH value of 7-8. Finally, about 156 mg NaMP-capped Ag nanoparticle powder were obtained. The obtained powders are also easily dispersible in water to form a stable intense yellow solution.

### 4.2.4 Synthesis of Rhenium carbonyl initial complex [*fac*-Re(H<sub>2</sub>O)<sub>3</sub>(CO)<sub>3</sub>](CF<sub>3</sub>SO<sub>3</sub>) for further coordination on nanoparticles' surface

The synthesis of this complex was carried out according to the reported method using [Re(CO)<sub>5</sub>(CF<sub>3</sub>SO<sub>3</sub>)]<sup>2</sup> as a precursor.

### 4.2.5 Reaction of Sodium Mercaptopropionate (NaMP)-Capped Au Nanoparticles with [*fac*-Re(H<sub>2</sub>O)<sub>3</sub>(CO)<sub>3</sub>](CF<sub>3</sub>SO<sub>3</sub>)

140 mg of the NaMP-Capped Au nanoparticles were suspended in 100 mL of a water solution containing (3.25 · 10<sup>-2</sup> mmol) of [*fac*-Re(H<sub>2</sub>O)<sub>3</sub>(CO)<sub>3</sub>](CF<sub>3</sub>SO<sub>3</sub>), under a N<sub>2</sub> atmosphere. The mixture was stirred for 24 h at room temperature and then purified by dialysis against pure water for 24h to remove residual inorganic ions. The dialyzed suspension was concentrated and dried at 45 °C under reduced pressure. 145 mg of black product were obtained. This black product is dispersible in water to form a stable intense red solution.

### 4.2.6 Reaction of Sodium Mercaptopropionate (NaMP)-Capped Au Nanoparticles with [*fac*-Re(H<sub>2</sub>O)<sub>3</sub>(CO)<sub>3</sub>](CF<sub>3</sub>SO<sub>3</sub>)

The reaction of sodium mercaptopropionate (NaMP)-Capped Ag nanoparticles with [Re(H<sub>2</sub>O)<sub>3</sub>(CO)<sub>3</sub>](CF<sub>3</sub>SO<sub>3</sub>) was carried out exactly by the same procedure described for the gold nanoparticles using in that case 140 mg of the NaMP-Capped Ag nanoparticles, and protecting the mixture reaction from light. 105 mg of black product were obtained. This black product is also easily dispersible in water to form a stable intense yellow solution.

## 4. Gold and silver nanoparticles surface functionalized

### 4.3 Characterization and result discussion

The resulting (gold and silver) nanoparticles characterization, as well as the obtained data discussion is described in this section. The characterization itself has been carried out via seven different analytical techniques:

- Transmission electron microscopy (TEM) Bright Field microphotographs.
- Infrared and Raman vibration spectroscopy.
- Powder X-Ray diffraction.
- Thermogravimetric analysis (TGA) and differential scanning calorimetry (DSC)
- UV-Visible spectroscopy.
- Z-Potential analysis.
- X-ray photoelectron spectroscopy surface analysis (XPS)

#### 4.3.1 TEM Bright Field microphotographs

Nanoparticle morphologies have been observed by using a Jeol 2011Gen transmission electron microscope (TEM) operating at an accelerating voltage of 200 kV.

TEM microphotographs of NaMP-Au and NaMP-Ag and the corresponding particle size distribution histograms are shown in **Figure 4.3.1.1** and **Figure 4.3.1.2**.

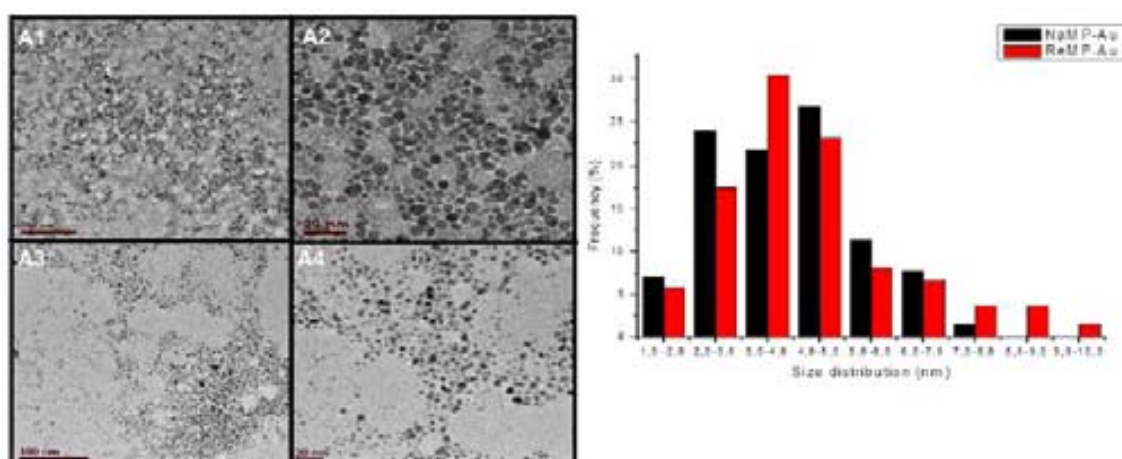


**Figure 4.3.1.1:** TEM images and particle size distribution of (A1,A2) NaMPAu and (B1,B2) ReMPAu nanoparticles.

#### 4. Gold and silver nanoparticles surface functionalized

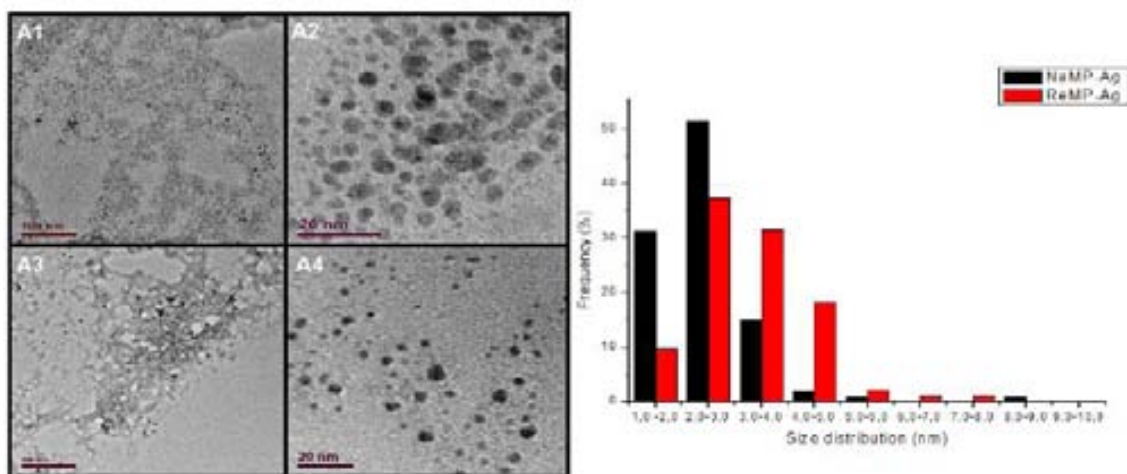


**Figure 4.3.1.2:** TEM images and particle size distribution of (A1,A2) NaMPAg and (B1,B2) ReMPAg nanoparticles.

Images of NaMP-Au show polydispersed nearly spherical particles with an average diameter of  $3.8 \pm 1.4$  nm. The corresponding images of NaMP-Ag show polydispersed nanoparticles of average size  $2.4 \pm 0.9$  nm. After complexing gold and silver nanoparticles with rhenium species, the particle size increases until  $4.2 \pm 1.8$  nm and  $3.2 \pm 1.0$  nm for ReMP-Au and ReMP-Ag respectively. All the obtained sizes, as well as their respectively distributions, are shown in Table 4.3.1.1.

	Without Re Carbonyls	With Re Carbonyls
NP Au	$3.8 \pm 1.4$ nm	$4.2 \pm 1.8$ nm
NP Ag	$2.4 \pm 0.9$ nm	$3.2 \pm 1.0$ nm

**Table 4.3.1.1:** Nanoparticle sizes of gold and silver nanoparticles before and after carrying out coordination with the rhenium carbonyl species.

These results suggest that core size of gold nanoparticles remained nearly identical when 3-mercaptopropionate surface monolayer was bonded to rhenium carbonyl metal fragments and that capping molecules are not bulky enough to be observed in TEM images. Silver nanoparticles coordinated with Rhenium carbonyl result in aggregation as shown in TEM microphotographs and UV- spectra. The obtained values are also consistent with the estimate particle size calculated from Scherrer's equation<sup>2</sup> on the line widths of the XRD peaks.

## 4. Gold and silver nanoparticles surface functionalized

### 4.3.2 X-ray powder diffraction

Powder X-ray diffraction (XRD) patterns have been recorded on A Philips XPERT diffractometer (PW3020), with Cu anode, graphite monochromator, working at 40 kV, 50 mA, and sample holder spinning has been used.

The X-ray powder diffraction patterns of sodium 3-mercaptopropionate capped NaMP-Au and NaMP-Ag and rhenium carbonyl ReMP-Au and ReMP-Ag capped nanoparticles are shown in Figure 3. Typical peaks assigned to (111), (200), (220) and (311) planes for face centered-cubic gold and silver are observed<sup>2,3</sup>. (Table 4.3.2.1)

Observed planes	NaMP-Au nanoparticles	ReMP-Au nanoparticles	NaMP-Ag nanoparticles	ReMP-Ag nanoparticles
(111)	Observed	Observed	Observed	Observed
(220)	Observed	Observed	Observed	Observed
(200)	Observed	Observed	Observed	Observed
(311)	Observed	Observed	Observed	Observed

**Table 4.3.2.1:** Observed diffraction planes in gold and silver NaMP capped nanoparticles, before and after rhenium carbonyl complexation.

As expected, the XRD peaks appear broadened compared to those of bulk gold and silver due to the very small size of particles. This result is in agreement with previous studies with thiol capped gold and silver nanoparticles. The obtained X-ray powder diffraction patterns are shown as follows (Figure 4.3.1.3):

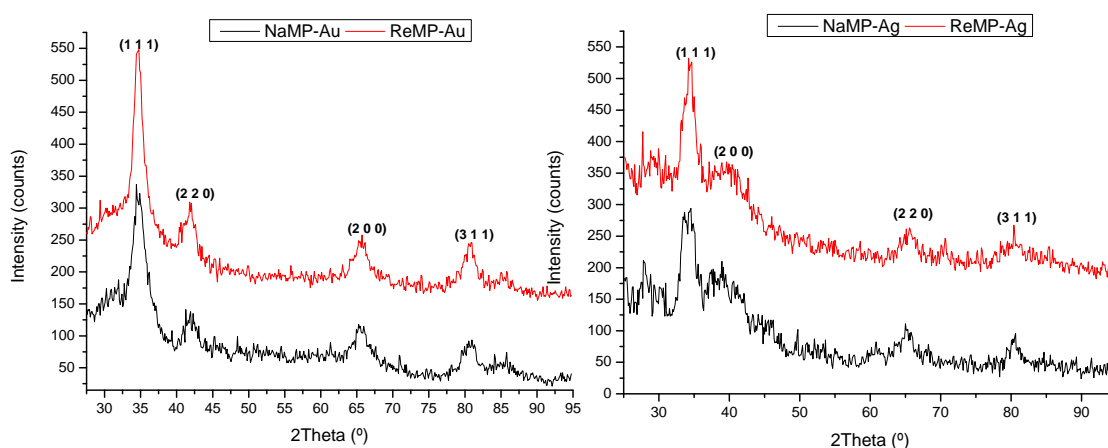


**Figure 4.3.2.1:** XRD patterns of (A) NaMPAu and ReMPAu and (B) NaMPAg and ReMPAg.

## 4. Gold and silver nanoparticles surface functionalized

### 4.3.3 Visible-UV spectroscopy

UV-Visible spectra have been recorded on a Hewlett Packard: model 8453.

Figure 4.3.3.1 shows the UV-visible spectra of water dispersions of **NaMP-Au** and **NaMP-Ag** nanoparticles before and after coating with the rhenium carbonyl species.

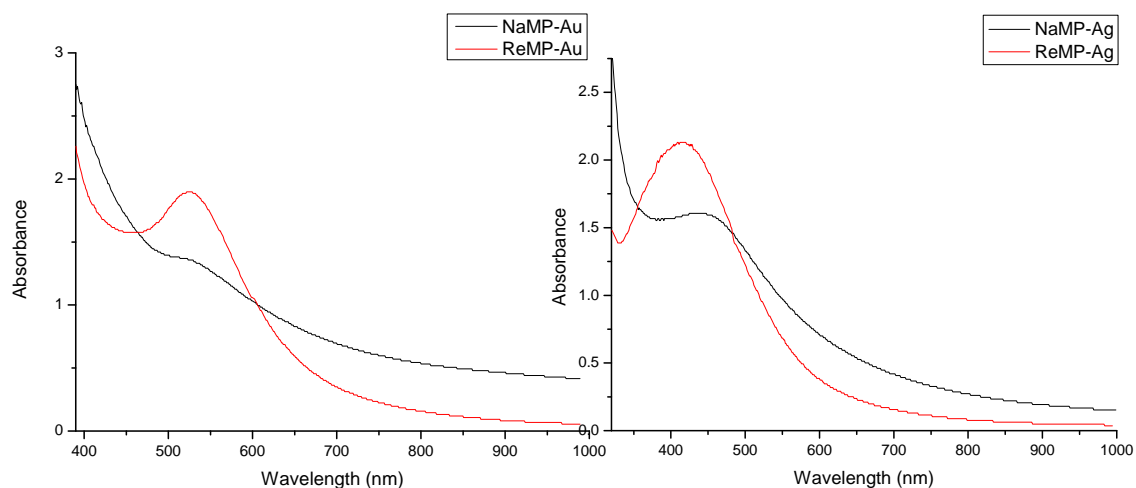


**Figure 4.3.3.1:** UV-Visible spectra of water dispersions of **NaMP-Au**, **NaMP-Ag**, **ReMP-Au** and **ReMP-Ag**.

The **NaMP-Au** sample displays a clear absorption at 525 nm while after being complexed with rhenium carbonyl species shows a broad band centered at 527 nm. Concerning to **NaMP-Ag** nanoparticles, a peak at 417 nm assigned to Ag surface plasmon resonance is observed in the spectrum, while after being complexed with the rhenium carbonyl species shows a broad band centered at 440 nm. (Table 4.3.3.1)

	<b>NaMP-Au</b>	<b>NaMP-Ag</b>
<b>Before Re coordination</b>	<b>525 nm</b>	<b>527 nm</b>
<b>After Re coordination</b>	<b>417 nm</b>	<b>440 nm</b>

**Figure 4.3.3.1:** Maximum peak values obtained in the UV-Visible spectra of water dispersions of **NaMP-Au**, **NaMP-Ag**, **ReMP-Au** and **ReMP-Ag**.

UV-visible spectra of water dispersions of rhenium containing nanoparticles show some differences with respect to **NaMP-Au** and **NaMP-Ag** samples. In both cases the distinctive plasmon resonance absorption of NaMP-Metal is shifted to slightly lower energy when the rhenium carbonyl species is coordinated to the surface of the nanoparticles. This result matches with increasing core size of nanoparticles upon

## 4. Gold and silver nanoparticles surface functionalized

coordination, particularly evident in silver nanoparticles, resulting from loss of repulsion charge in the surface and then in aggregation of the particles in solution.

### 4.3.4 XPS Analyses

**XPS** experiments have been performed in a PHI 5500 Multitechnique System (from Physical Electronics) with a monochromatic X-ray source (Aluminum K  $\alpha$  line of 1486.6 eV energy and 350 W), placed perpendicular to the analyzer axis and calibrated using the 3d<sub>5/2</sub> line of Ag with a full width at half maximum (**FWHM**) of 0.8 eV. The analyzed area was a circle of 0.8 mm diameter, and the selected resolution for the spectra was 187.5 eV of Pass Energy, 0.8 eV/step for the general spectra and 23.5 eV of Pass Energy, and 0.1 eV/step for the spectra of the different elements. All Measurements were made in an ultra-high vacuum (**UHV**) chamber pressure between  $5 \times 10^{-9}$  and  $2 \times 10^{-8}$  torr.

#### 4.3.4.1 General information obtained from the synthesized nanoparticles

The composition of surface coating was deduced from **XPS** spectra of **MPA-Au**, **MPA-Ag**, **ReMP-Au** and **ReMP-Ag**. This spectroscopy gives information about binding energies of inner shell electrons of all the elements expected in those functionalized nanoparticles that include the Au and Ag metal core, C, O, S and Re. Details of peak positions and the relative amounts of different atomic species are listed in **Table 4.3.4.1**, which shows **XPS** spectra of **Re-MPA** functionalized Au and Ag nanoparticles. Binding energy values were corrected by adjusting the Au 4f<sub>7/2</sub> peak at 84.0 eV and the Ag 3d<sub>5/2</sub> peak at 368.2 eV for Au and Ag nanoparticles, respectively.

#### 4. Gold and silver nanoparticles surface functionalized

	O (1s)	C (1s)	S (2p <sub>3/2</sub> 2p <sub>1/2</sub> )	Au (4f <sub>5/2</sub> 4f <sub>7/2</sub> )	Ag (3d <sub>3/2</sub> 3d <sub>5/2</sub> )	Re (4f <sub>5/2</sub> 4f <sub>7/2</sub> )
NaMP- Au	533.9 (30) <sup>b</sup>	288.7 (12) <sup>b</sup> 287.2 (16) <sup>b</sup>	163.3 (47) <sup>b</sup>	87.8 (45)		
	530.5 (70) <sup>b</sup>	284.1 (72)	162.0 (53) <sup>b</sup>	84.0 (55)		
NaMP- Ag	533.7 (41) <sup>b</sup>	289.3 (32) <sup>b</sup> 287.9 (19) <sup>b</sup>	164.6 (56) <sup>b</sup>		374.1 (42)	
	531.4 (59) <sup>b</sup>	284.7 (49)	163.3 (44) <sup>b</sup>		368.2 (58)	
ReMP- Au	534.8 (57) <sup>b</sup>	287.9 (26) <sup>b</sup> 286.1 (16) <sup>b</sup>	163.6 (53) <sup>b</sup>	87.8 (46)		43.5 (47)
	530.8 (43) <sup>b</sup>	284.1 (58) <sup>b</sup>	162.2 (47) <sup>b</sup>	84.0 (54)		41.6 (53)
ReMP- Ag	534.2 (59) <sup>b</sup>	288.7 (23) <sup>b</sup> 286.9 (15) <sup>b</sup>	163.7 (72) <sup>b</sup>		374.5 (42)	44.4 (46)
	531.4 (41) <sup>b</sup>	284.9 (62) <sup>b</sup>	162.4 (28) <sup>b</sup>		368.2 (58)	42.2 (54)
<sup>a</sup> Deconvoluted components of photoemission bands.						
<sup>b</sup> Relative peaks areas in brackets as percentages.						

**Table 4.3.4.1:** XPS binding-Energy Positions of Elements Present with Nanoparticle Samples<sup>a</sup>.

The XPS spectra of NaMP-Au and NaMP-Ag samples show emission peaks of Au or Ag core and those corresponding to NaMP. The Au 4f<sub>5/2</sub> and Au 4f<sub>7/2</sub> peaks at 87.8 and 84.0 eV, shown in **Figure 4.3.4.1**, correspond to those of metallic gold<sup>4</sup> and the Ag 3d<sub>3/2</sub> and Ag 3d<sub>5/2</sub> peaks at 374.1 and 368.2 eV, shown in **Figure 4.3.4.2**, are typical of metallic silver<sup>5</sup>. The absence of signals from Au(I) and Ag(I) indicates that there is no metal sulfide on the nanoparticle surface<sup>6,7</sup>.

#### 4. Gold and silver nanoparticles surface functionalized

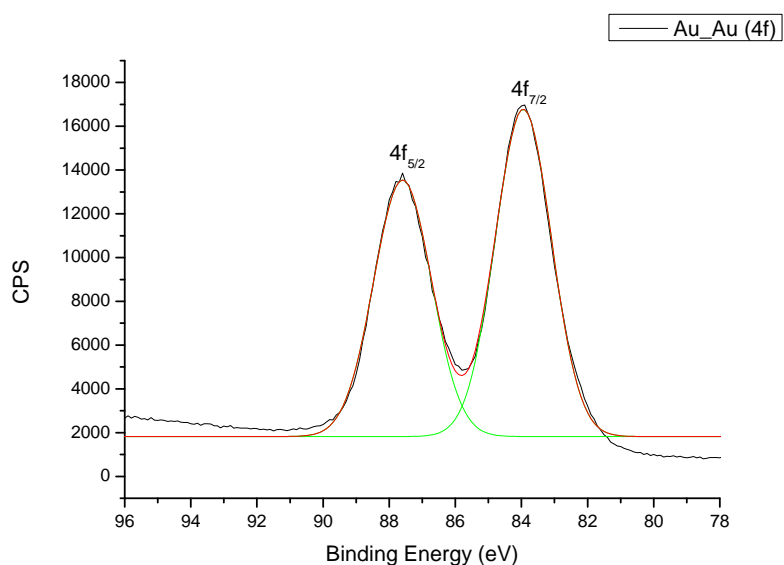


**Figure 4.3.4.1.1:** XPS of NaMP-Au, corresponding to  $4f_{5/2}$  and  $4f_{7/2}$  from Au region.

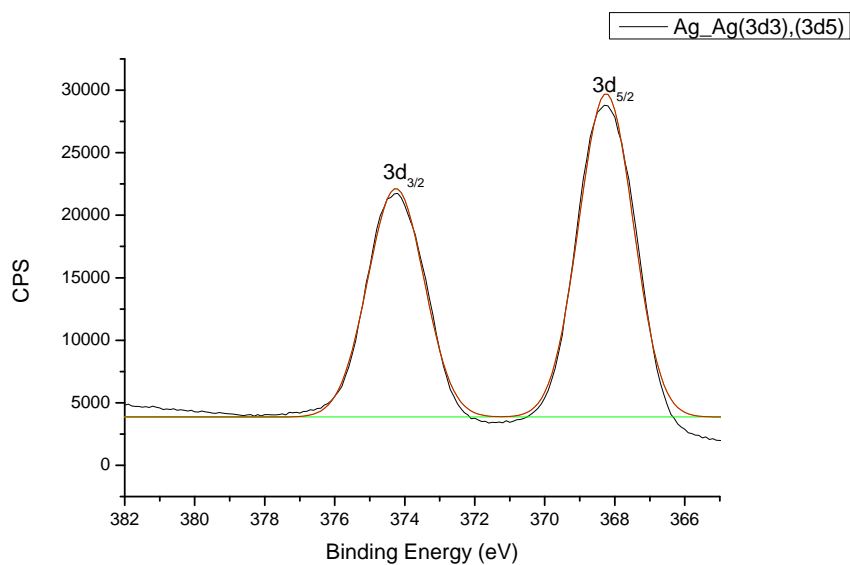


**Figure 4.3.4.1.2:** XPS of NaMP-Ag, corresponding to  $3d_{3/2}$  and  $3d_{5/2}$  from Ag region.

The XPS spectra of the **ReMP-Au** and **ReMP-Ag** show the corresponding Au  $4f_{5/2}$  and Au  $4f_{7/2}$  peaks at 87.8 and 84.0 eV, shown in **Figure 4.3.4.1.3**, in agreement with the metallic gold<sup>4</sup> and the Ag  $3d_{3/2}$  and Ag  $3d_{5/2}$  peaks at 374.5 and 368.2 eV, shown in **Figure 4.3.4.1.4**, which are typical values of metallic silver<sup>6</sup>.



#### 4. Gold and silver nanoparticles surface functionalized

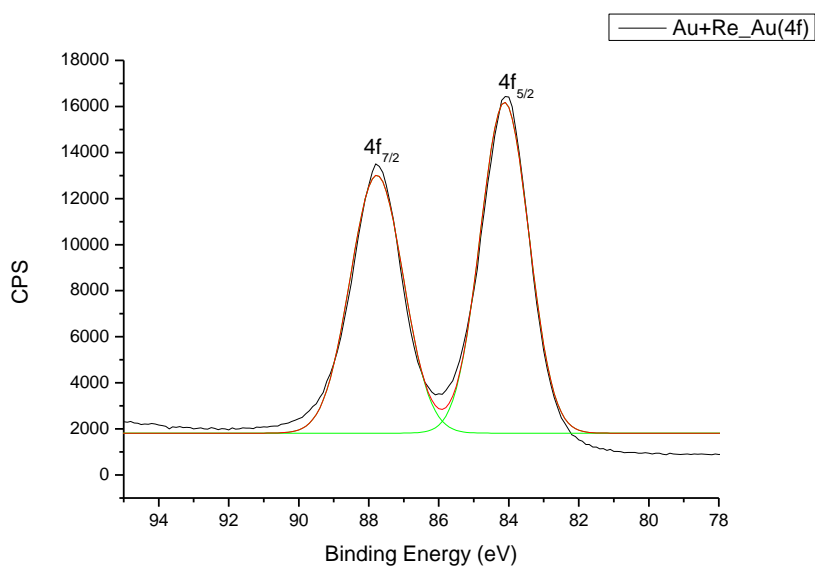


**Figure 4.3.4.1.3:** XPS of ReMP-Au, corresponding to  $4f_{5/2}$  and  $4f_{7/2}$  from Au region.

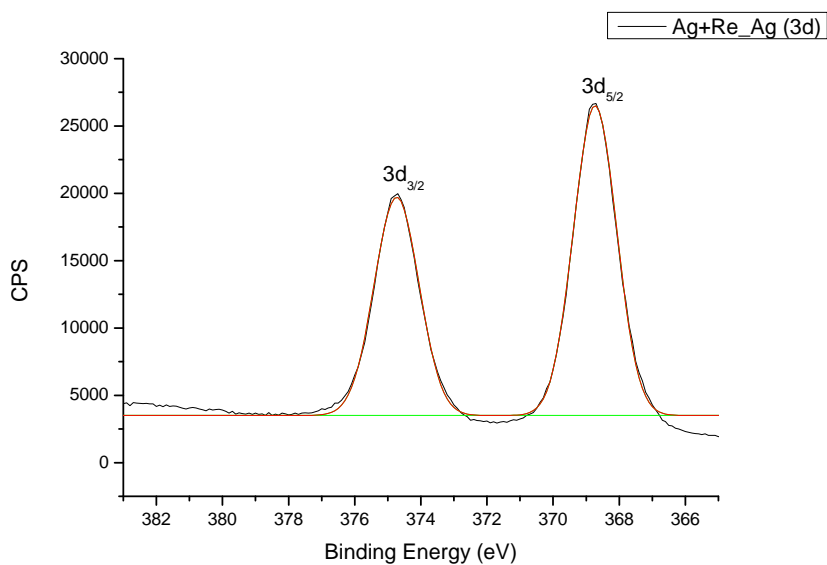


**Figure 4.3.4.1.4:** XPS of ReMP-Ag, corresponding to  $3d_{3/2}$  and  $3d_{5/2}$  from Ag region.

## 4. Gold and silver nanoparticles surface functionalized

### 4.3.4.2 Re (4f) analysis

Additional photoelectron signals at 43.5 and 41.6 eV in **ReMP-Au** and 44.4 and 42.2 eV in **ReMP-Ag** (**Figure 4.3.4.2.1**) samples corresponding to Re  $4f_{5/2}$  and  $4f_{7/2}$  energy levels show the presence of rhenium in these nanoparticle samples<sup>8</sup>. These values are also in agreement with Re 4f binding energy peaks in cationic Re(I) tricarbonyl complexes  $[\text{Re}(\text{bpy})(\text{CO})_3\text{L}]^+$ , where L is a phosphine or phosphinite monodentate ligand<sup>9</sup>, and do not show any peak attributed to metallic Rhenium. Some authors suggested that **XPS** is not sufficient to distinguish Re(0) and Re(I)<sup>10</sup>,] but higher oxidation states for Re can be well-differentiated since Re 4f peaks shift to higher binding energy when oxidation processes occurs<sup>10</sup>.

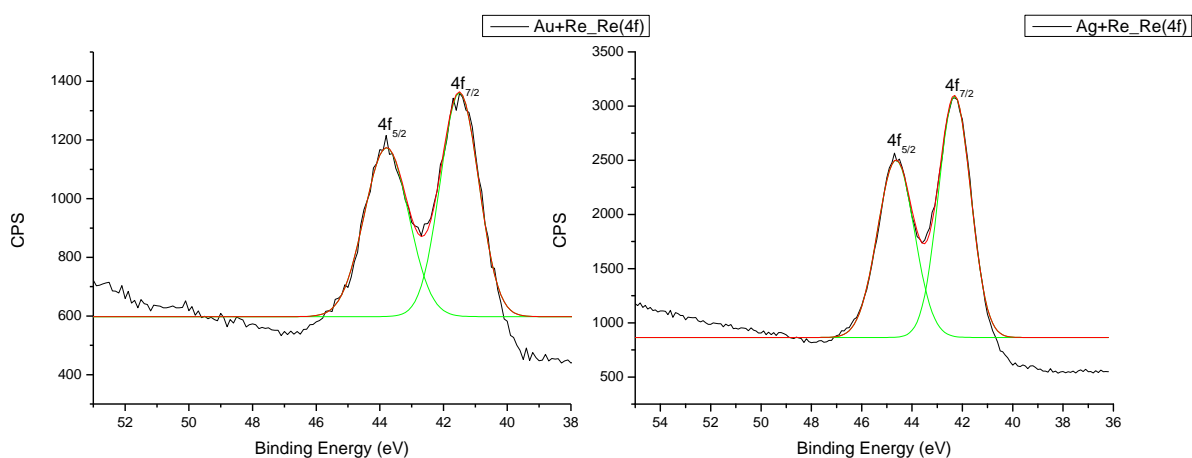


**Figure 4.3.4.2.1: XPS of ReMP-Au and ReMP-Ag, corresponding to  $4f_{5/2}$  and  $4f_{7/2}$  from Ag region.**

### 4.3.4.3 O (1s) analysis

The O 1s **XPS** spectra can be deconvoluted into an intense band at 530.5, 531.4 eV and a broad weak band at 533.9, 533.7 eV respectively for **NaMP-Au** and **NaMP-Ag** (**Figure 4.3.4.3.1**), that fits with two chemically distinct oxygen atoms at nanoparticles surface. In the case of alanine adsorbed on Au, peaks at 533.6 and 532.1 eV have been assigned to the two different bonding environments of the O atoms in the carboxylic group of the **MPA** [Ref]. In a recent study, the carboxylic O 1s emission peak of 3-**MPA** capped Au nanoparticles has been observed at 531.3 eV [Ref]. Taking into account that nanoparticles were synthesized in water it must not be excluded the possibility of having adsorbed O species derived from H<sub>2</sub>O on the Au surface. A recent **XPS** study of oxygen-containing layers made on stepped Au(111) film electrodes from aqueous solutions has assigned peaks at 532-533 eV to adsorbed O species (which include H<sub>2</sub>O) [Ref]. In the case of **NaMP-Au** and **NaMP-Ag** nanoparticles, the energy

#### 4. Gold and silver nanoparticles surface functionalized

separation of O 1s peaks of NaMP-Au and NaMP-Ag samples (3.9 and 2.3 eV, respectively) and their emission energies suggest that peaks at 533.9 and 533.7 eV correspond to O-adsorbed species and peaks at 530.5 and 531.4 eV to O-carboxylic atoms.

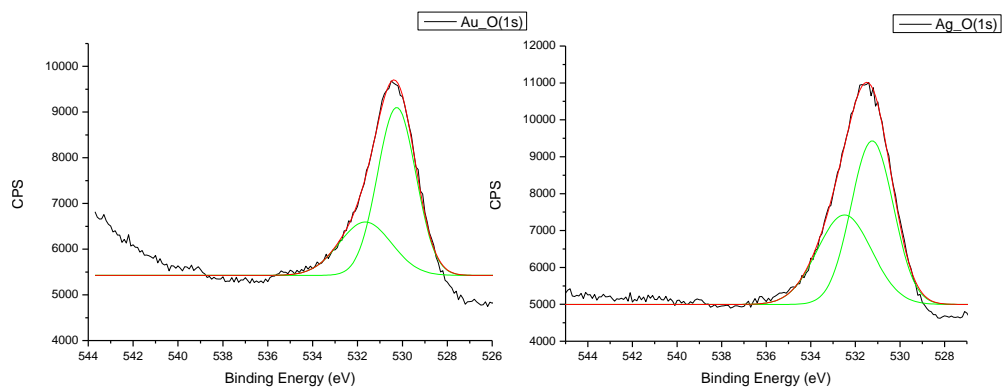


**Figure 4.3.4.3.1:** XPS of NaMP-Au (left) and NaMP-Ag (right), corresponding to 1s from O region.

The corresponding O 1s XPS binding energy photoemission peaks of Re capped nanoparticles (Figure 4.3.4.3.2) exhibit similar shapes to the ones observed in NaMP-Au and NaMP-Ag samples. These peaks can be deconvoluted into two different peaks: the most intense at 534.8, 534.2 and the weaker one at 530.8, 531.4 eV, respectively. As well as in the case of 3-MPA protected nanoparticles, this would mean that the most intense peaks correspond to overlapping signals of carboxylic and CO groups and the weaker broad peak can be assigned to O-adsorbed species. These results contrast with those obtained for Au nanoparticles encapsulated in Ru carboxylate shells where peaks corresponding to carboxylic and CO groups were clearly distinguished and assigned<sup>1</sup>.

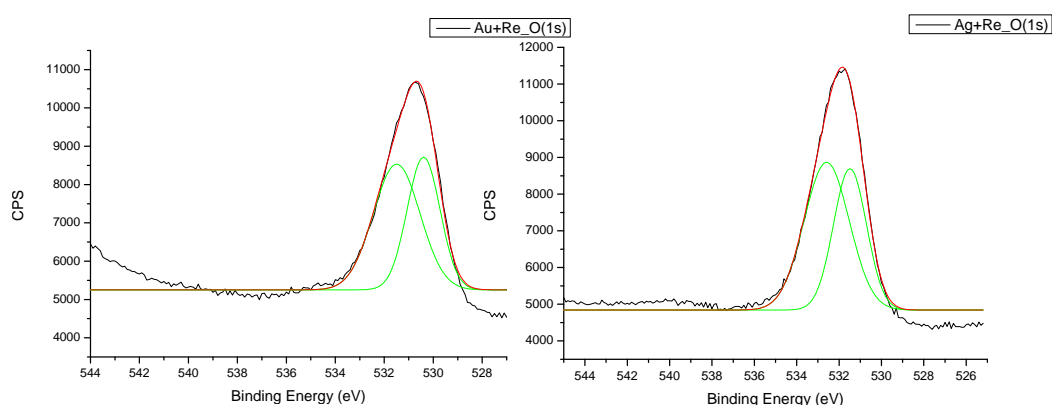


**Figure 4.3.4.3.2:** XPS of ReMP-Au (left) and ReMP-Ag (right), corresponding to 1s from O region.

## 4. Gold and silver nanoparticles surface functionalized

### 4.3.4.4 S (2p) analysis

The S 2p region shows a signal that can be deconvoluted in two different peaks at 163.3, 162.0 eV for **NaMP-Au** and 164.6, 163.3 eV for **NaMP-Ag**, respectively that correspond to the contributions of the 2p<sub>3/2</sub> and 2p<sub>1/2</sub> levels (**Figure 4.3.4.4.1**) as would be expected for sulfur atoms in the thiolate form bonded to metal surface nanoparticles<sup>7</sup>. These values are clearly different to the binding energies of the parent thiol<sup>1</sup>. The absence of S 2p peaks compatible with sulfide (S<sup>2-</sup>) ions confirms that no metal sulfide is present on the nanoparticles' surface<sup>7</sup>.

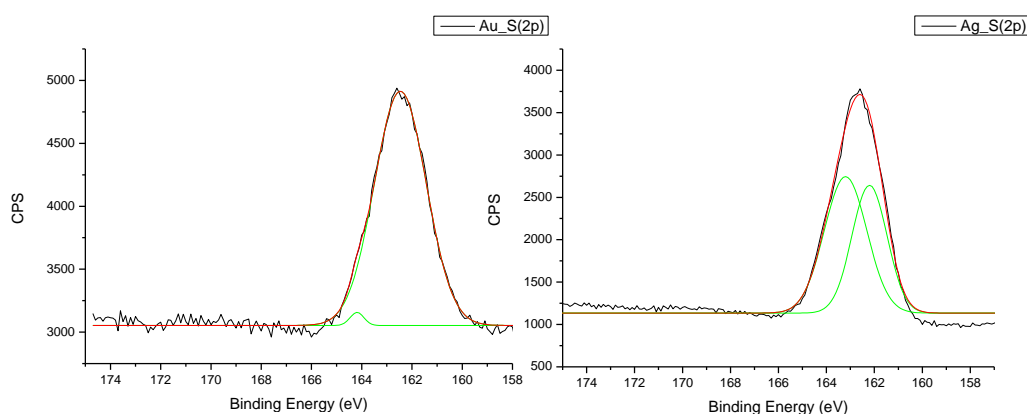


**Figure 4.3.4.4.1:** XPS of NaMP-Au (left) and NaMP-Ag (right), corresponding to 2p from s region.

On the other hand, the S 2p region shows a signal similar to that obtained for the **NaMP-Au** and **NaMP-Ag** samples. That signal can also be resolved in two peaks at 163.6, 162.2 eV for **ReMP-Au** and 163.7, 162.4 eV for **ReMP-Ag**, respectively. These that can be assigned to the contributions of 2p<sub>3/2</sub> and 2p<sub>1/2</sub> levels, that correspond to sulfur atoms forming a thiolate bond to the metal surface of the nanoparticles. As can be observed for **NaMP-Ag** and **NaMP-Au** nanoparticles, there are not evidences suggesting the presence of S 2p peaks typical of sulfide S<sup>2-</sup> ions on the nanoparticles' surface.

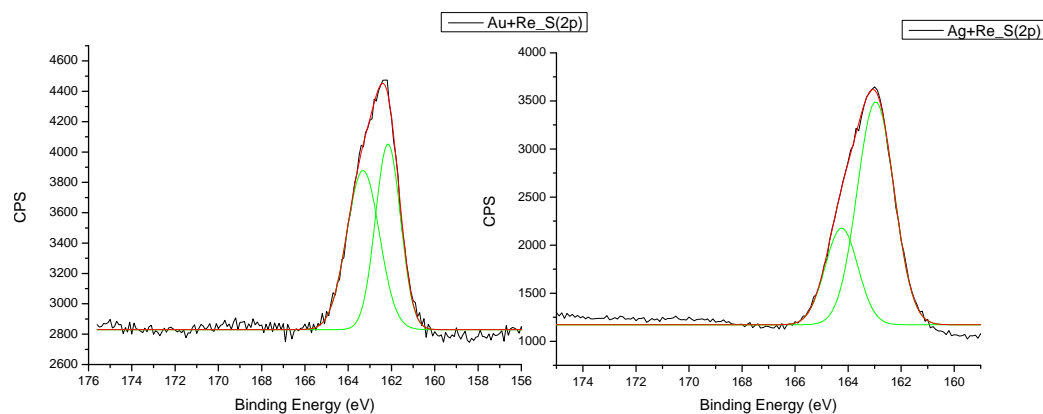


**Figure 4.3.4.4.2:** XPS of ReMP-Au (left) and ReMP-Ag (right), corresponding to 2p from s region.

## 4. Gold and silver nanoparticles surface functionalized

### 4.3.4.5 C (1s) analysis

The C 1s region shows an intense peak centered at 284.1 and 284.7 eV, for **NaMP-Au** and **NaMP-Ag** respectively, and a smaller broad photoemission that can be resolved into two peaks at 288.7, 287.2 and 289.3, 287.9 eV, respectively (**Figure 4.3.4.5**) Photoemission at higher binding energy can be ascribed to the most deficient carbon atoms bonded to carbonyl and hydroxyl oxygen atoms (-COOH/-COO)<sup>11</sup> [Ref]. The lower binding energy peak can be assigned to aliphatic carbon atoms of 3-MPA capping molecules<sup>11</sup>.

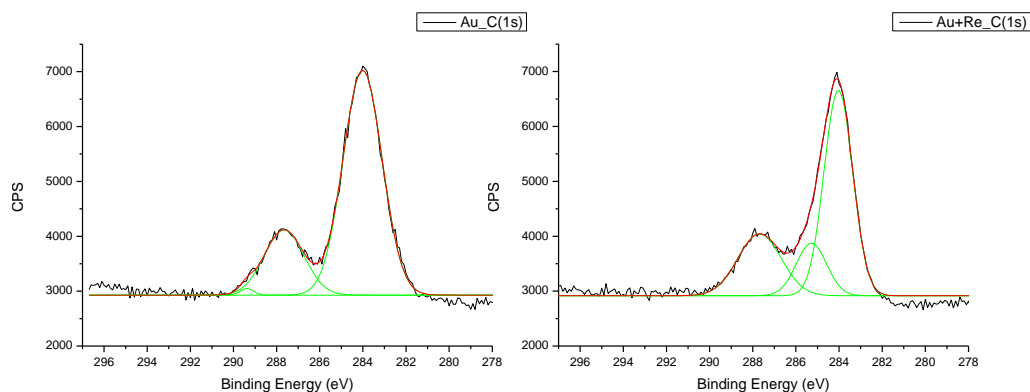


**Figure 4.3.4.5.1:** XPS of **NaMP-Au** (left) and **NaMP-Ag** (right), corresponding to 2p from s region.

The most informative region is that corresponding to C 1s emission. The resolved peaks of **ReMP-Au** samples fit with three maxima at 287.9, 286.1 and 284.1 eV that are assigned to carboxylic, carbonylic and aliphatic carbons respectively, in accordance with values reported in the literature. Same energy emission deconvoluted peaks are found for **ReMP-Ag** samples at 288.7, 286.9 and 288.0 eV, respectively. The corresponding COO/CO atomic carbon ratios calculated from the integrated areas are essentially equal to 1:0.7 for Au and Ag core nanoparticles. Assuming that samples contain  $\text{Re}(\text{CO})_3$  groups the COO/Re atomic ratio is ca. of 1:0.25 which is in accordance with the presence of non-coordinated carboxylic groups as suggested by the IR spectra of the samples, which are shown in the section 4.3.7 of this chapter. Photoemission peaks in the S 2p region are essentially similar to those of 3-MPA capped nanoparticles.

#### 4. Gold and silver nanoparticles surface functionalized

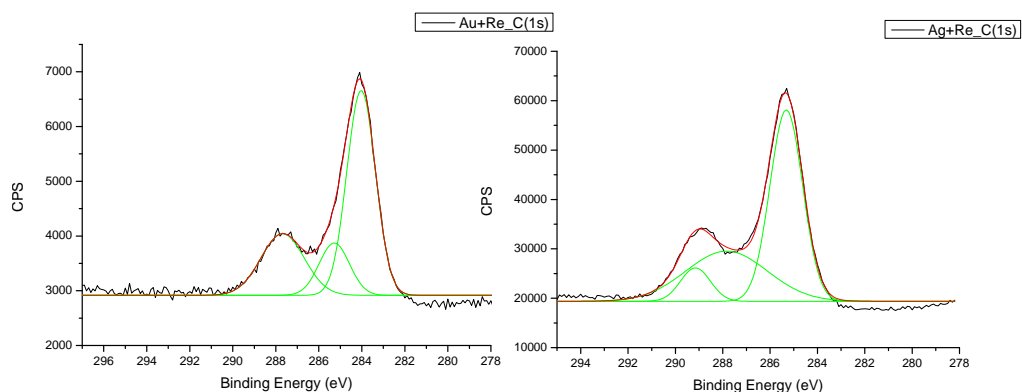


**Figure 4.3.4.5.2:** XPS of ReMP-Au (left) and ReMP-Ag (right), corresponding to 2p from s region.

#### 4.3.5 TGA Analyses

The thermal behavior of the samples has been studied with thermal analysis techniques. Thermogravimetric (TGA 7, Perkin Elmer) measurements have been carried out in continuous heating regimes (2 K/min) under Ar atmosphere.

**Figure 4.3.5.1.1** shows TGA curves of pure NaMPA, NaMP-Au,  $[\text{Re}(\text{H}_2\text{O})_3(\text{CO})_3](\text{SO}_3\text{CF}_3)$  and ReMPAu and **Figure 4.3.5.1.2** shows TGA curves of pure NaMP, NaMP-Ag,  $[\text{Re}(\text{H}_2\text{O})_3(\text{CO})_3](\text{SO}_3\text{CF}_3)$  and ReMP-Ag during the heating from 30 to 400 °C.

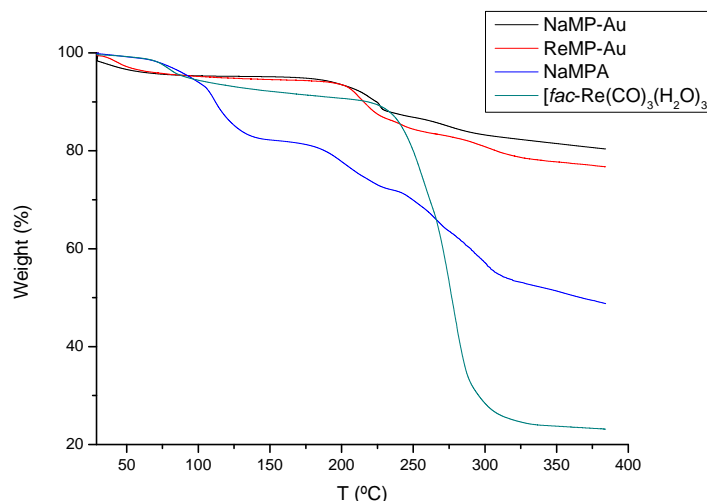


**Figure 4.3.5.1.1:** TGA curves of (a) NaMP-Au, (b) ReMP-Au, (c) NaMPA and (d)  $[\text{fac-Re}(\text{H}_2\text{O})_3(\text{CO})_3]$

#### 4. Gold and silver nanoparticles surface functionalized

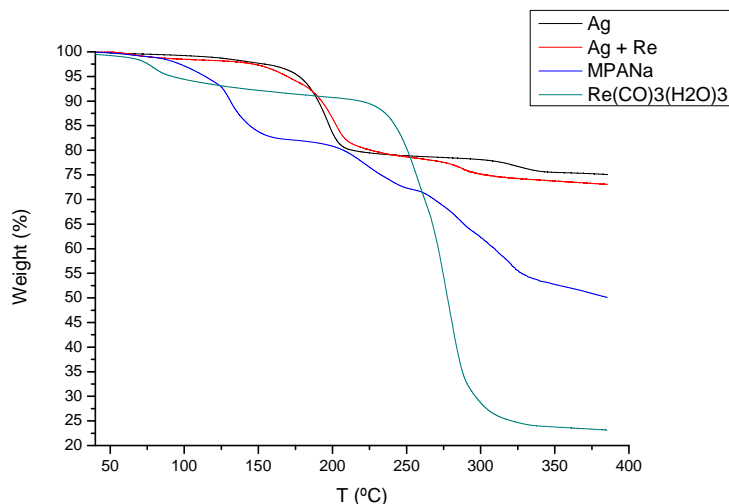


**Figure 4.3.5.1.2:** TGA curves of (a) NaMP-Ag, (b) ReMP-Ag, (c) NaMPA and (d) [*fac*-Re(H<sub>2</sub>O)<sub>3</sub>(CO)<sub>3</sub>]

The pure **NaMPA** decomposes at approximately at 125 °C while the decomposition temperatures of **ReMP-Au** and **NaMP-Ag** are around 200 °C, indicating the thermal stability of **NaMPA** is improved after capping Au and Ag nanoparticles. Before the onset decomposition temperature, both TGA curves of **NaMP-Au** and **NaMP-Ag** have a slope while that of pure **NaMPA** is fixed. Water is expected to be contained in **NaMP-Au** and **NaMP-Ag** nanoparticles and likely presented as hydration water in **NaMP-Au** and **NaMP-Ag** nanoparticles in accord with the results of **TEM** and **FTIR** characterizations of **NaMP-Au** and **NaMP-Ag** nanoparticles. The total mass loss of **NaMP-Au** and **NaMP-Ag** nanoparticles at 350 °C amounts to 20 % and 15 %, respectively. Taking into account 45% residues of pure **NaMPA** molecules at 350 °C and assuming the residues of **NaMPA** are equivalent to the loss of **NaMPA** in **NaMP-Ag** and **NaMP-Au**, the content of the gold core in **NaMP-Au** nanoparticles and that of the silver core in **NaMP-Ag** nanoparticles is more than 60% and 70%, respectively.

## 4. Gold and silver nanoparticles surface functionalized

### 4.3.6 Vibrational studies

Infrared spectra of the samples have been recorded on a IR TENSOR27, Bruker, ATR:SPECDC MKII Golden Gate.

Vibrational studies have been recorded for **MPA**, **NaMPA**, **NaMP-Au**, **NaMP-Ag**, **[*fac*-Re(CO)<sub>3</sub>(H<sub>2</sub>O)<sub>3</sub>] (Re carbonyl)**, **ReMP-Au** and **ReMP-Ag** species. The most characteristic bands of the analyzed compounds, corresponding to  $\nu(\text{OCO})_{\text{as}}$ ,  $\nu(\text{OCO})_{\text{sim}}$  and  $\nu(\text{CO})$  signals, are shown on **Table 4.3.7.1**:

	MPA	NaMPA	NaMP-Au	NaMP-Ag	Re carbonyl	ReMP-Au	ReMP-Ag
$\nu(\text{OCO})_{\text{as}}$	1560 cm <sup>-1</sup>	1700 cm <sup>-1</sup>	1561 cm <sup>-1</sup>	1561 cm <sup>-1</sup>	-----	1547 cm <sup>-1</sup>	1558 cm <sup>-1</sup>
$\nu(\text{OCO})_{\text{sim}}$	1391 cm <sup>-1</sup>	1404 cm <sup>-1</sup>	1404 cm <sup>-1</sup>	1390 cm <sup>-1</sup>	-----	1379 cm <sup>-1</sup>	1389 cm <sup>-1</sup>
$\Delta\nu(\text{OCO})$	169 cm <sup>-1</sup>	296 cm <sup>-1</sup>	157 cm <sup>-1</sup>	171 cm <sup>-1</sup>	-----	168 cm <sup>-1</sup>	169 cm <sup>-1</sup>
$\nu(\text{CO})$	-----	-----	-----	-----	1995 cm <sup>-1</sup>	2008 cm <sup>-1</sup>	2011 cm <sup>-1</sup>
$\nu(\text{CO})$	-----	-----	-----	-----	1846 cm <sup>-1</sup>	1863 cm <sup>-1</sup>	1869 cm <sup>-1</sup>

**Table 4.3.7.1:** Values of the most characteristic bands of the studied compounds.

**Figure 4.3.7.1** and **Figure 4.3.7.2** show the IR spectra of MPA ligand in the basic form (**NaMPA**), **MPA** gold and silver nanoparticles (**MPA-Au** and **MPA-Ag**) and rhenium carbonyl capped gold and silver nanoparticles (**ReMPAu** and **ReMP-Ag**).

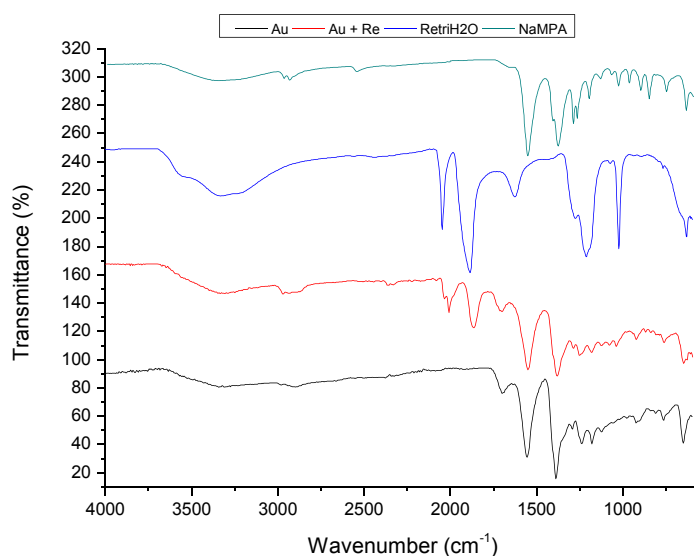


**Table 4.3.7.1:** Infrared spectra of (a) NaMP-Au, (b) ReMP-Au, (c) [*fac*-Re(H<sub>2</sub>O)<sub>3</sub>(CO)<sub>3</sub>](CF<sub>3</sub>SO<sub>3</sub>) and (d) NaMPA.



#### 4. Gold and silver nanoparticles surface functionalized

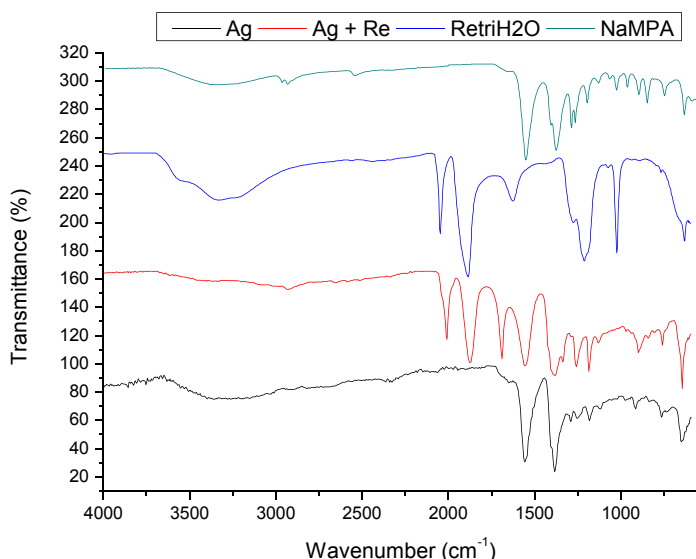


**Figure 4.3.7 .2:** Infrared spectra of (a) NaMP-Ag, (b) ReMP-Ag, (c) [*fac*-Re(H<sub>2</sub>O)<sub>3</sub>(CO)<sub>3</sub>](CF<sub>3</sub>SO<sub>3</sub>) and (d) NaMPA

The most characteristic bands of MPA compounds are those corresponding to asymmetric and symmetric vibrational stretching modes of the carboxylic OCO group. Stretching  $\nu(\text{OCO})$  absorptions at 1560 (vs) and 1391 (vs)  $\text{cm}^{-1}$  distinctive of the anionic carboxylate functionality are observed in the IR spectrum of NaMPA. The protonated form of MPA displays  $\nu(\text{OCO})$  bands at 1700 (vs) and 1404 (m)  $\text{cm}^{-1}$  respectively. IR spectra of MPA functionalized gold and silver nanoparticles display stretching  $\nu(\text{OCO})$  bands at 1561 (vs) and 1404 (m) (MPA-Au), and at 1561 (vs) and 1390 (m) (MPA-Ag)  $\text{cm}^{-1}$  respectively, corresponding to anionic COO<sup>-</sup> groups. A medium absorption at 1700  $\text{cm}^{-1}$  suggests that some of carboxylic groups are protonated (COOH). IR spectra of ReMP-Au and ReMP-Ag show strong absorptions assigned to the fragment “Re(CO)<sub>3</sub>” and carboxylic groups. Stretching  $\nu(\text{CO})$  bands of [Re(CO)<sub>3</sub>(H<sub>2</sub>O)<sub>3</sub>]<sup>+</sup> precursor appear at 1995 (vs) and 1846 (vs)  $\text{cm}^{-1}$ , which are expected for a *fac*-M(CO)<sub>3</sub> group. The IR spectrum of ReMP-Au shows  $\nu(\text{CO})$  bands at 2011 (vs) and 1869 (s, br)  $\text{cm}^{-1}$ , and  $\nu(\text{OCO})$  bands at 1703 (m, br), 1552 (s, br) and 1392 (s, br)  $\text{cm}^{-1}$ , respectively. On the other hand, ReMP-Ag displays similar absorptions  $\nu(\text{CO})$  at 2013 (vs) and 1880 (s, br)  $\text{cm}^{-1}$ , and  $\nu(\text{OCO})$  at 1696 (m, br), 1561 (s, br) and 1390 (s, br)  $\text{cm}^{-1}$ , respectively.

With respect to metal-carbonyl  $\nu(\text{CO})$  bands, it can be deduced that both ReMP-Au and ReMP-Ag samples contain a *fac*-Re(CO)<sub>3</sub> fragment probably coordinated to carboxylate ends. The most energetic absorption may be assigned to the A vibrational mode and lower energy broad bands to the E vibrational mode of the *fac*-Re(CO)<sub>3</sub> group considering an approximate C<sub>3v</sub> local symmetry.

#### 4. Gold and silver nanoparticles surface functionalized

The carboxylate ( $\text{COO}^-$ ) group can coordinate metals in different forms:  $\eta^1$ -monodentate (I),  $\eta^2$ -bidentate (II) or  $\mu, \eta^2$ -bidentate (III) (Figure 4.3.7.3) which can be distinguished by the extent of  $\Delta = \nu_{\text{asym}}(\text{OCO}) - \nu_{\text{sym}}(\text{OCO})$  shift. Experimentally, it is shown that  $\Delta(\text{II}) < \Delta(\text{III}) \approx \Delta(\text{uncoordinated } \text{COO}^-) < \Delta(\text{I})$ , consequently,  $\Delta$  values are good criteria to assign a mode of coordination to carboxylate ligands. IR spectra of rhenium coated nanoparticles exhibit three  $\nu(\text{OCO})$  absorptions that can be assigned to two types of carboxylic groups: uncoordinated  $-\text{COOH}$  groups and the rhenium-coordinated anionic carboxylate ligands. Whereas bands at  $1703\text{-}1696 \text{ cm}^{-1}$  are representative of protonated ( $\text{COOH}$ ) carboxylic groups, bands at  $1552\text{-}1561$  and  $1392\text{-}1390 \text{ cm}^{-1}$  with  $\Delta\nu = \nu_{\text{asym}}(\text{OCO}) - \nu_{\text{sym}}(\text{OCO})$  of  $160$  and  $171 \text{ cm}^{-1}$ , respectively, are characteristic of  $\mu, \eta^2$ -bidentate carboxylate ligands and are in agreement with other carboxylate metal complexes described in the literature<sup>12</sup>. A shoulder of  $\nu_{\text{sym}}(\text{OCO})$  band around  $1600 \text{ cm}^{-1}$  suggests the presence of absorptions due to uncoordinated  $\text{COO}^-$  or monodentate carboxylic groups. The water dispersion of rhenium carbonyl capped gold and silver nanoparticles together with the anionic charge deduced from Z-potential support the existence of uncoordinated anionic  $\text{COO}^-$  on the nanoparticle surface.

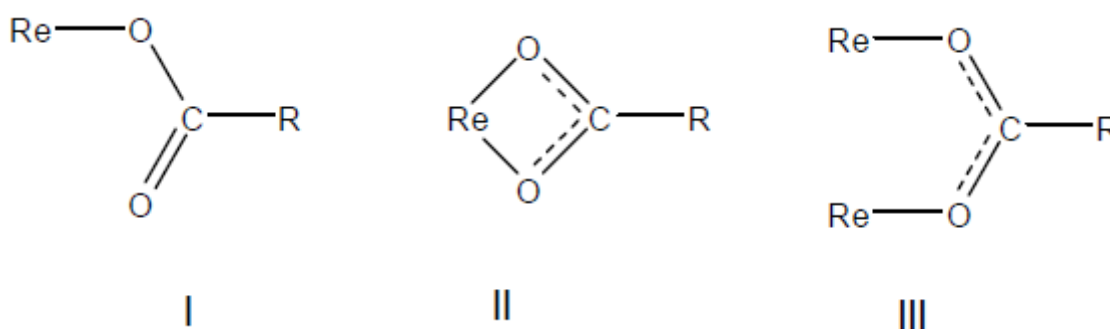


**Figure 4.3.7.3:** Possible coordination for metals between the carboxylate ( $\text{COO}^-$ ) group from MPA and different metals, as for example “Re”:  $\eta^1$ -monodentate (I),  $\eta^2$ -bidentate (II) or  $\mu, \eta^2$ -bidentate (III).

These IR data is consistent with the formation of hexacoordinated *fac*- $\text{Re}(\text{CO})_3$  complexes bridged by carboxylate anionic ligands. The coordination sphere of Re atoms can be completed by a  $\text{H}_2\text{O}$  ligand from the precursor octahedral Re complex  $[\text{Re}(\text{H}_2\text{O})_3(\text{CO})_3]^+$  or by a carboxylic end of residual metal surface bonded 3-MPA capping ligands (Figure 4.3.7.4).

#### 4. Gold and silver nanoparticles surface functionalized

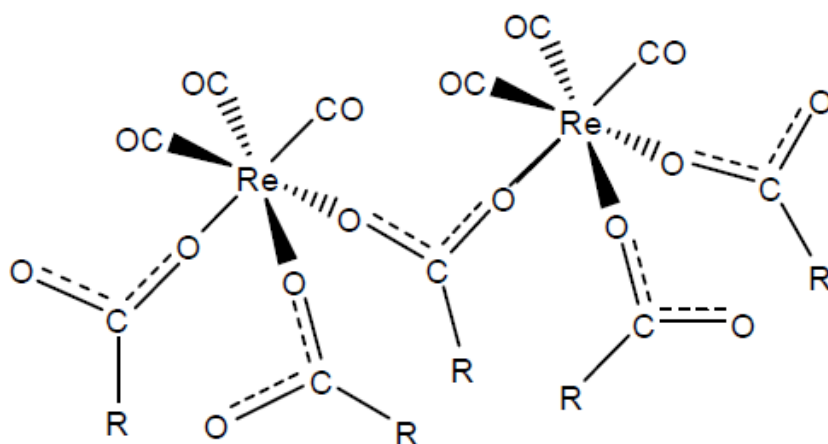


**Figure 4.3.7.4:** Coordination sphere of Re atoms formed during functionalization of Au or Ag nanoparticles with Re tricarbonyl groups.

As a conclusion, and according to the data obtained with this **IR** study, the most probably “metal-MP-Re(CO)” nanoparticle structure (both in case of silver and gold) can be represented as is shown in **Figure 4.3.7.5**:

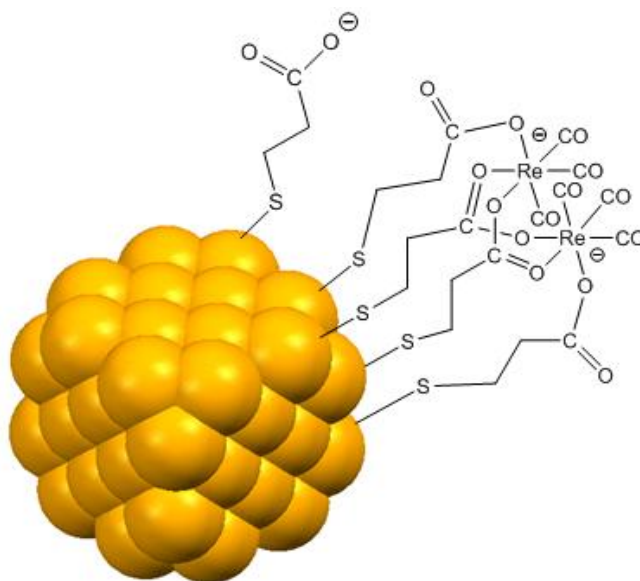


**Figure 4.3.7.5:** Most probably structure for the synthesized gold (or silver) “Re(CO)-MP” capped nanoparticles, according to the obtained **IR** data.

## 4. Gold and silver nanoparticles surface functionalized

### 4.4 Summary

In this work, four different kinds of water-dispersible nanoparticles have been synthesized:

- Gold nanoparticles capped with **NaMP**. (**NaMP-Au**)
- Gold nanoparticles capped with **NaMP** and coordinated with rhenium carbonyl species. (**ReMP-Au**)
- Silver nanoparticles capped with **NaMP**. (**NaMP-Ag**)
- Silver nanoparticles capped with **NaMP** and coordinated with rhenium carbonyl species. (**ReMP-Ag**)

In all cases, the synthesized nanoparticles have been fully characterized via different techniques.

As a result of this characterization, it has been concluded that rhenium species remain coordinated to  $\text{COO}^-$  carboxylic groups from **MPA** by the formation of hexacoordinated *fac*- $\text{Re}(\text{CO})_3$  complexes bridged by carboxylate anionic ligands. Since some carboxylic remain uncoordinated, the resulting nanoparticles can be dispersed on aqueous media.

### 4.5 Related literature

---

- <sup>1</sup> Wang S.; Sim W.S., *Langmuir*, **2006**, 22, 7861–7866.
- <sup>2</sup> Majiles Ara M. H.; Dehghani Z.; Sahraei R.; Daneshfar A.; Javadi Z.; Divsar F., *J. Quant. Spectrosc. Radiat. Transfer*, **2012**, 11, 366-372.
- <sup>3</sup> Zanchet D., Hall B.D.; Ugarte D., *J. Phys. Chem. B*, **2000**, 104, 11013-11018.
- <sup>4</sup> Zang H.-L.; Evans S.D.; Henderson J.R.; Miles R.E.; Shen T., *J. Phys. Chem. B*, **2003**, 107, 6087-6095.
- <sup>5</sup> Cao J.; Want Y.; Yu J.; Xia J.; Zhang C.; Yin D.; Hafeli U.O., *J. Magn. Magn. Mater.*, **2004**, 277, 165-174.
- <sup>6</sup> Shiraiishi Y.; Toshima N., *Colloids Surf. A.*, **2000**, 169, 59-66.
- <sup>7</sup> Mikhlin Y.; Likhatski M.; Tomashevich Y.; Romanchenko A.; Erenburg S.; Trubina S., *J. Electron. Spectrosc. Relat. Phenom.*, **2010**, 177, 24-29.
- <sup>8</sup> NIST XPS Database.
- <sup>9</sup> Hori H.; Koike K.; Ishizuka M.; Takeuchi K.; Ibusuki T.; Ishitani O., *J. Organomet. Chem.*, **1997**, 530, 169-176.
- <sup>10</sup> Fung A.S.; Tooley P.A.; Kelley M.J.; Koningsberger D.C.; Gates B.C., *J. Phys. Chem.*, **1991**, 95, 225-234.
- <sup>11</sup> Hutt D.A.; Lggett G.J., *Langmuir*, **1997**, 13, 2740-2748.
- <sup>12</sup> Nakamoto K., *Infrared and Raman Spectra of Inorganic and Coordination Compounds. Part B: Applications in Coordination, Organometallic and Bioinorganic Chemistry*, John Wiley & Sons, Inc, Hoboken, New Jersey, **2009**.

#### 4. Gold and silver nanoparticles surface functionalized

---

## Chapter 5

# One-pot synthesis of stable colloidal solutions of $MFe_2O_4$ nanoparticles using oleylamine as both solvent and stabilizer

### Contents

---

5.1 General description of the carried out work.....	137
5.2 Experimental procedure.....	139
5.2.1 Materials and reactants.....	139
5.2.2 Solvothermal synthesis of hexane colloidal dispersion of $Fe_3O_4$ magnetite nanoparticles.....	139
5.2.3 Solvothermal synthesis of hexane colloidal dispersion of $MFe_2O_4$ (M= Co, Mn, Cu, Zn) ferrite nanoparticles.....	139
5.2.4 Microwave-assisted synthesis of hexane colloidal dispersion of $Fe_3O_4$ magnetite nanoparticles.....	140
5.2.5 Microwave-assisted synthesis of hexane colloidal dispersion of $MFe_2O_4$ (M= Co, Mn, Cu, Zn) ferrite nanoparticles.....	140
5.3 Characterization and result discussion.....	141
5.3.1 TEM Bright Field microphotographs.....	141
5.3.2 Electron and X-ray diffraction.....	147
5.3.3 Electron-dispersive X-Ray Spectroscopy (EDX).....	149
5.3.4 Thermogravimetric analysis (TGA) and differential scanning calorimetry (DSC).....	154

## 5. Mixed ferrite nanoparticles

5.3.5 Infrared (IR) measurements.....	155
5.3.6 Magnetic measurements.....	156
5.4 Summary.....	158
5.5 Related literature.....	161



## 5. One-pot synthesis of stable colloidal solutions of $MFe_2O_4$ nanoparticles using oleylamine as both solvent and stabilizer.

This chapter explains the synthesis, stabilization and characterization of magnetite,  $Fe_3O_4$ , and magnetic mixed spinel ferrites,  $MFe_2O_4$  ( $M= Mn, Cu, Zn, Co$ ) made on a nanometric scale. In all cases, the resulting nanoparticles have been fully characterized via different techniques, such as transmission electron microscopy. Two different heating methods (solvothermal and microwave-assisted) have been used to synthesize the magnetite, manganese and cobalt ferrites, as long as zinc and copper ferrites have been synthesized only via the solvothermal heating method.

The discussion of the results obtained when carrying out the nanoparticles characterization is also explained in detail in this chapter.

For those kinds of ferrites synthesized via two different methods, the resulting data obtained when characterizing the resulting nanoparticles is also contrasted in this chapter.

### 5.1 General description of the carried out work

Non-polar media dispersible  $MFe_2O_4$  ferrites and magnetite nanoparticles have been synthesized by modifying a method previously described in the literature via one-pot thermal decomposition of iron and other metal acetylacetonates,  $Fe(acac)_3$  and  $M(acac)_2$  ( $M= Co, Mn, Cu$  and  $Zn$ ) respectively, in oleylamine, which works both as a reaction medium and as a capping ligand, producing stable colloidal dispersions, as shown in **figure 5.1.1.1**:

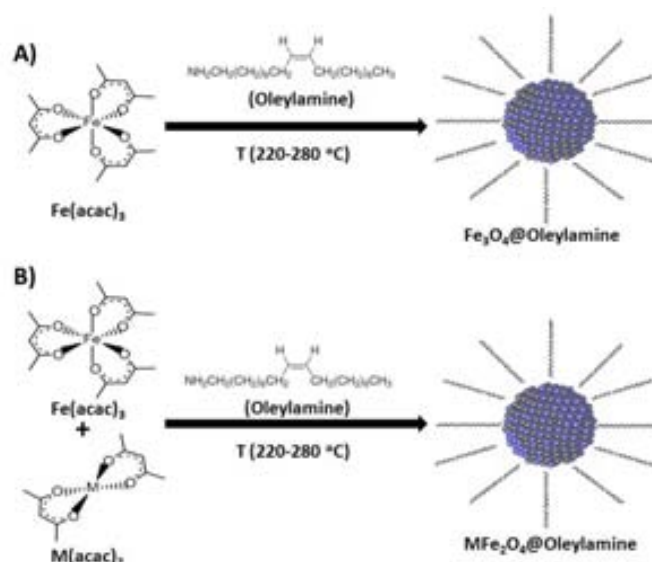


**Figure 5.1.1.1:** Synthetic procedures to obtain A)  $Fe_3O_4$  and B)  $MFe_2O_4$  oleylamine capped nanoparticles.

## 5. Mixed ferrite nanoparticles

Given the fact that the heating process has resulted to be a key factor when trying to obtain stable nanoparticles, controlling it has been a must during all the experimental procedure.

Therefore, two different heating systems have been used in order to heat the ‘acetylacetonate-oleylamine’ reaction mixture and consequently to obtain the desired nanoparticles:

- Solvothermal method: This method consists of heating the reaction mixture by placing it inside a reflux setup and heating the whole system until it reaches an optimal temperature.
- Microwave-assisted method: In this case the heating process is based on using a microwave device to heat the reaction mixture.

**Figure 5.1.1.2** shows two pictures taken from a reflux setup and a microwave device used to carry out the magnetic nanoparticles:



**Figure 5.1.1.2:** Pictures corresponding to a reflux setup (left) and a microwave device (right) used to carry on the different nanoparticles’ synthesis.

For both types of heating systems, it has been studied how reaction time and temperature affect to the resulting particles.

Once synthesized, nanoparticles have been magnetically separated from the reaction mixture and washed using ethyl ether and ethanol, obtaining in all cases a magnetic dark powder that can be easily dispersed in non-polar media, such as hexane, toluene, chloroform, and dichloromethane.

## 5.2 Experimental procedure

### 5.2.1 Materials and reactants.

Iron (III) acetylacetonate (Aldrich, 99,9 %), Cobalt (II) acetylacetonate (Aldrich, 97 %). Manganese (II) acetylacetonate (Aldrich), Copper (II) acetylacetonate (Aldrich, 99,9 %), Zinc (II) acetylacetonate (Aldrich, 99,9 %), Oleylamine (Panreac), Hexane (Panreac PA), Methanol (Panreac) and Ethanol (Panreac) were used as purchased without further purification.

### 5.2.2 Solvothermal synthesis of hexane colloidal dispersion of Fe<sub>3</sub>O<sub>4</sub> magnetite nanoparticles

Fe<sub>3</sub>O<sub>4</sub> nanoparticles were prepared via solvothermal decomposition of metal acetylacetonates in oleylamine. 0,350 g of Fe(acac)<sub>3</sub> (1.0 mmol) were added to 25 ml of oleylamine in a 100 ml round bottomed flask equipped with a condenser, a magnetic stirrer, a thermograph, a and heater. The initial red solution was heated, and it turned dark brown when the vessel mixture reached 120 °C. After keeping the temperature reaction at 120 °C for 20 minutes, it was then increased until 220 °C (or 280 °C) with a heating rate of 1 °C / 1 min. After 1,5 or 3 hours (depending on the case) of reaction, the final mixture was cooled until it reached room temperature. The obtained Fe<sub>3</sub>O<sub>4</sub> nanoparticles were then separated from the reaction medium by successive additions of ethanol (3x25 ml) and diethyl ether (3x25 ml) and magnetic precipitation. The separated nanoparticles were re-dispersed in hexane (with a certain volume in order to obtain the desired concentration of Fe<sub>3</sub>O<sub>4</sub>), forming a room temperature stable red-brown dispersion. The resulting nanoparticles may also be re-dispersed in toluene, chloroform or dichloromethane.

### 5.2.3 Solvothermal synthesis of hexane colloidal dispersion of MFe<sub>2</sub>O<sub>4</sub> (M= Co, Mn, Cu, Zn) ferrite nanoparticles

MFe<sub>2</sub>O<sub>4</sub> (M= Co, Mn, Cu, Zn) nanoparticles were also prepared via solvothermal decomposition of metal acetylacetonates in oleylamine. 0.236 g of Fe(acac)<sub>3</sub> (0.67 mmol) and 0.33 mmol of M(acac)<sub>2</sub> (which molecular weight of each acetylacetonate varies depending on M) were suspended in 25 ml of oleylamine in a 100 mL round bottomed flask equipped with a reflux setup, in the same way than for Fe<sub>3</sub>O<sub>4</sub> previously synthesized nanoparticles. The initial red solution was heated, and it turned dark brown when the vessel mixture reached more or less 120 °C, depending on the M acetylacetonate. After keeping the temperature reaction at 120 °C for 20 minutes, it was then increased until 220°C (or 280°C) with a heating rate of 1 °C / 1 min. After 1.5 or 3 hours (depending on the case) of reaction, the final mixture was cooled at room temperature. MFe<sub>2</sub>O<sub>4</sub> nanoparticles were then separated exactly in the same way used for Fe<sub>3</sub>O<sub>4</sub> nanoparticles separation. The separated nanoparticles were re-dispersed in

hexane (with a certain volume in order to obtain the desired concentration of  $MFe_2O_4$ ), forming a room temperature stable red-brown dispersion. The resulting nanoparticles may also be re-dispersed in toluene, chloroform or dichloromethane.

### **5.2.4 Microwave-assisted synthesis of hexane colloidal dispersion of $Fe_3O_4$ magnetite nanoparticles**

$Fe_3O_4$  nanoparticles were prepared via microwave-assisted decomposition of metal acetylacetonates in oleylamine. 0,350 g of  $Fe(acac)_3$  (1.0 mmol) were added to 25 ml of oleylamine in a 35 ml glass vessel specially designed for microwave heating processes. At this point, the microwave heated the reaction mixture from room temperature until 220 °C, 250 °C or 280 °C within 15 to 20 minutes and then kept at this temperature during 15, 20, 30, 45 or 60 minutes, under a controlled pressure of 10 atmospheres and with continuous stirring. After finishing the reaction, the resulting brown-dark dispersion was treated exactly in the same way than for all the other synthesized nanoparticles, by using ethanol and diethyl ether as separating agents and carrying on magnetic separation. The resulting nanoparticles may also be re-dispersed not only in hexane but also in toluene, chloroform or dichloromethane.

### **5.2.5 Microwave-assisted synthesis of hexane colloidal dispersion of $MFe_2O_4$ (M= Co, Mn, Cu, Zn) ferrite nanoparticles**

$MFe_2O_4$  (M= Co, Mn, Cu, Zn) nanoparticles were also prepared via microwave-assisted decomposition of metal acetylacetonates in oleylamine. 0.236 g of  $Fe(acac)_3$  (0.67 mmol) and 0.33 mmol of  $M(acac)_2$  (which molecular weight of each acetylacetonate varies depending on M) were suspended in 25 ml of oleylamine in a 35 ml glass vessel specially designed for microwave heating processes. At this point, the microwave heated the reaction mixture in an identical way than for the microwave-assisted  $Fe_3O_4$  nanoparticles. The separation process was also the same than for all the other cases and, again, the resulting nanoparticles may be re-dispersed not only in hexane but also in toluene, chloroform or dichloromethane.

### 5.3 Characterization and result discussion

The resulting ferrite nanoparticles characterization, as well as the obtained data discussion are described in this section. The characterization itself has been carried out via seven different analytical techniques:

- Transmission electron microscopy (**TEM**) and high resolution electron microscopy (**HRTEM**) Bright Field microphotographs.
- Fourier Fast Transformation image analysis.
- Electron diffraction.
- Powder X-Ray diffraction.
- Energy-dispersive X-Ray Spectroscopy (**EDX**)
- Thermogravimetric analysis (**TGA**) and differential scanning calorimetry (**DSC**)
- Infrared spectroscopy.
- **SQUID** and **FC/ZFC** magnetic studies.

#### 5.3.1 TEM Bright Field microphotographs

Transmission Electron Microscope (**TEM**) images were obtained on a Philips Tencai 20 at an accelerating voltage of 200 kV.

Transmission Electron Microscopy (**TEM**) images taken from different solvothermal synthesized nanoparticles are presented in **figure 5.3.1.1**.

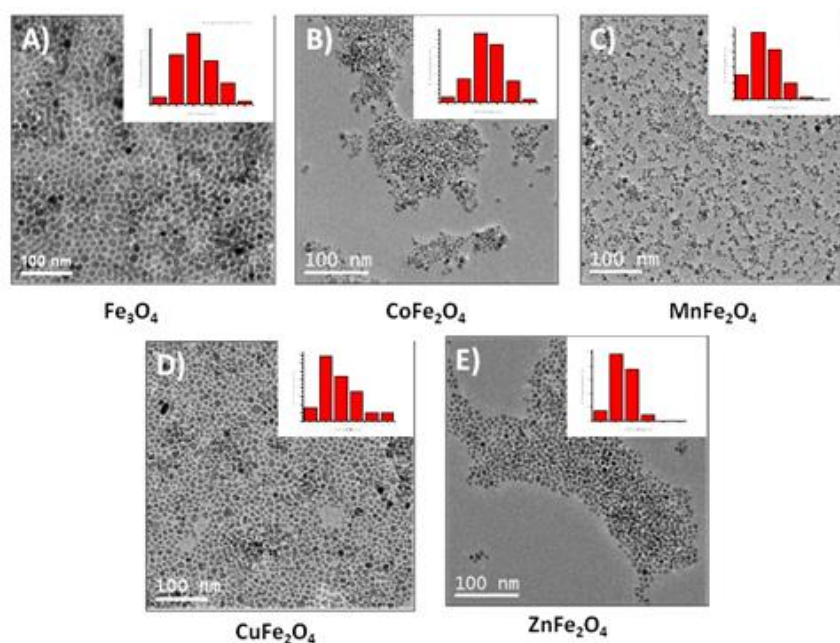


**Figure 5.3.1.1:** TEM images taken from the  $\text{Fe}_3\text{O}_4$  and  $\text{MFe}_2\text{O}_4$  oleylamine-capped nanoparticles synthesized at 220 °C with 3 h of annealing time using the solvothermal method.

It may be observed in this figure how in all cases the synthesized nanoparticles show a low aggregation and a relative narrow size distribution. All the different nanoparticle sizes obtained when varying the reaction temperature and the time reaction are shown in **Table 5.3.1.1.**:

	Temperature (°C)	Time (min)	Size (nm)
<b>Fe<sub>3</sub>O<sub>4</sub></b>	220	60	7.5 ± 1.7
	220	90	12.4 ± 2.2
	220	180	15.5 ± 2.6
	280	180	11.1 ± 2.4
<b>CoFe<sub>2</sub>O<sub>4</sub></b>	220	60	5.1 ± 0.9
	220	90	6.9 ± 1.2
	220	180	9.8 ± 1.4
	280	180	9.5 ± 2.1
<b>MnFe<sub>2</sub>O<sub>4</sub></b>	220	60	6.7 ± 1.3
	220	90	6.5 ± 1.0
	220	180	9.8 ± 2.0
	280	180	8.2 ± 1.6
<b>CuFe<sub>2</sub>O<sub>4</sub></b>	220	90	6.9 ± 1.4
	220	180	8.7 ± 3.1
	280	180	8.8 ± 2.2
<b>ZnFe<sub>2</sub>O<sub>4</sub></b>	220	180	6.8 ± 2.0
	280	180	7.0 ± 1.4

**Table 5.3.1.1:** Nanoparticle sizes obtained with the solvothermal method when working at different temperatures and for different annealing times.

The results show that reaction time is by far more influent than temperature in the nanoparticles growth. In fact, for time values inferior than 60 minutes in the cases of Fe<sub>3</sub>O<sub>4</sub>, CoFe<sub>2</sub>O<sub>4</sub> and MnFe<sub>2</sub>O<sub>4</sub> or than 90 and 180 minutes in the cases of CuFe<sub>2</sub>O<sub>4</sub> and ZnFe<sub>2</sub>O<sub>4</sub>, respectively, no nanoparticles formation were observed, regardless of the applied temperature. It is also worth mentioning that when temperature is increased from 220 to 280 °C, no growth, but a decrease of the nanoparticles size is observed.

Another significant piece of information arises when comparing the Fe<sub>3</sub>O<sub>4</sub> size average (for any time and temperature) with any kind of mixed ferrite. As it can be observed, magnetite nanoparticles tend to be bigger than others. This fact may be explained by the partial Fe (III) to Fe (II) reduction that takes place during the Fe<sub>3</sub>O<sub>4</sub> formation, which does not take place in the case of mixed ferrites. When Fe<sub>3</sub>O<sub>4</sub> is synthesized, the Fe(acac)<sub>3</sub> molecules decompose and release the Fe (III) cations, which gather and form Fe (III) oxide nuclei that are partially reduced to Fe (II), forming the typical Fe<sub>3</sub>O<sub>4</sub> spinel structure, which is stable and grows forming the resulting nanoparticle. On the other hand, no Fe (III) reduction occurs since M (II) cations are already in the reaction medium when the initial nuclei are formed, given the decomposition of M(acac)<sub>2</sub>. Therefore, since Fe<sub>3</sub>O<sub>4</sub> formation requires the Fe (III) to Fe

(II) reduction, this process is slower than for any kind of  $MFe_2O_4$  and so is its nuclei formation. In this vein, in the case of  $Fe_3O_4$ , fewer nuclei are formed during the heating process, allowing the formation of bigger nanoparticles.

Despite their narrow size distribution, nanoparticles synthesized via solvothermal method, especially those that have been heated during 3 h at 280 °C, show a wide range of different shapes, as can be observed in **Figure 5.3.1.2**:

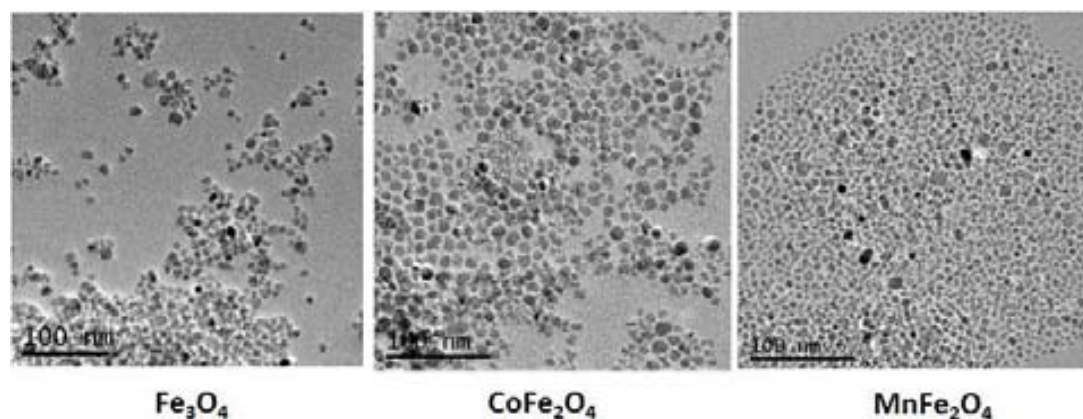


**Figure 5.3.1.2:** TEM images taken from the  $Fe_3O_4$  and  $MFe_2O_4$  ( $M = Co, Mn$ ) oleylamine-capped nanoparticles synthesized at 280 °C with 3 h of annealing time using the solvothermal method.

It can be observed in this figure how in all cases nanoparticles have lost their spherical-like shape, becoming more irregular. As shown in **Table 5.3.1.1**, nanoparticle size standard deviation increases for larger annealing times and higher reaction temperatures. However, the way in which the initial acetylacetonates are heated is by far the most important factor when synthesizing magnetite or mixed ferrite nanoparticles. In fact, whether the initial reaction mixture is heated faster than 1 °C/min and the temperature is not kept at 120 °C (temperature in which the initial acetylacetonates decompose) during 20 minutes, the resulting nanoparticles show an enormous size and shape dispersion, and they usually form unstable dispersions in any organic medium, precipitating after few minutes or even seconds.

As described in literature<sup>1,2</sup>, the final nanoparticle shape strongly depends on how the capping agent, as well as the medium<sup>3</sup>, interacts with its surface. Thus, when an anisotropic capping process takes place over the nanoparticles surface, its growth may be either eased or hindered in certain plane directions, allowing the crystal to form different shapes. On the other hand, a perfect isotropic capping process leads to a spherical-like nanocrystal. Since oleylamine acts as a capping agent, it limits and controls the nanoparticles growth and, therefore, their final size and shape. In other words, when the initial reaction mixture is properly heated, it allows oleylamine to surround and cap the nanoparticle surface and to force it to grow in a spherical-like shape.



## 5. Mixed ferrite nanoparticles

**Figure 5.3.1.3** shows the effect of not keeping the reaction temperature during 20 minutes after reaching the 120 °C at which acetylacetonates decompose starting the nucleation process and increasing T until 220 °C faster than 1 °C/min, not giving time to oleylamine to “control” the nanocrystal growth properly. Larger time (3h) and temperature (280 °C) conditions also ease anisotropic growth to occur via Ostwald ripening effect<sup>4,5</sup>, in which the biggest generated crystals grow at expense of the smaller ones due to the difference of energy among them.

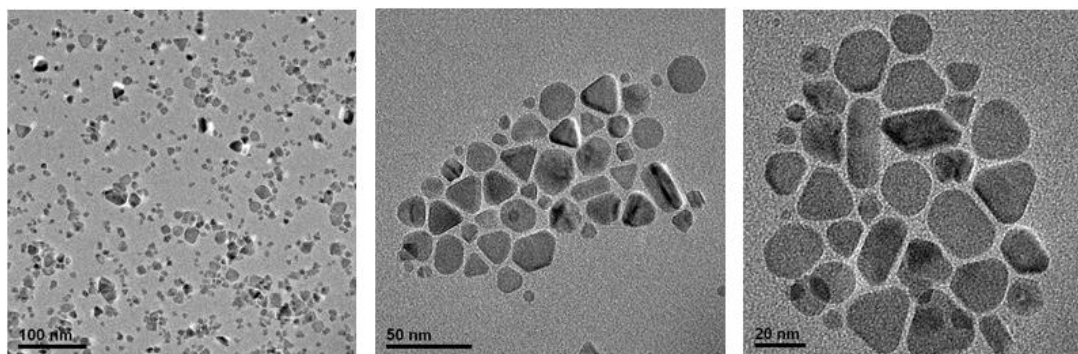


**Figure 5.3.1.3:** TEM images taken from multi-shaped and unstable  $\text{Fe}_3\text{O}_4$  nanoparticles synthesized by increasing the temperature reaction at a rate faster than 1 °C/min and without keeping the reaction temperature at 120 °C during 20 minutes.

Since the heating process has resulted to be a key factor when carrying out the nanoparticle synthesis reaction, a microwave-assisted heating process has been carried out with magnetite, and  $\text{MFe}_2\text{O}_4$  (M= Co, Mn) mixed ferrites so as to study how this method affects the final nanoparticle size and shape.

Therefore,  $\text{Fe}_3\text{O}_4$ ,  $\text{CoFe}_2\text{O}_4$  and  $\text{MnFe}_2\text{O}_4$  have also been synthesized via microwave-assisted heating method. **Figure 5.3.1.4** shows some TEM images taken from those synthesized particles:

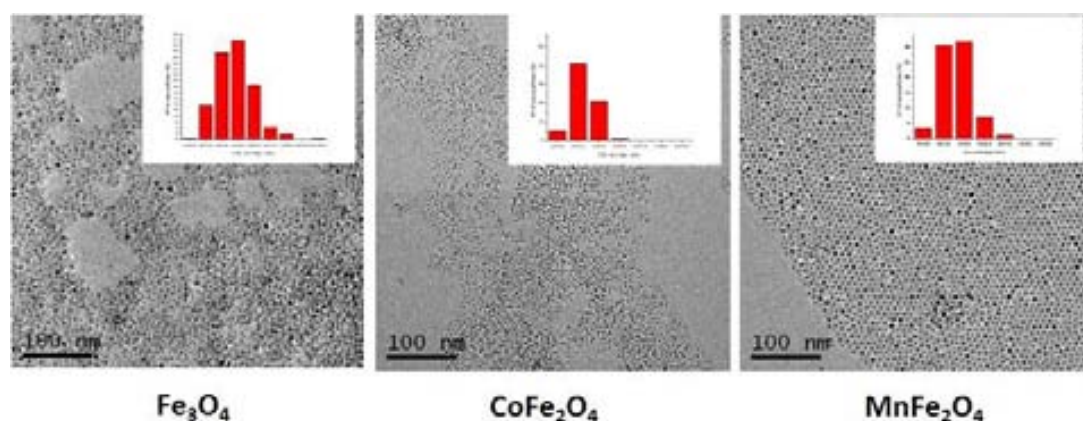


**Figure 5.3.1.4:** TEM images taken from the  $\text{Fe}_3\text{O}_4$  and  $\text{MFe}_2\text{O}_4$  oleylamine-capped nanoparticles synthesized at 250 °C with 20 min of annealing time using the solvothermal method.



All the different nanoparticle sizes obtained when varying the reaction temperature and the time reaction for the nanoparticles synthesized via microwave-assisted method are shown in **Table 5.3.1.2.**:

	Temperature (°C)	Time (min)	Size (nm)
<b>Fe<sub>3</sub>O<sub>4</sub></b>	220	15	-----
	220	20	-----
	220	30	-----
	250	15	5,8 ± 1,2
	250	20	5,8 ± 1,1
	250	30	6,6 ± 1,2
	250	45	6,8 ± 1,3
	250	60	6,9 ± 1,2
	280	20	7,1 ± 1,1
	280	60	8,5 ± 1,5
<b>CoFe<sub>2</sub>O<sub>4</sub></b>	220	15	-----
	220	20	-----
	220	30	-----
	250	15	3,7 ± 0,6
	250	20	4,1 ± 0,7
	250	30	4,3 ± 0,6
	250	45	5,4 ± 1,2
	250	60	6,2 ± 0,8
	280	20	6,4 ± 1,0
	280	60	6,8 ± 1,3
<b>MnFe<sub>2</sub>O<sub>4</sub></b>	220	15	-----
	220	20	-----
	220	30	-----
	250	15	-----
	250	20	3,7 ± 0,5
	250	30	4,1 ± 0,7
	250	45	4,2 ± 0,8
	250	60	4,6 ± 0,9
	280	20	5,3 ± 1,0
	280	60	6,1 ± 1,2

**Table 5.3.1.2:** Nanoparticle sizes obtained with the microwave-assisted method when working at different temperatures and for different annealing times.

The first important fact that arises when comparing this table with the previous one is that it is possible to reduce the reaction time considerably via using this heating method instead of the solvothermal one. Despite the fact that no nanoparticles may be obtained at 220 °C, when working at 250 or 280 °C it is possible to obtain nanoparticles for reaction times of 15 or 20 minutes. Another important piece of data is that in all cases, the size average standard deviation of the microwave-assisted method nanoparticles is much smaller than for the solvothermal ones. In fact, microwave-

assisted nanocrystals are far more spherical-like than their solvothermal analogous, as it is shown in **Figure 5.3.1.5**:

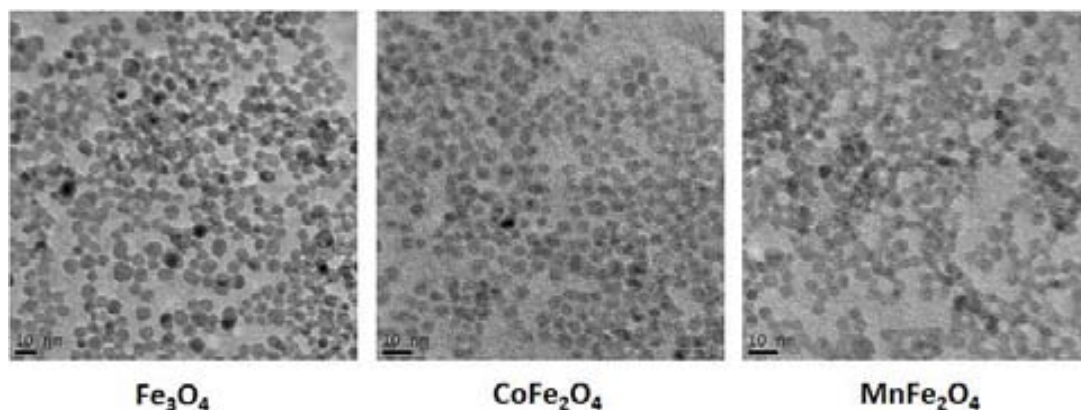


**Figure 5.3.1.5:** TEM images taken from  $\text{Fe}_3\text{O}_4$ ,  $\text{CoFe}_2\text{O}_4$  and  $\text{MnFe}_2\text{O}_4$  nanoparticles synthesized via microwave-assisted method at 250 °C during 20 minutes of annealing time.

Therefore, microwave heating controls the final shape and further dispersion stability of the growing nanoparticles by supplying energy to the reaction mixture in a more homogeneous way than solvothermal heaters do. It is worth mentioning that despite the fact that the heating rate is way faster than the used for solvothermal synthesis (in all cases the 250 or 280 °C are reached in less than 20 minutes) no irregular forms are obtained. On the other hand, since reaction time has been significantly decreased when using this heating method, no important size changes may be observed between nanoparticles synthesized in 20 minutes from others synthesized in 1 hour. In fact, when using this method, temperature seems to be slightly more important than annealing time when trying to increase the nanocrystals size.

The **HRTEM** study on  $\text{Fe}_3\text{O}_4$ ,  $\text{MnFe}_2\text{O}_4$  and  $\text{CoFe}_2\text{O}_4$  nanocrystals (**Figure 5.3.1.6**) shows their single crystalline structure. Fourier Fast Transformation images corresponding to the **HR** bright field images are in agreement with the planes of the general spinel-like structure of the synthesized nanoparticles:

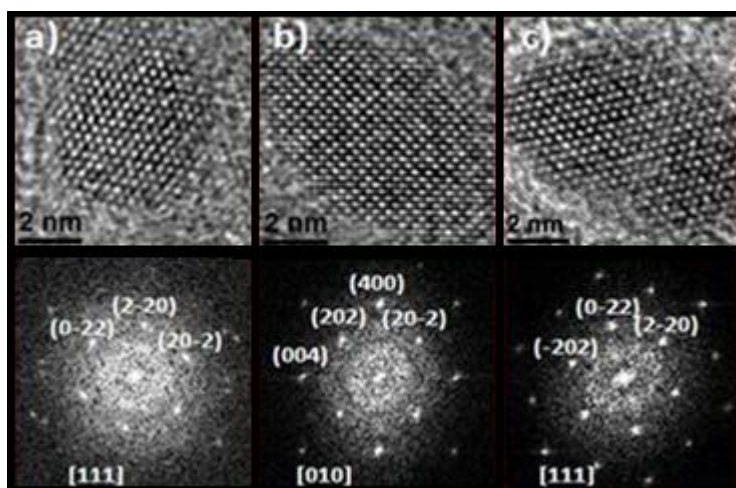


**Figure 5.3.1.5:** HRTEM images taken from a) Fe<sub>3</sub>O<sub>4</sub>, b) CoFe<sub>2</sub>O<sub>4</sub> and c) MnFe<sub>2</sub>O<sub>4</sub> nanoparticles synthesized via microwave-assisted method at 250 °C during 20 minutes of annealing time and their respective FFT images.

### 5.3.2 Electron and X-ray diffraction

Electron diffraction patterns were obtained on a Philips Tencai 20 at an accelerating voltage of 200 kV. X-ray powder diffraction (**XRD**) patterns of the samples were recorded with a Rigaku D diffractometer equipped with a rotating anode and a CuK<sub>α</sub> source ( $\lambda = 0.154056$  nm)

Both solvothermal and microwave-assisted nanoparticles' crystal structures have been studied using electron and X-ray diffraction.

**Figure 5.3.2.1** shows three electron diffraction patterns taken from microwave-assisted synthesised magnetite, cobalt and manganese ferrite nanoparticles:

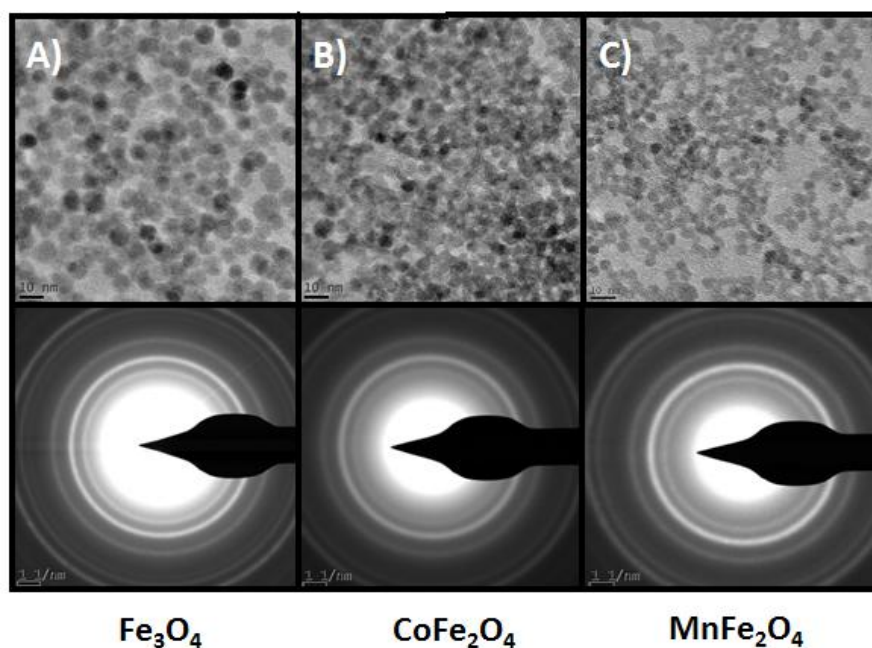


**Figure 5.3.2.1:** Bright field TEM images of A) Fe<sub>3</sub>O<sub>4</sub>, B) CoFe<sub>2</sub>O<sub>4</sub> and C) MnFe<sub>2</sub>O<sub>4</sub> microwave synthesized nanoparticles and their respective diffraction patterns.

For both solvothermal and microwave synthesized nanoparticles, the observed planes match with those expected for magnetite and mixed ferrite structures (spatial group Fd3m), which have the following Miller's Indexes: (2 2 0), (3 1 1), (4 0 0), (4 2 2), (5 1 1), (4 4 0) and (6 2 2).

As well as electron diffraction, **XRD** diffractograms carried out for both solvothermal and microwave synthesized nanoparticles show the characteristic Bragg peaks expected for a spinel-like structure: (2 2 0), (3 1 1), (4 0 0), (4 2 2), (5 1 1), (4 4 0), as shown in **Figure 5.3.2.2**:

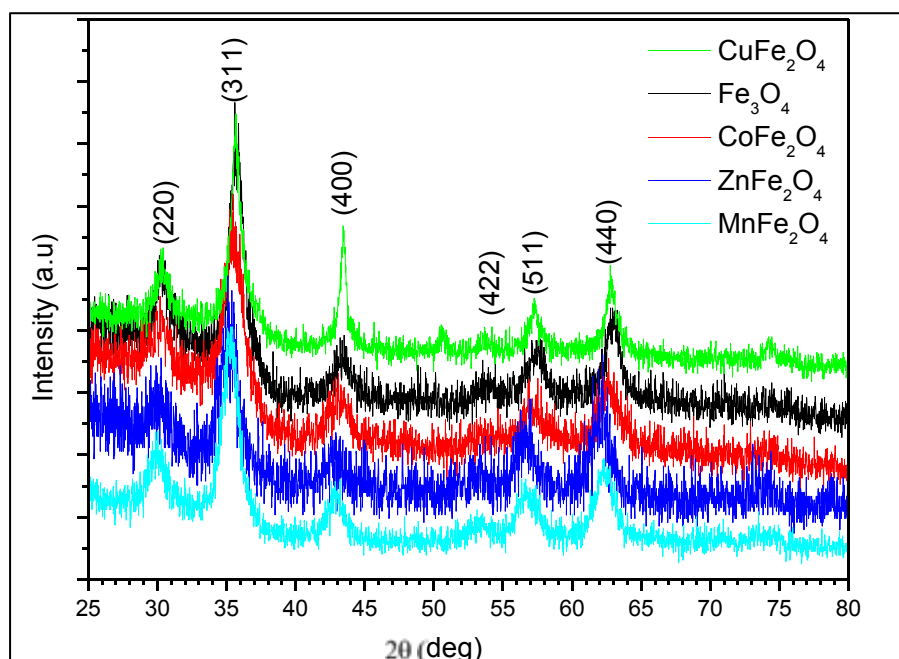


**Figure 5.3.2.2:** X ray diffraction patterns for oleylamine stabilized nanoparticles synthesized via solvothermal method. The main Bragg peaks of the spinel structure are identified.

Therefore, it can be concluded by analyzing **XRD** and electron diffraction results that both solvothermal and microwave synthesized nanoparticles have spinel-like structures that match with the expected results for Fe<sub>3</sub>O<sub>4</sub> and MFe<sub>2</sub>O<sub>4</sub> (M= Co, Mn, Cu, Zn). However, in the case of Fe<sub>3</sub>O<sub>4</sub>, it cannot be concluded via electron or X-ray diffraction if the resulting nanoparticles are formed only by magnetite, by a mixture of magnetite and maghemite ( $\gamma$ -Fe<sub>2</sub>O<sub>3</sub>), or even entirely by maghemite. Since X-ray and electron diffraction patterns of maghemite and magnetite are indistinguishable, it is undecidable to confirm/deny this fact.

### 5.3.3 Electron-dispersive X-Ray Spectroscopy (EDX)

Energy-dispersive X-ray spectra have been obtained at 200 kV using Titan and FEI Tecnai F20 field emission gun (FEG) TEMs.

All the acquired spectra have been taken from different regions (with or without particles) of the specimens, both for solvothermal and microwave synthesized nanoparticles.

**Figure 5.3.3.1** shows representative spectra obtained from microwave synthesized  $\text{Fe}_3\text{O}_4$ ,  $\text{MnFe}_2\text{O}_4$  and  $\text{CoFe}_2\text{O}_4$  nanoparticles:

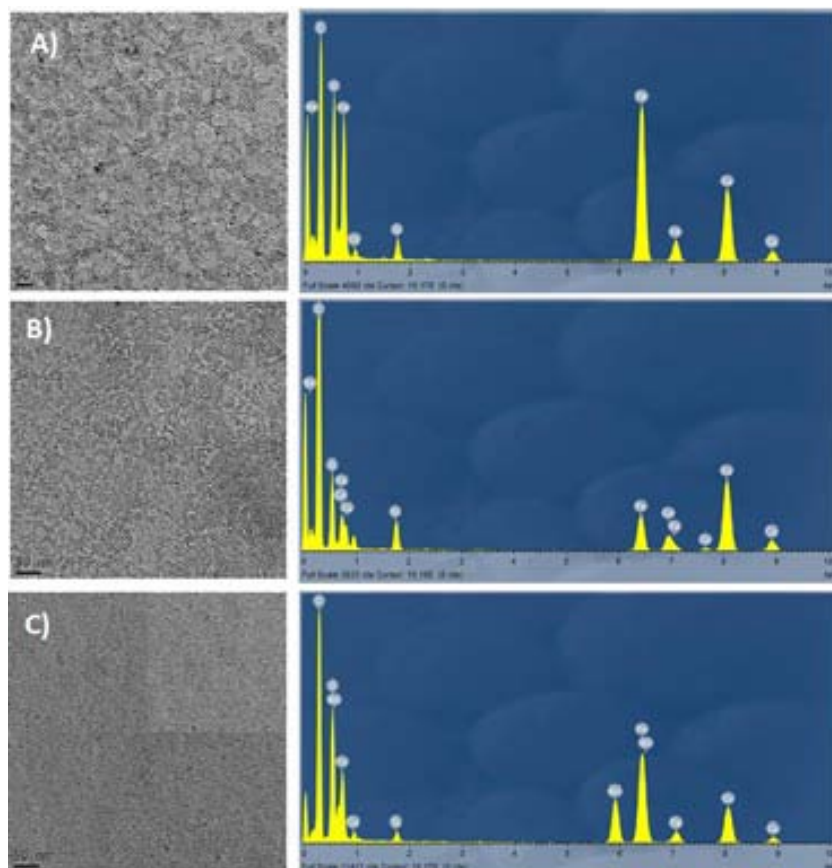


**Figure 5.3.3.1:** Representative spectra acquired from A)  $\text{Fe}_3\text{O}_4$ , B)  $\text{CoFe}_2\text{O}_4$  and C)  $\text{MnFe}_2\text{O}_4$  microwave-synthesized nanoparticles at 250 °C during 20 minutes of time reaction.

Intensity peaks corresponding to Be, C, Cu, Fe, O and Co or Mn (in the cases of mixed ferrites) have been found and quantified when analyzing the specimen. In all cases, as expected, the signals corresponding to C, Be and Cu have been obtained because of the grid in which the specimen has been prepared, and O values are not accurate because possible  $\text{CO}_2$  and  $\text{H}_2\text{O}$  adsorbed molecules on the specimen's surface. Thus, they have been obviated from the specimen analysis, focusing just in Fe, Si, and, depending on the mixed ferrite, Co or Mn signals. All their relative amounts are shown in **table 5.3.3.1**:

## 5. Mixed ferrite nanoparticles

	<b>Fe (% At)</b>	<b>Co (% At)</b>	<b>Mn (% At)</b>	<b>Si (% At)</b>
<b>Fe<sub>3</sub>O<sub>4</sub> 250 °C 20 min</b>	<b>86.8 ± 5.0</b>	-----	-----	<b>13.2 ± 5.0</b>
<b>Fe<sub>3</sub>O<sub>4</sub> 280 °C 20 min</b>	<b>92.6 ± 2.6</b>	-----	-----	<b>7.4 ± 2.6</b>
<b>CoFe<sub>3</sub>O<sub>4</sub> 250 °C 20 min</b>	<b>60.5 ± 4.3</b>	<b>31.5 ± 2.1</b>	-----	<b>8.0 ± 0.0</b>
<b>CoFe<sub>3</sub>O<sub>4</sub> 280 °C 20 min</b>	<b>62.3 ± 1.1</b>	<b>27.7 ± 1.2</b>	-----	<b>10.0 ± 2.1</b>
<b>MnFe<sub>3</sub>O<sub>4</sub> 250 °C 20 min</b>	<b>59.5 ± 6.5</b>	-----	<b>30.9 ± 3.7</b>	<b>9.6 ± 1.1</b>
<b>MnFe<sub>3</sub>O<sub>4</sub> 280 °C 20 min</b>	<b>57.7 ± 3.2</b>	-----	<b>29.5 ± 2.0</b>	<b>12.8 ± 4.8</b>

**Table 5.3.3.1:** Relative amounts (in atomic %) of Fe, Co, Mn and Si found in different samples of microwave-synthesized mixed ferrite nanoparticles.

Basically, two important pieces of data arise from that table. In the first place, it can be seen that every mixed ferrite has two iron atoms for each cobalt (or manganese) atom, which matches with the stoichiometric formulas expected for those kinds of compounds,  $MFe_2O_4$  ( $M = Co$  or  $Mn$ ). On the other hand, it has been found an unexpected silicon contamination in all the prepared specimens, being around a 10 % of silicon in each specimen (relative values calculated just taking into account just Fe, Co, Mn and Si atoms). Since it has been described in literature that silicon cations may strongly affect the magnetic properties of ferrites<sup>6,7,8</sup>, it has been studied whether silicon atoms are inside the synthesized nanoparticles or surrounding them. With that purpose, part of the black powders obtained during the synthetic process have been washed five times with ethanol so as to remove the oleylamine capping the nanoparticles without destroying the already formed nanocrystals and, therefore, to make sure that the silicone atoms are around and not within the synthesized particles.

**Figure 5.3.3.2** shows an **EDX** spectrum obtained from  $\text{MnFe}_2\text{O}_4$  microwave synthesized nanoparticles after being cleaned with ethanol:

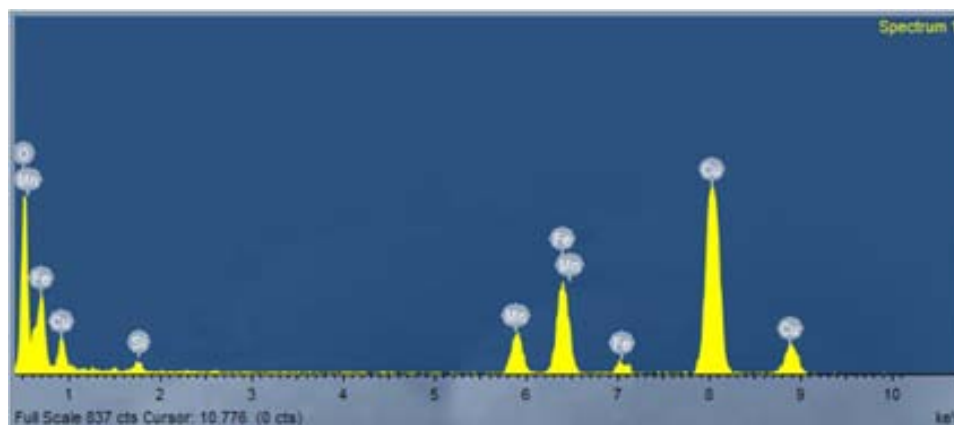


**Figure 5.3.3.2:** Representative spectrum acquired after drying the synthesized powder five times with ethanol and removing all the remaining oleylamine. This spectrum corresponds to the  $\text{MnFe}_2\text{O}_4$  microwave-synthesized nanoparticles at 250 °C during 20 minutes of time reaction.

As shown in the spectrum, the amount of silicon has significantly decreased after carrying out the cleaning process. **Table 5.3.3.2** shows the differences in atomic % of Fe, Mn and Si after and before cleaning up the synthesized nanoparticles:

	<b>Fe (% At)</b>	<b>Co (% At)</b>	<b>Mn (% At)</b>	<b>Si (% At)</b>
<b><math>\text{MnFe}_3\text{O}_4</math> 250 °C 20 min before</b>	<b><math>59.5 \pm 6.5</math></b>	-----	<b><math>30.9 \pm 3.7</math></b>	<b><math>9.6 \pm 1.1</math></b>
<b><math>\text{MnFe}_3\text{O}_4</math> 250 °C 20 min after</b>	<b><math>61.9 \pm 5.2</math></b>	-----	<b><math>37.1 \pm 4.2</math></b>	<b><math>0.4 \pm 1.1</math></b>

**Table 5.3.3.2:** Relative amounts (in atomic %) of Fe, Mn and Si found in the same sample before and after cleaning it up five times with ethanol.

From these data, it can be assumed that a high % of the silicon found in the sample is surrounding and not inside the nanoparticles structure. Thus, their effect in the magnetic properties of nanoparticles, in case there were, would not be significant. The same silicon amount reduction has taken place when cleaning the other synthesized nanoparticles with ethanol.

The source of the silicon contamination has been identified also via **EDX** as the commercial iron (III) acetylacetonate. In fact, silicon traces were heterogeneously dispersed among the reactant. No silicon traces, however, have been found in the rest of used acetylacetonates.



### 5.3.4 Thermogravimetric analysis (TGA) and differential scanning calorimetry (DSC)

Thermogravimetric analyses (TGA) and differential scanning calorimetry (DSC) were performed under oxygen atmosphere at a heating rate of 5°C/min going from room temperature up to 800 °C using a NETZSCH STA 449 C analyzer.

The presence of oleylamine on the nanoparticles surface is supported by thermogravimetric analysis (TGA). **Figure 5.3.3.1** shows the TGA corresponding curves of the Fe<sub>3</sub>O<sub>4</sub> (a) and CoFe<sub>2</sub>O<sub>4</sub> (b) solvothermal synthesized nanoparticles, respectively. In both images of the figure, a mass loss can be observed between 300-450°C. This fact can be attributed to a decoordination of the oleylamine from the nanoparticle surface, indicating that, in both cases, nanoparticles are formed by a 20 % mass of oleylamine surrounding the spinel (magnetite or mixed ferrite) nanocrystal. In addition, in the case of Fe<sub>3</sub>O<sub>4</sub> (a), the differential scanning calorimetry (DSC) shows a signal around 700 °C, indicating a phase change from Fe<sub>3</sub>O<sub>4</sub> to α-Fe<sub>2</sub>O<sub>3</sub>, which is an oxidative exothermic process. This fact suggests that, even in case there were a mixture of Fe<sub>3</sub>O<sub>4</sub> and α-Fe<sub>2</sub>O<sub>3</sub> in the original formed nanoparticles, a part of the synthesized nanoparticles are formed by magnetite; otherwise, the exothermic peak at 700 °C would not appear.

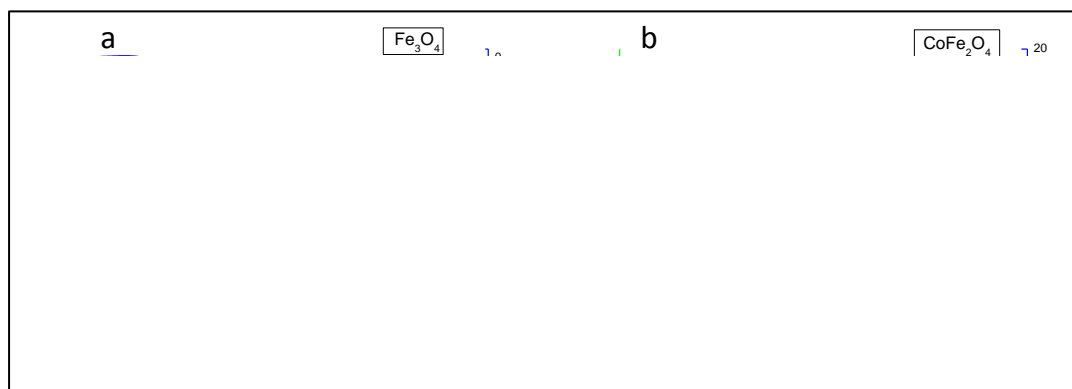


**Figure 5.3.4.1:** TGA analysis of Fe<sub>3</sub>O<sub>4</sub> and CoFe<sub>2</sub>O<sub>4</sub> synthesized via solvothermal method during 3 hours at 220 °C.

## 5. Mixed ferrite nanoparticles

In all the other solvothermal or microwave-synthesized nanoparticles, the resulting TGAs show a loss of about 20-30 % in weight between 200-400 °C and, for  $\text{Fe}_3\text{O}_4$  nanoparticles, DSC results show an exothermic peak around 600 °C, suggesting a magnetite-maghemite phase change, as shown in **figure 5.3.4.2**.

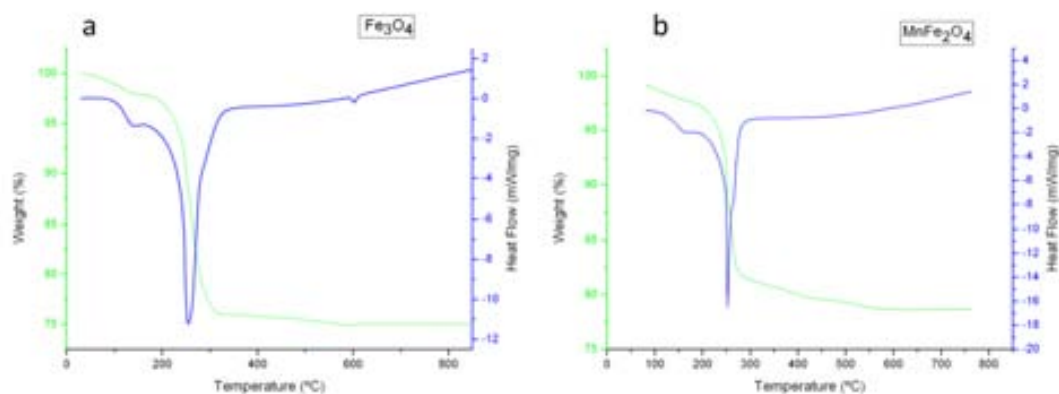


**Figure 5.3.4.2:** TGA analysis of  $\text{Fe}_3\text{O}_4$  and  $\text{MnFe}_2\text{O}_4$  synthesized via microwave heating method during 3 hours at 220 °C.

Apart from TGA analysis, the presence of oleylamine on the nanoparticles surface is also supported by IR-spectra, as is shown in the following section.

### 5.3.5 Infrared (IR) measurements

Fourier transform infrared (**FT-IR**) spectra were recorded on a Bruker IR Tensor 27 ATR:SPECDC MKII Golden Gate.

As mentioned in the previous section, **IR** spectra confirm the presence of amino ligands on the nanoparticles surface. As can be observed in **Figure 5.3.4.1**, peaks at 1376, 1527 (N-H), 2849 and 2917  $\text{cm}^{-1}$  (C-H) confirm the presence of oleylamine.

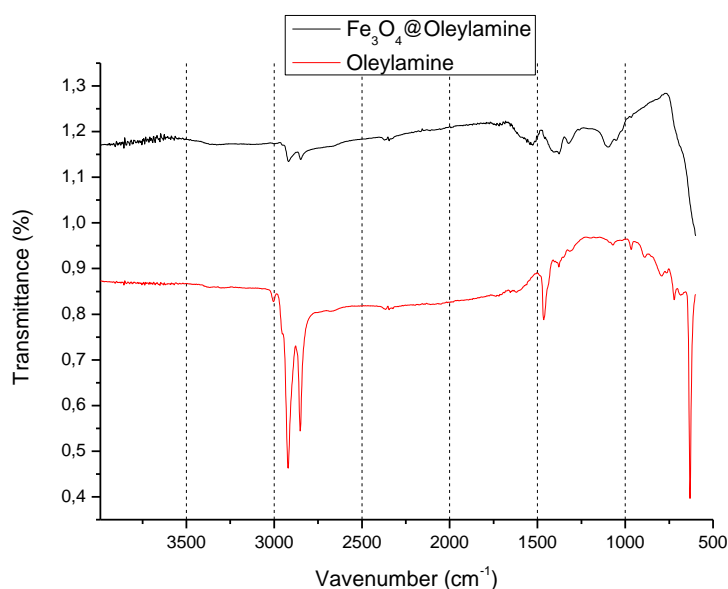


**Figure 5.3.5.1:** Infrared spectra of (black line)  $\text{Fe}_3\text{O}_4$ @Oleylamine MW synthesized nanoparticles and (red line) Commercial Oleylamine.

Since oleylamine has been confirmed via both **TGA** and **IR** data analysis, the percentage of mass loss measured with the **TGA** has been used to correct all magnetic analyses, which are explained in depth as follows.

### 5.3.6 Magnetic measurements

Magnetic properties of the  $M\text{Fe}_2\text{O}_4$  nanoparticles have been measured on a **SQUID** magnetometer. Hysteresis loops measurements have been performed up to 70 kOe at two different temperatures: 10 K and 300 K. Complementarily, zero-field cooled and field cooled measurements have been carried out at 50 Oe of applied magnetic field.

As aforementioned, the absolute values of magnetization have been obtained after correcting the weighted nanoparticles mass with the mass loss associated to the organic ligands observed by **TGA**.

Since nanoparticles' size and shape may strongly affect their resulting magnetic behaviour and it has been observed how these characteristic vary depending on the used heating method, this section is focused on studying the different magnetic behaviours between the solvothermal and the microwave-synthesized nanoparticles.

In this vein, solvothermal-synthesized nanoparticles magnetic study is explained as follows:

**Figure 5.3.6.1. (left)** shows the hysteresis loops of  $\text{CoFe}_2\text{O}_4$  synthesized at 280 °C during 3 hours of reaction. Two different measurements at two different temperatures are presented. At 10 K, the nanoparticles show clearly a ferrimagnetic behaviour with a coercivity field of 12.5 kOe, while at 300 K (over the blocking temperature), the nanostructures act like superparamagnetic. Despite the high available external magnetic field (70 kOe), the sample is not completely saturate and magnetic hysteresis persists up to very high magnetic fields, indicating a very strong magnetic anisotropy. Extrapolating the high field magnetization it has been obtained a saturation value for the magnetization of  $\text{CoFe}_2\text{O}_4$  nanoparticles of 82 emu/g.

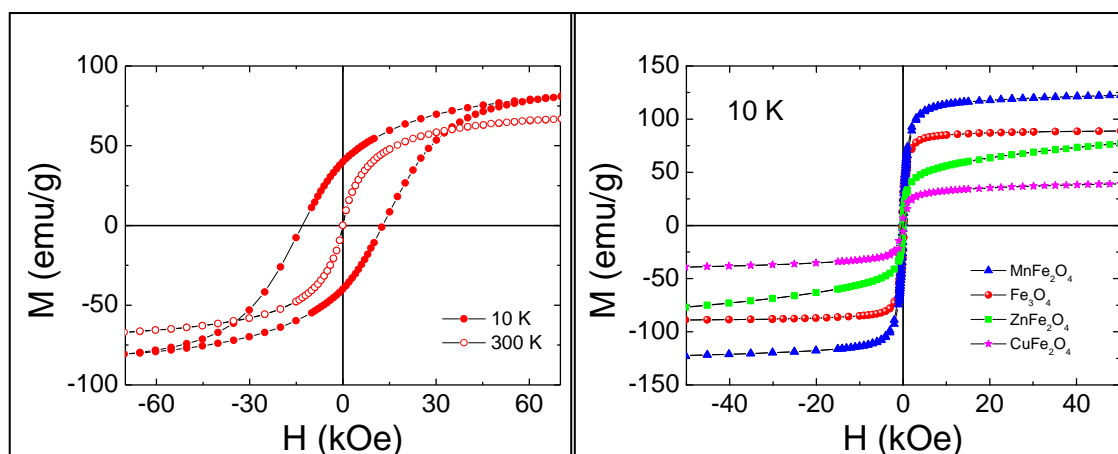


**Figure 5.3.5.1:** Magnetic hysteresis loops for oleylamine stabilized  $M\text{Fe}_2\text{O}_4$  nanoparticles. (a) Loops for  $\text{CoFe}_2\text{O}_4$  particles at 10 K and 300 K. (b) Loops at 10 K for  $M\text{Fe}_2\text{O}_4$  (M=Mn, Fe, Cu, Zn) nanoparticles.

**Figure 5.3.6.1. (right)** shows the magnetic hysteresis loops at 10 K of  $MFe_2O_4$  (M= Mn, Fe, Cu, Zn) nanoparticles also synthesized at 280 °C during 3 h of reaction. The obtained values of saturation and coercivity corresponding to these particles are shown in **Table 5.3.6.1.**

	<b>Ms (emu/g)</b>	<b><math>\mu_0H_c</math> (Oe)</b>
<b>Fe<sub>3</sub>O<sub>4</sub></b>	76	290
<b>MnFe<sub>2</sub>O<sub>4</sub></b>	116	80
<b>CoFe<sub>2</sub>O<sub>4</sub></b>	82	12500
<b>CuFe<sub>2</sub>O<sub>4</sub></b>	33	250
<b>ZnFe<sub>2</sub>O<sub>4</sub></b>	41	50

**Table 5.3.6.1:** Magnetization Saturation (Ms) and coercivity field ( $\mu_0H_c$ ) for the different magnetic synthesized nanoparticles.

All these values are in good agreement with the expected ones for bulk ferrimagnetic analogous materials. In the case of  $ZnFe_2O_4$  nanoparticles it can be seen that there is a high-field susceptibility and magnetization does not saturate. This fact indicates that a non-collinear ferrimagnetic structure has been developed instead of the antiferromagnetic one typical of  $ZnFe_2O_4$  ferrites. Extrapolating to zero it has been estimated a saturation magnetization of 40,6 emu/g. This value indicates a strong redistribution of  $Zn^{2+}$  and  $Fe^{3+}$  among the A and B sites of the spinel structure. This feature, observed by other groups as Beji et al.<sup>9</sup> is in accordance to different studies which explain that the cation distribution in the zinc ferrite spinel is dependent on multiple factors, such as the synthetic methodology<sup>10</sup>, crystal size at nanoscale<sup>10</sup>, annealing temperature<sup>11</sup>, etc., affecting principally to the magnetic behaviour of the nanoparticles synthesized<sup>12</sup>. Cation distribution among the tetrahedral and octahedral of the  $ZnFe_2O_4$  crystallographic sites is under study jointly with a deeper study of their magnetic properties.

Field-cool and zero field-cool analysis demonstrate that the blocking temperature ( $T_B$ ) is below room temperature in all cases, indicating that all  $MFe_2O_4$  nanoparticles are superparamagnetic at room temperature and ferrimagnetic at low temperature, as shown in **figure 5.3.6.2.**

## 5. Mixed ferrite nanoparticles

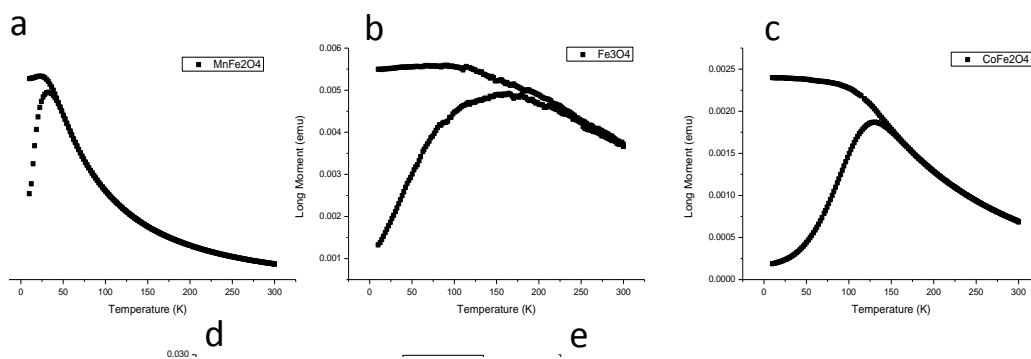


**Figure 5.3.6.2:** FC/ZFC analysis for different ferrite nanoparticles synthesized: a)  $\text{MnFe}_2\text{O}_4$ ; b)  $\text{Fe}_3\text{O}_4$ ; c)  $\text{CoFe}_2\text{O}_4$ ; d)  $\text{CuFe}_2\text{O}_4$ ; e)  $\text{ZnFe}_2\text{O}_4$ . As it can be observed, the blocking temperature is lower than room temperature in all cases.

Additional analyses have been performed in order to confirm the TGA observation of the existence of an oxidative process. Magnetic measurements for the  $\text{Fe}_3\text{O}_4$  nanoparticles before and after a thermal treatment (from room temperature to  $800^\circ\text{C}$ ), have been carried out and are presented in **figure 5.3.5.3**. In this case, an antiferromagnetic behaviour is observed.

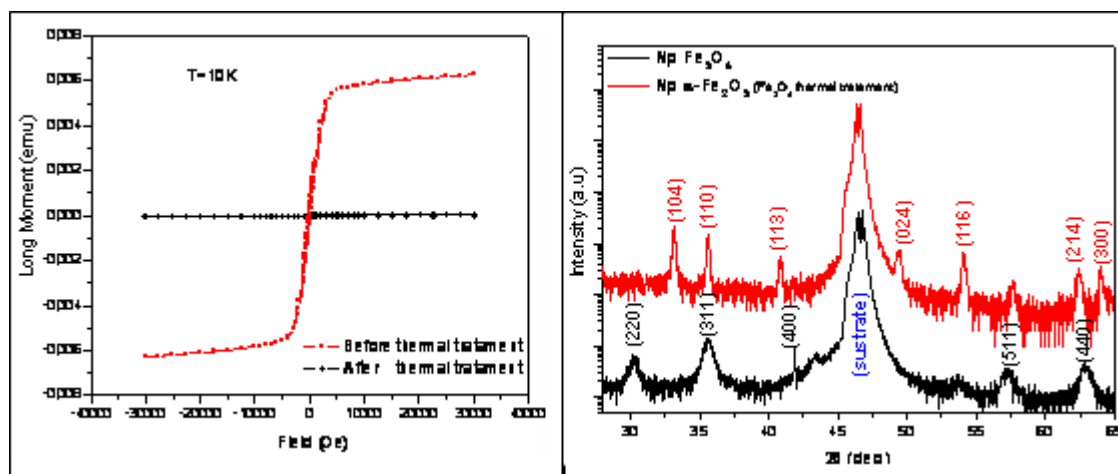


**Figure 5.3.6.3:** Magnetic hysteresis loops and x-ray diffraction pattern of  $\text{Fe}_3\text{O}_4$  nanoparticles before and after a thermal treatment (heat until  $800^\circ\text{C}$ ). Note the antiferromagnetic behavior after the thermal treatment

## 5. Mixed ferrite nanoparticles

When studying the magnetic behaviour of the microwave-synthesized nanoparticles, on the other hand, the following results were observed:

As it is shown in **table 5.3.6.2**, very similar **Ms** values were observed when comparing both microwave and solvothermal-synthesized nanoparticles, which is in agreement with all the already studied results, since both kinds of nanoparticles do not differ neither substantially in size nor in shape. Specifically, the ‘microwave’ studied nanoparticles correspond to those obtained after 20 minutes of reaction at 250 °C.

	<b>Ms for MW NPs</b>	<b>Ms for Solvothermal NPs</b>
<b>Fe<sub>3</sub>O<sub>4</sub></b>	77 emu/g	76 emu/g
<b>CoFe<sub>2</sub>O<sub>4</sub></b>	89 emu/g	82 emu/g
<b>MnFe<sub>2</sub>O<sub>4</sub></b>	118 emu/g	116 emu/g

**Table 5.3.6.1:** Magnetization Saturation (Ms) and coercivity field ( $\mu_0 H_c$ ) for the different magnetic synthesized nanoparticles.

Figure 5.3.6.4 shows the hysteresis loops corresponding to the MW studied samples:

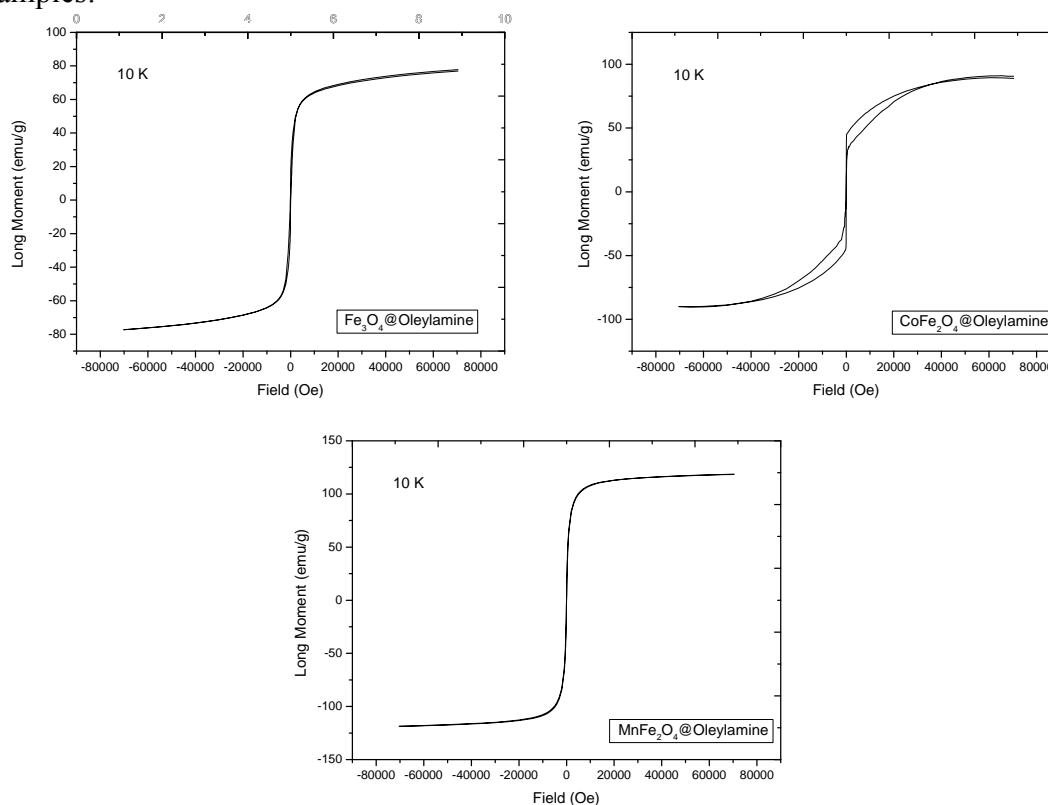


**Figure 5.3.6.4:** Magnetic hysteresis loops corresponding to Fe<sub>3</sub>O<sub>4</sub>, CoFe<sub>2</sub>O<sub>4</sub> and MnFe<sub>2</sub>O<sub>4</sub> microwave-synthesized nanoparticles. All measurements were taken at 10 K.

### 5.4 Summary

In this work, magnetite, as well as some mixed ferrite nanoparticles have been synthesized via heating metallic acetylacetonate complexes in oleylamine, which works both as a solvent and capping agent. The heating process has been carried out via two different ways:

- Solvothermal method.
- Microwave-assisted method.

It has been concluded that the heating process is a key factor when trying to obtain stable nanoparticle dispersions. Thus, the reaction temperature must be increased linearly (at 1 °C / min for solvothermal heating) in order to allow oleylamine to properly control the nanoparticles' growth. Microwave assisted method highly decreases the reaction time since it provides energy to the reaction system in a more homogeneous and controlled way.

In all cases, the synthesized nanoparticles have been fully characterized via different techniques.

As a result of this characterization, it has been concluded that the formed nanoparticles are indeed surrounded by oleylamine, which allows them to be perfectly dispersed in organic solvents such as hexane or toluene, and also that nanoparticles show a narrow size and shape distribution. The microwave heating method has shown to be better at keeping the spherical shape of nanoparticles. The solvothermal heating, on the other hand, allows obtaining a wider nanoparticle size average, although for large times and higher temperature conditions it leads to less stable dispersions and more anisotropic nanoparticle shapes.



### 5.5 Related literature

---

- <sup>1</sup> Zhang L.; He R.; Gu H.-C., *Mater. Res. Bull.*, **2006**, 41, 260-267.
- <sup>2</sup> Taniguchi T.; Nakagawa K.; Watanabe T.; Matsushita N.; Yoshimura M., *J. Phys. Chem. C*, **2009**, 113, 839-843.
- <sup>3</sup> Jia C.-J., *J. Am. Chem. Soc.*, **2008**, 130, 16968-16977.
- <sup>4</sup> McNaught A.D.; Wilkinson A., IUPAC. Compendium of Chemical Terminology – Gold Book, Blackwell Scientific Publications: Oxford, **1997**.
- <sup>5</sup> Kuo C. L.; Hwang K. C., *Chem. Mater.*, **2013**, 25, 365-371.
- <sup>6</sup> Paulsen J. A.; Lo C.C.H.; Snyder J.E.; ring A.P.; Jones L.L.; Jiles D.C., *IEEE Trans. Magn.*, **2003**, 39, 3316-3318.
- <sup>7</sup> Uzma G., *Eur. Phys. J. Appl. Phys.*, **2010**, 50, 30302p1-30302p4.
- <sup>8</sup> Shinde S. S.; Jadhav K. M., *J. Mater. Sci. Lett.*, **1998**, 17, 849-851.
- <sup>9</sup> Beji Z., *Thin Solid Film*, **2010**, 518, 2592-2598.
- <sup>10</sup> Li F. S.; Wang L.; Wang J.B.; Zhou Q.G.; Zhou X.Z.; Kunkel H.P.; Williams G., *J. Magn. Magn. Mater.*, **2004**, 268, 332-339.
- <sup>11</sup> Blanco-Gutie V.; Jimenez-Villacorta F.; Bonville P.; Torralvo-Fernandez M.J.; Saez-Puche R., *J. Phys. Chem. C*, **2011**, 115, 1627-1634.
- <sup>12</sup> Braestrup F.; Hauback B.C.; Hansen K.K., *J. Solid State Chem.*, **2008**, 181, 2364-2369.



## Chapter 6

# Synthesis and characterization of Goethite nanorods. TEM ‘In-situ’ study of the phase change from Goethite to Hematite

### Contents

---

6.1 General description of the carried out work.....	165
6.2 Experimental procedure.....	167
6.2.1 Materials and reactants.....	167
6.2.2 Synthesis of Hexa- $\mu_2$ -acetato-triaqua- $\mu_3$ -oxo-triiron(III) nitrate acetic acid solvate, $[\text{Fe}_3\text{O}(\text{OCOCH}_3)_6(\text{H}_2\text{O})_3]\cdot\text{NO}_3$ .....	167
6.2.3 Hydrothermal synthesis of goethite nanorods.....	167
6.2.4 Modified hydrothermal synthesis of goethite nanorods.....	168
6.3 Basic information of all the different iron oxide species found (and formed) during the sample analyses.....	169

## 6. Goethite – Hematite nanorods TEM transformation

6.4 Characterization and results discussion.....	171
6.4.1 TEM Bright Field microphotographs.....	171
6.4.2 Electron and X-ray diffraction.....	178
6.4.3 Mössbauer spectroscopy.....	180
6.4.4 Magnetic measurements (SQUID, FC-ZFC and Electron holography).....	181
6.4.5 Energy-dispersive X-ray spectroscopy (EDX).....	184
6.4.6 Energy Filtered Transmission Electron Microscopy (EFTEM).....	186
6.4.7 Nanorods synthetic procedure carried out using $[\text{Fe}_3\text{O}(\text{OCOCH}_3)_6(\text{H}_2\text{O})_3]\cdot\text{NO}_3$ as a source of iron (III) and without adding any source of iron (II).....	187
6.5 Summary.....	189
6.6 Related literature.....	190

## 6. Synthesis and characterization of Goethite nanorods. TEM ‘In-situ’ study of the phase change from Goethite to Hematite

This chapter explains the synthesis and characterization of water-dispersible goethite  $\text{FeO}(\text{OH})$  nanorods capped with ethylenediamine (en) as well as their transformation into hematite nanorods via the effect of the TEM electron beam. The synthesized nanorods have been characterized via different techniques, both before and after undergoing the electron-beam transformation.

Both the discussion of the data obtained when carrying out the nanorods characterization and their ‘in-situ’ transformation study are also explained in detail in this chapter.

### 6.1 General description of the carried out work

Water-dispersible goethite nanorods coated with ethylenediamine (en) ligand, have been prepared via hydrothermal synthesis by following a method previously described in literature<sup>1</sup>. However, the initial purpose when carrying out this synthesis was to obtain magnetite nanorods so as to surround them with a gold shell and to form a  $\text{Fe}_3\text{O}_4@\text{Au}$  core-shell structure. In fact, according to literature, this synthetic method is supposedly based on forming the magnetite nanorods by dissolving iron (II) and iron(III) salts in water and adding ethylenediamine, which works as a capping agent and also provides a basic medium necessary to form the iron oxide. The reaction itself takes place when heating the initial mixture at  $180^\circ\text{C}$  during 20 h inside an autoclave device. The performed procedure, as described in literature, is shown in **figure 6.1.1.1**:

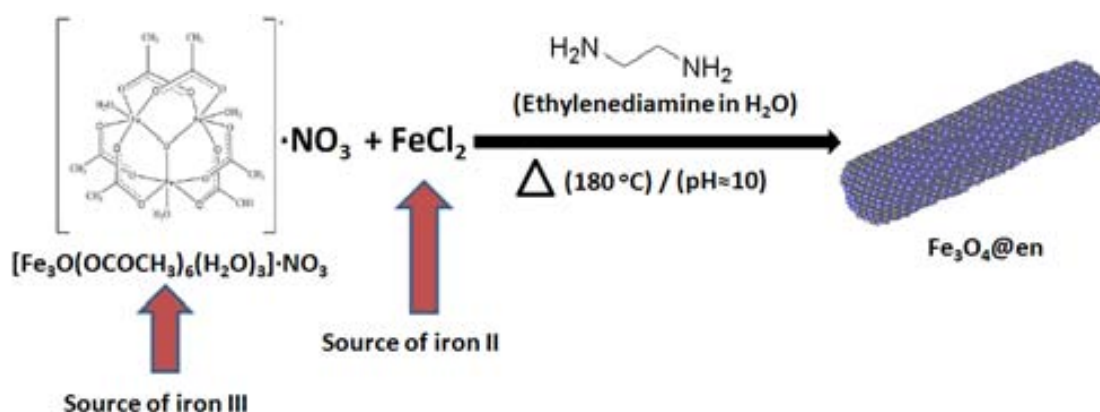


**Figure 6.1.1.1:** Synthetic procedure with which it was supposed to obtain magnetite nanorods.

## 6. Goethite – Hematite nanorods TEM transformation

Nevertheless, as it is explained in this chapter, by performing this reaction of magnetite yet goethite nanorods are obtained, mixed with other magnetite and goethite particles that show different sizes and shapes, as pictured in **figure 6.1.1.2**.

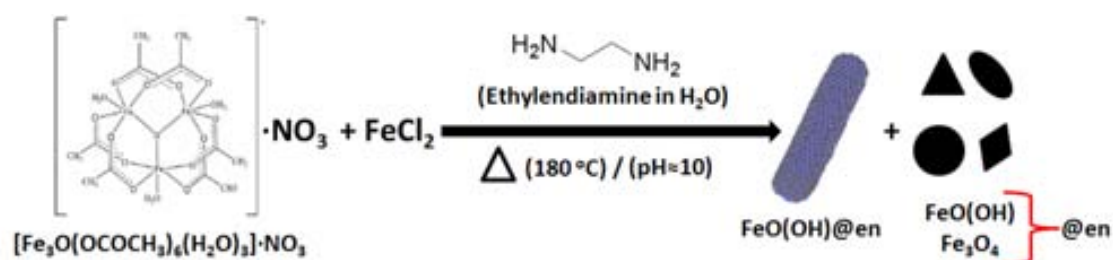


**Figure 6.1.1.2:** Sketch showing the actual reaction products obtained when carrying out the synthetic procedure described in literature.

All the obtained nanoparticles have been separated via centrifugation and subsequently washed with a mixture of water and ethanol, obtaining a water-dispersible black powder, as shown in **figure 6.1.1.3**.

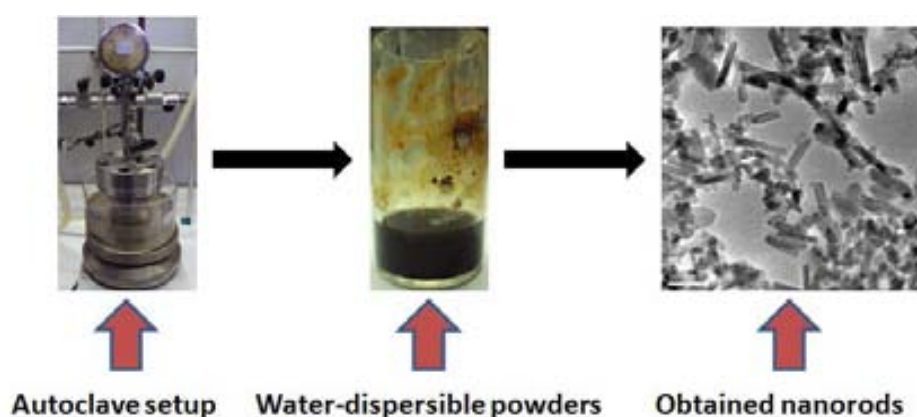


**Figure 6.1.1.3 :** Pictures corresponding to the autoclave setup (left) the obtained water-dispersible powders (middle) and the final obtained water-dispersion nanoparticles (right).

It is mandatory to point out that this reaction has been carried out thrice, and in all the cases the resulting synthesized nanorods were formed by goethite. Also in all cases the goethite-hematite nanorod transformation has been observed when studying those particles under the electron beam of the **TEM**.

### 6.2 Experimental procedure

#### 6.2.1 Materials and reactants

$\text{Fe}(\text{NO}_3)_3 \cdot 9\text{H}_2\text{O}$  (Aldrich,  $\geq 98\%$ ),  $\text{FeSO}_4$  (Aldrich,  $\geq 99,5\%$ ), Ethylenediamine (Aldrich,  $\geq 99\%$ ), NaOH (Aldrich,  $\geq 97,0\%$ ), Acetic acid (Fluka, 99,5%), All reactions were carried out in Millipore water, and the resulting nanoparticles were washed with Millipore water and absolute ethanol (AR grade)

#### 6.2.2 Synthesis of Hexa- $\mu_2$ -acetato-triaqua- $\mu_3$ -oxo-triiron(III) nitrate acetic acid solvate, $[\text{Fe}_3\text{O}(\text{OCOCH}_3)_6(\text{H}_2\text{O})_3] \cdot \text{NO}_3$

$[\text{Fe}_3\text{O}(\text{OCOCH}_3)_6(\text{H}_2\text{O})_3] \cdot \text{NO}_3$ , which works as an iron (III) source for the further iron oxide nanoparticles synthesis, was prepared by following a procedure similar than the one described in literature by S. Yao, et al.<sup>2</sup>. 1,21 g (3,0 mmol) of  $[\text{Fe}_3\text{O}(\text{OCOCH}_3)_6(\text{H}_2\text{O})_3] \cdot \text{NO}_3$  were dissolved in 15 ml of water and 12 ml of NaOH 1M (13,2 mmol) were added dropwise to produce a brown precipitate, then 25 ml of acetic acid were added to the mixture, turning the brown precipitate into an intense red solution. It was stirred under reflux for 3 h and the resulting red solution was filtered and cooled to room temperature. Finally, it was dried using a vacuum line and 2,09 g of a red solid were obtained.

#### 6.2.3 Hydrothermal synthesis of goethite nanorods

The synthesis of goethite nanorods was performed, as aforementioned, by following a previously reported procedure by Dong *et al*.<sup>1</sup>. 0,67 m mols of  $[\text{Fe}_3\text{O}(\text{OCOCH}_3)_6(\text{H}_2\text{O})_3] \cdot \text{NO}_3$  and 1,0 m mols of  $\text{FeSO}_4$  were dissolved in 20 ml of deoxygenated Millipore water. Organic base ethylenediamine was added to the previously prepared solution until reaching pH=10.6 under vigorous magnetic stirring. The resulting solution was then put into a 50 ml. Teflon-lined autoclave. The autoclave was sealed and maintained at 180 °C during 20 h, and then cooled to room temperature. The resulting nanoparticles were separated via centrifugation and washed with a mixture of Millipore water and absolute ethanol three times and then dried using a vacuum line. Finally, 0,132 g of a black solid powder were obtained. The resulting nanoparticles that form this black powder are totally water-dispersible.

## 6. Goethite – Hematite nanorods TEM transformation

### 6.2.4 Modified hydrothermal synthesis of goethite nanorods

The synthesis of goethite nanorods was performed, by modifying the previously explained procedure, using in this case only a source of iron (III), so as to avoid obtaining magnetite nanoparticle. 1,67 mmol of  $[\text{Fe}_3\text{O}(\text{OCOCH}_3)_6(\text{H}_2\text{O})_3]\cdot\text{NO}_3$  were dissolved in 20 mL of deoxygenated Millipore water. Organic base ethylenediamine was added to the previously prepared solution until reaching  $\text{pH} = 10.6$ , under vigorous magnetic stirring. The resulting solution was then put into a 50 mL Teflon-lined autoclave. The autoclave was sealed and maintained at  $180^\circ\text{C}$  during 20 h, and then cooled to room temperature. The resulting nanoparticles were separated via centrifugation and washed with a mixture of Millipore water and absolute ethanol three times and then dried using a vacuum line. Finally, 0,127 g of a brown solid powder were obtained. The resulting nanoparticles that form this brown powder are totally water-dispersible.



### 6.3 Basic information of all the different iron oxide species found (and formed) during the sample analyses

Basically, as it has been mentioned before, three different iron oxide phases have been found during the analysis of the synthesized specimen: magnetite, goethite and hematite, which have been ‘in-situ’ formed as a result of goethite’s TEM-assisted transformation, as shown in **figure 6.3.1.1**:

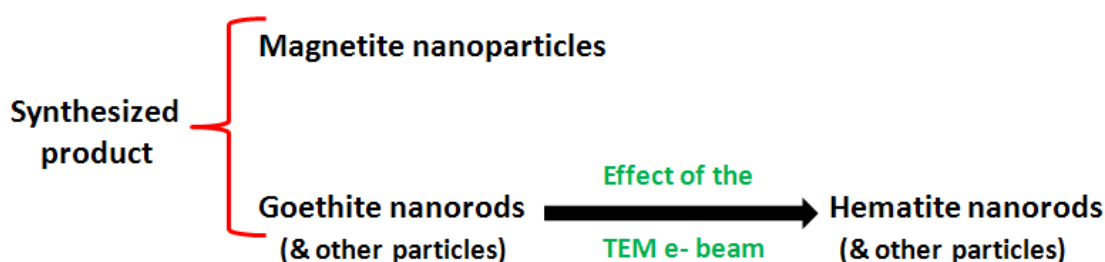
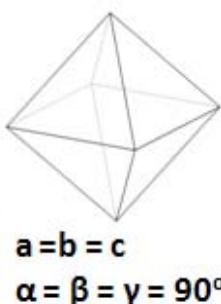
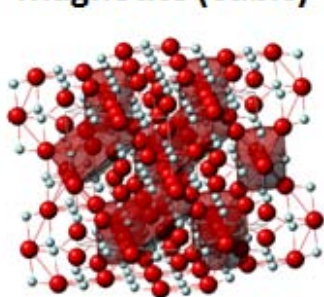


**Figure 6.3.1.1:** Sketch showing the different reaction products observed after studying and TEM changing the synthesized nanoparticles.

As it has been explained in **Chapter 1**, **magnetite (Fe<sub>3</sub>O<sub>4</sub>)** and **hematite (α-Fe<sub>2</sub>O<sub>3</sub>)** are two of the most common kinds of iron oxides in nature. Magnetite, as aforementioned, has a cubic crystallographic system formed by both iron (II) and iron (III) cations inside its oxygen-formed lattice structure<sup>3</sup>, and it shows a ferromagnetic behaviour, yet magnetite nanoparticles may present a superparamagnetic behaviour if they are small enough<sup>4,5</sup>, as shown in **figure 6.3.1.2**:

#### Magnetite (cubic)



<b>Mol. Formula:</b>	<b>Fe<sub>3</sub>O<sub>4</sub></b>
<b>Fe oxid. State:</b>	<b>+2 / +3</b>
<b>% Fe</b>	<b>42.86</b>
<b>% O</b>	<b>57.14</b>
<b>Magnetically</b>	<b>Ferrimagnetic</b>

**Figure 6.3.1.1:** Image showing the cubic crystallographic structure of magnetite and its magnetic behavior. Its molecular formula, as well as its atomic percentage of iron and oxygen inside the structure is also shown.

## 6. Goethite – Hematite nanorods TEM transformation

**Goethite ( $\alpha$ -FeOOH)** and **hematite ( $\alpha$ -Fe<sub>2</sub>O<sub>3</sub>)**, on the other hand, are iron (III) oxides with different crystallographic systems and also different magnetic properties. Thus, goethite has an orthorhombic structure and magnetically behaves as an antiferromagnetic material with a Neel Temperature of 130 °C, while hematite shows a hexagonal crystallographic system and it is weakly ferromagnetic<sup>1</sup>. Another important difference between goethite and hematite lies in the fact that goethite is a hydrated iron (III) oxide, which means that it has water molecules inside its crystallographic structure, meanwhile hematite does not<sup>6</sup>.

The main characteristics and differences between goethite and hematite are shown in **figure 6.3.1.2**:

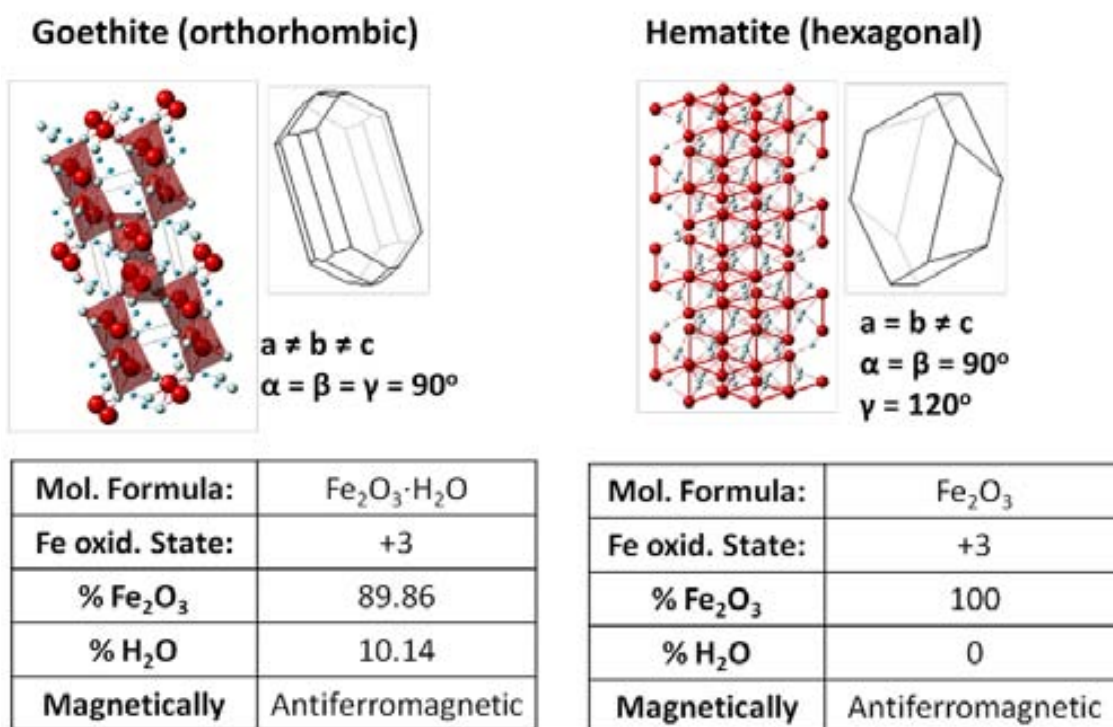


**Figure 6.3.1.2:** Images showing the orthorhombic and hexagonal crystallographic structures of goethite and hematite, respectively, and their respective magnetic behavior. Their molecular formulas, as well as their molecular percentages of iron oxide and water are also shown.

## 6.4 Characterization and result discussion

The resulting goethite nanorods (as well as the other synthesized particles) characterization, their ‘in-situ’ transformation into hematite nanorods and the obtained data discussion are described in this section. The whole study has been carried out via the following characterization techniques:

- Transmission electron microscopy (TEM) and high resolution electron microscopy (HRTEM) Bright Field microphotographs.
- Fourier Fast Transformation image analysis.
- Electron diffraction.
- Powder X-Ray diffraction.
- Mössbauer spectroscopy.
- EF-TEM analysis.
- Electron holography.
- SQUID and FC/ZFC magnetic studies

### 6.4.1 TEM Bright Field microphotographs

Transmission Electron Microscope (TEM) images were obtained on a Philips Tencai 20 at an accelerating voltage of 200 kV.

TEM images taken from the synthesized nanoparticles specimen are shown in figure 6.4.1.1:

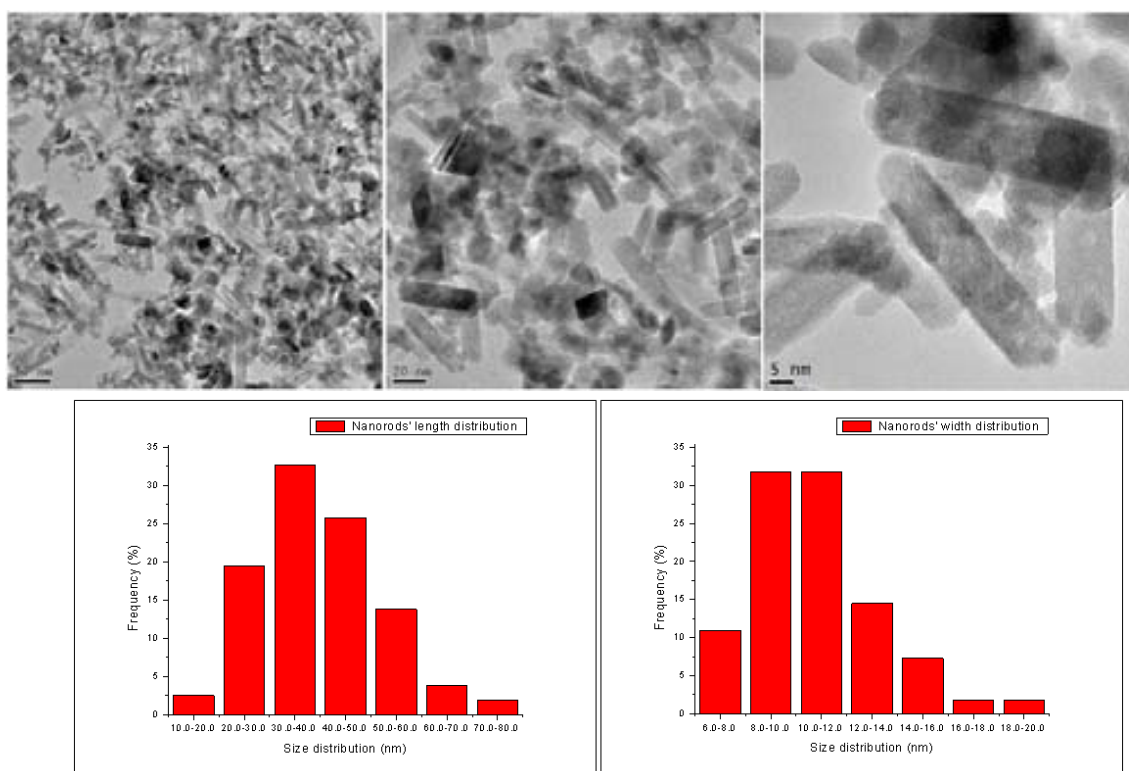


**Figure 6.4.1.1:** TEM images and particle length (left) and width (right) distribution of the obtained goethite nanorods.

## 6. Goethite – Hematite nanorods TEM transformation

that the synthesized nanorods show normal-like Gaussian distributions for both length and width measurements, they are quite length-polydispersed yet width-monodispersed. This fact suggests that ethylenediamine controls and restricts better the nanorods thickness growth than their length growth.

HR TEM images taken from these nanorods (**figure 6.4.1.2**) show the typical (1 0 1) interplanar d-spacing expected for goethite in the nanorods length axis direction, as it has been described in literature<sup>7,8</sup>.

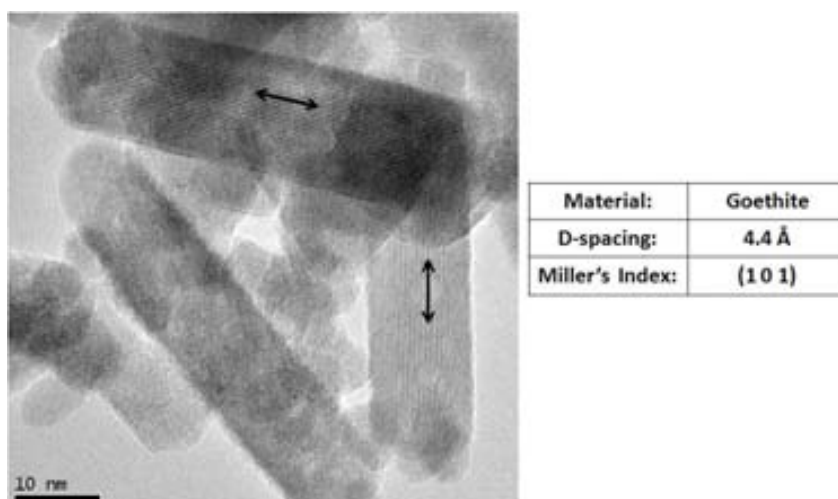


**Figure 6.4.1.2:** HR TEM images showing some goethite nanorods in which it is possible to see the plane whose Miller index is (1 0 1) along the particles axis direction.

As a forementioned, when focusing the electron beam on the nanoparticles with certain intensity and during 5 seconds or more, they undergo a transformation into hematite nanorods. As a consequence, a clear degradation and hollow formation on the nanorods structure may be observed. Similar processes, produced by other energy sources, such as simply heating<sup>9,10</sup> at hydrothermal conditions, have also been described in literature. In fact, Gualtieri, A. F., et al.<sup>6</sup>, explained the goethite-hematite transformation for bulk materials as a process in which the following changes take place:

- There is a migration of hydroxyl (OH<sup>-</sup>) anions, as well as Fe<sup>3+</sup> and H<sup>+</sup> cations.
- As a result of the cation migrations, Fe<sup>3+</sup> occupies 1/2 of the octahedral cavities in goethite and 2/3 in hematite. Sometimes it is possible to obtain Fe-defective hematite.
- There is a change of the crystal structure from orthorhombic to hexagonal
- There is a water loss during the process that leads to the voids formation and the crystal degradation.

## 6. Goethite – Hematite nanorods TEM transformation

The nanorod degradation process has been followed in real time by taking different TEM images from the same nanorods within a few seconds of difference, as shown in figure 6.4.1.3:

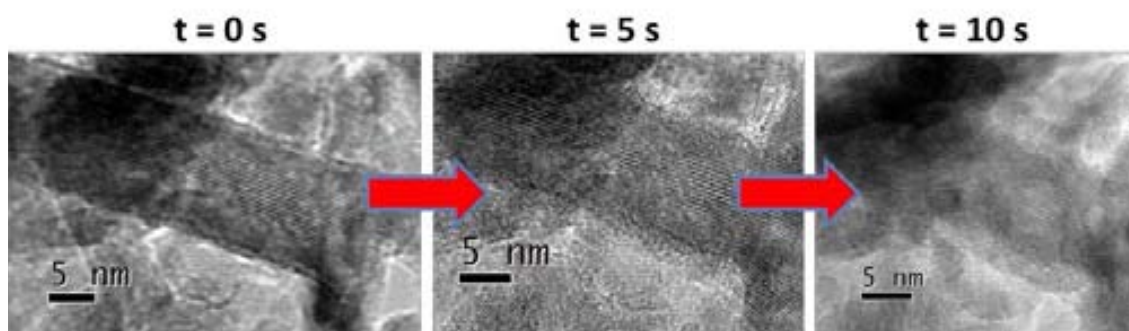


**Figure 6.4.1.3:** HR TEM images showing the goethite-hematite transformation produced by the electron beam effect at different times: 0, 5 and 10 seconds.

This sequence of images shows how the (101) goethite planes that can be identified at  $t=0$  s become less visible at  $t=5$  s and disappear at  $t=10$  s. Apart from the typical goethite planes disappearance, both crystal degradation and hollow formation may be observed.

Once transformed into hematite, the resulting nanorods have also been characterized via analyzing both TEM and HRTEM images. For all the analyzed particles, two main d-spacings of 2,7 Å and 3,7 Å corresponding to hematite planes (104) and (012) respectively, can be identified, as shown in figure 6.4.1.4:

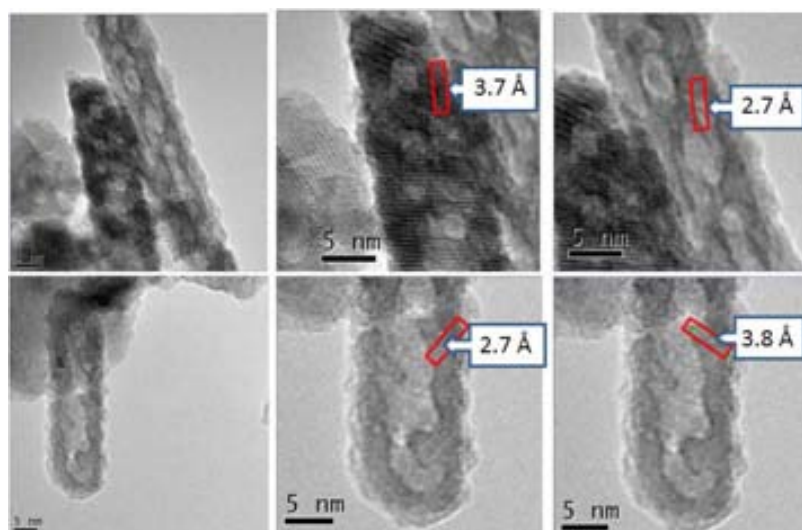


**Figure 6.4.1.4:** TEM images showing the hematite formed nanorods and their hematite-expected d-spacings. Both hollows and degradation effects can be observed.



## 6. Goethite – Hematite nanorods TEM transformation

Via **HRTEM** studies, it has been possible to unequivocally determine the resulting phase of the transformed nanorods via generating Fourier Fast Transformation images, as shown in **figure 6.4.1.5**:

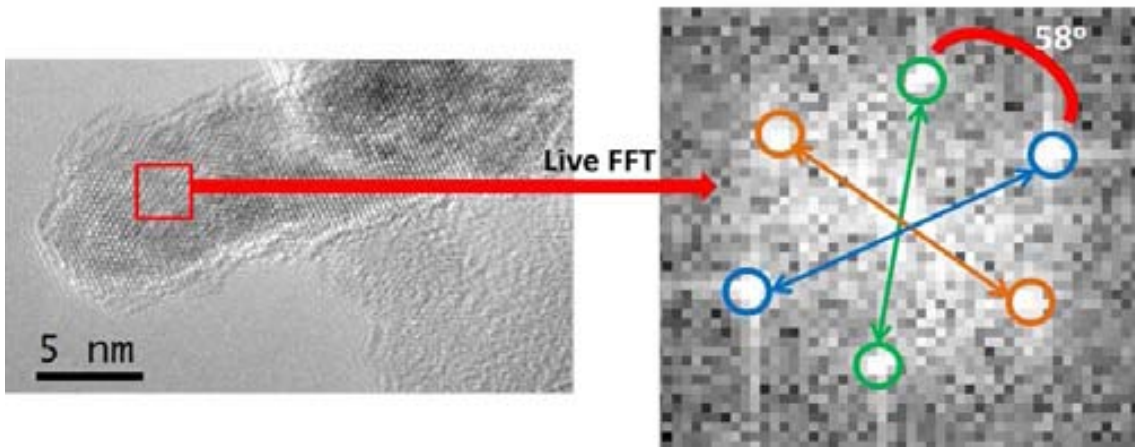


**Figure 6.4.1.5:** HRTEM BF micrograph of a hematite nanorod and the corresponding FFT image taken from the selected zone of the specimen.

By measuring the respective light spot distances from the  $(0\ 0\ 0)$  in the reciprocal space, as well as the angle between the different spots, both  $(1\ 1\ 0)$  and  $(1\ 0\ 4)$  hematite planes corresponding to the blue and green marked signals, respectively, have been identified. Afterwards, the direction in which the electron beam hit the crystal, which is  $(-4\ 4\ 1)$ , has been calculated via applying cross vector, using the two previously obtained planes. The third plane, whose corresponding spot is marked with an orange circle, has been identified as  $(0\ -1\ 4)$  by comparing the FFT image with a theoretical pattern obtained from a simulated hematite structure, shown in **figure 6.4.1.6**:

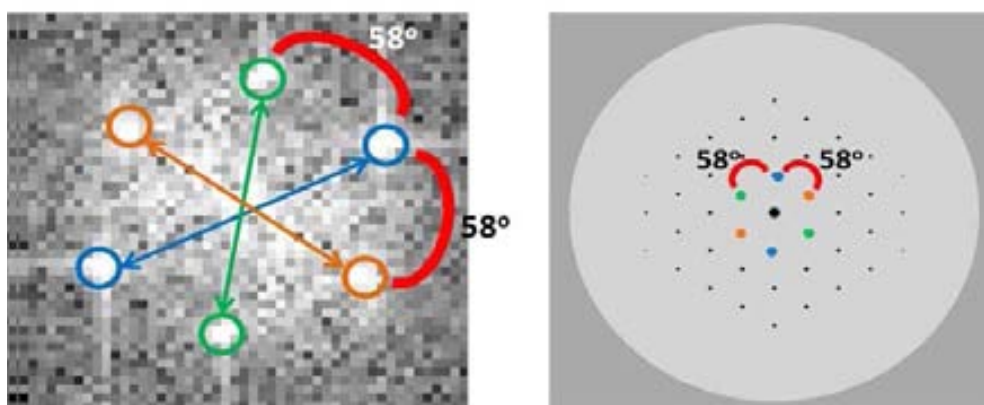


**Figure 6.4.1.6:** Comparison between the obtained FFT (left) and its corresponding simulated pattern (right).

## 6. Goethite – Hematite nanorods TEM transformation

All the planes data observed in this image have been summarized in **table 6.4.1.1**:

	Spot distance from (0 0 0)	Interplanar distance	Plane vector
<b>P1</b>	7.711 1/nm	2.5 Å	(1 1 0)
<b>P2</b>	7.511 1/nm	2.6 Å	(1 0 4)
<b>P3</b>	7,511 1/nm	2.6 Å	(0 -1 4)
	Angle between P1 and P2	58 °	
	Angle between P1 and P3	58 °	
	Direction of the e <sup>-</sup> beam	(-4 4 1)	

**Figure 6.4.1.1:** Data obtained from the FFT corresponding to a single nanorod.

After identifying all the different planes, the orientation of the unitary cell inside the structure has been also studied, showing that its 'z' axis is perpendicular to the length axis of the nanorod, as shown in **figure 6.4.1.7**:

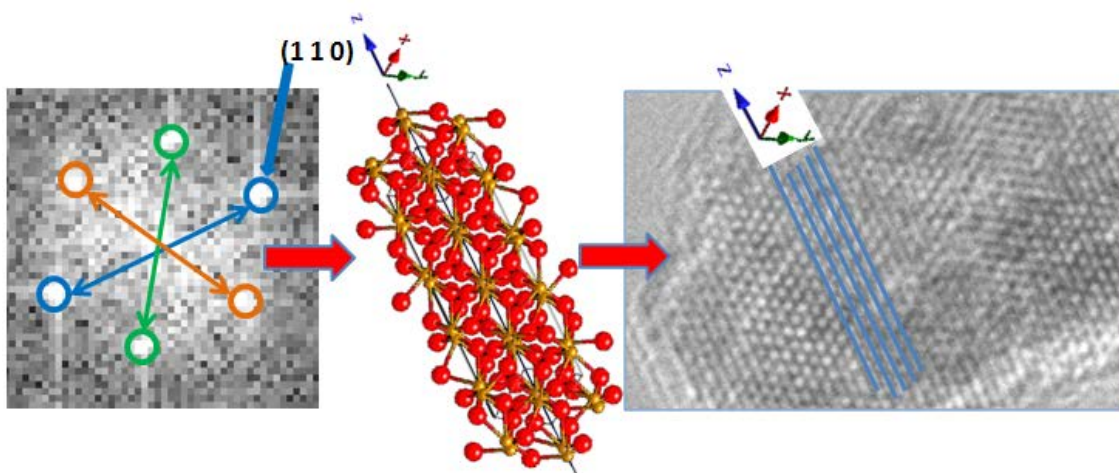


**Figure 6.4.1.7:** Determination of the unitary cell orientation inside the hematite nanorod.

This procedure has been carried out on some nanorods after being transformed by the electron beam effect and in all cases hematite has been confirmed as the resulting crystal structure. However, it has been observed that the orientation of the unitary cell that forms the crystal may vary depending on the nanorod. In **figure 6.4.1.8**, for instance, it can be observed how the crystal that forms the nanorod has the 'z' axis of its unitary cell is oriented parallel to its length axis. This fact suggests that despite the constant relation between the orientation of both goethite and hematite unitary cells reported so far in literature<sup>6</sup> for previous goethite-hematite transformation studies, the nanorods degradation may affect to the final orientation of the crystal forming the particle.

## 6. Goethite – Hematite nanorods TEM transformation

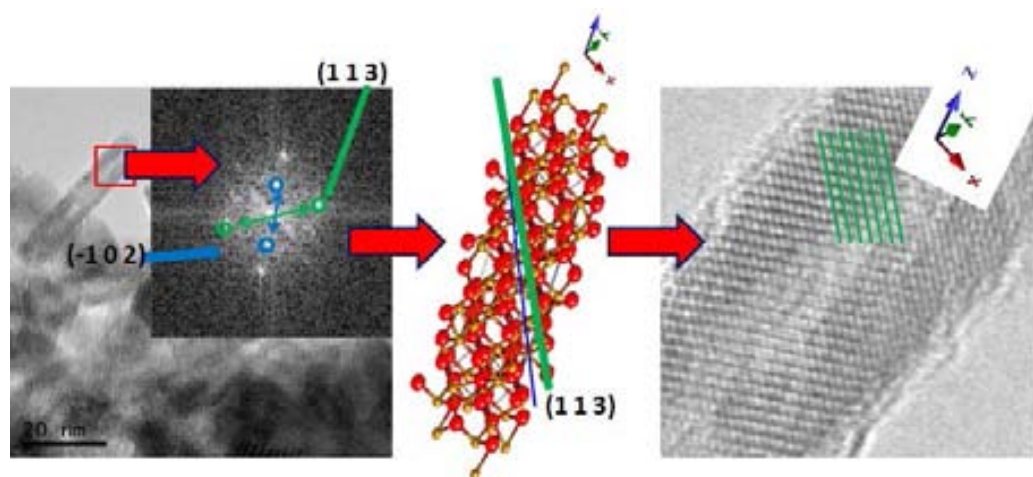


**Figure 6.4.1.8:** Determination of the unitary cell orientation inside another hematite nanorod.

As aforementioned, other kinds of particles have been observed via **BFTEM** analysis apart from goethite nanorods. As it can be observed in **figure 6.4.1.9**, there is a few number of goethite nanoparticles with rectangular or rhombus-like shape that also undergo a degradation process under the effect of the electron beam.

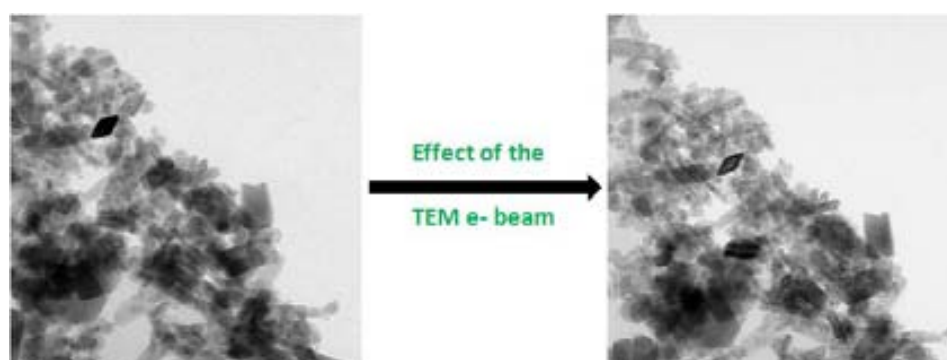


**Figure 6.4.1.9:** BFTEM images showing the transformation process of different-shaped nanoparticles turning from goethite to hematite under the electron beam effect.

Apart from goethite synthesized nanoparticles, the **TEM** study has shown the presence of multishaped nanoparticles that are not affected by the electron beam, which implies that they are not formed by goethite. Given the fact that the black powder resulting from the synthetic procedure show magnetic properties (see section 6.4.4) that don't match with those expected for either goethite or hematite, and according to both electron and X-ray diffraction results, they are formed by magnetite or maghemite. However, since those particles appear mainly forming aggregation clusters, it has been unfeasible to study them via **HRTEM** analysis. Thus, it has been necessary to analyze their crystallographic structure via electron diffraction. **Figure 6.4.1.10** shows a **TEM** image taken from the non-goethite rounded nanoparticles.



## 6. Goethite – Hematite nanorods TEM transformation

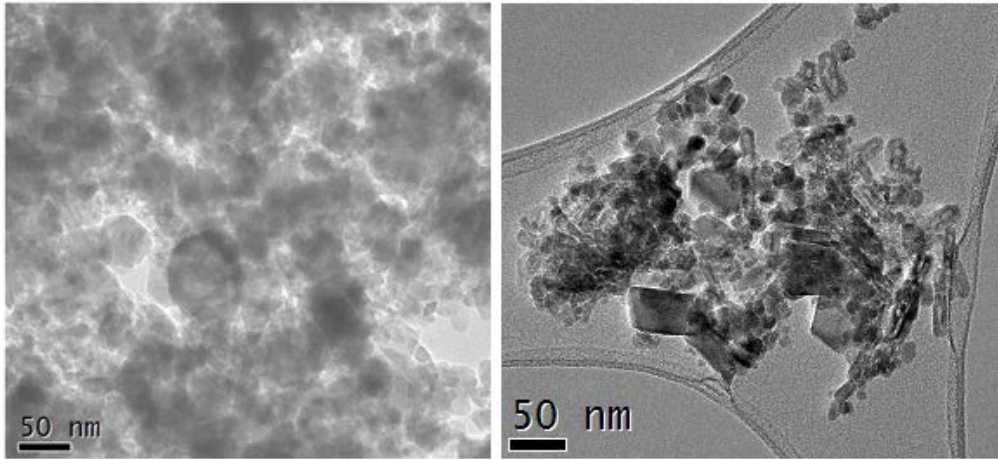


**Figure 6.4.1.10:** Different images showing an attachment of the other kind of not electron beam-sensitive nanoparticles found during the **TEM** analysis of the sample.

As it can be observed in both images, some goethite nanoparticles have been found in all the other kinds of particles attachments.

The results suggest that the synthetic method described in literature leads basically to two different kinds of nanoparticles: goethite nanorods (which turn into hematite under the effect of the electron beam) and magnetite multiple-shaped nanoparticles, which tend to aggregate.

## 6. Goethite – Hematite nanorods TEM transformation

### 6.4.2 Electron and X-ray diffraction

Electron diffraction patterns were obtained on a Philips Tencai 20 at an accelerating voltage of 200 kV. X-ray powder diffraction (XRD) patterns of the samples were recorded with a Rigaku Ddiffractometer equipped with a rotating anode and a  $\text{CuK}\alpha$  source ( $\lambda = 0.154056 \text{ nm}$ ).

The synthesized nanoparticles have been studied taking both X-ray and electron diffraction patterns from the whole obtained product or from specific regions of the prepared specimen, respectively.

X-ray diffraction has been carried out in order to determine all the predominant crystallographic structures in the synthesized product. X-ray patterns have been carried out on different commercial goethite and magnetite samples, as well as on the synthesized nanoparticles, obtaining the diffraction patterns shown in **figure 6.4.2.1**:

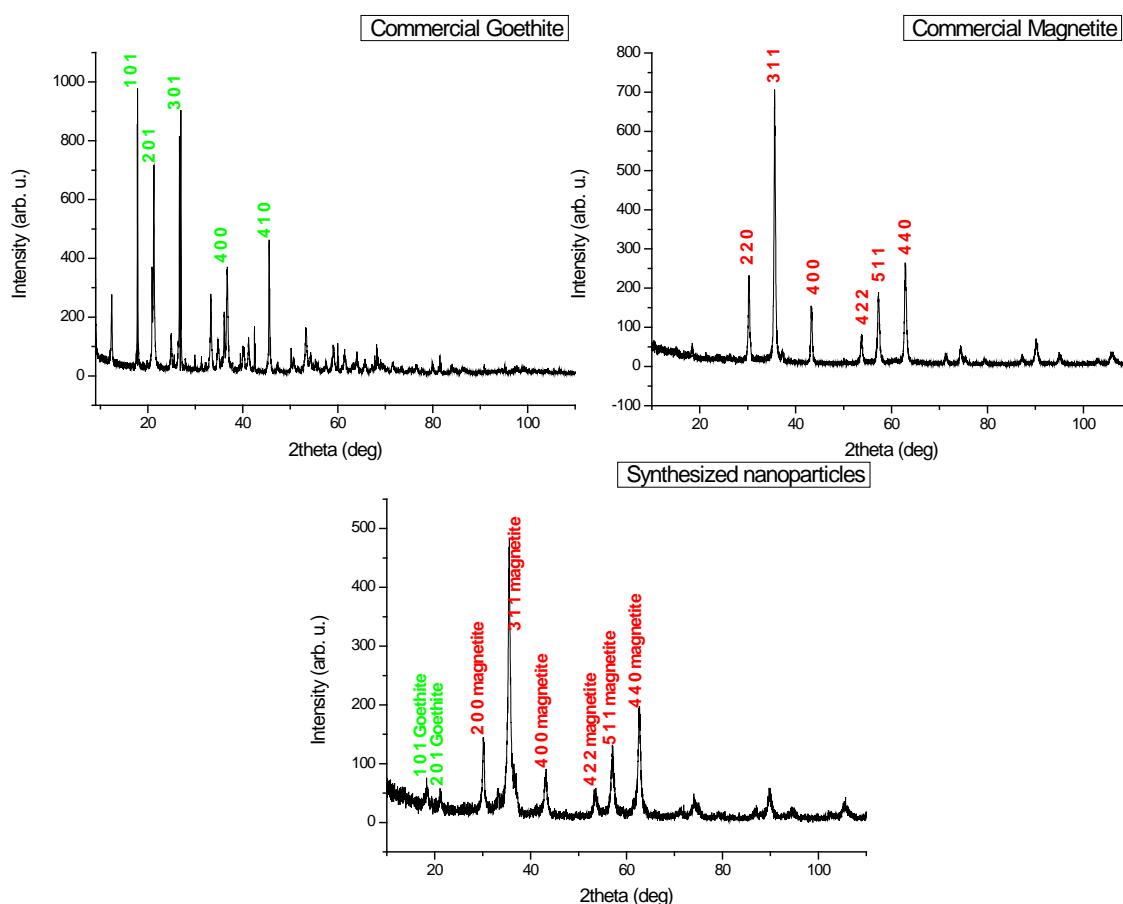


**Figure 6.4.2.1:** Different images showing an attachment of the other kind of not electron beam-sensitive nanoparticles found during the TEM analysis of the sample.

As shown in the figure, there is a mixture of both magnetite and goethite in the prepared sample, since both kinds of peaks may be observed in the complete diffraction

## 6. Goethite – Hematite nanorods TEM transformation

pattern, especially in the case of magnetite. No important hematite peaks, however, have been detected in the sample, which backs the hypothesis that all the hematite found during the **TEM** analyses was the result of the electron beam-induced goethite's 'in situ' transformation.

In the case of electron diffraction, some analyses have been carried out from different parts of the prepared specimen, mainly focusing all efforts in analyzing the crystallographic structure of the electron beam non-sensitive nanoparticles that tend to form aggregates.

Three electron diffraction patterns taken from different regions of the specimen are shown in **figure 6.4.2.2**:

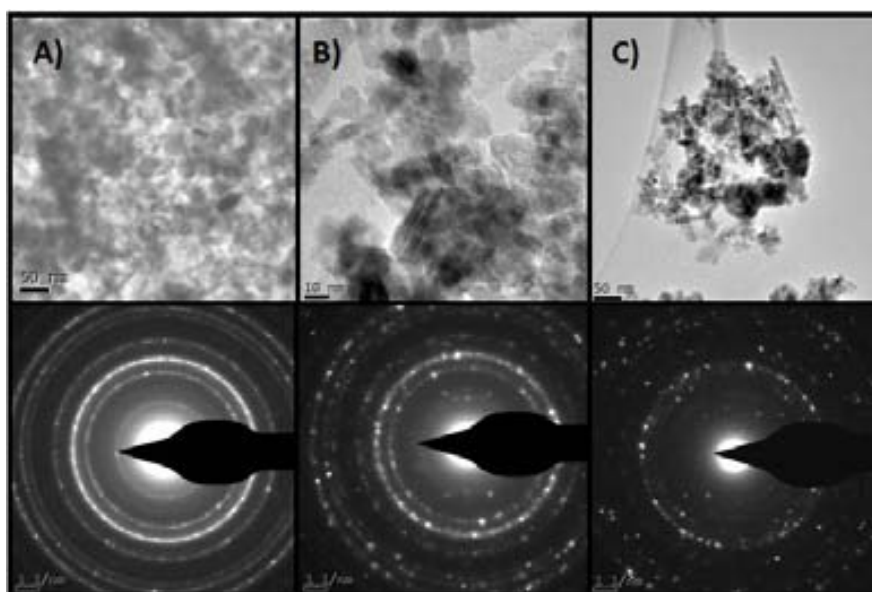


**Figure 6.4.2.2:** Bright field **TEM** images of A) a region with aggregated nanoparticles, B) a region with less aggregated nanoparticles mixed with visible goethite nanorods and C) a region only with hematite nanorods.

In both A) and B) cases, the found planes match with those expected for magnetite and hematite crystal structures. Particularly in A), the signals corresponding to magnetite planes appear much more intense in the diffraction pattern than those corresponding to hematite. In the case of C), however, the hematite planes predominate clearly. That fact suggests that the irregular nanoparticles that form the aggregates are indeed formed by magnetite or maghemite. On the other hand, no goethite planes have been found in any electron diffraction pattern due to the fact that all particles have been transformed when carrying on the diffraction procedure.

## 6. Goethite – Hematite nanorods TEM transformation

**Table 6.4.2.1** shows all the different planes obtained via electron diffraction from different regions of the analyzed specimen:

Crystallographic structure	Interplanar distance	Plane family
Magnetite (or maghemite)	2,95 Å	(2 2 0)
	2,87 Å	(1 1 1)
	2,51 Å	(3 1 1)
	2,09 Å	(4 4 0)
	1,70 Å	(4 2 2)
	1,61 Å	(5 1 1)
	1,46 Å	(4 4 0)
Hematite	3,85 Å	(0 1 2)
	2,20 Å	(1 1 3)
	1,82 Å	(0 2 4)

**Figure 6.4.2.1:** Different planes found in the obtained electron diffraction patterns.

The results obtained via both X-ray and electron diffraction are in agreement with those obtained when carrying out **TEM** and **HRTEM** microscopy analyses, since they confirm the presence of magnetite (or maghemite) and goethite in the X-ray patterns that have been transformed into hematite when focusing the electron beam when performing electron diffraction. It has also been confirmed that the observed aggregates are mainly formed by attached magnetite (or maghemite) nanoparticles with a few goethite nanorods ‘trapped’ inside the particle aggregates.

### 6.4.3 Mössbauer spectroscopy

<sup>57</sup>Fe Mössbauer spectra were obtained with conventional Mössbauer spectrometers in the constant acceleration mode. The sources were <sup>57</sup>Co in Rh and a foil of  $\alpha$ -Fe was used for calibration of the spectrometer at room temperature. Spectra obtained at temperatures between 80 K and room temperature were recorded in a liquid nitrogen cryostat. Spectra obtained between 20 and 80 K were recorded in a closed cycle helium refrigerator. All the spectra were recorded in a zero magnetic field. Mössbauer spectroscopy has been carried out in order to identify and quantify all the different iron species in the synthesized product. The spectrum acquired at low temperature (20 K) consists of a sextet with relatively narrow lines; meanwhile the spectrum acquired at room temperature (295 K) becomes more complex, showing multiple signals that correspond to a mixture formed by a 60 % of magnetite and a 40 % of goethite. Both different spectra are shown in **figure 6.4.3.1**:

## 6. Goethite – Hematite nanorods TEM transformation

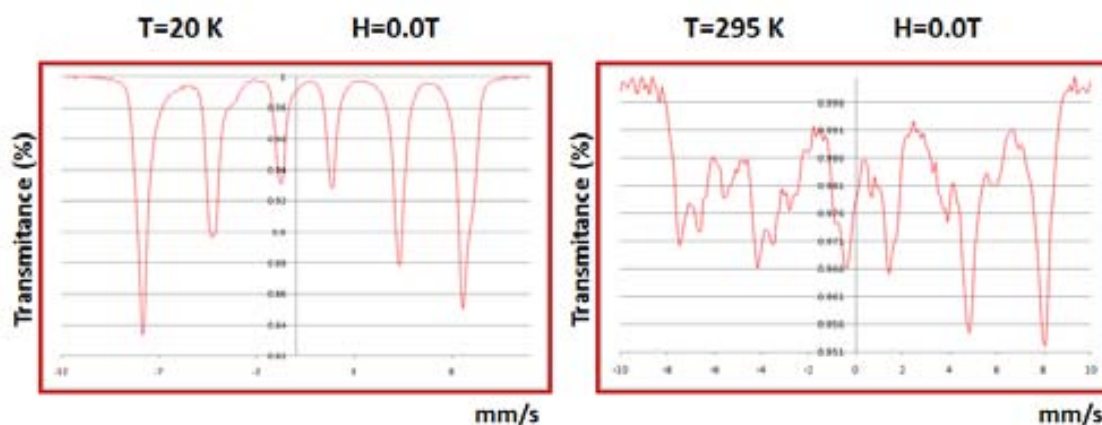


**Figure 6.4.3.1:** Mössbauer spectra obtained at 20 K (left) and at 295 K (right) in a zero magnetic field.

The results are in agreement with those obtained via X-ray diffraction as well as all the previous described results, showing that the carried out synthetic procedure leads to a mixture of magnetite and goethite nanoparticles. Given the fact that no hematite signals have been found neither via X-ray diffraction nor Mössbauer spectroscopy, it may be concluded that all the hematite found when performing **TEM** and electron diffraction analysis is ‘in situ’ synthesized by the effect of the electron beam.

### 6.4.4 Magnetic measurements (SQUID, FC-ZFC and Electron holography)

Magnetic properties of the resultant reaction mixture have been measured on a SQUID magnetometer. Hysteresis loops measurements have been performed up to 70 KOe at 10 K.

Phase images have been obtained FEI Titan 80 -300 field-emission-gun TEM operated at 300 kV and treated using a special software called “Semper”.

**Figure 6.4.4.1** shows the magnetic hysteresis loop at 10 K taken from the resulting powder obtained via the described synthetic method. As it can be seen, the synthesized nanoparticles present a clear magnetic response, whose coercivity field has a value of 0,6 kOe, which means that not all the particles that form the sample are superparamagnetic, making necessary a magnetic study at nanometric scale.

## 6. Goethite – Hematite nanorods TEM transformation

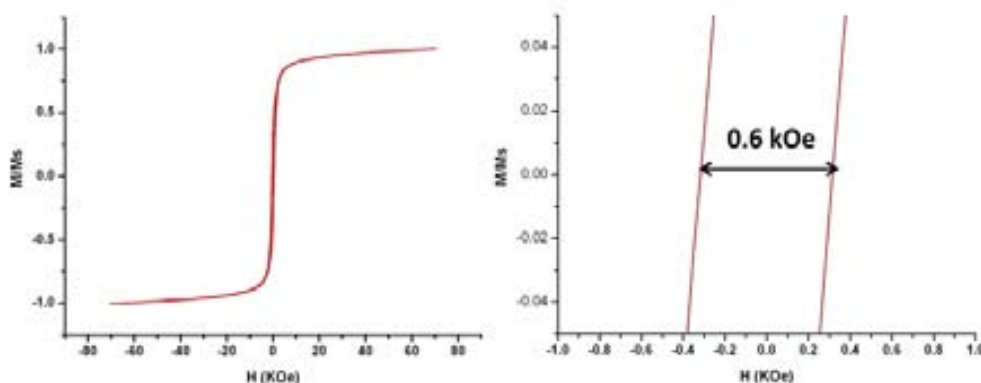


**Figure 6.4.4.1:** Magnetic hysteresis loop taken from the synthesized nanoparticles powder (left) and enlargement from the central region of the hysteresis loop showing a remanent coercivity field (right)

Concurrently to macroscopic magnetic studies, electron holography has been performed so as to study the magnetic behaviour of the different particles separately. **Figure 6.4.5.1**, shows the Bright-Field TEM images of goethite nanorods and its corresponding phase image:

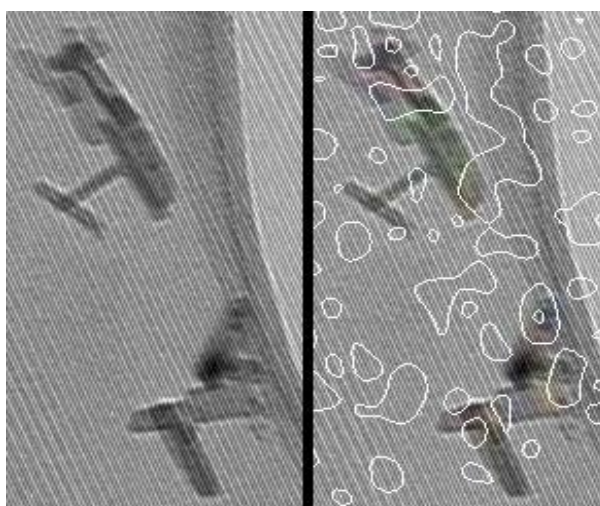


**Figure 6.4.5.1:** BF amplitude image taken from isolated nanorods (left) and phase image taken from the same region.

As it may be observed, nanorods show no response to the magnetic field applied during the technique performance. That happens because neither goethite nor hematite have magnetization levels high enough to generate any response to the technique, since they both are antiferromagnetic materials. Magnetite/maghemite nanoparticles, on the other hand, clearly present magnetic response to the applied field, as shown in **figure 6.4.5.2**:

## 6. Goethite – Hematite nanorods TEM transformation

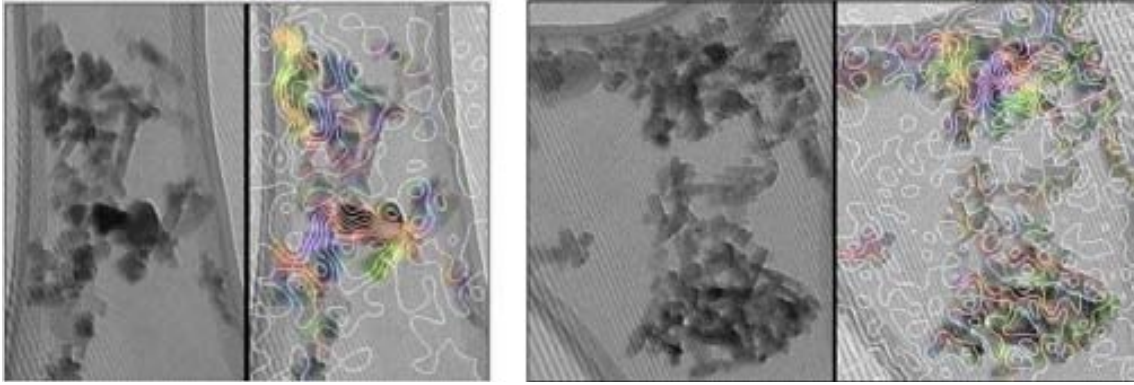


**Figure 6.4.5.2:** Amplitude and phase images of two different regions of the specimen with both nanorods and magnetite/maghemite nanoparticles attached to them.

The magnetic signal obtained when treating these images is  $\Phi = 0,042$  rad/spacing, and the calculated magnetization value obtained from the magnetically active nanoparticles is 0.54 T, which matches with the theoretical value of magnetite, 0.60 T and overtakes the theoretical value of maghemite, 0.2 T. Therefore, and despite the possible interferences that may arise from the carbon grid and the surrounding goethite nanorods, it can be concluded that the particles found apart from the described nanorods are formed by magnetite.



## 6. Goethite – Hematite nanorods TEM transformation

### 6.4.5 Energy-dispersive X-ray spectroscopy (EDX)

Energy-dispersive X-ray spectra have been obtained at 200 kV using Titan and FEI Tecnai F20 field emission gun (FEG) TEMs.

All the acquired spectra have been taken from three different kinds of specimen regions:

- Regions showing magnetite nanoparticle aggregates.
- Regions showing isolated (or partially mixed with magnetite nanoparticles) goethite nanorods.
- Regions showing no nanoparticles.

Figure 6.4.5.1 shows a representative spectrum obtained from each kind of region:

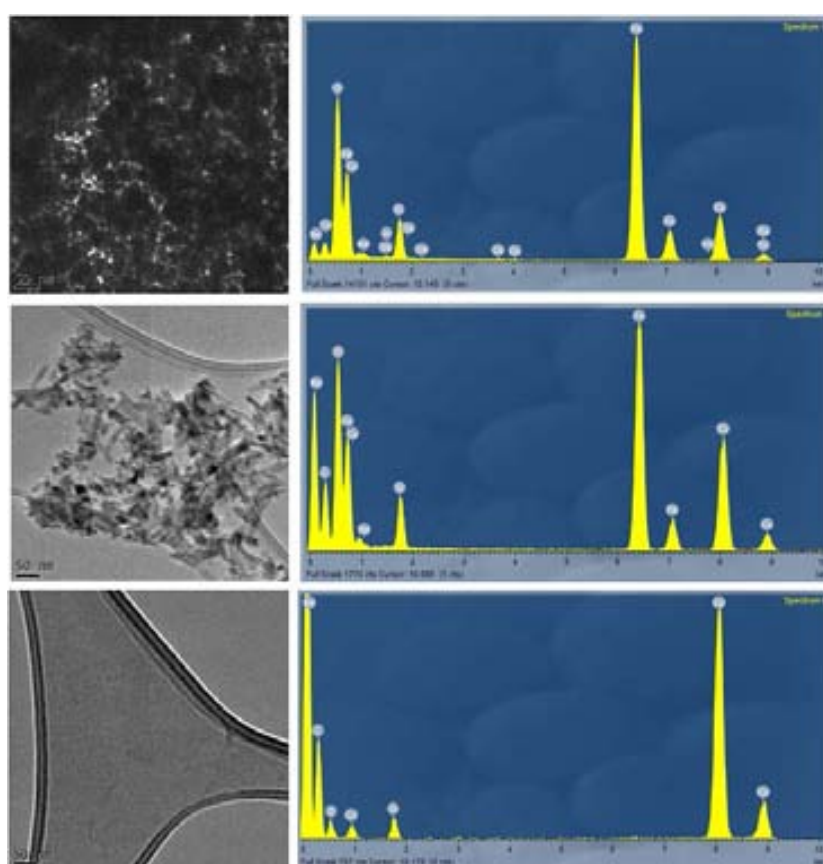


**Figure 6.4.5.1:** Representative spectra acquired from different regions of the specimen.

Intensity peaks corresponding to Be, C, Cu, Fe, O and Si have been found and quantified when analyzing the specimen. In all cases, as expected, the signals corresponding to C, Be and Cu have been obtained because of the grid in which the specimen has been prepared. Therefore, they have been omitted from the specimen



## 6. Goethite – Hematite nanorods TEM transformation

analysis, focusing just in Fe, O and Si signals, whose relative amounts are shown in table 6.4.5.1:

	Fe (Atomic %)	O (Atomic %)	Si (Atomic %)
<b>Magnetite aggregates</b>	14.4 ± 2.7	61.2 ± 2.1	3.7 ± 0.9
<b>Goethite nanorods</b>	5.3 ± 1.5	40.8 ± 5.0	1.6 ± 0.4
<b>Particles-free regions</b>	0.1 ± 0.1	12.9 ± 1.4	1.3 ± 0.4

**Table 6.4.5.1:** Relative amounts (in atomic %) of Fe, O and Si found in different regions of the specimen.

As it may be observed, the amounts of both iron and oxygen increase significantly when analyzing regions with goethite nanorods or magnetite aggregates, especially in the case of the attached magnetite regions, in which the nanoparticle density is higher. This result is in agreement with the fact that both goethite and magnetite are iron oxides. The O/Fe ratio, on the other hand, does not match neither with the stoichiometric ratio expected for goethite, FeOOH (2O/1Fe) nor for the ratio expected for magnetite, Fe<sub>3</sub>O<sub>4</sub> (4O/3Fe). In fact, the oxygen/iron ratio is always higher than the expected for those iron oxides and it changes depending on the specimen region. This fact, as well as the presence of almost an atomic 13 % of oxygen in the regions with no particles, suggests that there is oxygen in the sample that does not form part of the nanoparticles structure; it possibly comes from O<sub>2</sub>, H<sub>2</sub>O or CO<sub>2</sub> molecules attached to the carbon grid or adsorbed on the nanoparticles.

Another important piece of information arises when analysing the silicon found in the sample. Given the fact that none of the used reactants has silicon, its presence can only be explained by a degradation of the glass vessel in which the reaction was carried out. Since it was repeated several times at a basic pH (= 10,5), heating and stirring the reaction mixture under pressure during 20 hours, it is likely that a part of the inner wall of the vessel may have been affected. However, as it can be seen in all cases, silicon has been found in all the analyzed regions, and its atomic percentage barely increases when studying a region with nanoparticles. This fact suggests that silicon is likely dispersed in the aqueous medium with the nanoparticles and not inside them.

So as to study the elemental distribution in the specimen, energy filtered transmission electron microscopy (EFTEM) has also performed on the same specimen.

## 6. Goethite – Hematite nanorods TEM transformation

### 6.4.6 Energy Filtered Transmission Electron Microscopy (EFTEM)

Different elemental maps have been obtained at 200 kV using Titan and FEI Tecnai F20 field emission gun (FEG) TEMs.

Iron, oxygen, carbon and silicon maps, as well as the **BFTEM** image corresponding to the same region of the analyzed specimen are shown in **figure 6.5.5.1**:

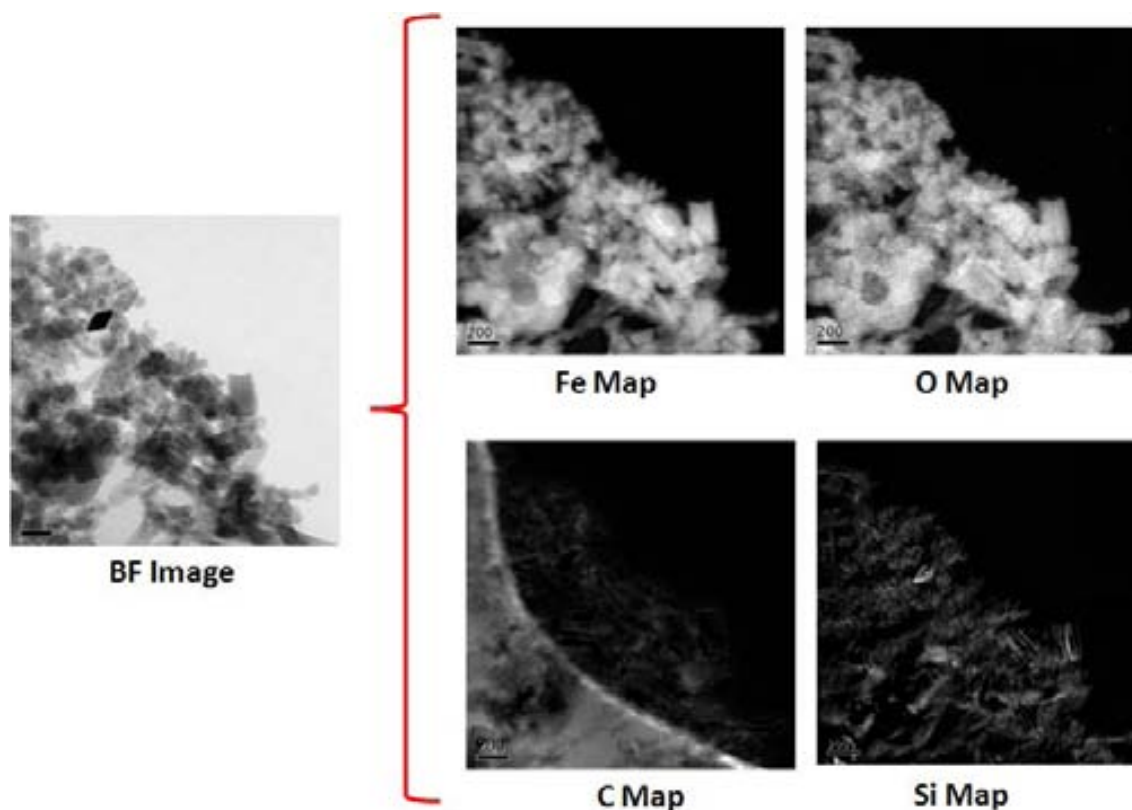


**Table 6.4.5.1:** BF and EF TEM images taken from a region of the specimen with goethite nanoparticles.

It can be clearly deduced by comparing the **BF** image with the iron and oxygen maps that the main parts of the particles are indeed formed by both Fe and O, as expected for iron oxide nanoparticles. Carbon map, on the other hand, shows its more intense signal at the left part of the image, corresponding to the carbon grid that supports the nanoparticles. It also shows that nanoparticles are surrounded by a thin shell of carbon, which is likely formed by the ethylenediamine used as a capping agent during the synthetic procedure. Silicon also seems to be surrounding but not forming the nanoparticles, since no homogeneous distribution may be observed in the crystal structures. On the contrary, it seems to be attached to some crystallographic defects or to the rims of some nanoparticles. This data, as well as the obtained via performing **EDX**, suggests that silicon is dispersed in the aqueous medium with the nanoparticles, but not forming part of their crystal structure.

## 6. Goethite – Hematite nanorods TEM transformation

### 6.4.7 Nanorods synthetic procedure carried out using $[\text{Fe}_3\text{O}(\text{OCOCH}_3)_6(\text{H}_2\text{O})_3]\cdot\text{NO}_3$ as a source of iron (III) and without adding any source of iron (II)

The synthetic procedure described in **section 6.2.3** was carried out as an attempt to obtain isolated goethite nanorods, avoiding the formation of magnetite without adding iron (II) to the medium. After performing **TEM** analyses to the resulting nanoparticles, two different kinds of particles were observed, as shown in **figure 6.4.7**:

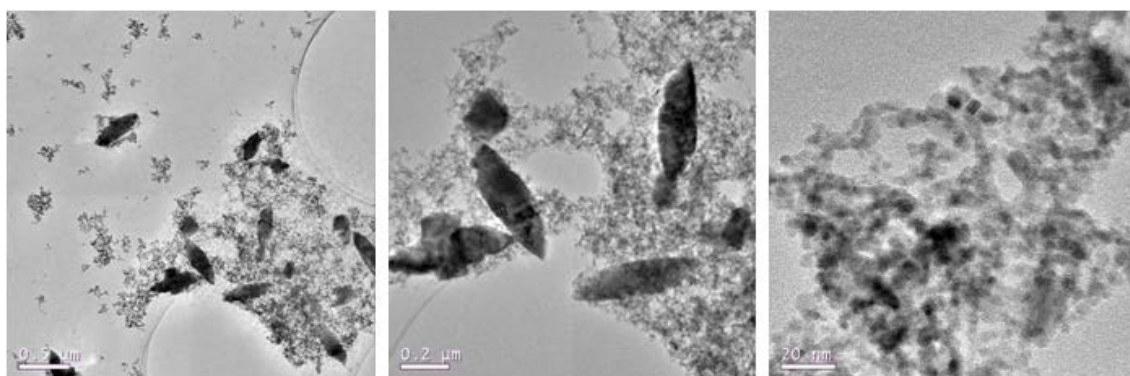


**Figure 6.4.7.1:** BFTEM images taken from the modified synthetic procedure described in **section 6.2.3**.

All images show rod-like nanoparticles with a wide average length of  $378 \pm 185$  nm and a relatively narrow average width of  $148.0 \pm 20.9$  nm. In all cases those particles are surrounded by smaller ones with an average size of  $5.1 \pm 1.2$  nm.

In order to determine the crystalline structure of both kinds of nanostructures, **HR-BFTEM** microphotographs were taken and analyzed via obtaining local **FFT** images, which are shown in **figure 6.4.7.2**. This study resulted hindered by the fact that all the regions of the sample resulted to contain very concentrated regions of nanoparticles for performing such a study, and moreover they were covered by the smaller particles mentioned before. Those tiny structures, which appear all around the prepared **TEM** grid (regions yellow encircled in the figure), could be studied and characterized more in depth. Displayed in the figure some examples of these particles may be found oriented along different zone axes, showing a crystalline structure compatible with maghemite,  $\gamma\text{-Fe}_2\text{O}_3$ , and incompatible with other  $\text{Fe}_2\text{O}_3$  species, such as goethite or hematite. In this case, it may be assured with no doubt that the obtained crystallographic structure of the smaller particles is maghemite and not magnetite, since neither any source of iron (II) nor any reducing agent had been added to the reaction medium.

## 6. Goethite – Hematite nanorods TEM transformation

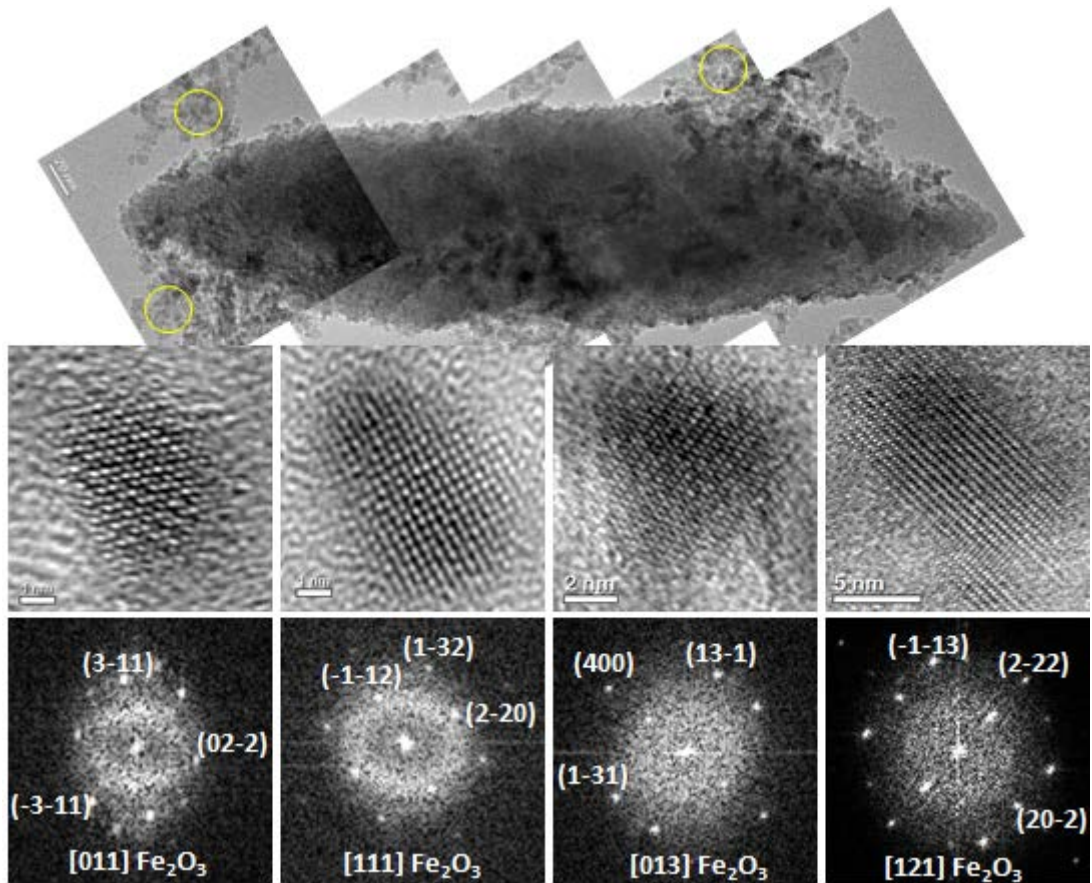


**Figure 6.4.7.2:** HRTEM images taken from the obtained nanostructures via modifying the original nanorods synthetic procedure.

### 6.5 Summary

In this work, goethite nanorods have been synthesized via a hydrothermal method using a source of iron III and ethylenediamine in an aqueous medium. After analyzing the obtained product via different characterization techniques, it has been found that it is formed by:

- Goethite nanorods.
- Magnetite multi-shaped nanoparticles forming big aggregates.

The whole prepared specimen has been studied via advanced **TEM** techniques, such as **HRTEM** analysis, **EFTEM** images and electron holography, as well as macroscopic techniques, like Mössbauer spectroscopy, X-Ray diffraction and magnetic **SQUID** and **FC-ZFC** studies.

As a result of this characterization, it has been observed that, by the effect of the **TEM** electron beam, goethite nanorods undergo a transformation into hematite nanorods. During this process, crystal degradation takes place.

It has been therefore concluded that the synthetic procedure described in literature does not lead to magnetite nanorods, as it has been claimed by Dong Q., et al., but to goethite nanorods and magnetite multi-shaped nanoparticles that tend to aggregate themselves. In this vein, the **TEM** images that they show in their manuscript actually correspond to the formed goethite nanorods, and the magnetic results they carried out in the work, which resulting data match with magnetite, come from the magnetite aggregates generated during the synthetic procedure.

### 6.6 Related literature:

---

- <sup>1</sup> Dong Q., Kumada N.; Yonesaki Y.; Takei T.; Kinomura N., *J. Ceram. Soc. Jpn.*, **2009**, 117, 881-886.
- <sup>2</sup> Yao S.; Liu J.; Han Q., *Acta Crystallogr., Sect. E: Struct. Rep. Online*, **2008**, E64, m989.
- <sup>3</sup> Bideaux J. W.; Bladh K. W.; Nichols Anthony M.C., *Handbook of Mineralogy: Halides, Hydroxides, Oxides*, Mineral Data Pub., **1997**.
- <sup>4</sup> Jha D. K.; Sameen M.; Patel A.B.; Kostka A.; Schneider P.; Erbe A.; Deb P., *Mat. Lett.*, **2013**, 95, 186-189.
- <sup>5</sup> Anteneh B.; Karsten M., *Drug Dev. Ind. Pharm.*, **2013**, 39, 186-196.
- <sup>6</sup> Gualtieri A. F.; Venturelli P., *Am. Mineral.*, **1999**, 84, 895-904.
- <sup>7</sup> Madsen D. E.; Cervera-Gontard L.; Kasama T.; Dunin-Borkowski R.E.; Koch C.B.; Hansen M.F.; Frandsen C.; Moerup S., *J. Phys.: Condens. Matter.*, **2009**, 21, 016007/1-016007/11.
- <sup>8</sup> Yue J.; Jiang X.; Yu A., *Solid State Sci.*, **2011**, 13, 263-270.
- <sup>9</sup> Almeida T. P., *Cryst. Eng. Comm.*, **2010**, 12, 1700-1704.
- <sup>10</sup> Almeida T.; Fay M.; Zhu Y.; Brown P.D., *J. Phys. Conf. Ser.*, **2010**, 241, 012087/1-012087/4.

# Chapter 7

## Synthesis and characterization of Fe<sub>3</sub>O<sub>4</sub>@Au Core-Shell structures

### Contents

---

7.1 General description of the carried out work.....	193
7.1.1 Water-dispersible Fe <sub>3</sub> O <sub>4</sub> @Au Core-Shell structures.....	193
7.1.2 Organic media-dispersible Fe <sub>3</sub> O <sub>4</sub> @Au Core-Shell structures.....	194
7.2 Basic information about the most relevant works related to Fe <sub>3</sub> O <sub>4</sub> @Au described in literature.....	195
7.3 Experimental procedure.....	199
7.3.1 Materials and reactants.....	199
7.3.2 Water-dispersible core-shell structures.....	199
7.3.2.1 Synthesis of Tetramethylammonium hydroxide (TMAOH)-capped Fe <sub>3</sub> O <sub>4</sub> nanoparticles.....	199
7.3.2.2 Synthesis of Hexa- $\mu_2$ -acetato-triaqua- $\mu_3$ -oxo-triiron (III) nitrate acetic acid solvate, [Fe <sub>3</sub> O(OCOCH <sub>3</sub> ) <sub>6</sub> (H <sub>2</sub> O) <sub>3</sub> ] $\cdot$ NO <sub>3</sub> .....	199
7.3.2.3 Hydrothermal synthesis of hydrazine (NH <sub>2</sub> NH <sub>2</sub> )- capped Fe <sub>3</sub> O <sub>4</sub> nanoparticles.....	200
7.3.2.4 Synthesis of 1,6-hexanediamine (H <sub>2</sub> N(CH <sub>2</sub> ) <sub>6</sub> NH <sub>2</sub> )- capped Fe <sub>3</sub> O <sub>4</sub> nanoparticles using FeSO <sub>4</sub> as an iron source.....	200
7.3.2.5 Synthesis of 1,6-hexanediamine (H <sub>2</sub> N(CH <sub>2</sub> ) <sub>6</sub> NH <sub>2</sub> )- capped Fe <sub>3</sub> O <sub>4</sub> nanoparticles using FeCl <sub>2</sub> as an iron source.....	200
7.3.2.6 Formation of the gold shell around the previously synthesized magnetite cores.....	201

7.3.2.7 Gold nanoparticles formation with HAuCl <sub>4</sub> and NH <sub>2</sub> OH·HCl.....	201
7.3.3 Organic media-dispersible core-shell structures.....	201
7.3.3.1 Solvothermal synthesis of toluene colloidal dispersion of Fe <sub>3</sub> O <sub>4</sub> magnetite nanoparticles.....	201
7.3.3.2 Formation of the gold shell around the previously synthesized Fe <sub>3</sub> O <sub>4</sub> @Oleylamine cores in toluene medium.....	202
7.3.3.3 Formation of the gold shell around the previously synthesized Fe <sub>3</sub> O <sub>4</sub> @Oleylamine cores in oleylamine medium.....	202
7.3.3.4 Synthesis of oleylamine capped- gold nanoparticles.....	202
7.4 Characterization and results discussion.....	203
7.4.1 Organic media-dispersible Fe <sub>3</sub> O <sub>4</sub> @Au using Fe <sub>3</sub> O <sub>4</sub> @Oleylamine as a core.....	203
7.4.2 Water-dispersible Fe <sub>3</sub> O <sub>4</sub> @Au using Fe <sub>3</sub> O <sub>4</sub> @TMAOH as a core.....	206
7.5 Summary.....	213
7.6 Related literature.....	214



## 7. Synthesis and characterization of Fe<sub>3</sub>O<sub>4</sub>@Au Core-Shell structures.

This chapter explains the different synthetic procedures carried out with the aim of obtaining Fe<sub>3</sub>O<sub>4</sub>@Au core-shell nanostructures, as well as the characterization of the obtained nanoparticles, mainly performed via **TEM** techniques. It is mandatory to say that, despite performing some different synthetic routes, it has not been possible to obtain clear evidences showing that the desired core-shell nanostructures have been obtained.

The discussion of the data obtained when carrying out the synthesized nanoparticles characterization is explained in detail in this chapter.

### 7.1 General description of the carried out work

Water or organic media dispersible Fe<sub>3</sub>O<sub>4</sub>@Au core-shell nanostructures have been tried to obtain via some different methodologies, which are all based on previously synthesized magnetite nanoparticles that will form the nuclei of the resulting core-shell, and surrounding them with a gold shell by reducing gold ions on their surface.

Depending on the synthetic procedure, different kinds of magnetic nanoparticles with different properties (such as size, coating agents and dispersibility) have been produced in order to obtain the desired core-shells. The used gold source, on the other hand, has always been tetrachloroauric acid, HAuCl<sub>4</sub>, which supplies Au (III) cations to the medium.

Basically, all the performed synthetic routes may be classified in those focused in obtaining water-dispersible or organic media-dispersible core-shell structures:

#### 7.1.1 Water-dispersible Fe<sub>3</sub>O<sub>4</sub>@Au Core-Shell structures

Those kinds of gold-capped iron oxide nanoparticles have been attempted to synthesize via modifying a method described in the literature that presumably leads to Fe<sub>3</sub>O<sub>4</sub>@Au core-shells. This method is based on using previously synthesized water-dispersible Fe<sub>3</sub>O<sub>4</sub> nanoparticles and capping them with gold via HAuCl<sub>4</sub> reduction by using sodium citrate: Na<sub>3</sub>C<sub>6</sub>H<sub>5</sub>O<sub>7</sub>, and hydroxylamine hydrochloride: NH<sub>2</sub>OH·HCl. In order to study this synthetic procedure and to obtain proper core-shell structures with different core and shell sizes, various kinds of magnetite nanoparticles have been synthesized and 'surrounded' by gold via this methodology. The relative amounts of gold and hydroxylamine have been also modified in order to optimize the synthetic method.

Figure 7.1.1 shows the basics of the synthetic methodology carried out in aqueous media:

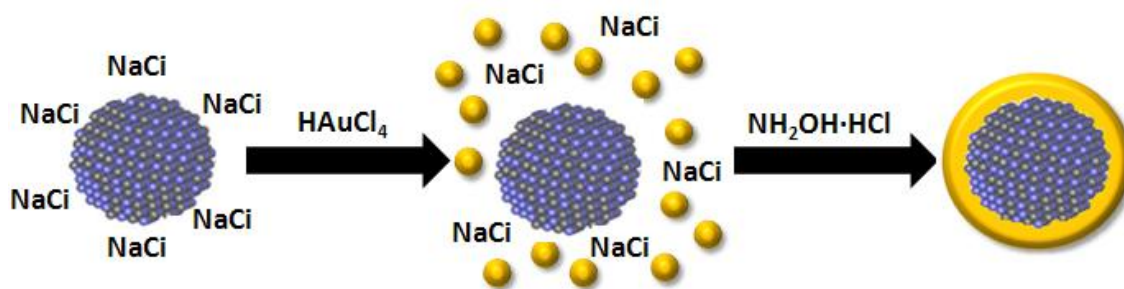


**Figure 7.1.1:** General steps followed when carrying out every attempt to form the Fe<sub>3</sub>O<sub>4</sub>@Au core-shell structures in aqueous media.

### 7.1.2 Organic media-dispersible Fe<sub>3</sub>O<sub>4</sub>@Au Core-Shell structures

By taking advantage of the oleylamine-capped iron oxide nanoparticles synthesized in chapter 5, which are dispersible in both hexane and toluene, it has been tried to form the desired core-shell structures by transferring the Au<sup>3+</sup> ions (which come from HAuCl<sub>4</sub>) from water to toluene and to reduce them on the surface of the previously obtained Fe<sub>3</sub>O<sub>4</sub>@Oleylamine nanoparticles via different methods, such as using NaBH<sub>4</sub> or even using oleylamine as reducing agents. Figure 7.1.2 shows the basics of the synthetic methodology carried out in organic (toluene) media:

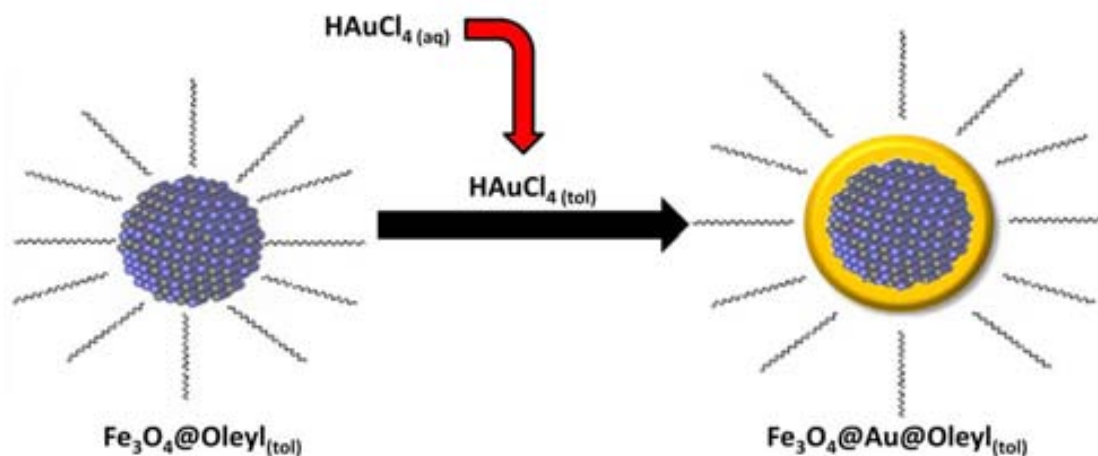


**Figure 7.1.2:** Basics of the synthetic methodology carried out when working in toluene media.

As aforementioned, despite the fact that we have not been able to synthesize core-shell structures properly synthesized so far neither in aqueous nor in organic media, some interesting data have been obtained during this study. Thus, it has been consequently explained and analyzed in detail during this chapter.

## 7.2 Basic information about the most relevant works related to Fe<sub>3</sub>O<sub>4</sub>@Au described in literature

As aforementioned, coating magnetite nanoparticles with a gold shell allows combining the advantages of both kinds of materials, which provides a large amount of potential applications, such as developing sensors and other analytical methods<sup>1,2</sup>, protein separation<sup>3</sup> or biomedical applications<sup>4,5</sup>. With this aim, a large number of works have been published recently offering different synthetic routes to obtain gold-coated magnetic nanoparticles.

However, and despite all the different methods described so far, most of them do not provide enough evidences to conclude that the desired core-shell structures have been successfully obtained.

First of all, it must be mentioned that in spite of being cubic both of them, magnetite and gold have two different kinds of unitary cell structures, as shown in figure 7.3.1:

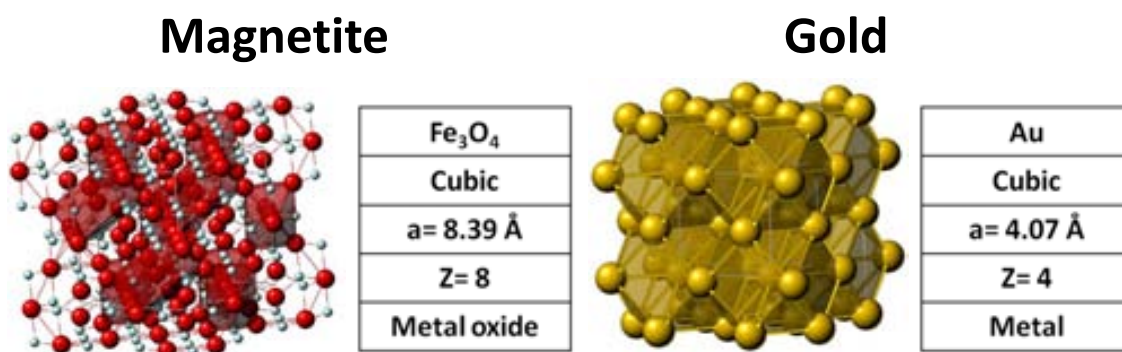


**Figure 7.2.1:** Image showing the cubic crystallographic structure of both magnetite and gold, as well as their main structural characteristics.

As it can be seen, magnetite is a metal oxide; meanwhile gold is a metal. Since they have different properties, such as different surface energies<sup>6</sup>, it becomes challenging to cover magnetite with gold, because it tends to nucleate rapidly forming discrete nanoparticles in solution without coating the magnetite surface.

Given the difficulty of forming proper Fe<sub>3</sub>O<sub>4</sub>@Au structures, some different approaches have been described (either in aqueous or in organic media) in literature to attach both gold and magnetite in different ways. *J. Bao, et al.*<sup>7</sup>, for instance, synthesized Fe<sub>3</sub>O<sub>4</sub>-Au structures via using a ligand as a chemical bond linkage between the two different kinds of particles. Similar works, reported by *L. Lou*<sup>8</sup> and *J. Ren*<sup>9</sup> synthesized magnetite nanoparticles capped by ethylene glycol (EG) and polyethyleneimine (PEI), respectively, and attached gold nanoparticles on their

surfaces, synthesizing Fe<sub>3</sub>O<sub>4</sub>-Au pseudo core-shells or heterodimer structures, as shown in **figure 7.2.2**:

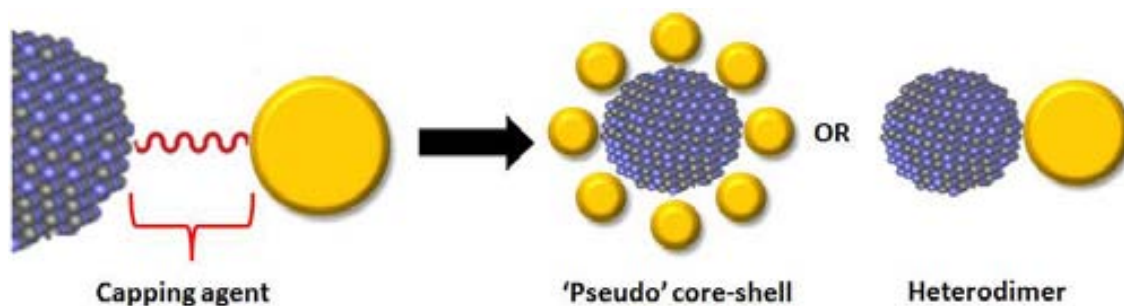


**Figure 7.2.2:** Fe<sub>3</sub>O<sub>4</sub>-Au ‘pseudo’ core-shell and heterodimer structures described in literature.

Both kinds of magnetite-gold structures have been synthesized and fully characterized via microscopic and non-microscopic techniques. In all cases, **TEM** images show clear evidence of those kinds of structures formation. It becomes more problematic, however, to synthesize actual Fe<sub>3</sub>O<sub>4</sub>@Au core-shell nanoparticles. Some works, such as those reported by *Z. Xu et al.*<sup>10</sup>, *H. Liu et al.*<sup>11</sup> and *D.A. Wheeler et al.*<sup>12</sup>, claim to have synthesized water-dispersible Fe<sub>3</sub>O<sub>4</sub>@Au core-shells via reducing a Au<sup>3+</sup> salt on previously synthesized magnetite nanoparticles surface in a similar procedure than the one described in **figure 7.1.1**, but no one provides clear evidence of the successfulness of their syntheses. In all cases **SQUID** analyses, UV-Vis plasmonic resonance and **XRD** patterns have been performed on the obtained products, but they result to be useless since they can only confirm the presence/absence of gold and magnetite in the analyzed specimen, but not whether the two different phases are forming a core-shell, not even when combined with the shown **TEM** images. In the case of *D.A. Wheeler et al.*<sup>13</sup>, they also show an interesting **TEM EDX** mapping, in which it may be observed that gold and magnetite particles are both attached together forming aggregates, but as aforementioned that fact does not imply that the Fe<sub>3</sub>O<sub>4</sub>@Au structure has been formed. In all these cases, as well as in most of the works based on this kind of core-shell formation, it is claimed that after ‘covering’ the magnetite with gold, the resulting magnetization decreases in **SQUID** analyses, and that the peaks corresponding to the Fe<sub>3</sub>O<sub>4</sub> **XRD** pattern disappear after several gold additions. Those results, however, do not mean that the core-shell has been formed. For **SQUID** analyses, this process can be explained since magnetization is expressed as ‘emu/g’ and, after adding gold, some non-magnetic-contributing mass has been added to the medium. About the claims referring to the decrease of the Fe<sub>3</sub>O<sub>4</sub> peaks in the **XRD** in favour of Au peaks increase, this fact just means that the relative amount of Fe<sub>3</sub>O<sub>4</sub>/Au changes when adding gold to the medium. In the case of UV-Vis spectra, in some works the tendency is to obtain the typical plasmon resonance centred at 500 or 550 nm after ‘coating’ the magnetite with gold, as expected for gold nanoparticles, and to undergo a blue-shift as the gold shell grows when reducing more gold on the nanostructures surface.

A similar work reported by *S. Pal, et al.*<sup>13</sup>, which is based on synthesizing hexane-dispersible gold-capped magnetite via directly reducing gold on previously formed Fe<sub>3</sub>O<sub>4</sub>@Oleylamine nanoparticles, has also been reported with no clear evidences of the desired core-shell formation.

Among all the reported magnetite-gold core-shell structures, however, a few ones show enough evidences to confirm that the desired nanostructures may have been synthesized:

*I.Y. Goon, et al.*<sup>14</sup>, for instance, have reported a very interesting work based on attaching gold nanoparticles on polyethyleneimine (PEI) – capped Fe<sub>3</sub>O<sub>4</sub> seeds (in a similar way than the ones described before) and subsequently reducing more gold around them, and obtaining the desired core-shell structure. This process, however, tend to lead to structures whose cores are formed by several magnetite nanoparticles, which remain embedded among the reduced gold, as it can be seen in the TEM images shown in the paper, which allow Fe<sub>3</sub>O<sub>4</sub> and gold phase identifications inside the obtained structures. **Figure 7.2.3** shows the general steps of the synthetic procedure:

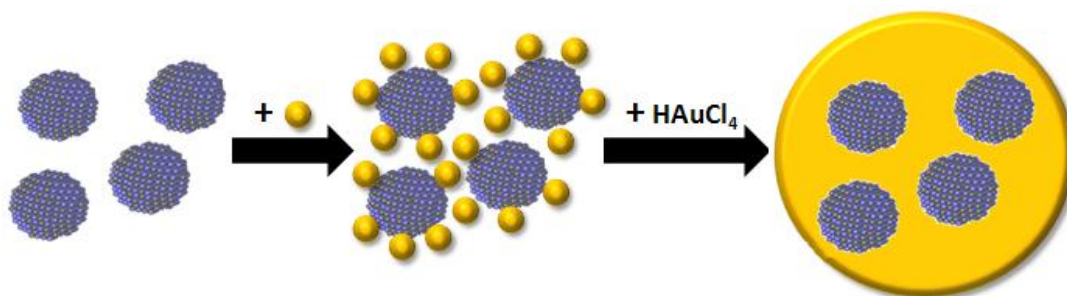


**Figure 7.2.3:** Fe<sub>3</sub>O<sub>4</sub>-Au core-shell like structures obtained by *I.Y. Goon*.

According to the authors of this work, attaching gold nanoparticles to the initially formed Fe<sub>3</sub>O<sub>4</sub> seeds is the key step of the process. In this vein, by doing so, it is likely to focus the further gold reductions on the already formed gold nanoparticles, which also protect the Fe<sub>3</sub>O<sub>4</sub> from being affected by the reduction process itself. Other similar works, such as the one reported by *S.F. Chin et al.*<sup>15</sup>, also claim to have obtained Fe<sub>3</sub>O<sub>4</sub>@Au structures via similar procedures. In those cases, however, the resulting electron microscopy pictures can only prove the formation of gold nanoparticles attached on the surface of bigger magnetite particles that act as a ‘core’, but not the further Fe<sub>3</sub>O<sub>4</sub>@Au core-shells supposedly formed when reducing HAuCl<sub>4</sub> around them.

Another interesting work, published by *S. Banerjee et al.*<sup>16</sup>, explains the synthesis of Fe<sub>3</sub>O<sub>4</sub>@Au structures obtained via reducing HAuCl<sub>4</sub> in an aqueous Fe<sub>3</sub>O<sub>4</sub> dispersion, using sodium citrate as a reducing agent and heating the reaction mixture in order to trigger the reduction process. As it can be observed in the electron microscopy images, this procedure leads to a great number of separated magnetite and gold nanoparticles,

with a few number of bigger (about 200 nm) gold structures which show a clearer region at their centre, which looks like a hollow. Despite the fact that the **TEM** images do not provide unquestionable evidences about the formation of the Fe<sub>3</sub>O<sub>4</sub>@Au structure since the clearer regions inside the gold nanoparticles could indeed be hollows, the very presence of these regions suggests that the initial magnetite nanoparticles affect the gold reduction in some way, leading to the creation of these structures. Another important piece of data arises when analyzing the magnetic behaviour of these nanostructures: unlike most of the published works, the magnetic studies carried out in this paper show that Magnetization of Saturation 'Ms' increases (instead of decreasing) after forming the core-shell structure. According to the authors, this fact takes place only with magnetic cores big enough to generate a Fe<sub>3</sub>O<sub>4</sub>-Au capable of trapping the conduction electrons from the Au shell and inducing a large orbital moment at the interface. Therefore, and in spite of not providing clear evidences about the Fe<sub>3</sub>O<sub>4</sub>@Au core-shell formation, this work evidences that the presence of magnetite nanoparticles in the medium affects the further gold reduction and therefore it offers some interesting data to take into account when studying core-shell formation processes.

Finally, a work published by *L. Lyon, et al.*<sup>17</sup>, explains a synthetic procedure to obtain water-dispersible Fe<sub>3</sub>O<sub>4</sub>@Au core-shells via gold reduction of HAuCl<sub>4</sub> using a mixture of sodium citrate and hydroxylamine hydrochloride, NH<sub>2</sub>OH·HCl. Again, and like most of the previous reported works, the provided **TEM** images may not confirm the formation of the desired core-shell structures, neither the magnetic studies carried out, which show no special effect of the gold shell on the magnetic behaviour. On the other hand, a very curious piece of data shows up when studying the UV-Vis spectra obtained when analyzing the synthesized nanostructures. As aforementioned, plasmon resonance usually becomes useless to determine/discard the presence of core-shells because in all works it shows the same tendency of undergoing a blue-shift when reducing more gold in the medium, as a consequence of the gold nanoparticles growth. In this case, however, it happens otherwise, since the first gold reduction leads to a blue dispersion and the further ones turns it red. According to the authors of the work, this fact happens because the magnetic core of the Fe<sub>3</sub>O<sub>4</sub>@Au alters the resulting plasmon, generating the observed atypical behaviour.

In conclusion, and after studying all the previous works, this part of the thesis has been focused in finding a way to synthesize actual gold-capped magnetite core-shells and to verify the successfulness of the work, via supplying proper evidences of the Fe<sub>3</sub>O<sub>4</sub>@Au formation.

## 7.3 Experimental procedure

### 7.3.1 Materials and reactants

Fe(NO<sub>3</sub>)<sub>3</sub>·9H<sub>2</sub>O (Aldrich, ≥98%), FeSO<sub>4</sub> (Aldrich, ≥99.5%), FeCl<sub>2</sub> (Aldrich, 98%), FeCl<sub>3</sub> (Aldrich, 97%), Hydrazine monohydrate (Aldrich, ≥98%), NaOH (Aldrich, ≥97.0%), Acetic acid (Fluka, 99.5%), HAuCl<sub>4</sub>·H<sub>2</sub>O (Aldrich, ≥49% Au basis), HCl (Panreac, 37% wt), NH<sub>3</sub> (Aldrich, 32% wt), HClO<sub>4</sub> Panreac, 32% wt), Hydroxylamine hydrochloride (ACS reagent, 98.0%), Sodium citrate dihydrate (Aldrich, ≥99%), Tetramethylammonium hydroxide (Aldrich, 25% wt), Tetraoctylammonium bromide (Aldrich, 98%) Oleylamine (Panreac), NaBH<sub>4</sub> (Fluka, >96%). All reactions were carried out in either Millipore water or toluene (AR Grade), and the resulting nanoparticles were washed with Millipore water and absolute ethanol (AR grade)

### 7.3.2 Water-dispersible core-shell structures

The following described syntheses are focused on synthesizing water-dispersible Fe<sub>3</sub>O<sub>4</sub>@Au core-shell nanostructures:

#### 7.3.2.1 Synthesis of Tetramethylammonium hydroxide (TMAOH)-capped Fe<sub>3</sub>O<sub>4</sub> nanoparticles

Fe<sub>3</sub>O<sub>4</sub>@TMAOH nanoparticles were synthesized as a precursor for the further Fe<sub>3</sub>O<sub>4</sub>@Au core-shells following a procedure similar than the one described in literature by Andrade A.L. et al,<sup>18</sup> via preparing a 25 ml acidified aqueous solution containing 1.30 g (1.03·10<sup>-2</sup> mol) of FeCl<sub>2</sub>, 3.12 g (1.98·10<sup>-2</sup> mol) of FeCl<sub>3</sub> and 0.85 ml of HCl (37% wt.) and adding it dropwise into 250 ml of aqueous KOH 1M, forming a black precipitate of Fe<sub>3</sub>O<sub>4</sub>, which was magnetically separated and washed with water and with a 0,1M TMAOH water solution. Finally, the obtained Fe<sub>3</sub>O<sub>4</sub>@TMAOH nanoparticles were redispersed in 50 ml of water.

#### 7.3.2.2 Synthesis of Hexa-μ<sub>2</sub>-acetato-triaqua-μ<sub>3</sub>-oxo-triiron (III) nitrate acetic acid solvate, [Fe<sub>3</sub>O(OCOCH<sub>3</sub>)<sub>6</sub>(H<sub>2</sub>O)<sub>3</sub>]·NO<sub>3</sub>

[Fe<sub>3</sub>O(OCOCH<sub>3</sub>)<sub>6</sub>(H<sub>2</sub>O)<sub>3</sub>]·NO<sub>3</sub>, which works as an iron (III) source for some of the further iron oxide nanoparticles synthesis, was prepared by following the procedure described in **section 6.2.2**.



### 7.3.2.3 Hydrothermal synthesis of hydrazine (NH<sub>2</sub>NH<sub>2</sub>)- capped Fe<sub>3</sub>O<sub>4</sub> nanoparticles

The synthesis of Fe<sub>3</sub>O<sub>4</sub>@NH<sub>2</sub>NH<sub>2</sub> was performed by following a procedure similar to the one described in **section 6.2.3**. 0.67 mmol of [Fe<sub>3</sub>O(OCOCH<sub>3</sub>)<sub>6</sub>(H<sub>2</sub>O)<sub>3</sub>]·NO<sub>3</sub> were dissolved in 20 ml of deoxygenated Millipore water. Hydrazine was added to the previously prepared solution until reaching pH= 8.60 under vigorous magnetic stirring. The resulting solution was then put into a 50 ml. Teflon-lined autoclave. The autoclave was sealed and maintained at 180 °C during 20 h, and then cooled to room temperature. The resulting nanoparticles were separated via centrifugation and washed with a mixture of Millipore water and absolute ethanol three times and then dried using a vacuum line. Finally, 0.125 g of a black solid powder were obtained. The resulting nanoparticles that form this black powder are totally water-dispersible.

### 7.3.2.4 Synthesis of 1,6-hexanediamine (H<sub>2</sub>N(CH<sub>2</sub>)<sub>6</sub>NH<sub>2</sub>)- capped Fe<sub>3</sub>O<sub>4</sub> nanoparticles using FeSO<sub>4</sub> as an iron source

Fe<sub>3</sub>O<sub>4</sub>@H<sub>2</sub>N(CH<sub>2</sub>)<sub>6</sub>NH<sub>2</sub> nanoparticles were synthesized as a precursor for the further Fe<sub>3</sub>O<sub>4</sub>@Au core-shells following a procedure described by *H. Iida, et al*<sup>19</sup>. In this vein, two solutions, one containing FeSO<sub>4</sub> 5.0·10<sup>-2</sup> M and other containing H<sub>2</sub>N(CH<sub>2</sub>)<sub>6</sub>NH<sub>2</sub> 0.25 M were prepared separately and afterwards mixed, forming a black precipitate. After vigorous stirring for 24 h, the precipitate was filtered off with a porous membrane and washed with water three times to remove excess amine molecules. The resulting Fe<sub>3</sub>O<sub>4</sub> nanoparticles were finally obtained as 0.153 g of a black powder after drying at room temperature.

### 7.3.2.5 Synthesis of 1,6-hexanediamine (H<sub>2</sub>N(CH<sub>2</sub>)<sub>6</sub>NH<sub>2</sub>)- capped Fe<sub>3</sub>O<sub>4</sub> nanoparticles using FeCl<sub>2</sub> as an iron source

Fe<sub>3</sub>O<sub>4</sub>@H<sub>2</sub>N(CH<sub>2</sub>)<sub>6</sub>NH<sub>2</sub> nanoparticles were synthesized as a precursor for the further Fe<sub>3</sub>O<sub>4</sub>@Au core-shells following a procedure similar than the one described in section 7.2.2.5 but using this time FeCl<sub>2</sub>, instead of FeSO<sub>4</sub>, as a source of iron. Also in this case, the resulting Fe<sub>3</sub>O<sub>4</sub> nanoparticles were finally obtained as 0.145 g of a black powder after drying at room temperature.

The following procedure has been carried out in order to cover the previously synthesized Fe<sub>3</sub>O<sub>4</sub> cores with a gold shell. In all cases, the used methodology has been the same, based on a modification of a method described by *L. Lyon, et al.*<sup>18</sup>, but using one different kind of synthesized Fe<sub>3</sub>O<sub>4</sub> cores in each case:



### 7.3.2.6 Formation of the gold shell around the previously synthesized magnetite cores

The previously synthesized Fe<sub>3</sub>O<sub>4</sub> nanoparticles were dispersed and diluted to 1.1 mM in 100 ml of water and then mixed with an equal volume of sodium citrate, NaCi, 0.1 M. After stirring the mixture for 60 minutes, 10 ml of the resulting solution were diluted to 100 ml of pure water, achieving a dispersion containing [Fe<sub>3</sub>O<sub>4</sub>] 5.5·10<sup>-5</sup> M and a [NaCi] 0.05 M. After stirring for 30 minutes, 1 ml of HAuCl<sub>4</sub> was added to the medium, and the reaction mixture was stirred during 30 more minutes until it reached a yellow colouring. Finally, 0.5 ml of NH<sub>2</sub>OH·HCl were added to the medium, reducing the gold cations around the magnetite cores and supposedly forming the desired core-shell structures.

Apart from changing the initial Fe<sub>3</sub>O<sub>4</sub> core when trying to obtain the core-shell, different kinds of HAuCl<sub>4</sub> and NH<sub>2</sub>OH·HCl additions have been tested, via changing the volume, frequency and medium conditions of the reaction, in order to optimize the recovering process, as it will be explained in detail during this chapter.

### 7.3.2.7 Gold nanoparticles formation with HAuCl<sub>4</sub> and NH<sub>2</sub>OH·HCl

Gold nanoparticles have been synthesized using exactly the same procedure described to form the gold shell around the previously synthesized magnetite cores. In this case, however, there were no Fe<sub>3</sub>O<sub>4</sub> nanoparticles in the medium, so the initial 100 ml of 1.1 mM dispersed magnetite has been replaced by 100 ml of pure water, leaving the rest of the synthetic procedure to be identical.

## 7.3.3 Organic media-dispersible core-shell structures

The following described syntheses are focused on trying to synthesize organic media-dispersible Fe<sub>3</sub>O<sub>4</sub>@Au core-shell nanostructures, even though all the tested methods have resulted unsuccessful.

### 7.3.3.1 Solvothermal synthesis of toluene colloidal dispersion of Fe<sub>3</sub>O<sub>4</sub> magnetite nanoparticles

Fe<sub>3</sub>O<sub>4</sub> nanoparticles were prepared via solvothermal decomposition of metal acetylacetonates in oleylamine, following exactly the same synthetic procedure described in **section 5.2.2**, yet dispersing the obtained nanoparticles in 25 ml of toluene.

### 7.3.3.2 Formation of the gold shell around the previously synthesized Fe<sub>3</sub>O<sub>4</sub>@Oleylamine cores in toluene medium

0.055 g (1.60·10<sup>-4</sup> mol) of HAuCl<sub>4</sub> were firstly dissolved in 10 ml of water and afterwards passed to 50 ml of toluene via successive extractions using 0.060 g (1.08·10<sup>-4</sup> mol) of tetraoctylammonium bromide (TOAB) as a transfer agent. 10 ml of the resulting gold-TOAB toluene solution were mixed with 2 ml of the toluene dispersed

Fe<sub>3</sub>O<sub>4</sub>@Oleylamine nanoparticles and 60 µl ( $1.28 \cdot 10^{-4}$  mol) of oleylamine. The resulting dispersion was flushed to 50 ml of toluene and heated to 120 °C during 3h, but no change was observed indicating the formation of gold nanoparticles or core-shell structures. This procedure was repeated via doubling and tripling the amount of oleylamine, without obtaining different results.

### 7.3.3.3 Formation of the gold shell around the previously synthesized Fe<sub>3</sub>O<sub>4</sub>@Oleylamine cores in oleylamine medium

2 ml of the previously obtained toluene dispersed Fe<sub>3</sub>O<sub>4</sub>@Oleylamine nanoparticles ( $2.64 \cdot 10^{-6}$  mol of Fe<sub>3</sub>O<sub>4</sub>) were mixed with 5 ml of Oleylamine and then heated to 85 °C. 0.110 g ( $3.20 \cdot 10^{-4}$  mol) of HAuCl<sub>4</sub> were firstly dissolved in 2 ml of ethanol (96% w) and then added dropwise into the oleylamine hot dispersion. It was kept at the same temperature during 3 h with magnetic stirring, obtaining a red dispersion. The resulting product was separated via centrifugation, washed with ethanol and re-dispersed in 25 ml of hexane, obtaining a room temperature stable red dispersion.

### 7.3.3.4 Synthesis of oleylamine capped- gold nanoparticles

This synthesis was carried out in a similar way than the previous core-shell described procedure, but without adding magnetite nanoparticles to the medium. 0,110 g ( $3.20 \cdot 10^{-4}$  mol) of HAuCl<sub>4</sub> were firstly dissolved in 2 ml of ethanol (96% w) and then added dropwise into 5 ml of oleylamine at 85 °C. It was kept at the same temperature during 3 h with magnetic stirring, obtaining a red dispersion. The resulting product was separated via centrifugation, washed with ethanol and re-dispersed in 25 ml of hexane, obtaining a room temperature stable red dispersion.

## 7.4 Characterization and results discussion

All the experiments carried out in order to synthesize the desired Fe<sub>3</sub>O<sub>4</sub>@Au core-shell structures, as well as all the obtained results, are described and discussed in this section. The whole study has been carried out via the following analytical techniques:

- Transmission electron microscopy (**TEM**) and high resolution electron microscopy (**HRTEM**) Bright Field microphotographs.
- Fourier Fast Transformation image analysis.
- Electron diffraction.
- Powder X-Ray diffraction.
- **EF-TEM** analysis.
- High Angle Annular Dark Field (**HAADF**)
- **SQUID** and **FC/ZFC** magnetic studies

Transmission Electron Microscope (TEM) images were obtained on a Philips Tencai 20 at an accelerating voltage of 200 kV. Electron diffraction patterns were obtained on a Philips Tencai 20 at an accelerating voltage of 200 kV. X-ray powder TEM (HRTEM) analysis was carried out in a Jeol JEM2010F field emission gun (FEG) microscope with a 0.19 nm point to point resolution. The obtained data have been treated using the Gatan software package, Digital Micrograph. Energy-dispersive X-ray spectra have been obtained at 200 kV using Titan and FEI Tecnai F20 field emission gun (FEG) TEMs. UV-Visible spectra have been recorded on a Hewlett Packard: model 8453. diffraction (XRD) patterns of the samples were recorded with a Rigaku D diffractometer equipped with a rotating anode and a CuK $\alpha$  source ( $\lambda$ = 0.154056 nm).

#### 7.4.1 Organic media-dispersible Fe<sub>3</sub>O<sub>4</sub>@Au using Fe<sub>3</sub>O<sub>4</sub>@Oleylamine as a core

The results obtained when trying to synthesize organic media-dispersible Fe<sub>3</sub>O<sub>4</sub>@Au core-shells are described and discussed as follows:

With the aim of synthesizing organic-media dispersible Fe<sub>3</sub>O<sub>4</sub>@Au core-shells, the already synthesised and described (see Chapter 5 of this thesis) oleylamine-capped magnetite nanoparticles were used as a core for the further gold shell formation. Toluene was chosen as a medium where to carry out the synthetic attempts since gold cations from HAuCl<sub>4</sub> may be transferred from water to this medium via following a method reported by *M. Brust et al*<sup>20</sup>, which uses tetraoctylammonium bromide (TOAB) as a transfer agent. After transferring all the gold to a toluene dispersion of Fe<sub>3</sub>O<sub>4</sub>@Oleylamine nanoparticles, the gold reduction was carried out via two different methods: using sodium borohydride (NaBH<sub>4</sub>) as a reducing agent or adding more oleylamine and heating the reaction mixture to 110 °C during 3 h. In the first case, which was based on the idea of reducing the previously transferred gold<sup>21</sup>, it was doable to synthesize gold nanoparticles in absence of magnetite ones, but not to obtain any gold particle or shell formation when there were Fe<sub>3</sub>O<sub>4</sub> nanoparticles in the toluene. Similar results were obtained when trying to reduce the transferred gold by adding oleylamine and heating, leading both reactions to totally non-dispersible gold and magnetite precipitates. TEM images were taken from the final toluene dispersion, but no particles were found in any case. **Figure 7.4.1.1** shows the gold nanoparticles obtained when reducing gold in toluene using NaBH<sub>4</sub> in absence of Fe<sub>3</sub>O<sub>4</sub>@Oleylamine nanoparticles, as well as the different resulting dispersions obtained when carrying out the same reaction in presence or absence of them:

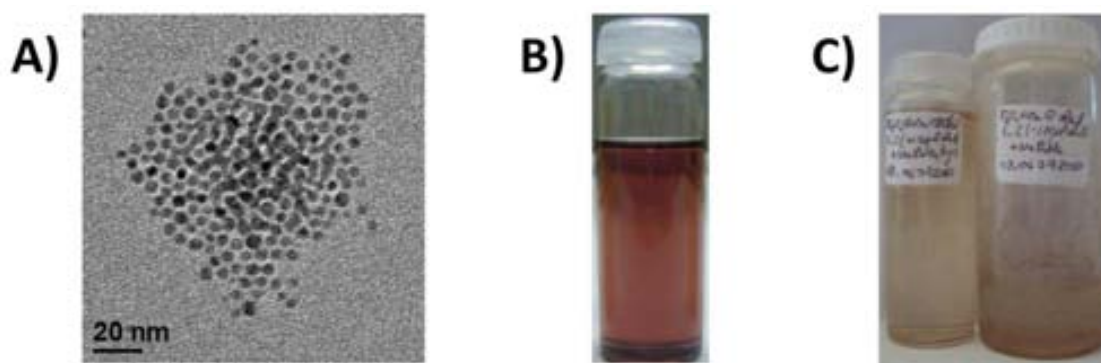


**Figure 7.4.1.1:** Images of A) Gold nanoparticles synthesized in toluene in absence of Fe<sub>3</sub>O<sub>4</sub>@Oleylamine, B) Appearance of the dispersion corresponding to the nanoparticles shown in 'A' and C) Appearance of the dispersion corresponding to the gold reductions in toluene with using NaBH<sub>4</sub> (left) and Oleylamine (right) as a reducing agents.

The obtained results suggest that, far from working as a seeds where to reduce the gold and form the desired gold shell, the magnetite nanoparticles make the medium unstable for the gold to form nanoparticles when reducing it in toluene. This happens especially in the case of gold reduction via NaBH<sub>4</sub>, in which the formed nanoparticles are stabilized only by electrostatic charges and not by a proper ligand. Similar conclusions may be reached from the results obtained when oleylamine has been used as a reducing agent. Even though it has proved to be a good capping agent (see chapter 5), it results to be useless when just adding a small quantity to the reaction medium.

As a consequence, the Fe<sub>3</sub>O<sub>4</sub>@Au synthesis was tested via reducing gold in a oleylamine medium in which magnetite nanoparticles had been previously dispersed. In this case, the initially yellow dispersion turned intense red after heating to 85 °C and keeping it for 3 h. The gold reduction was also carried out without previously dispersing magnetite nanoparticles into the medium, also observing a change in the dispersion's colour from yellow to red. The **TEM** analyses carried out on both syntheses (with and without any presence of Fe<sub>3</sub>O<sub>4</sub>@Oleylamine nanoparticles) are shown in **figure 7.4.1.2**:

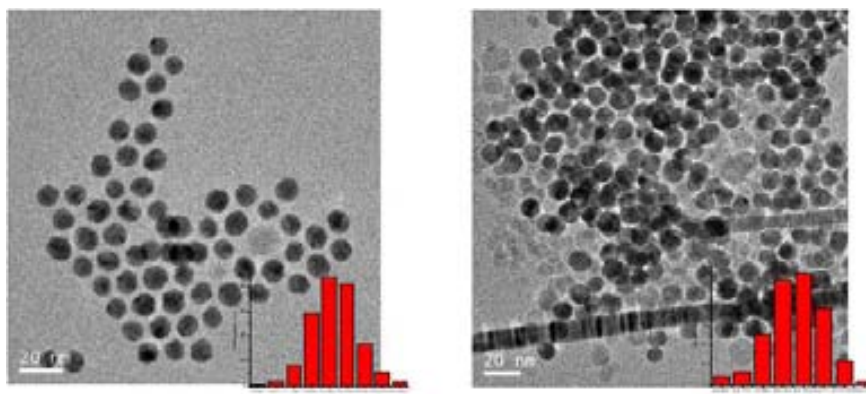


**Figure 7.4.4.2:** TEM images corresponding to Au@Oleylamine nanoparticles synthesized in absence (left) or presence (right) of magnetite seeds.

The first important piece of data that arises when studying the TEM images reveals that no core-shell structures have been formed, since magnetite nanoparticles can be clearly seen (with less contrast) in the image, without any kind of coating, and separated from the formed gold nanoparticles, which show more contrast. Apart from this fact, it can also be seen that in both cases gold nanoparticles are properly formed, with no general changes neither in their size (about 8-9 nm) nor in their shape, since most of them have a spherical-like shape. However, it has been observed that the presence of magnetite nanoparticles lead to the formation of a certain number of gold nanorods, which confirms that the very Fe<sub>3</sub>O<sub>4</sub>@Oleylamine particles affect the gold reduction process.

### 7.4.2 Water-dispersible Fe<sub>3</sub>O<sub>4</sub>@Au using Fe<sub>3</sub>O<sub>4</sub>@TMAOH as a core

The results obtained when trying to synthesize water-dispersible Fe<sub>3</sub>O<sub>4</sub>@Au core-shells are described as well as discussed as follows:

As aforementioned, different kinds of magnetite nanoparticles have been synthesized with the aim of using them as a magnetic core for the further core-shell formation. In the most cases, the gold-capping method has been based on a modification of the one described by *L. Lyon, et al.*<sup>18</sup>, since it appears to offer more chances of controlling and limiting the gold reduction process around the previously synthesized Fe<sub>3</sub>O<sub>4</sub> nanoparticles, in comparison with all the other described methods. This one involves combining both sodium citrate, NaCi, and hydroxylamine hydrochloride, NH<sub>2</sub>OH·HCl, as reducing agents. The use of citrate to reduce gold, which has been studied in depth in some different works<sup>21,22</sup>, involves adding a gold salt to a sodium citrate solution and heating to trigger the reduction process. When adding NH<sub>2</sub>OH·HCl to the medium, however, this process occurs at room temperature, softening the reaction conditions, which turns out to be mandatory when trying to control the capping process. In addition, a work published by *L. O. Cisneros, et al.*<sup>23</sup>, establishes that hydroxylamine decomposes when dissolved in water, either alone or in the presence of some metal surfaces, such as iron oxides with a release of energy. This fact may ease the control of the gold reduction around the Fe<sub>3</sub>O<sub>4</sub> nanoparticles surface since it specially triggers the reaction in the regions surrounding the further magnetic cores.

Tetramethylammonium hydroxide (TMAOH) -capped Fe<sub>3</sub>O<sub>4</sub> nanoparticles were first synthesized as a core for the further Fe<sub>3</sub>O<sub>4</sub>@Au core-shell formation following the previously described method (see **section 7.2.2.1**). TEM images show the presence of aggregated nanoparticles with an average diameter of  $9.4 \pm 1.9$  nm (**figure 7.4.2.1**). The electron diffraction spectrum showed the expected interplanar distances for Fe<sub>3</sub>O<sub>4</sub>:

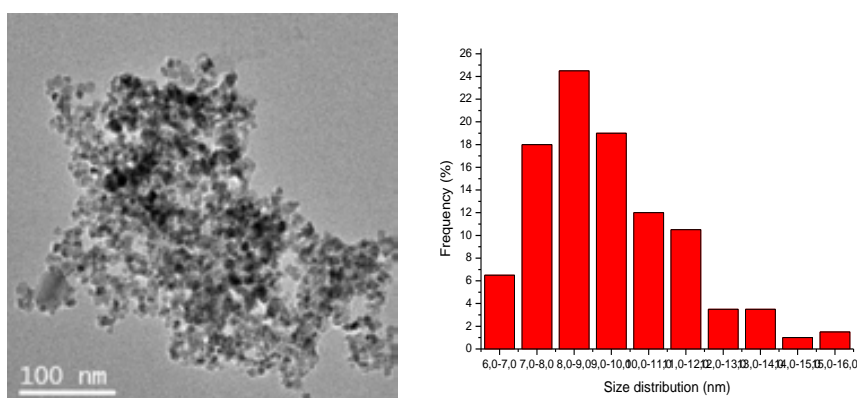


**Figure 7.4.2.1:** TEM image (left) corresponding to Fe<sub>3</sub>O<sub>4</sub>@TMAOH nanoparticles and their corresponding size distribution histogram (right).

Gold reduction around Fe<sub>3</sub>O<sub>4</sub>@TMAOH nanoparticles was carried out via using NH<sub>2</sub>OH·HCl and NaCl as described in **section 7.2.2.7**. After adding gold and hydroxylamine for the first time, the initially colourless (as a result of the small concentration of particles) magnetite dispersion turned purple. Further Au/NH<sub>2</sub>OH·HCl additions made the dispersion end up turning intense red. **Figure 7.4.2.2** shows aliquots taken from the original dispersion after every gold or hydroxylamine addition:

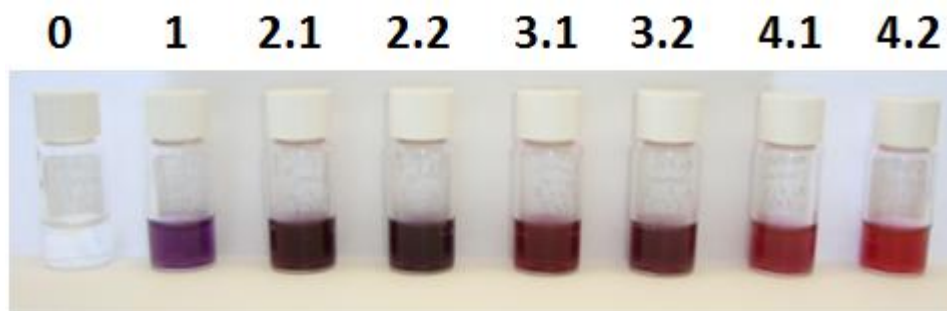


**Figure 7.4.2.2:** Different aliquots obtained from the original Fe<sub>3</sub>O<sub>4</sub> and Au dispersion (0) after further gold (X.1) and hydroxylamine (X.2) additions.

Therefore, a blue-shift was observed in the plasmon resonance series, which matches with the results obtained by *L. Lyon, et al.*<sup>18</sup>, which is shown in **figure 7.4.2.3**.

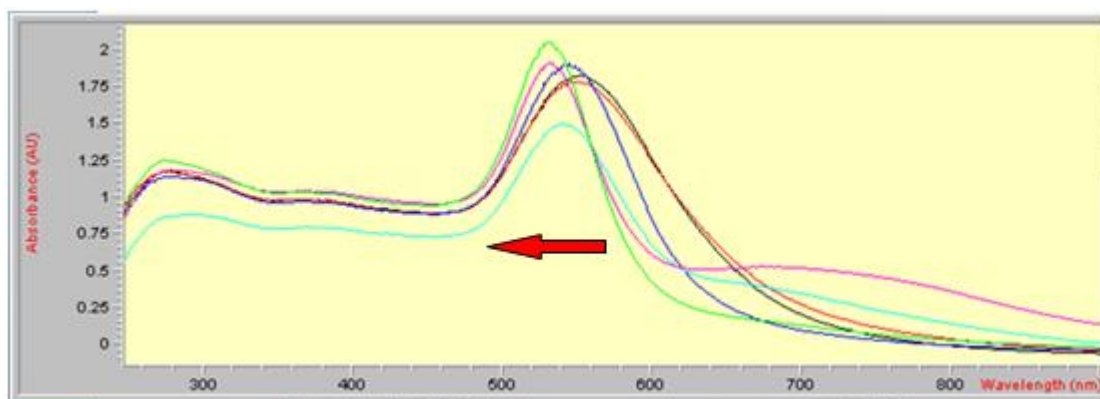


**Figure 7.4.2.3:** Plasmon resonance series obtained from the aliquots shown in the previous image.

**TEM** images show a clear growth in nanoparticles size when adding more gold to the medium, as it can be seen in **table 7.4.2.1**, which also matches with the inverse tendency of the plasmon resonance of undergoing a blue-shift displacement when gold nanoparticles grow. However, the results also show that the size deviation increases with the gold nanoparticles size after each addition and further reduction of gold. This fact is explained by the formation of smaller and irregular-shaped gold nanoparticles (of about 8.0 nm) which are formed during the whole process. Therefore, the observed blue-shift displacement of the plasmon resonance series may be given by the formation of those smaller particles and not by the magnetic effect of the supposed magnetite cores.

Addition	Size average
1	21,6 ± 5,3nm
2.2	24,7 ± 5,8nm
3.2	29,2 ± 6,5nm
4.2	33.3 ± 7.0 nm

**Table 7.4.2.1:** Size average of the gold nanoparticles obtained after each addition of both gold and hydroxylamine.

**Figure 7.4.2.4** shows **TEM** images corresponding to different aliquots of the analyzed series, as well as the smaller gold nanoparticles formed during the whole process:

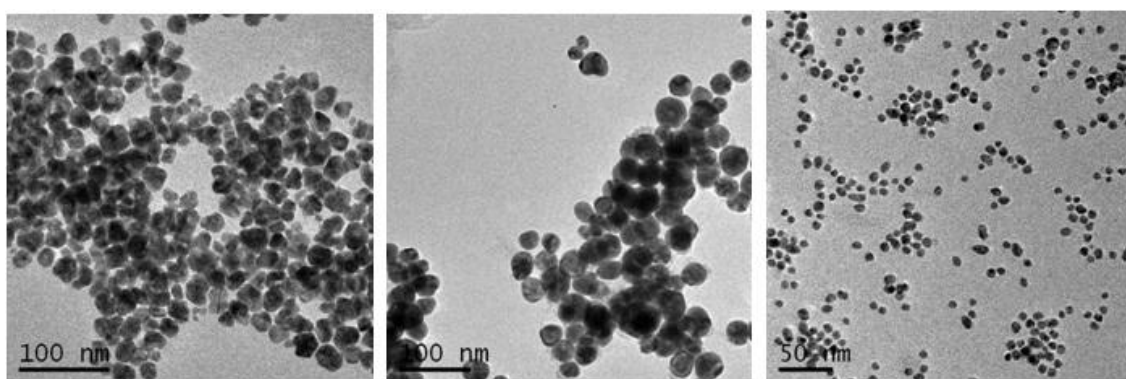


**Figure 7.4.2.4:** TEM images corresponding to aliquots 1 (left) and 4.2 (middle) of the obtained series, as well as the smaller nanoparticles (right) formed during the gold reduction process.

A very important piece of data, however, arises when analyzing the **TEM** images in depth. As it can be observed in the middle image of the last figure, the biggest formed nanoparticles have inner regions that appear brighter than the rest of the surrounding gold. So as to study those particles more in depth, High resolution Bright field (**HR BFTEM**) images have been taken from those particles, confirming the presence of these regions of less electron density. In all cases spherical regions of about 7-9 nm showing different electronic density can be observed, as shown in **figure 7.4.2.5**. By comparing both the size and the shape of these regions with the Fe<sub>3</sub>O<sub>4</sub>@TMAOH nanoparticles used as a 'core', it is perfectly right to affirm that the gold has been successfully reduced around the magnetite particles surface.



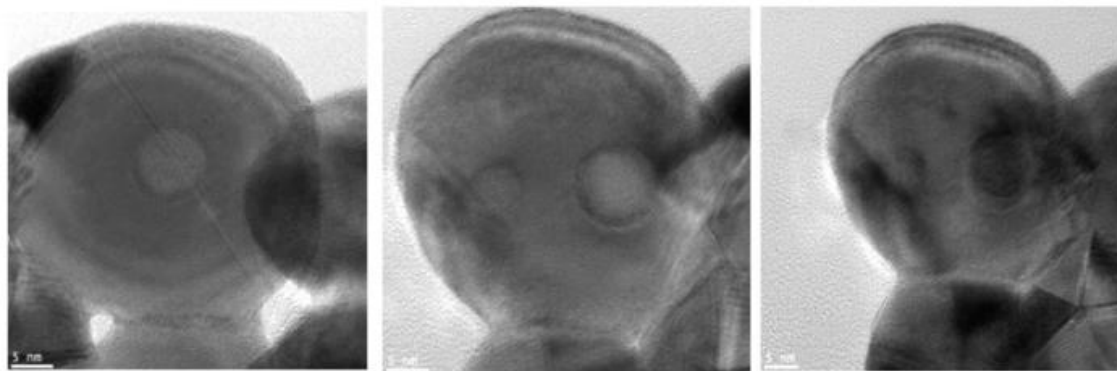


**Figure 7.4.2.5:** High resolution BF images taken from the supposed Fe<sub>3</sub>O<sub>4</sub>@Au synthesized nanoparticles, confirming the presence of cores with different sizes inside the gold structures.

In order to confirm/discard the presence of magnetite inside the formed gold nanoparticles, Z-Contrast (or HAADF) was carried out, taking EELS spectra from the inner regions of the nanostructures. The Z-Contrast images, as shown in **figure 7.4.2.6**, confirm the presence of different regions (with less electron density) inside the formed particles. EELS spectra obtained from those regions, however, may not confirm the presence of Fe<sub>3</sub>O<sub>4</sub> for no iron signal may be observed (see **figure 7.4.2.7**)

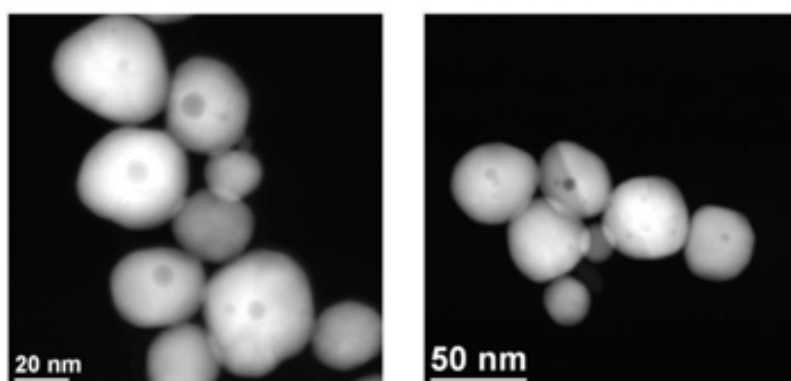


**Figure 7.4.2.6:** Z-Contrast images taken from the biggest formed gold nanoparticles with different regions inside them.

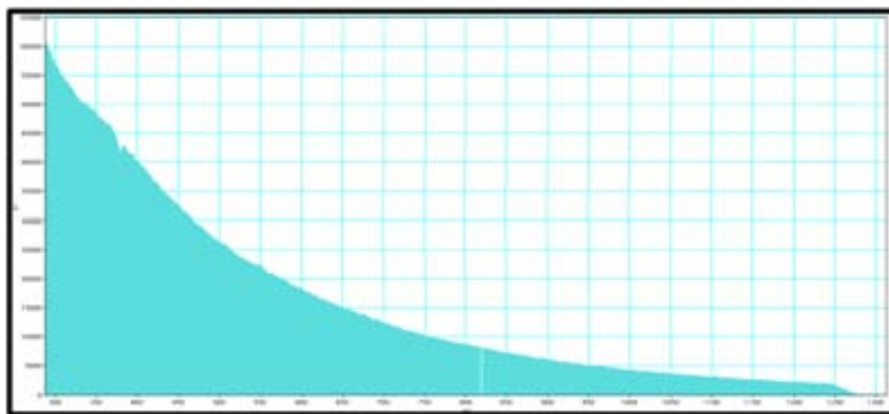


**Figure 7.4.2.6:** Example of an **EELS** spectrum taken from the inner regions that observed in the Z-Contrast images.

In spite of not being able to confirm the presence of magnetite inside the synthesized gold nanoparticles, it can neither be discarded because the gold shell formed around the observed different regions is thick enough to hinder the iron detection of the EELS analysis.

Therefore, and in order to reduce the thickness of the formed gold shell, **HR BF TEM** analyses were carried out on aliquots with less Au/NH<sub>2</sub>OH·HCl additions. In those cases, however, it may be observed that a large number of magnetite nanoparticles still remain free and surrounding the formed gold clusters, as it has been determined via both direct **TEM** and live **FFT** images. **Figure 7.4.2.7** shows a region formed by small Fe<sub>3</sub>O<sub>4</sub> and gold nanoparticles, which may be found along the entire prepared specimen, surrounding the bigger gold clusters formed during the gold/hydroxylamine additions:

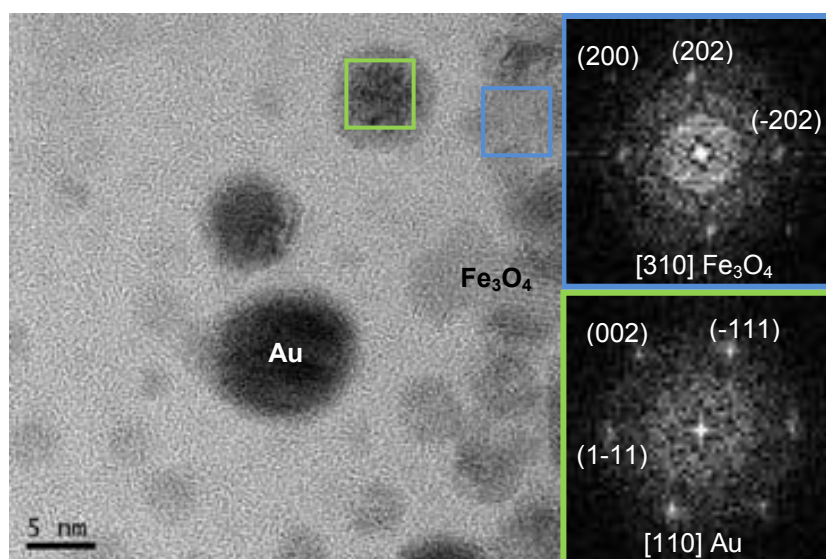


**Figure 7.4.2.7:** **BF TEM** and live **FFT** images taken from aliquots with less Au/NH<sub>2</sub>OH·HCl additions.

Since the presence of magnetite nanoparticles makes further **EELS** analyses useless when trying to determine the presence of Fe<sub>3</sub>O<sub>4</sub> inside the formed gold clusters, another approach based on using bigger magnetite nanoparticles as a ‘seeds’ for the further gold reduction was carried out. This synthetic procedure was done in order to synthesize and properly analyze the desired core-shells which could be more likely detected when carrying out Z-contrast analyses. With this aim, two different magnetite nanoparticles, recovered by hydrazine and 1,6-hexanediamine, respectively, were synthesized.

The first ones were bigger than the previously used Fe<sub>3</sub>O<sub>4</sub>@TMAOH particles but proved to be a wrong choice when trying to cover them with gold. Different attempts have led to gold nanoparticles showing no sign of any different phase inside, mixed with the non-covered magnetite nanoparticles, as it can be seen in **figure 7.4.2.8**:

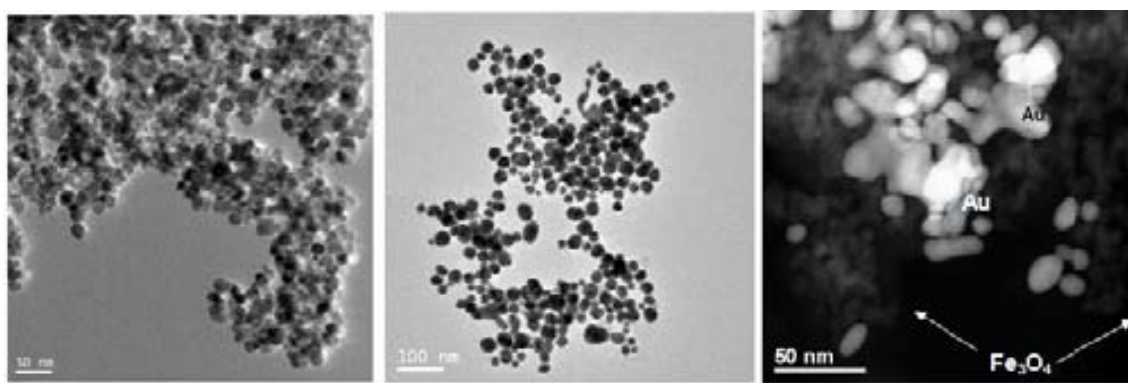


**Figure 7.4.2.8:** BF TEM and Z-contrast images of the hydrazine-capped magnetite nanoparticles used as a ‘core’ (left image) and the resulting magnetite and gold mixture of nanoparticles (center and right images)

The total failure when reducing gold around these magnetite nanoparticles, in which it may not even be suspected a magnetite-gold interaction, cannot be attributed to the original magnetite aggregation since both these nanoparticles and the Fe<sub>3</sub>O<sub>4</sub>@TMAOH ones used previously as a ‘core’ had shown a certain aggregation degree. In addition, in both cases the magnetite particles were re-dispersed in a sodium citrate solution and surrounded by citrate anions before adding the gold and reducing it with hydroxylamine. This fact leads to considering the effect of both the nature of the original capping agent, which may interfere with the subsequent gold reduction process, and the cores size, which may play an important role when trying to reduce the gold.

Bigger magnetite nanoparticles (capped with 1,6-hexanediamine) were synthesized in order to check the size effect in the further gold reduction process. By following the procedure described in literature<sup>24</sup>, 1,6-hexanediamine- capped Fe<sub>3</sub>O<sub>4</sub> nanoparticles with a size of  $24.0 \pm 6.3$  nm and a faceted shape were obtained and used as a seeds were to grow the desired gold shell. In that case, as it can be observed in **figure 7.4.2.9**, the

obtained gold shells, which have a medium size of  $37.0 \pm 8.9$  nm clearly show faceted regions with less electron density that look clearer in the **BF TEM** images:

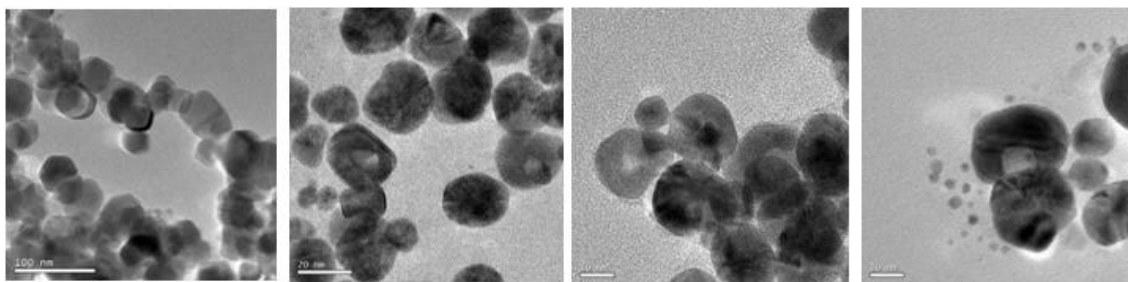


**Figure 7.4.2.9:** BF TEM images taken from the 1,6-hexadamine – capped Fe<sub>3</sub>O<sub>4</sub> nanoparticles (left) and gold shells with clearer inner regions.

As observed when analyzing the first core-shell obtained with the Fe<sub>3</sub>O<sub>4</sub>@TMAOH nanoparticles, the inner clear regions of the gold shells match in size (but not in shape) with the magnetite nanoparticles, which indicates that those gold structures have been formed around the magnetite nanoparticles and confirms that the core size does not interfere with the further gold reduction process, being the capping agent a key factor in this process. In this case, besides, it can be observed when paying attention to the last image of the **figure 7.4.2.9**, in which one gold particle is properly oriented, that those clearer regions are not magnetite nanoparticles yet holes formed as a result of iron oxide decomposition during the gold reduction process. This hypothesis is backed by the fact that smaller magnetite nanoparticles, which did not appear when studying the original magnetic cores, are surrounding the gold structures. This decomposition is attributed to the very nature of the gold source, HAuCl<sub>4</sub>, which acts as an acid when solved in water, and may decompose some kinds of iron oxides.

## 7.5 Summary

In this work, Fe<sub>3</sub>O<sub>4</sub>@Au core-shell nanoparticles have been attempted to synthesize via reducing a source of gold (HAuCl<sub>4</sub>) in both aqueous and organic media, with unsuccessful results in both cases. The whole processes have been studied chiefly via TEM techniques, such as **BF TEM** images, Z-Contrast and **EELS**.

The organic media approach has been based on using the oleylamine capped magnetite nanoparticles described in chapter 5 as a 'core' where to perform the gold reduction, which has been tested in both toluene and oleylamine, using sodium borohydride, NaBH<sub>4</sub>, and oleylamine, respectively, as reducing agents. When the reaction has been carried out in toluene, a precipitate formed by gold and magnetite, unredispersable in any medium has been obtained, clearly showing that the synthetic procedure had failed. When running the reaction in oleylamine, however, it has been observed a gold nanoparticles formation, but not the desired core-shell structures.

The aqueous medium tests, on the other hand, have shown very interesting results, yet not core-shells have been obtained. As it can be observed after reducing the HAuCl<sub>4</sub> around some of the magnetite nanoparticles, the resulting gold structures show inner regions with less electron density than the outer shells. In addition, those regions match both in size and shape with the Fe<sub>3</sub>O<sub>4</sub> nanoparticles used as cores, which suggests that the gold reduction has, indeed, took place around the magnetite's surface.

Unfortunately, it has also been observed that the iron oxide particles decompose during the gold reduction process, fact that is attributed to the very acidic nature of the HAuCl<sub>4</sub>.

## 7.6 Related literature

- 
- <sup>1</sup> Liang R.-P.; Yao G.-H.; Fan L.-X.; Qiu J.-D., *Anal. Chim. Acta*, **2012**, 737, 22-28.
- <sup>2</sup> Qiu J.-D.; Xiong M.; Liang R.-P.; Peng H.-P.; Liu F., *Biosens. Bioelectron.*, **2009**, 24, 2649-2653.
- <sup>3</sup> Cui Y.-R.; Hong C.; Zhou Y.L.; Li Y.; Gao X.-M.; Zhang X.-X., *Talanta*, **2011**, 85, 1246-1252.
- <sup>4</sup> Reddy A. N., *Chem. Plus. Chem.*, **2012**, 77, 284-292.
- <sup>5</sup> Lou, L.; Yu K.; Zhang Z.; Huang R.; Zhu J.; Wang Y.; Zhu Z., *Nano. Res.*, **2012**, 5, 272-282.
- <sup>6</sup> Lim J.; Eggeman A.; Lanni F.; Tilton R.D.; Majetich S.A., *Adv. Mater.*, **2008**, 20, 1721-1726.
- <sup>7</sup> Bao J.; Chen W.; Liu T.; Zhu Y.; Jin P.; Wang L.; Liu J.; Wei Y., Li Y., *ACS Nano*, **2007**, 1, 293-298.
- <sup>8</sup> Lou L.; Yu K.; Zhang Z.; Huang R.; Wang Y.; Zhu Z., *Appl. Surf. Sci.*, **2012**, 258, 8521-8526.
- <sup>9</sup> Ren J., Shen S.; Pang Z.; Lu X.; Deng C.; Jiang X., *Chem. Commun.*, **2011**, 47, 11692-11694.
- <sup>10</sup> Xu Z.; Hou Y.; Sun S., *J. Am. Chem. Soc.*, **2007**, 129, 8698-8699.
- <sup>11</sup> Liu H.; Hou P.; Zhang W.X.; Wu J.H., *Colloids Surf., A*, **2010**, 356, 21-27.
- <sup>12</sup> Wheeler D. A.; Adams S.A.; Lopez-Luke T.; Torres-Castro A.; Zhang J.Z., *Ann. Phys.*, **2012**, 524, 670-679.
- <sup>13</sup> Pal S.; Morales M.; Mukherjee P.; Srikanth H., *J. Appl. Phys.*, **2009**, 105, 07B504/1-07B504/3.
- <sup>14</sup> Goon I. Y.; Lai L.M.H.; Lim M.; Munroe P.; Gooding J. Justin; Amal R., *Chem. Mater.*, **2009**, 21, 673-681.
- <sup>15</sup> Chin S. F., Iyer K.S.; Raston C.L., *Cryst. Growth Des.*, **2009**, 9, 2685-2689.
- <sup>16</sup> Banerjee S.; Raja S.O.; Sardar M.; Gayathri N.; Ghosh B.; Dasgupta A., *J. Appl. Phys.*, **2011**, 109, 123902/1-123902/7.
- <sup>17</sup> Lyon L. J.; Fleming D.A.; Ston M.B.; Schiffer P.; Williams M.E., *Nano Lett.*, **2004**, 4, 719-723.
- <sup>18</sup> Andrade A.L.; Souza D.M.; Pereira M.C.; Fabris J.D.; Domingues R.S., *Química Nova*, **2010**, 33, 524-527.
- <sup>19</sup> Iida H.; Takayanagi K.; Nakanishi T.; Osaka T., *J. Colloid Interface Sci.*, **2007**, 314, 274-280.
- <sup>20</sup> Brust M.; Walker M.; Bethell D.; Schiffrin D.J.; Whyman R., *J. Chem. Soc. Chem. Comm.*, **1994**, 7, 801-802.
- <sup>21</sup> Ramos M.; Ortiz-Jordan L.; Hurtado-Macias A.; Flores S.; Elizalde-Galindo J.T.; Rocha C.; Torres B.; Zarei-Chaleshtori M.; Chianelli R.R., *Materials*, **2013**, 6, 198-205.
- <sup>22</sup> Li C.; Li D.; Wan G.; Xu J.; Hou W., *Nanoscale Res. Lett.*, **2011**, 6, 440-450.
- <sup>23</sup> Cisneros L. O., *J. Chem. Eng. Data*, **2003**, 48, 1165-1169.
- <sup>24</sup> Iida H.; Takayanagi K.; Nakanishi T.; Osaka T., *J. Colloid Interface Sci.*, **2007**, 314, 274-280.

# Notes







